

NATIONAL AERONAUTICS AND SPACE ADMINISTRATION

Technical Report 32-1526

Volume XVII

The Deep Space Network

Progress Report

For July and August 1973

JET PROPULSION LABORATORY
CALIFORNIA INSTITUTE OF TECHNOLOGY
PASADENA, CALIFORNIA

October 15, 1973

Prepared Under Contract No. NAS 7-100
National Aeronautics and Space Administration

Preface

This report presents DSN progress in flight project support, TDA research and technology, network engineering, hardware and software implementation, and operations. Each issue presents material in some, but not all, of the following categories in the order indicated:

Description of the DSN

Mission Support

- Interplanetary Flight Projects
- Planetary Flight Projects
- Manned Space Flight Projects
- Advanced Flight Projects

Radio Science

Supporting Research and Technology

- Tracking and Ground-Based Navigation
- Communications, Spacecraft/Ground
- Station Control and Operations Technology
- Network Control and Data Processing

Network Engineering and Implementation

- Network Control System
- Ground Communications
- Deep Space Stations

Operations and Facilities

- Network Operations
- Network Control System Operations
- Ground Communications
- Deep Space Stations
- Facility Engineering

In each issue, the part entitled "Description of the DSN" describes the functions and facilities of the DSN and may report the current configuration of one of the five DSN systems (Tracking, Telemetry, Command, Monitor and Control, and Test and Training).

The work described in this report series is either performed or managed by the Tracking and Data Acquisition organization of JPL for NASA.

Contents

DESCRIPTION OF THE DSN

DSN Functions and Facilities	1
---	----------

N. A. Renzetti

MISSION SUPPORT

Planetary Flight Projects

Mariner Venus/Mercury 1973 Mission Support	5
---	----------

E. K. Davis

NASA Code 311-03-21-60

Viking Mission Support	9
---	----------

D. J. Mudgway

NASA Code 311-03-21-70

Pioneer 10 and 11 Mission Support	14
--	-----------

R. B. Miller

NASA Code 311-03-21-20

SUPPORTING RESEARCH AND TECHNOLOGY

Tracking and Ground-Based Navigation

X-Band Waveguide Step Transitions	17
--	-----------

H. R. Buchanan

NASA Code 310-10-64-03

High-Power Microwave Transmitter Switch	21
--	-----------

C. P. Wiggins, H. R. Buchanan, and R. L. Leu

NASA Code 310-10-64-01

Efficient Antenna Systems: DSS 14 64-Meter-Diameter Antenna Polarization Properties	28
--	-----------

P. D. Potter

NASA Code 310-10-61-04

Demonstration of Intercontinental DSN Clock Synchronization by VLBI	39
--	-----------

W. J. Hurd

NASA Code 310-10-61-01

Contents (contd)

Digital DC Offset Compensation of Analog-to-Digital Converters 45

S. S. Brokl and W. J. Hurd
NASA Code 310-10-61-01

A System Analysis of Error Sources in the Technique Used for Ionospheric Calibration of Deep Space Probe Radio Metric Data 48

K. W. Yip and B. D. Mulhall
NASA Code 310-10-60-52

Communications, Spacecraft/Ground

S/X Experiment: Preliminary Tests of the Zero Delay Device 68

T. Y. Ootshi and P. D. Batelaan
NASA Code 310-20-66-06

Computation of RF Boresight Direction From Reflector Distortions 78

M. S. Katow and M. Mori
NASA Code 310-20-65-01

A Note on Noisy Reference Detection 83

J. W. Layland
NASA Code 310-20-67-08

64-Meter-Diameter Antenna Hydrostatic Bearing Runner Joint Leak Tests 89

G. P. Gale and H. P. Phillips
NASA Code 310-20-65-01

64-Meter-Diameter Antenna With New Braces: Installation Description and Computed Performance for Gravity Loads 93

V. B. Lobb and M. S. Katow
NASA Code 310-20-65-01

Station Control and Operations Technology

DSN Research and Technology Support 100

E. B. Jackson
NASA Code 310-30-69-02

Precise Measurement of Spacecraft Signal Power 104

J. W. Newton
NASA Code 310-30-68-03

Contents (contd)

Dual-Carrier Intermodulation Caused by a Zero-Memory Nonlinearity	108
--	------------

C. A. Greenhall
NASA Code 310-30-69-01

NETWORK ENGINEERING AND IMPLEMENTATION

Network Control System

Network Control System Development	113
---	------------

J. N. Edwards
NASA Code 311-03-32-40

Deep Space Stations

A New Dual Ignitron High-Voltage Crowbar	120
---	------------

E. J. Finnegan
NASA Code 311-03-42-48

X-Band Traveling Wave Maser Amplifier	123
--	------------

D. L. Trowbridge
NASA Code 311-03-42-48

X-Band Antenna Feed Cone Assembly	131
--	------------

R. W. Hartop
NASA Code 311-03-42-48

X-Band Traveling Wave Resonator	134
--	------------

R. B. Kolbly
NASA Code 311-03-14-61

OPERATIONS AND FACILITIES

Deep Space Stations

A Re-Examination of Subcarrier Demodulator Performance	137
---	------------

J. R. Lesh
NASA Code 311-03-14-52

Bibliography	145
-------------------------------	------------

DSN Functions and Facilities

N. A. Renzetti
Mission Support Office

The objectives, functions, and organization of the Deep Space Network are summarized. The Deep Space Instrumentation Facility, the Ground Communications Facility, and the Network Control System are described.

The Deep Space Network (DSN), established by the National Aeronautics and Space Administration (NASA) Office of Tracking and Data Acquisition under the system management and technical direction of the Jet Propulsion Laboratory (JPL), is designed for two-way communications with unmanned spacecraft traveling approximately 16,000 km (10,000 mi) from Earth to planetary distances. It supports or has supported, the following NASA deep space exploration projects: Ranger, Surveyor, Mariner Venus 1962, Mariner Mars 1964, Mariner Venus 67, Mariner Mars 1969, Mariner Mars 1971, Mariner Venus-Mercury 1973 (JPL); Lunar Orbiter and Viking (Langley Research Center); Pioneer (Ames Research Center); Helios (West Germany); and Apollo (Manned Spacecraft Center), to supplement the Spaceflight Tracking and Data Network (STDN).

The Deep Space Network is one of two NASA networks. The other, STDN, is under the system management and technical direction of the Goddard Space Flight Center. Its function is to support manned and unmanned Earth-orbiting and lunar scientific and communications satellites. Although the DSN was concerned with unmanned lunar spacecraft in its early years, its primary objective now and into the future is to continue its support of planetary and interplanetary flight projects.

A development objective has been to keep the network capability at the state of the art of telecommunications and data handling and to support as many flight projects as possible with a minimum of mission-dependent hardware and software. The DSN provides direct support of each flight project through that project's tracking and

data system. This management element is responsible for the design and operation of the hardware and software in the DSN which are required for the conduct of flight operations.

Beginning in FY 1973 a modified DSN interface has been established with the flight projects. In lieu of the SFOF, a multimission Mission Control and Computing Center (MCCC) has been activated as a separate functional and management element within JPL. This function, as negotiated with each flight project, will provide all computing and mission operations support for missions controlled from JPL. DSN computing support will be provided separately by the DSN. Radio metric, telemetry, and command data interfaces with the DSN are a joint DSN, MCCC, and flight project responsibility. The organization and procedures necessary to carry out these new activities will be reported in this document in the near future.

The DSN function, in supporting a flight project by tracking the spacecraft, is characterized by five network systems:

- (1) DSN Tracking System. Generates radio metric data; i.e., angles, one- and two-way doppler and range, and transmits raw data to mission control.
- (2) DSN Telemetry System. Receives, decodes, records, and retransmits engineering and scientific data generated in the spacecraft to Mission Control.
- (3) DSN Command System. Accepts coded signals from mission control via the GCF and transmits them to the spacecraft in order to initiate spacecraft functions in flight.
- (4) DSN Monitor and Control System. Instruments, transmits, records, and displays those parameters of the DSN necessary to verify configuration and validate the network. Provides operational direction and configuration control of the network and primary interface with flight project Mission Control personnel.
- (5) DSN Test and Training System. Generates and controls simulated data to support development, test, training and fault isolation within the DSN. Participates in mission simulation with flight projects.

The facilities needed to carry out these functions have evolved in three technical areas: (1) the Deep Space Stations (DSSs) and the telecommunications interface

through the RF link with the spacecraft is known as the Deep Space Instrumentation Facility (DSIF); (2) the Earth-based point-to-point voice and data communications from the stations to Mission Control is known as the Ground Communications Facility (GCF); (3) the network monitor and control function is known as the Network Control System (NCS).

I. Deep Space Instrumentation Facility

A. Tracking and Data Acquisition Facilities

A world-wide set of Deep Space Stations with large antennas, low-noise phase-lock receiving systems, and high-power transmitters provide radio communications with spacecraft. The DSSs and the deep space communications complexes (DSCCs) they comprise are given in Table 1.

Radio contact with a spacecraft usually begins when the spacecraft is on the launch vehicle at Cape Kennedy, and it is maintained throughout the mission. The early part of the trajectory is covered by selected network stations of the Air Force Eastern Test Range (AFETR) and the STDN of the Goddard Space Flight Center.¹ Normally, two-way communications are established between the spacecraft and the DSN within 30 min after the spacecraft has been injected into lunar, planetary, or interplanetary flight. A compatibility test station at Cape Kennedy (discussed later) tests and monitors the spacecraft continuously during the launch checkout phase. The deep space phase begins with acquisition by 26-m DSSs. These and the remaining DSSs listed in Table 1 provide radio communications until the end of the mission.

To enable continuous radio contact with spacecraft, the DSSs are located approximately 120 deg apart in longitude; thus a spacecraft in deep space flight is always within the field-of-view of at least one DSS, and for several hours each day may be seen by two DSSs. Furthermore, since most spacecraft on deep space missions travel within 30 deg of the equatorial plane, the DSSs are located within latitudes of 45 deg north and south of the equator. All DSSs operate at S-band frequencies: 2110-2120 MHz for Earth-to-spacecraft transmission and 2290-2300 MHz for spacecraft-to-Earth transmission. An X-band capability is being readied for future missions beginning in 1973.

¹The 9-m (30-ft) diam antenna station established by the DSN on Ascension Island during 1965 to act in conjunction with the STDN orbital support 9-m (30-ft) diam antenna station was transferred to the STDN in July 1968.

To provide sufficient tracking capability to enable returns of useful data from around the planets and from the edge of the solar system, a 64-m (210-ft) diam antenna subnet will be required. Two additional 64-m (210-ft) diam antenna DSSs are under construction at Madrid and Canberra and will operate in conjunction with DSS 14 to provide this capability. These stations are scheduled to be operational by the middle of 1973.

B. Compatibility Test Facilities

In 1959, a mobile L-band compatibility test station was established at Cape Kennedy to verify flight-spacecraft/DSN compatibility prior to the launch of the Ranger and Mariner Venus 1962 spacecraft. Experience revealed the need for a permanent facility at Cape Kennedy for this function. An S-band compatibility test station with a 1.2-m (4-ft) diameter antenna became operational in 1965. In addition to supporting the preflight compatibility tests, this station monitors the spacecraft continuously during the launch phase until it passes over the local horizon.

Spacecraft telecommunications compatibility in the design and prototype development phases was formerly verified by tests at the Goldstone DSCC. To provide a more economical means for conducting such work and because of the increasing use of multiple-mission telemetry and command equipment by the DSN, a Compatibility Test Area (CTA) was established at JPL in 1968. In all essential characteristics, the configuration of this facility is identical to that of the 26-m (85-ft) and 64-m (210-ft) diameter antenna stations.

The JPL CTA is used during spacecraft system tests to establish the compatibility with the DSN of the proof test model and development models of spacecraft, and the Cape Kennedy compatibility test station is used for final flight spacecraft compatibility validation testing prior to launch.

II. Ground Communications Facility

The GCF provides voice, high-speed data, wideband data, and teletype communications between the Mission Operations Center and the DSSs. In providing these capabilities, the GCF uses the facilities of the worldwide NASA Communications Network (NASCOM)² for all long

²Managed and directed by the Goddard Space Flight Center.

distance circuits, except those between the Mission Operations Center and the Goldstone DSCC. Communications between the Goldstone DSCC and the Mission Operations Center are provided by a microwave link directly leased by the DSN from a common carrier.

Early missions were supported by voice and teletype circuits only, but increased data rates necessitated the use of high-speed and wideband circuits for DSSs. Data are transmitted to flight projects via the GCF using standard GCF/NASCOM formats. The DSN also supports remote mission operations centers using the GCF/NASCOM interface.

III. Network Control System

The DSN Network Control System is comprised of hardware, software, and operations personnel to provide centralized, real-time control of the DSN and to monitor and validate the network performance. These functions are provided during all phases of DSN support to flight projects. The Network Operations Control Area is located in JPL Building 230, adjacent to the local Mission Operations Center. The NCS, in accomplishing the monitor and control function does not alter, delay, or serially process any inbound or outbound data between the flight project and tracking stations. Hence NCS outages do not have a direct impact on flight project support. Voice communications are maintained for operations control and coordination between the DSN and flight projects, and for minimization of the response time in locating and correcting system failures.

The NCS function will ultimately be performed in data processing equipment separate from flight project data processing and specifically dedicated to the NCS function. During FY 1973, however, DSN operations control and monitor data will be processed in the JPL 360/75 and in the 1108. In FY 1974 the NCS data processing function will be partly phased over to an interim NCS processor, and finally, in FY 1975, the dedicated NCS data processing capability will be operational. The final Network Data Processing Area will be located remote from the Network Operations Control Area so as to provide a contingency operating location to minimize single point of failure effects on the network control function. A preliminary description of the NCS appears elsewhere in this document.

Table 1. Tracking and data acquisition stations of the DSN

DSCC	Location	DSS	DSS serial designation	Antenna		Year of initial operation
				Diameter, m (ft)	Type of mounting	
Goldstone	California	Pioneer	11	26(85)	Polar	1958
		Echo	12	26(85)	Polar	1962
		(Venus) ^a	13	26(85)	Az-El	1962
		Mars	14	64(210)	Az-El	1966
Tidbinbilla	Australia	Weemala (formerly Tidbinbilla)	42	26(85)	Polar	1965
		Ballima (formerly Booroomba)	43	64(210)	Az-El	1973
—	Australia	Honeysuckle Creek ^b	44	26(85)	X-Y	1973
—	South Africa	Hartebeesthoek	51	26(85)	Polar	1961
Madrid	Spain	Robledo	61	26(85)	Polar	1965
		Cebreros	62	26(85)	Polar	1967
		Robledo	63	64(210)	Az-El	Under construction

^aA maintenance facility. Besides the 26-m (85-ft) diam Az-El mounted antenna, DSS 13 has a 9-m (30-ft) diam Az-El mounted antenna that is used for interstation time correlation using lunar reflection techniques, for testing the design of new equipment, and for support of ground-based radio science.

^bTo be shared with STDN until January 1974.

Mariner Venus/Mercury 1973 Mission Support

E. K. Davis

DSN Systems Engineering Office

During July and August 1973, the DSN continued activities to complete open hardware and software implementation tasks for Mariner Venus/Mercury 1973 (MVM'73). However, the primary activity during this period was DSN testing/training for MVM'73, including DSN system testing, DSN/spacecraft compatibility testing, and DSN support for mission operations system testing.

I. Planning Activities

A. NASA Support Plan

In August 1973, the DSN received NASA Headquarters correspondence directing that the NASA Support Plan (NSP) for MVM'73 be revised and resubmitted for final approval. The revised NSP will be submitted for NASA Headquarters' approval during the next reporting period.

B. DSN Operations Plan

The final, unsigned version of the DSN Operations Plan for MVM'73, which was released in May 1973, proved to

be very satisfactory for use during test activities. Therefore, effort on the approved version was reduced, resulting in an expected September 15, 1973, issue date rather than mid-July as planned.

C. DSN Support Team

Since the active members of the DSN Support Team for MVM'73 are now all from the DSN Operations Organization, it has been decided that the former activity shall terminate. The DSN Manager and Network Operations Project Engineer shall continue to meet as necessary to discuss matters normally handled by the support team.

II. Program Control

A. DSN Operational Readiness Review

The DSN Operational Readiness Review for MVM⁷³ is now scheduled for September 26, 1973. This shall be a detailed presentation of all factors in DSN Engineering and DSN Operations which have a bearing on DSN operational readiness. The agenda includes implementation status, training/test accomplishments and results, DSN/spacecraft compatibility verification results, and Review Board assessment.

B. Network Briefing

During August 1973, the DSN Manager for MVM⁷³ visited Deep Space Stations (DSS) in Australia and Spain. The purpose of this trip was to review DSS preparations for MVM⁷³, to discuss problem areas, and to present MVM⁷³ mission sequence information. Discussions were held with DSS managers and with system engineers of each technical area. This briefing will be conducted in September 1973 for local DSSs.

III. Implementation Activities

A. Ground Communications Facility (GCF) Status

During July 1973, technical problems were encountered in the wideband coded multiplexers during final acceptance tests at the contractor's facility. This caused further delays in accomplishing final wideband capabilities required to support DSN system tests. Shipment was made to all required DSS locations in August 1973, and installation is now essentially complete. DSS internal testing of high-rate telemetry capabilities can now continue. The coded multiplexer power supplies, however, do not meet specifications and are scheduled for replacement in October 1973. Implementation of the 230-kilobits/s wideband circuit between DSS 14 and JPL was completed on schedule, August 1, 1973. It has been used successfully during Project tests for real-time transmission of 117.6-kilobits/s imaging data.

B. DSS Status

There has been a significant improvement in accomplishment of delinquent, minor implementation tasks carried on Engineering Change Orders. Major implementation tasks, except planetary ranging and S/X-band which are committed to be operational at later dates, have been completed. Revision A to the DSS telemetry and command software program nears completion but somewhat later than requested.

1. **Telemetry and command data subsystem (TCD).** The previous article described a potential schedule problem in accomplishing an update to the TCD software program DOI-5050-OP. For test support purposes, it was desired that this update (Revision A) be available on August 15, 1973. However, software development resources and development requirements of other projects precluded this. Negotiations resulted in a planned availability date of September 1, 1973, an improvement over the advertised October 15, 1973, date. Work on the revision continued on schedule until late August, at which time software development resources were fully applied to resolve a command software problem for Pioneer. Therefore, completion of acceptance tests for MVM⁷³ TCD software was delayed about 10 days. To meet Mission Operations System test support requirements beginning September 5, copies of the Revision A program were shipped to all DSSs on August 31, 1973. This version has not been formally transferred and will be used only for test support purposes until receipt of the operational version about September 15, 1973.

2. **Digital instrumentation subsystem (DIS).** The new DIS software program (DOI-5046-OP) received by the DSSs in June 1973 has been integrated and utilized to transmit high-speed monitor and tracking data during tests. Minor format anomalies have been detected, and all DSSs are having difficulty with the new monitor printer device and its interface with the DIS. Cognizant engineers are working these problems; an update to DOI-5046 is planned for release in September 1973.

3. **Tracking data handling subsystem (TDH).** Previously reported TDH hardware problems involving the sample-rate selector have been resolved. All stations have now received, installed, and tested this unit. Implementation of the planetary ranging assembly hardware continues on schedule. Delivery of the first unit from the contractor is expected in mid-September 1973. After integration with associated software and testing at JPL, the first unit will be installed at DSS 12. Installation at DSS 12 rather than DSS 14 is a significant change in the planetary ranging implementation plan. This action was taken to assure the availability of ranging data for MVM⁷³ during November–December 1973 when the Pioneer Project has priority use of the 64-meter subnetwork.

The planetary ranging software still appears to be on a critically tight schedule. However, the developers assure that an interim version will be available for initial installation and test purposes in mid-September 1973.

4. S/X-band equipment. The Block IV receiver/exciter implementation required for the DSS 14 S/X-band research and development experiment is essentially on schedule. Installation at DSS 14 is scheduled for October 8, 1973, versus the originally planned October 1, 1973, date. Final receiver hardware components are now being received and assembled at JPL for subsystem testing. In early August, the exciter portion was installed temporarily at CTA 21 and successfully employed to demonstrate command capabilities and compatibility with the spacecraft. The coherent reference generator was installed and successfully tested at DSS 14. The improved S-band maser for this experiment completed assembly and laboratory testing at JPL as planned. This maser is fitted with the experimental superconducting magnet structure and incorporates improved design. Measurements show a reduction in temperature from 4.2 kelvins to about 2.2 kelvins. The zero-delay calibration equipment is ready for final system-level checkout during tests planned for September-October 1973 at DSS 14.

IV. Test and Training Activities

July and August 1973 was a period of intensive DSN testing for MVM⁷³. Accelerated testing with the DSSs resulted in the recovery of most time lost due to late hardware and software deliveries. CTA 21 was used to conduct DSN/spacecraft compatibility verification tests during the spacecraft thermal test activity at JPL. CTA 21 also supported Mission Operations System/spacecraft compatibility tests during this period. These tests have demonstrated compatibility with the MVM⁷³ spacecraft and DSN operational readiness to support Mission Operations System launch and encounter training exercises which were initiated in early August 1973. Exceptions are noted in the following discussion.

A. Ground Data System Tests

It was reported in the previous article that the DSN was approaching a state of readiness to support the Ground Data System (GDS) demonstration test on July 2, 1973. This proved to be true, in that DSSs 42, 62, and 14 successfully supported the 24-h test as scheduled. DSS original data record retransmission could not, however, be demonstrated due to the nonavailability of this capability in the current TCD software. Revision A of the software will contain this function, requiring additional testing in September 1973.

GDS tests were conducted with DSSs 43 and 71. A special test was run to verify end-to-end performance of

117-kilobits/s video from DSS 14 to JPL via the 230 kilobits/s wideband circuit. Follow-up GDS tests have been conducted to clear discrepancies noted in early tests. GDS tests for DSS 63 are scheduled for September 1973. Planning has been initiated for testing of DSS 14's S/X-band capabilities in October 1973.

B. DSN Tests and Training

On-site training for DSSs supporting MVM⁷³ continued during July and August. This consisted of reviewing video tapes, review of MVM⁷³ documentation, and participation in DSN internal simulations. DSN system performance tests were completed at each DSS. DSN Operational Verification Tests (OVT) were initiated and completed such that each operations crew at each DSS participated in at least two OVTs. A total of twenty-nine 8-h OVTs were conducted at the MVM⁷³ supporting DSSs, with DSS 63 being an exception. At DSS 63, on-site training and system performance tests were initiated in early August; OVTs are scheduled to follow. Successful DSN performance demonstration tests (PDT) were conducted at each DSS, except DSSs 63 and 71. The PDT for DSS 71 must be repeated in early September 1973 to complete checkout of the wideband subsystem. The PDT for DSS 63 is scheduled for late September 1973. All DSSs, except DSS 63, have participated in Mission Operations System launch and encounter exercises conducted in August. To date, this testing at DSSs 43 and 63 has excluded wideband data due to the nonavailability of wideband data terminals prior to late August. Due to cost considerations, wideband data circuits will not be available for long-loop tests with these stations until late September 1973. DSN testing and training will continue during the next 2 months as necessary to achieve the required state of readiness for MVM⁷³ launch and mission support.

C. DSN/Spacecraft Compatibility Tests

The spacecraft compatibility tests were performed between 18 and 29 July 1973 and on August 3, 1973 via an RF link between CTA 21 and the flight spacecraft in the JPL thermal-vacuum facility. Tests totaling approximately 44 hours were conducted during four separate test periods: 1-sun, 2-suns, 4.8-suns, and ambient temperature. Only minor incompatibility problems were observed in command, telemetry, and tracking; however, discrete ranging test results indicated a possible significant interference problem. Telemetry channel signal-to-noise ratios showed an increase rather than a decrease. This problem requires further investigation to determine the extent of telemetry degradation. Block IV exciter (S-band) command capa-

bility was established during the tests on August 3. The S/X-band receiver tests were not accomplished as planned, due to nonavailability of Block IV receiver equipment.

Upon acquiring the spacecraft signal for the first time, it was noted that the downlink signal level was unstable, indicating an RF leakage problem. Through the use of various test configurations, the leakage was isolated to the spacecraft. By adding a 20-dB pad at the Compatibility

Test Area (CTA 21) antenna at JPL, the multi-path was attenuated to the extent that it did not affect testing.

Compatibility verification tests are now in progress at Cape Kennedy between the Compatibility Test Station (DSS 71) and the spacecraft. Specific attention is being given in these tests to open areas resulting from the July test at JPL. The detailed test report provides a full description of these tests and results.

Viking Mission Support

D. J. Mudgway

DSN Systems Engineering Office

D. W. Johnston

DSN Operations Office

This article reflects the finalization of the Viking 1975 hardware configurations and the initial application of these configurations to detailed Viking 1975 strategies and associated operations procedures.

I. Introduction

The publication of the DSN Preparation Plan for Viking 1975 (614-20) on August 15, 1973, constitutes a major milestone in laying the foundation of budgeted hardware, software, and schedules, upon which the detailed operations planning may be based. Work is now in progress in the various working groups supported by DSN Operations in the Viking Flight Team Working Organization, to formulate strategies for use by the mission planners. These mutually agreed-on strategies then lead to the generation of supporting procedures by each of the groups concerned. This procedure generation in the DSN case is slightly different from that of the other groups, in that DSN procedures exist, many of which can be utilized as is, many more need to be modified for Viking 1975 use, and some others, unique to Viking 1975, need to be generated to fill the Viking 1975 requirements. With the publication of the basic system configurations in the DSN Preparation Plan, work has now started on the production of various configurations (and backups) for each mission phase, and the

reviewing, modification, and generation of associated operations procedures for inclusion in the Network Operations Plan.

II. Documentation

The DSN Preparation Plan (614-20) was released on August 15, 1973. The next issue of the Network Operations Plan (614-21) has been delayed to November 1, 1975, in order to reflect the systems capabilities and configurations defined in the Preparation Plan.

III. Viking Configurations

Practically all of the implementation/operational conflicts on the Viking 1975 configurations have now been resolved.

The requirement for dual uplink carriers (single-station) has been deleted and the proposed 100-kW transmitter

installation at DSSs 43 and 62 has now been postponed until after the Viking 1975 mission. These stations will have the currently operational 20-kW transmitters, and dual uplinks will be provided by dual station operation.

Some major long-lead-time items on the implementation schedules, such as station block updates during the Viking 1975 orbital operations phase, appear to be an unacceptable operational constraint, and several of these items, though they do not have any impact at this time, will require discussion and resolution in the near future.

IV. Voltage-Controlled Oscillators

Stations are being supplied with Quad voltage-controlled oscillators (VCOs) crystallized for channels 9, 13, 16, and 20. Channels 9 and 20 are for Orbiters A and B, respectively, while channel 16 is the spare Orbiter frequency. Channel 13 will be used for Lander A, Lander B, and the spare.

During certain mission periods, doppler conditions will cause frequency excursions to the extent that VCOs will be taken to the extreme end of their operating range; therefore, it has been decided that offset VCOs are required in the prime 26-m network Block III receivers and exciters. The 64-m station Block IV receivers and exciters do not require crystals.

V. Viking Lander Acquisition and Command Strategy

One of the Viking 1975 strategies which has involved DSN participation is the subsequence to be used to acquire the Viking Lander (VL) S-band carrier and command detector. A nonstandard strategy is required because the VLs have severe power limitations which result in nominal maximum spacecraft transmitter and receiver programmed *on* times of approximately 70 min and 3 h, respectively, each 24.6-h (Mars day) period. This, coupled with a predicted round trip light time (RTLTL) of approximately 40 min, poses some problems when it is realized that the spacecraft receiver best-lock frequency uncertainty may be extremely large due to exceptionally large temperature variations. As the spacecraft transmitter will be turned off each day, there will be no telemetry data to monitor these temperature variations immediately prior to the acquisition, and the transmitter *on* time is so short that to wait and acquire in a one-way tracking mode would use 20 min of transmitter *on* time ($\frac{1}{2}$ RTLTL). Even though telemetry is then available, the spacecraft temperature would not be static, due to the transmitter turn-on, so an uplink acquisition sweep would still be necessary to

acquire (nominally 10 min at expected uplink power levels). If we then waited the 40-min RTLTL to observe the S-band acquisition via telemetry before turning on command modulation to load the commands, we would possibly see the acquisition and immediately drop lock on the ground receiver as we would have come to the end of that day's spacecraft transmitter *on* period; i.e.,

$$20 \text{ min} = \frac{1}{2} \text{ RTLTL} = \text{VL transmitter on to DSS lock}$$

$$10 \text{ min} = \text{uplink sweep}$$

$$40 \text{ min} = \text{RTLTL} = \text{end of sweep to DSS two-way lock}$$

$$= 70 \text{ min} = \text{total VL transmitter on time}$$

We would thus have achieved two-way lock and confirmed this only seconds before losing it for another 24-h period. We would then be in a one-way (uplink) tracking mode capable of acquiring command detector lock and transmitting commands to the VL, but without any downlink (telemetry) to confirm command lock or command receipt. When it is realized that some of these are commands to turn the VL receiver and transmitter *off* and *on*, it becomes immediately obvious that this rather conservative subsequence, which would be the type used with a spacecraft having large variations in best-lock frequency, is completely unacceptable for use with the VL spacecraft.

A group of Martin Marietta Aerospace Lander Flight Team personnel was given the task of generating a series of VL acquisition strategies for consideration. Seventeen tentative strategies were produced and critiqued by DSN Operations personnel, and the field was narrowed down to the three shown in Figs. 1, 2, and 3.

It should be borne in mind that the VL will be subjected to internally produced variations in temperature (and thus frequency) due to the heat dissipated by the various experiments (instruments) whose work load will vary widely from day to day, superimposed on the day/night variations on the planet surface.

A further point is that the heavy electrical power consumption of the transmitter and traveling wave tube amplifier (TWTA) occurring with transmitter switch *on*, is also increased as the VL high-gain antenna is rotated at this time to boresight on Earth.

VI. Strategy Analysis

A. Strategy 1A

Strategy 1A (Fig. 1) shows the VL transmitter and receiver programmed *on*, together with the ground trans-

mitter tuning scheduled to start 20 min prior to VL turn-on. This enables the 40-min full-acquisition uplink sweep to be monitored via telemetry on the downlink.

The VL receiver is then programmed *off* at the end of the 40-min sweep and programmed *on* again.

After a 10-min possible retune of the spacecraft receiver static phase error (SPE) to zero or to reduce it to within acceptable limits, the command modulation is then turned on and command transmission started.

This strategy allows full monitoring of the S-band acquisition but does not provide monitoring of command acquisition or receipt, and does not allow for a reacquisition or retransmission of commands.

Strategy 1A, or a modified version with split transmitter times, may be used for the initial VL acquisition only.

B. Strategy 2A

Strategy 2A (Fig. 2) is similar to 1A except that the transmitter *on* time is programmed to occur after two-way lock.

This strategy would be used if experience proves that the VL spacecraft SPE tolerance during commanding is relatively small, and the best-lock frequency uncertainties are large, requiring large full-scale tuning sweeps, with the possible requirement for retuning to zero SPE.

S-band acquisition is confirmed, command lock is confirmed, and the first 20 min of the nominal 30-min command load is confirmed, with the possibility of blind retransmission of commands if required.

C. Strategy 3B

The main difference in Strategy 3B (Fig. 3) is that the S-band acquisition, command acquisition, and command transmission are all carried out "in the blind."

Assuming reasonable probability of realistic tolerances on acceptable SPE and reasonably precise best-lock frequency predicts (short sweeps—no retuning), this strategy would be the prime choice. This gives confirmation of S-band acquisition and command receipt. It also gives time for a second complete command retransmission and confirmation with the ability to command an extension of the transmitter and receiver *on* times.

Also, if necessary, the VL could be acquired using the Block IV receiver-exciter which, although deleting the X-band from the Viking Orbiter support, would enable the tuning rates to be increased, thereby reducing the tuning sweeps by approximately half.

The strategies above will be checked out during the spacecraft/DSN RF compatibility tests at CTA 21 during June, July, and August, 1974.

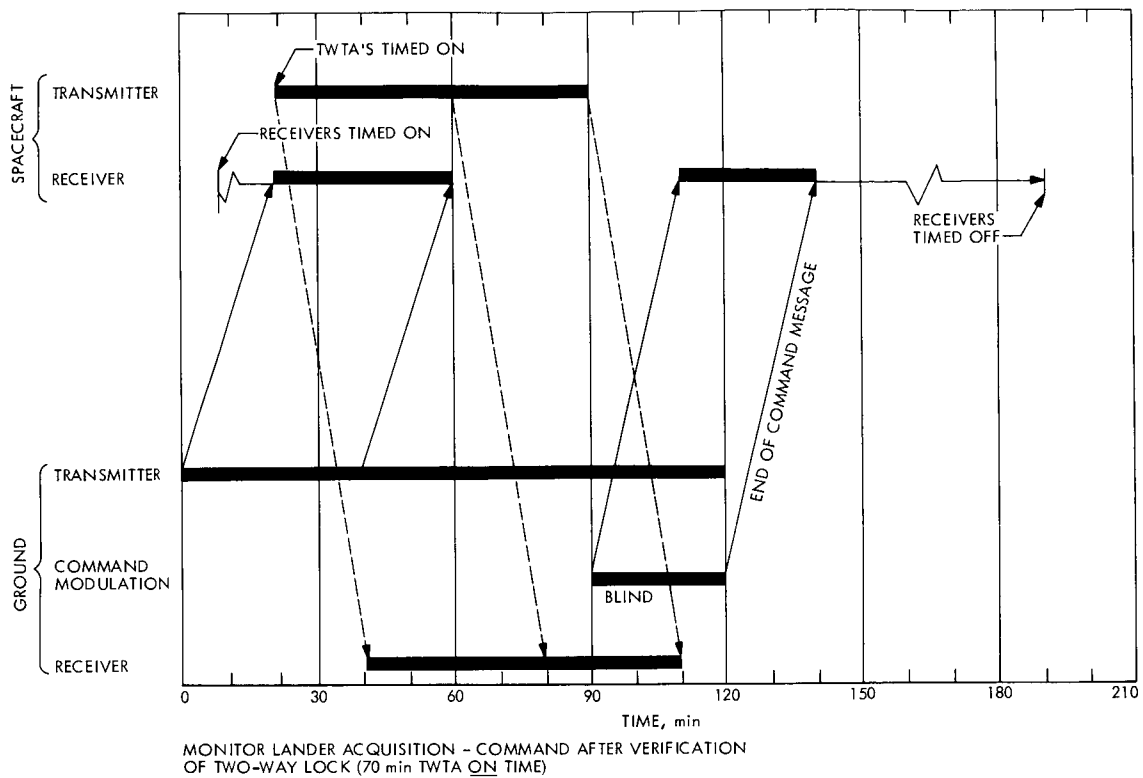


Fig. 1. Lander Command Strategy 1A

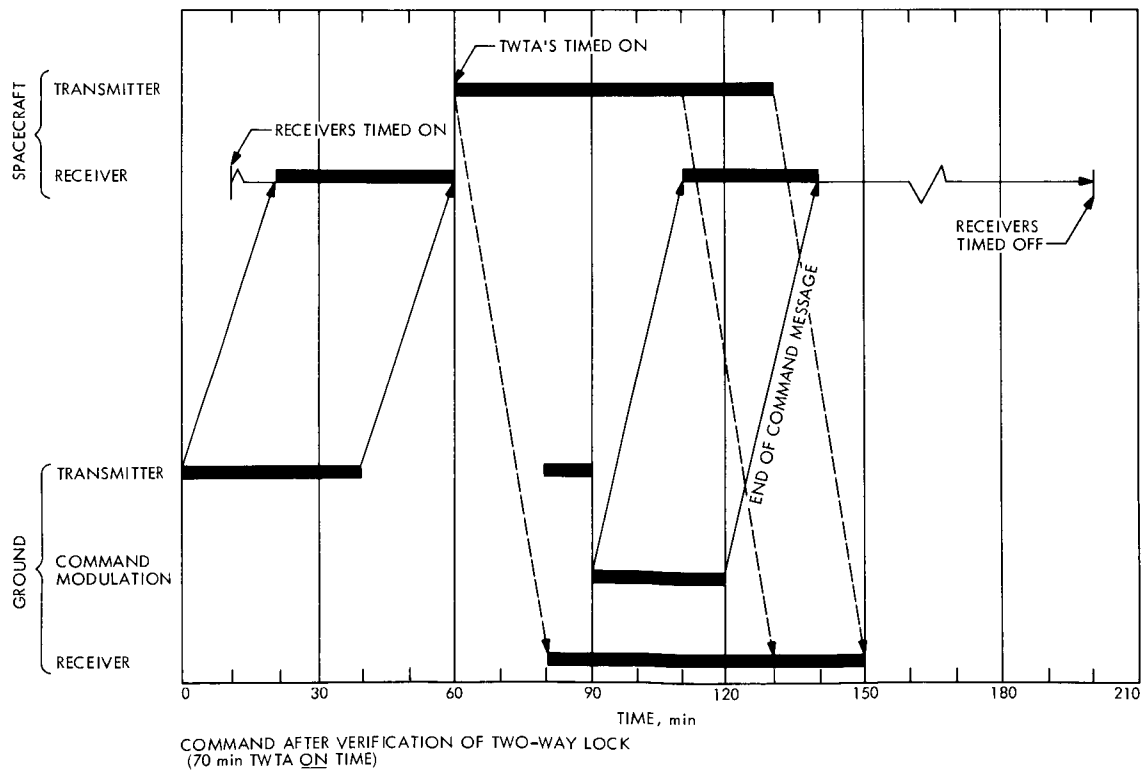


Fig. 2. Lander Command Strategy 2A

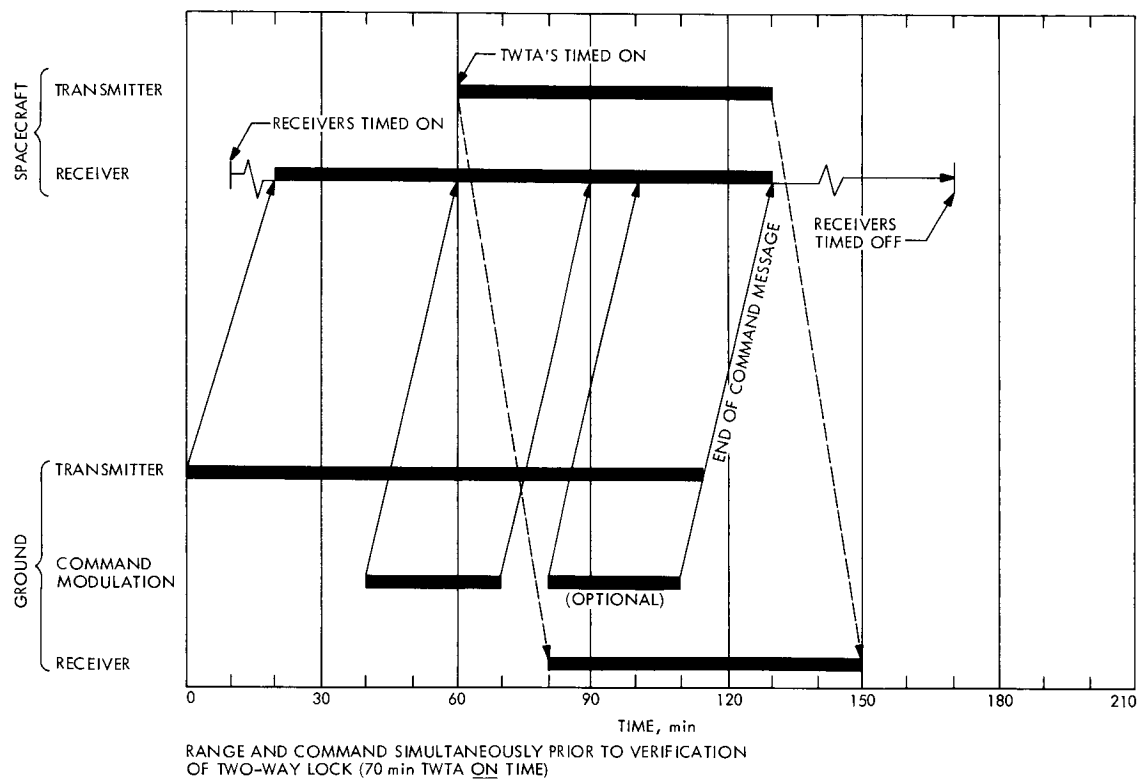


Fig. 3. Lander Command Strategy 3B

Pioneer 10 and 11 Mission Support

R. B. Miller
DSN Systems Engineering

A general description is presented of the Pioneer 10 Jupiter Encounter objectives and the resulting operations plan.

I. Introduction

Pioneer 10 has been supported in cruise mode for over a year and a half and Pioneer 11 for six months. Cruise activities have included a solar conjunction by Pioneer 10, zodiacal light observations using the imaging photopolarimeter, Jupiter observations, various instrument calibrations and observations, and continuous measurements of the characteristics of a region of space no prior man-made spacecraft has seen. Pioneer 10 is fast approaching its encounter with Jupiter in December of this year. The Pioneer Project defines the encounter period as extending from November 4 to January 4 of 1974. Closest approach to the planet Jupiter occurs on the fourth of December around 0300 GMT. The Pioneer support article in the preceding

issue of the *DSN Progress Report* (Ref. 1) described in great detail the manner in which a particular instrument, the imaging photopolarimeter, would be operated during the encounter sequence. As was described, that instrument dominates the encounter sequence activity and is the source of the most stringent requirements on Ground Data System reliability. This article describes in general terms the entire encounter sequence.

II. Pioneer 10 Encounter Objectives

The Pioneer 10 spacecraft carries eleven on-board experiments, and the mission includes two ground-based experiments that utilize the radio link. These experiments, which will be utilized in various combinations to attempt

to meet the scientific objectives described herein, are listed as follows together with the cognizant experiment team facilities:

Magnetometer	Jet Propulsion Laboratory
Plasma analyzer	Ames Research Center
Charged particle detector	University of Chicago
Geiger tube telescope	University of Iowa
Cosmic ray telescope ...	Goddard Space Flight Center
Trapped radiation detector	University of California, San Diego
Ultraviolet photometer	University of Southern California
Imaging photopolarimeter	University of Arizona
Infrared radiometer	California Institute of Technology
Asteroid meteoroid detector	General Electric
Meteoroid detector	Lewis Research Center
S-band occultation	Jet Propulsion Laboratory
Celestial mechanics	Jet Propulsion Laboratory

It is expected that Jupiter will have a magnetic field anywhere from 3 to 30 times the strength of the magnetic field of Earth. The Pioneer 10 spacecraft will attempt to measure the strength of that field and map its characteristics along the flight path of the spacecraft. Because of the presence of a magnetic field, it is also expected that the planet Jupiter will have radiation belts similar to the Van Allen Belts of Earth. The presence and characteristics of these high-energy electron and proton radiation belts will be measured.

Various decimetric and decametric radio emissions have been observed on Earth from the planet Jupiter. It is hoped to find a basis for interpreting the source of these radio emissions from Jupiter by the measurements performed during the flyby.

The instruments will be used to detect and measure the bowshock and magnetospheric boundary and its interaction with the solar wind.

The objectives of the atmospheric measurements will be to investigate the thermal balance and temperature distribution of the outer atmosphere, to measure the hydrogen/helium ratio in the atmosphere, and to measure

the structure of the ionosphere and upper atmosphere. In addition, the brightness, color, and polarization of reflected light from the upper atmosphere will be measured.

The last objective involving on-board experiments is the production of two-color visible light images of the disk of the planet.

The objectives of the ground-based experiments will be to increase the accuracy of the ephemeris and known mass properties of the planet Jupiter and its associated satellites and to measure atmospheric properties as the radio link passes through the atmosphere.

III. Major Pioneer 10 Jupiter Encounter Events

The far encounter starts on November 4. Beginning on that date there will be significant spacecraft activity approximately 8 hours per day. By November 12 the disk of Jupiter will extend across approximately 15 pixels (a pixel constitutes a picture element in the imaging system). By November 18 the planet will extend across 20 pixels and enlarge to 30 pixels by November 24. The region of 30 pixels is considered comparable to Earth-based resolution. It is at this time that the encounter sequence moves to 24-h/day operations. Even though the imaging prior to November 24 is below Earth-based resolution, it is considered valuable because it constitutes viewing of the planet Jupiter from phase angles impossible from Earth. Because Jupiter is so far from Earth, Earth observation is always of the full disk of the planet under flat light conditions. The Pioneer spacecraft will see the planet Jupiter over a wide range of phase angles, which will be important for possible shadowing of cloud layers to enable the atmosphere to be seen in greater detail, and the polarimetry measurements at these varying phase angles will contain valuable information about the particle size in the atmosphere. The imaging photopolarimetry resolution decreases symmetrically on the other side of closest approach.

Since estimates of the magnetic field strength of Jupiter vary over such a wide range, there is a large uncertainty as to the extent of the magnetosphere. It is therefore expected that the bowshock of the magnetosphere will be crossed somewhere between November 25 and December 1. Two instruments are important for measuring the fine structure of the bowshock: the plasma analyzer and the trapped radiation detector. Upon detecting that the spacecraft has crossed through the bowshock when approaching the planet Jupiter, the spacecraft must be commanded into a mode which replaces the imaging data in the telemetry with plasma analyzer measurements and gives the trapped

radiation detector a higher service rate. Because of the large uncertainty as to when the bowshock crossing will occur, this event will have to be detected in real-time by observing the output of some of the on-board instruments, and the IPP sequence interrupted in order to send the commands to the plasma analyzer and trapped radiation detector.

The ultraviolet photometer will observe the planet between November 30 and December 2 and again on December 3. The infrared radiometer will observe the planet on December 4 during the periapsis passage. The spacecraft is expected to enter the radiation belt of Jupiter at about 2200 GMT on December 3 and to exit the radiation belt at about 0700 GMT on December 4. It is during the time period when the spacecraft is within the radiation belt that there is the most concern about damage occurring to the spacecraft. Charged-particle environments around planets are comprised of both protons, which constitute the plasma, and free electrons. Any charges that build up on a spacecraft due to the free electrons are usually bled off by the plasma. However, as has been discovered in the case of satellites orbiting the Earth, there are circumstances which arise in which the plasma can be pushed to a lower altitude than the free electrons, and it is in these circumstances that very large charges can build up on a spacecraft. Estimates of the potential charge buildup on the Pioneer spacecraft vary over a wide range. There are two possible impacts of a large charge buildup: (1) actual damage to electrical components in the spacecraft and (2) false commanding of the

spacecraft because of electrical discharges taking place. The project has been developing contingency plans in the event that false commanding does occur.

Two Earth occultations will take place during the Jupiter encounter. The first will be an occultation of the satellite Io, which will occur at approximately 0243 GMT on December 4. The Io occultation will last from 60 to 90 seconds. It is hoped to get measurements of the atmosphere of Io as the radio link occults the satellite. The Jupiter-Earth occultation will occur at approximately 0340 GMT on December 4 and will last about 60 minutes. During the Jupiter occultation the spacecraft will be placed in a low data rate state and a limited amount of science data stored on board for readout after emergence from occultation.

The solar occultation will occur at approximately 0415 on December 4 and last approximately 50 min. The spacecraft will have to be placed in a spin averaging mode during this time period because of the loss of solar reference.

In order to maintain the capability to receive a maximum amount of telemetry at the required 1024-bit rate, it will be necessary to maintain the pointing of the spacecraft 9-ft-diameter high-gain antenna within 1 deg of Earth. This will necessitate several spacecraft precession maneuvers during the two-month encounter period. The last of the precession maneuvers prior to the periapsis pass will occur on about November 24.

Reference

1. Miller, R. B., "Pioneer 10 and 11 Mission Support," in *The Deep Space Network Progress Report*, Technical Report 32-1526, Vol. XVI, pp. 15-21, Jet Propulsion Laboratory, Pasadena, Calif., Aug. 15, 1973.

X-Band Waveguide Step Transitions

H. R. Buchanan
R.F. Systems Development Section

Two types of waveguide-to-waveguide transitions have been developed which permit accurate low-power laboratory tests on WR 125 waveguide components using more universally available WR 112 test equipment. A rather generally useful program for computer-aided analysis of tandem rectangular waveguide sections is being developed as a part of this effort.

I. Introduction

The X-band radar equipment requires transmission of a nominal 400-kW signal at 8.495 GHz. A study of the high-power problems associated with this requirement resulted in the choice of a new waveguide size, WR 125 (Ref. 1). This waveguide size is near optimum for both the radar frequency and anticipated frequency requirements for the DSIF (7.1 to 8.5 GHz).

The development of a well-matched waveguide-to-waveguide transition for adapting WR 125 components to WR 112 test equipment has been undertaken. Such a transition permits accurate low-power measurements using test equipment which is generally available to any microwave component manufacturer.

II. Design Considerations

The two waveguide sizes involved, WR 125 (3.175×1.588 cm) and WR 112 (2.850×1.262 cm), have relatively modest width-to-width and height-to-height ratios—1.114

and 1.258, respectively. It was decided that a carefully designed step transition would probably exhibit an acceptably low mismatch. The step type of transition has the advantage of compactness and ease of fabrication.

Two types of step transitions were designed and fabricated—a single-section and a two-section Chebyshev quarter-wave transformer. The design details were based upon the formulas and tables in Ref. 2, using the following assumptions:

- (1) Waveguide characteristic impedance Z_0 is given by

$$Z_0 = \frac{377\pi b}{2a} \cdot \frac{\lambda_g}{\lambda_0}$$

where b and a are the waveguide height and width, respectively (Ref. 3).

- (2) Junction discontinuity effects were neglected due to the small steps at each junction and the partial discontinuity cancellation resulting from simultaneous steps in both height and width (Ref. 4).

III. Results

The calculated geometry of the two transitions is given in Table 1. Samples of each transition have been fabricated and tested. The measured test data are given in Fig. 1. The single-section transition exhibits a voltage standing wave ratio (VSWR) under 1.010 over the frequency range of 8.3 to 8.6 GHz. The two-section transition exhibits an unexplained poor performance as shown in Fig. 1. However, the addition of a small capacitive tuning screw at the midpoint of the smaller section reduces the VSWR to a maximum of 1.020 over the range of 7.0 to 8.7 GHz.

An effort has been initiated to develop a computer-aided analytic technique applicable to an N-section array of tandem rectangular waveguide elements. This technique should prove useful in the improvement of the two-section filter and have general applicability to other waveguide computations. The mathematical model incorporates junc-

tion discontinuities at each step (Ref. 3) as well as lumped susceptances at any location.

IV. Conclusions

A single-section quarter-wave transformer has been designed and tested. This compact, easily reproducible transition can be used for low-power testing of WR 125 waveguide components using WR 112 test equipment. The resulting measurement accuracy is adequate for all but the most critical tests for the X-band radar frequency range.

Further improvements in the two-section transition will be investigated for future broadband applications (7.1 to 8.5 GHz). It is expected that the computer-aided analysis will be helpful in this effort. Progress on this technique and further test results will be reported at a later date.

References

1. Buchanan, H. R., "X-Band Uplink Microwave Components," in *The Deep Space Network Progress Report*, Technical Report 32-1526, Vol. XII, pp. 22-25, Jet Propulsion Laboratory, Pasadena, Calif., Dec. 15, 1972.
2. Matthaei, G. L., Young, L., and Jones, E. M. T., *Microwave Filters, Impedance-Matching Networks, and Coupling Structures*, McGraw-Hill Book Company, New York, 1964, pp. 259-283.
3. Barlow, H. M., *Micro-Waves and Waveguides*, Dover Publications, Inc., 1949, pp. 65-67.
4. Marcuvitz, N., *Waveguide Handbook*, M.I.T. Radiation Laboratory Series, Vol. 10, McGraw-Hill Book Co., New York, 1951, pp. 296-309.

Table 1. Step transition dimensions

Dimensions	Input/Output		Single-section $F_0 = 8.45$ GHz	Two-section $F_0 = 7.80$ GHz, $wq = 0.2$	
	WR 112	WR 125		Section 1	Section 2
Height, cm	1.262	1.588	1.415	1.354	1.471
Width, cm	2.850	3.175	3.007	2.946	3.048
Length, cm	–	–	1.097	1.268	1.234

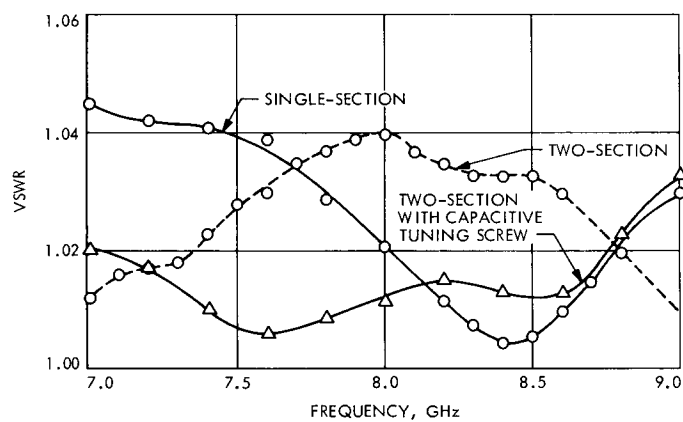


Fig. 1. Voltage standing wave ratio of step transitions

High-Power Microwave Transmitter Switch

C. P. Wiggins, H. R. Buchanan, and R. L. Leu
R.F. Systems Development Section

A technique for high-speed switching or pulse-modulating the X-band radar transmitter is described in this article. Additional equipment is not needed, and mechanical switches and a high-power modulator are eliminated. Conventional modulation schemes usually result in early failure of the klystron amplifier tubes from thermal stresses; this approach does not have this limitation.

I. Introduction and Summary of Conclusions

A technique for high-speed switching or pulse-modulating the X-band radar transmitter is described in this article. Additional equipment is not needed and mechanical switches and a high-power modulator are eliminated. Conventional modulation schemes usually result in early failure of the klystron amplifier tubes from thermal stresses; this approach does not have this limitation. The conclusions have been verified by tests and the phase stability has been measured (Ref. 1).

II. Modulation Requirements and Associated Problems

Initially, the transmitter will be used for radar ranging of Jovian moons and the rings of Saturn. The experimenter has chosen the following mode of operation. The transmitter will be pulsed on and off, 50% duty cycle, a pulse repetition rate (PRR) between 1 and 30 seconds. This will be continued for one round trip time of flight of the radio signal to the target and back (30 minutes to 2 hours); the transmitter will be switched off and the

receiver switched on for one round trip time of flight. This cycle will be continued as long as the target is in view.

During the receive cycle, the receiver will detect the reflected signal plus noise ($S + N$) alternately with noise only (N), corresponding to the transmitter on-off modulation. The information can then be processed by a computer:

$$(S + N) - N \approx S$$

The scheme is analogous to conventional (Dicke) radiometric techniques.

Long pulse modulation of conventional klystron amplifier tubes subjects them to severe thermal stresses and greatly reduces their operating life. The tube efficiency is

$$100 \times \frac{\text{RF power output}}{\text{DC power in}} \leq 40\%$$

Thus for 200-kW output per tube, the dc input power is 500 kW. With drive off (no RF input to the tube) all of the dc power is dissipated in the collector or anode as heat. With drive on, 200 kW is transmitted through the output window as RF and 300 kW is dissipated as heat in the collector. The collector is a thick-walled forged copper cylinder, approximately 60 cm long and 3 cm thick, with an ID of 10 cm. It has drilled coolant passages to remove the heat. When the drive is off, the electron beam does not disperse uniformly and the maximum power densities are very high in certain areas. Modulation techniques such as switching the drive on and off produce 200-kW power pulses in the collector from a 300-kW base, while switching the dc beam power on and off produces 300-kW collector power pulses. Although the collector is efficiently cooled for CW operation, the interior surface temperature is quite high and has a thermal lag due to gradients through the thick copper. Long pulse modulation can be expected to produce rapid grain growth in the copper and cracks and spalling with ultimate tube failure due to the collector cracking open or copper particles falling into the electron beam and arcing (Ref. 2). This failure mode was also experienced during the first Mars radar experiment with the 100-kW S-band klystron and continued until pulse modulation was discontinued.

Should we elect to proceed with this approach in the face of a warning to expect early tube failure, a high-power modulator must be designed and the high-voltage power supply redesigned. Power supply regulation is

obtained by feedback control of the field of the ac generator, which supplies power to the high-voltage transformer. The generator field time constant is the limiting factor and will produce poor rise time and severe overshoots in the dc power pulses.

III. Description of Combining Technique

Economic considerations dictated use of two 250-kW klystrons (Ref. 3) of an existing design rather than sponsorship of the development of a 400-kW unit. Technical feasibility of the latter has been demonstrated by the 1-MW, 8-GHz klystron developed by Varian Associates (Ref. 4), but an operational tube has not been produced.

The outputs of the two klystrons will be combined into a single waveguide by use of a four-port, 90-deg hybrid junction (Ref. 5). An oversimplified description of the combiner is two parallel waveguides connected by a coupling slot or opening in the adjacent walls of the two waveguides (Fig. 1). The design applies for either broad or narrow wall coupling. We have chosen the latter since it simplifies the waveguide configuration for this particular installation.

If a signal is applied to port 1, a signal of one-half the power will appear at port 3, and one-half will appear at port 4, advanced 90 deg in phase relative to the signal at port 3.

If a second signal of the same power is applied at port 2, -90 deg out of phase with the signal at port 1, the two combine at port 3 with a total power almost equal to the sum of the ports 1 and 2 signals. A small component of output power at port 4 (typically 30 dB less than the power level at 3) is a function of the unbalance in the hybrid.

By changing the phase of the port 2 signal to +90 deg with respect to the port 1 signal, the two combine so that most of the power output is at port 4 and the small residue at port 3. Thus a ± 90 -deg biphasic change in one input signal with respect to the other transfers the signal from one output port to the other. The ratio of the residual power to the combined power (switching isolation) for the ± 90 -deg biphasic change is shown in Fig. 2 for a typical hybrid as a function of relative gain and phase variations of the two input signals. A mathematical analysis of the hybrid combiner performance is presented in Appendix A.

IV. Description of Transmitter

A functional block diagram of the transmitter as originally planned (Ref. 6) is shown in Fig. 3. The waster load is normally required to absorb only the small component of output power due to the combiner hybrid unbalance. During the initial phasing of the klystrons, the waster load power can be greater, so a 150-kW RF water load was selected. No load with a higher power rating is available. It was planned to employ two such loads, with a power

divider for each power amplifier and four loads and three power dividers to absorb the total output power of 400 kW.

To accommodate the new concept of phase-shift switching of the output power, the waster load is required to absorb 400 kW during the interpulse period. The configuration shown in Fig. 4 uses the power amplifier loads with an additional power divider to terminate the combiner instead of the smaller waster load.

References

1. Kolbly, R. B., "High Power Switching and Combining Technique," in *The Deep Space Network Progress Report*, Technical Report 32-1526, Vol. XVI, pp. 105-109, Jet Propulsion Laboratory, Pasadena, Calif., Aug. 15, 1973.
2. McCune, E., Varian Associates, private communication.
3. Smith, R. H., "X-Band 250-kW Klystron," in *The Deep Space Network Progress Report*, Technical Report 32-1526, Vol. XVI, pp. 38-41, Jet Propulsion Laboratory, Pasadena, Calif., Aug. 15, 1973.
4. *First Annual Report*, Contract AF30 (602) 2756, Rome Air Development Center, Rome, N.Y., Sept. 19, 1963.
5. Riblet, H. J., "The Short Slot Hybrid Junction," *Proc. IRE.*, Vol. 40, Feb. 1952, pp. 18-184.
6. Wiggins, C. P., "X-Band Radar Development," in *The Deep Space Network Progress Report*, Technical Report 32-1526, Vol. XII, pp. 19-21, Jet Propulsion Laboratory, Pasadena, Calif., Dec. 15, 1972.

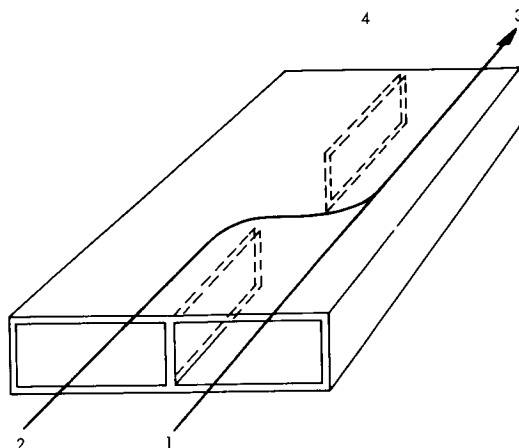


Fig. 1. Simplified diagram of combiner

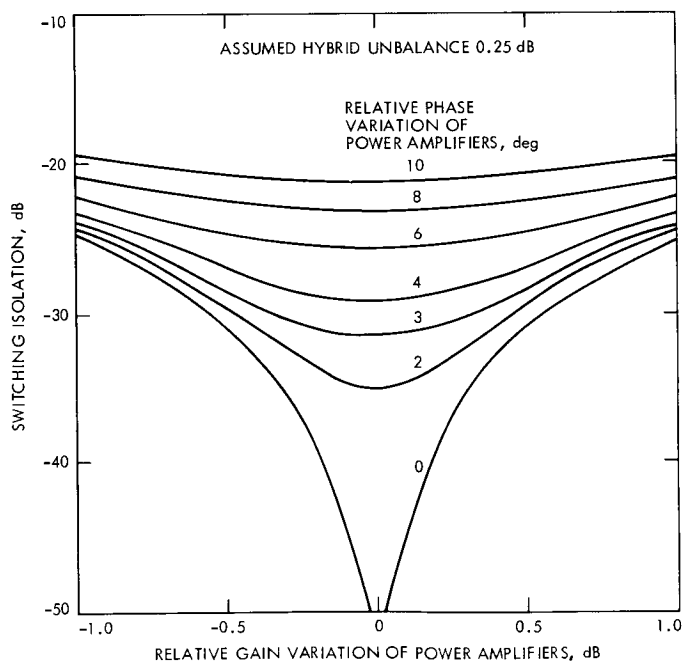


Fig. 2. Hybrid combiner switching isolation (computed)

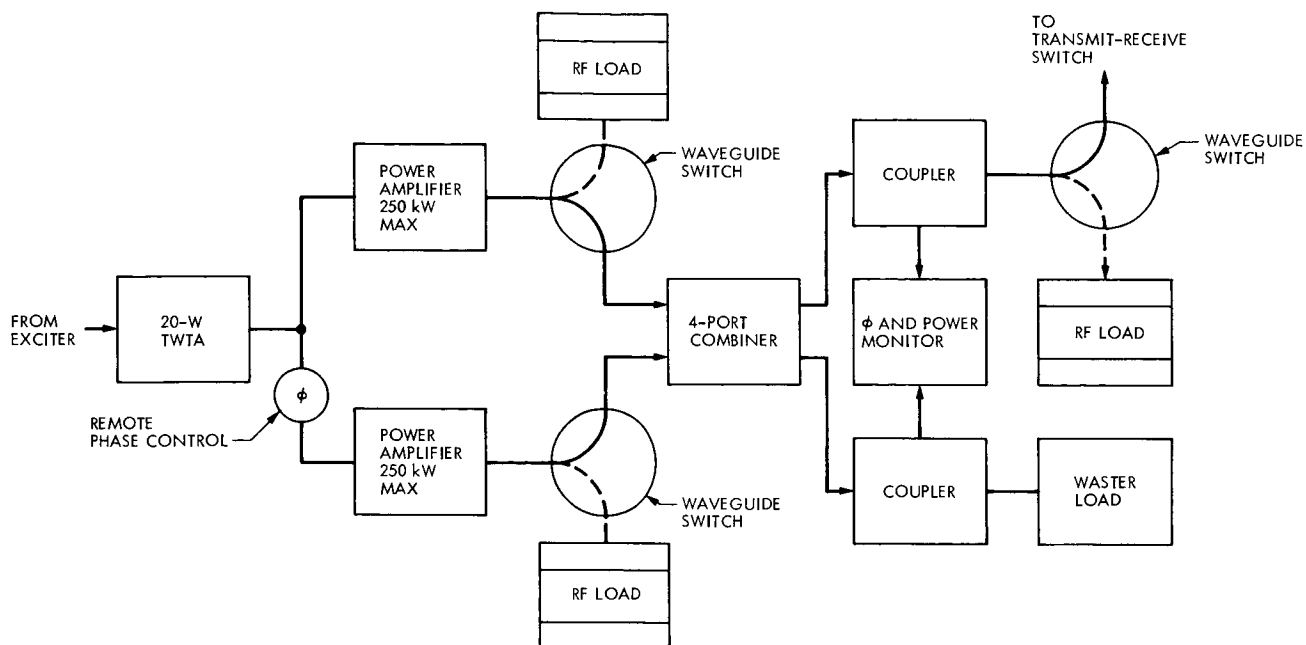


Fig. 3. 400-kW X-band radar transmitter

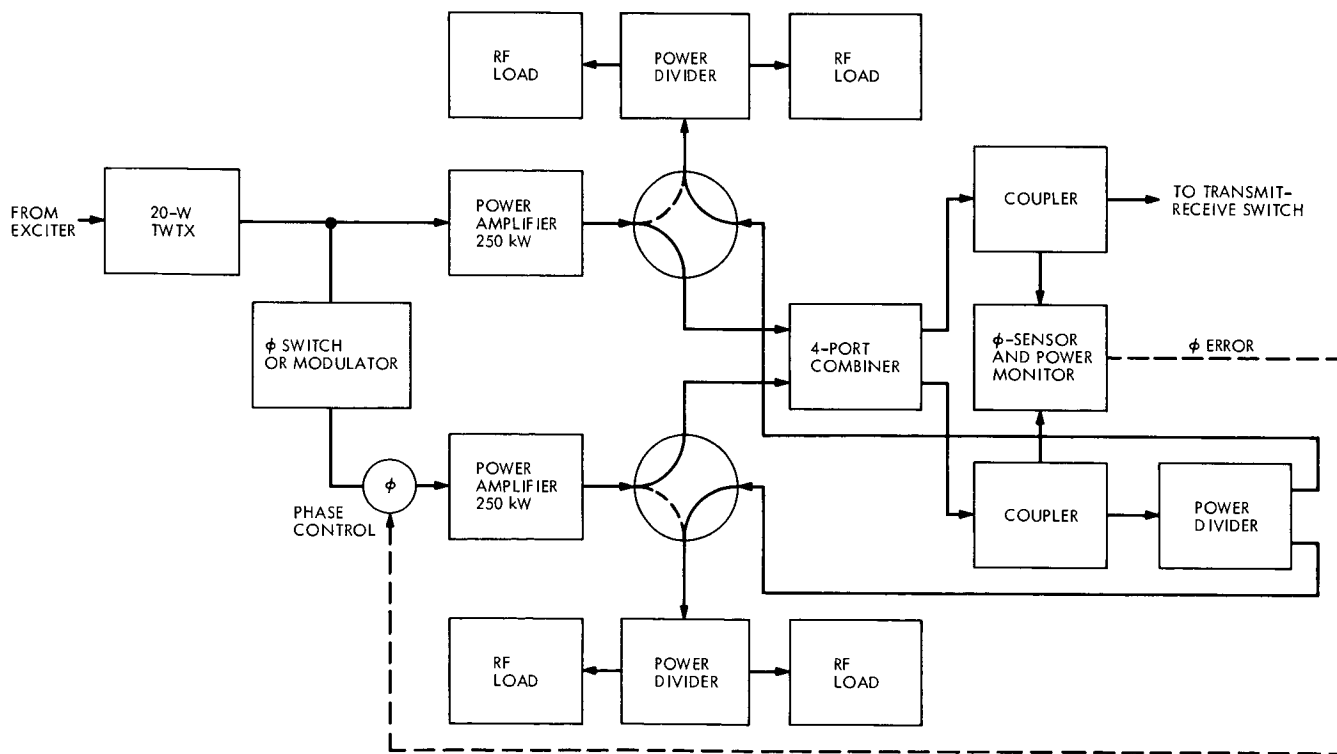


Fig. 4. RF power switching using phase shifting technique

Appendix

The performance of a hybrid combiner used as a high-power switch can be analyzed by employing the scattering matrix of the four-port hybrid. The hybrid, shown schematically in Fig. A-1, is assumed to be lossless, and its scattering matrix is therefore unitary. The matrix elements can be represented as given by Eq. (A-1), assuming symmetry.

$$S = \begin{bmatrix} A_1 e^{j\phi_1} & A_2 e^{j\phi_2} & A_3 e^{j\phi_3} & A_4 e^{j\phi_4} \\ A_2 e^{j\phi_2} & A_1 e^{j\phi_1} & A_4 e^{j\phi_4} & A_3 e^{j\phi_3} \\ A_3 e^{j\phi_3} & A_4 e^{j\phi_4} & A_1 e^{j\phi_1} & A_2 e^{j\phi_2} \\ A_4 e^{j\phi_4} & A_3 e^{j\phi_3} & A_2 e^{j\phi_2} & A_1 e^{j\phi_1} \end{bmatrix} \quad (\text{A-1})$$

The A elements are real. The following bounds may be stated for a practical hybrid following the analysis in Ref. 5.

For a minimum isolation of 30 dB between ports 1 and 2,

$$A_1 \cong A_2 \leq 0.0316 \quad (\text{A-2})$$

For a maximum unbalance of 0.25 dB between ports 3 and 4,

$$A_3 = KA_4 \quad (\text{A-3})$$

where $0.972 \leq K \leq 1.09$, and

$$\phi_3 = \phi_4 - (90^\circ + \delta) \quad (\text{A-4})$$

where $-0.1^\circ \leq \delta \leq 0.1^\circ$

By proper assignment of reference planes, ϕ_3 may be set to 0. Hence,

$$\phi_3 = 0, \phi_4 = 90^\circ + \delta \quad (\text{A-5})$$

Since the hybrid's matrix is unitary,

$$A_1^2 + A_2^2 + (KA_4)^2 + A_4^2 = 1$$

or

$$A_4 = \sqrt{\frac{1 - (A_1)^2 - (A_2)^2}{1 + K^2}} \approx \sqrt{\frac{1}{1 + K^2}} \quad (\text{A-6})$$

The hybrid is utilized with two power amplifiers in the circuit given in Fig. A-2. It is assumed that an initial gain and phase adjustment has been made to power amplifier 2 which sets its output to $KE_1 e^{-j\theta}$. In the water load position (+90 deg), this adjustment nulls the signal at port 3 for the gain G and phase θ variable parameters equal to unity and zero, respectively. The voltage scattered from the four ports is described in Fig. A-2 as functions of the relative gain G and phase θ variations and the hybrid parameters discussed above.

The subject of particular interest is the ratio of power impressed on the antenna for the two biphasic conditions. This switching isolation ratio R is expressed by

$$R = \frac{b_3 b_3^* (+90^\circ)}{b_3 b_3^* (-90^\circ)}$$

or

$$R = \frac{1 + G^2 - 2G \cos \theta}{1 + G^2 + 2G \cos \theta} \quad (\text{A-7})$$

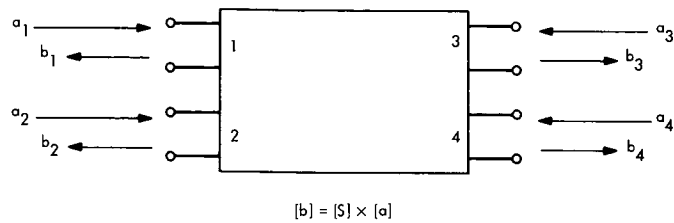
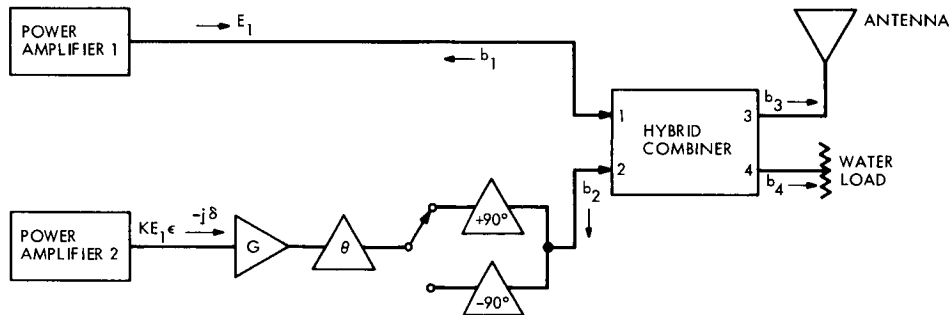


Fig. A-1. Four port hybrid



$$\begin{aligned}
 b_1 &= E_1 A_1 \left[\epsilon^{j\phi_1} \pm jKG \epsilon^{j(\phi_2 - \delta + \theta)} \right] \\
 b_2 &= E_1 A_1 \left[\epsilon^{j\phi_2} \pm jKG \epsilon^{j(\phi_1 - \delta + \theta)} \right] \\
 b_3 &= E_1 \frac{K}{\sqrt{1+K^2}} \left[1 \mp G \epsilon^{j\theta} \right] \\
 b_4 &= j E_1 \frac{1}{\sqrt{1+K^2}} \left[1 \pm K^2 G \epsilon^{j(\theta - 2\delta)} \right]
 \end{aligned}$$

Fig. A-2. Combiner circuit

Efficient Antenna Systems: DSS 14 64-Meter-Diameter Antenna Polarization Properties

P. D. Potter

Communications Elements Research Section

The polarization clock angle of a linearly polarized paraboloidal antenna is a function of both its secondary pattern characteristics and the pointing error relative to the antenna axis of revolution. For polarization tracking scientific experiments such as those planned in support of Project Helios, it is necessary to have an understanding of the relationship between the feed system polarization clock angle (a physically measured quantity) and the overall antenna polarization clock angle. In particular, the S- and X-band reflex feed system introduces significant antenna beam asymmetry which gives rise to polarization error. In this reporting, the DSS 14 64-m antenna secondary pattern characteristics are developed as a function of the reflex feed characteristics previously reported. The polarization angle error is computed as a function of antenna pointing error, typical antenna open-loop pointing errors are reviewed, and the expected polarization distortion is given.

I. Analysis

The coordinate system selected for the secondary pattern analysis is a standard right-handed rectangular system, as shown in Fig. 1. Completely general expressions for the far-field polar and azimuthal pattern components are (Ref. 1)

$$E_{\theta}(\theta, \phi) = \sum_M E_{\theta me}(\theta) \sin(m\phi) \quad (\text{even}) \\ + \sum_M E_{\theta mo}(\theta) \cos(m\phi) \quad (\text{odd}) \quad (1a)$$

$$E_{\phi}(\theta, \phi) = \sum_M E_{\phi me}(\theta) \cos(m\phi) \quad (\text{even}) \\ + \sum_M E_{\phi mo}(\theta) \sin(m\phi) \quad (\text{odd}) \quad (1b)$$

From geometry, the rectangular field components are given by

$$E_X(\theta, \phi) = E_{\theta}(\theta, \phi) \cos \theta \cos \phi - E_{\phi}(\theta, \phi) \sin \phi \quad (2a)$$

$$E_Y(\theta, \phi) = E_{\theta}(\theta, \phi) \cos \theta \sin \phi + E_{\phi}(\theta, \phi) \cos \phi \quad (2b)$$

In general, the antenna response in a particular θ, ϕ direction is elliptically polarized; this response is conveniently described by a polarization ellipse, as shown in Fig. 2. At a given point in space, the X- and Y-field components can be expressed as follows:

$$E_X(\theta, \phi) = E_{X0}(\theta, \phi) \cos(\omega t) \quad (3a)$$

$$E_Y(\theta, \phi) = E_{Y0}(\theta, \phi) \cos(\omega t + \delta) \quad (3b)$$

where ω is angular frequency and t is time.

From geometry (Fig. 2):

$$E_U(\theta, \phi) = E_X(\theta, \phi) \cos \tau + E_Y(\theta, \phi) \sin \tau \quad (4a)$$

$$E_V(\theta, \phi) = -E_X(\theta, \phi) \sin \tau + E_Y(\theta, \phi) \cos \tau \quad (4b)$$

With some algebraic manipulation (Ref. 2) it is found that

$$\tau = \frac{1}{2} \arctan \left[\frac{2 E_{X0}(\theta, \phi) \times E_{Y0}(\theta, \phi) \times \cos \delta}{E_{X0}^2(\theta, \phi) - E_{Y0}^2(\theta, \phi)} \right] \quad (5)$$

It is assumed that the feedhorn input is linearly polarized at a clock angle β . By linearity, the overall vector antenna pattern $E_T(\theta, \phi, \beta)$ is given by

$$\mathbf{E}_T(\theta, \phi, \beta) = \mathbf{E}_1(\theta, \phi) \sin \beta + \mathbf{E}_2(\theta, \phi) \cos \beta \quad (6)$$

where

$$\mathbf{E}_1(\theta, \phi) \text{ is the antenna pattern for } \beta = 90 \text{ deg} \quad (7a)$$

and

$$\mathbf{E}_2(\theta, \phi) \text{ is the antenna pattern for } \beta = 0 \text{ deg} \quad (7b)$$

The assumption is now made that $|\mathbf{E}_T|$ is independent of β . This assumption is tantamount to assuming that the feedhorn main beam radiation pattern is independent of β , an excellent approximation for the 64-m corrugated feedhorns. It is readily shown that this assumption can only be satisfied by the following conditions:

$$E_{2\phi}(\theta, \phi) = \pm E_{1\phi}(\theta, \phi) \quad (8a)$$

$$E_{2\theta}(\theta, \phi) = \mp E_{1\theta}(\theta, \phi) \quad (8b)$$

where $E_{1\theta}(\theta, \phi)$ and $E_{2\theta}(\theta, \phi)$ are the polar field components of $\mathbf{E}_1(\theta, \phi)$ and $\mathbf{E}_2(\theta, \phi)$, and $E_{1\phi}(\theta, \phi)$ and $E_{2\phi}(\theta, \phi)$ are the azimuthal field components of $\mathbf{E}_1(\theta, \phi)$ and $\mathbf{E}_2(\theta, \phi)$.

Combining (6) and (8):

$$E_\theta(\theta, \phi, \beta) = E_{1\theta}(\theta, \phi) \sin \beta \pm E_{1\phi}(\theta, \phi) \cos \beta \quad (9a)$$

$$E_\phi(\theta, \phi, \beta) = E_{1\phi}(\theta, \phi) \sin \beta \mp E_{1\theta}(\theta, \phi) \cos \beta \quad (9b)$$

For the case of $\phi = \beta$, from (2) and (9),

$$E_X(\theta, \beta) = E_{1\phi}(\theta, \beta) \cos(2\beta) + E_{1\theta}(\theta, \beta) \sin(2\beta) \quad (10a)$$

$$E_Y(\theta, \beta) = -E_{1\theta}(\theta, \beta) \cos(2\beta) + E_{1\phi}(\theta, \beta) \sin(2\beta) \quad (10b)$$

where the $\cos \theta$ factor has been removed from (2) because of the narrow secondary pattern beamwidth, and the upper signs are used in (9).

The functions $E_{1\phi}(\theta, \beta)$ and $E_{1\theta}(\theta, \beta)$ correspond to the "even" modes in (1) and can be readily computed using

JPL software. Using (3), (5), and (10), the polarization clock angle τ may be computed. Ideally, τ would equal β , the physically measured polarization quantity. Asymmetry in the reflex feed system, however, introduces a difference between τ and β , i.e., a polarization error.

II. Computed Results

The reflex feed system radiation pattern, in the form of Eq. (1), is already available from previous calculations and 1/7-scale model tests (Refs. 1, 3). Excellent agreement between computed and measured patterns is achieved by using only the $m = 0$ and $m = 2$ asymmetrical components in addition to the nominal, desired $m = 1$ component. Fields scattered by the slightly asymmetrical antenna subreflector can be calculated using the Ludwig scattering program (Ref. 4). It has been previously determined, however, that the pattern asymmetry introduced by the subreflector is minor compared to the asymmetry in the reflex feed system (see Ref. 3, p. 143). In the interest of economy, therefore, a subreflector "symmetrically equivalent" to the actual subreflector was determined. Subreflector patterns were then calculated using an upgraded version of the Rusch scattering program (Ref. 5). This program is extremely fast and economical to use, as it can perform the azimuthal (physical optics) integration analytically (rather than numerically) by virtue of the assumption of a scattering surface of revolution. Professor W. V. T. Rusch (University of Southern California, Consultant to JPL Communications Elements Research Section) originally formulated the scattering program to handle asymmetrical illumination patterns of the form of Eq. (1), but this capability was never utilized. For the polarization problem, the capability was exercised and checked out numerically with Ludwig's flat plate scattering technique (Ref. 4). The ability to perform highly economical scattering calculations of asymmetrically illuminated symmetrical reflectors with the Rusch program is felt to be a powerful new capability.

The three ($m = 0, 1, 2$) azimuthal Fourier component subreflector scattered patterns are shown in Fig. 3. For comparison, the standard corrugated feedhorn patterns are shown in Fig. 4. Figures 5 and 6 show the total (sum of the $m = 0, 1, 2$ components) scattered patterns. As seen in the phase patterns, the $m = 1$ component is symmetrical with respect to the $z(\theta = 0)$ axis, whereas the $m = 0$ and 2 components are antisymmetrical (this is also clear from Eq. 1). Slight pattern asymmetry results in the $\phi = 0/180$ -deg cut total pattern (Fig. 5). Also, a cross-polarized component arises in the $\phi = 90/270$ -deg cut (Fig. 6). These data were used as input to the Rusch program again to

compute the antenna secondary patterns (subreflector scatterings off the paraboloid). Figures 7, 8, 9, and 10 show the secondary patterns analogous to the subreflector patterns in Figs. 3 through 6. The (minor) effect of the 64-m antenna quadripod structure is not included in these patterns.

Using the data shown in Fig. 7 and the analysis developed in the preceding section, the polarization error ($\tau - \beta$) was computed as a function of the feedhorn polarization clock angle β ; the results are shown in Fig. 11. The polarization error is very nearly sinusoidally related to β , with a peak amplitude which is very nearly linearly related to the antenna pointing error θ .

III. 64-Meter-Diameter Antenna Pointing Errors

In February 1973, two days of high-precision Ku-band DSS 14 antenna pointing data were taken by Arthur Niell of the Planetary Atmospheres Section. These data were

corrected for station timing and ephemeris errors and then least-squares-fitted to a cubic spline in antenna elevation angle; the result is shown in Fig. 12. Three different radio sources, 3C273, 3C274, and 3C84 were utilized by Niell in his tests. As seen in Fig. 12, the peak pointing errors are 0.010 – 0.020 deg and more typically less than 0.010 deg. These data are ideal, however, since great care was taken to point the antenna properly. Typical open-loop tracking mission pointing is presumably not as good.

IV. Conclusions

From a comparison of the computed polarization errors shown in Fig. 11 with ideal condition antenna pointing errors measured by A. Niell, it appears that proper antenna pointing is critical to the Project Helios polarization rotation experiment, but that if the antenna is properly pointed, the polarization distortion caused by reflex feed can be held within acceptable limits.

References

1. Potter, P. D., "S- and X-Band RF Feed System," in *The Deep Space Network Progress Report*, Technical Report 32-1526, Vol. VIII, pp. 53–60. Jet Propulsion Laboratory, Pasadena, Calif., April 15, 1972.
2. Rusch, W. V. T., and Potter, P. D., *Analysis of Reflector Antennas*, Academic Press, New York, 1970, pp. 61–68.
3. Potter, P. D., "S- and X-Band RF Feed System," in *The Deep Space Network Progress Report*, Technical Report 32-1526, Vol. IX, pp. 141–146. Jet Propulsion Laboratory, Pasadena, Calif., June 15, 1972.
4. Ludwig, A. C., *Calculation of Scattered Patterns from Asymmetrical Reflectors*, Technical Report 32-1430, Jet Propulsion Laboratory, Pasadena, Calif., Feb. 15, 1970.
5. Ludwig, A. C., and Rusch, W. V. T., *Digital Computer Analysis and Design of a Subreflector of Complex Shape*, Technical Report 32-1190, Jet Propulsion Laboratory, Pasadena, Calif., Nov. 15, 1967.

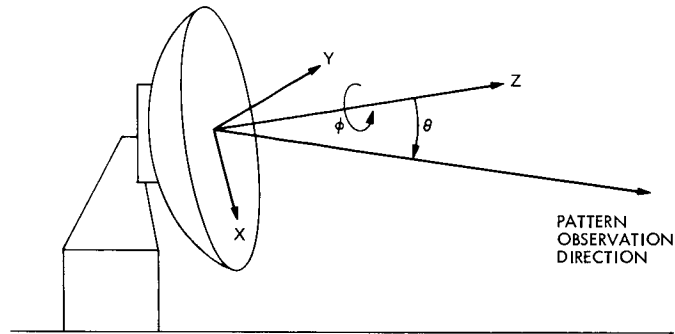


Fig. 1. Antenna pattern coordinate system

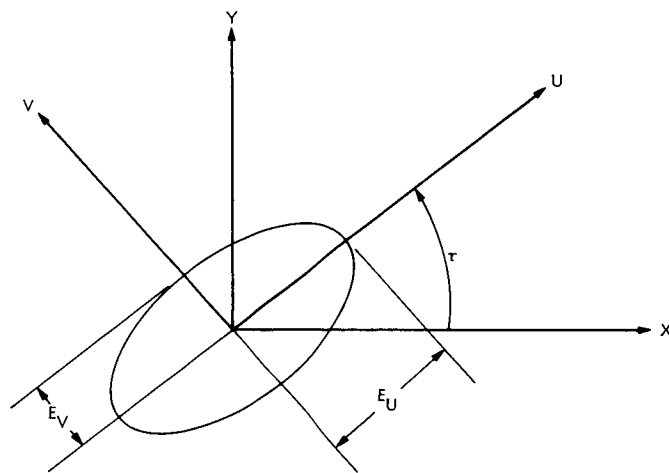


Fig. 2. Polarization ellipse

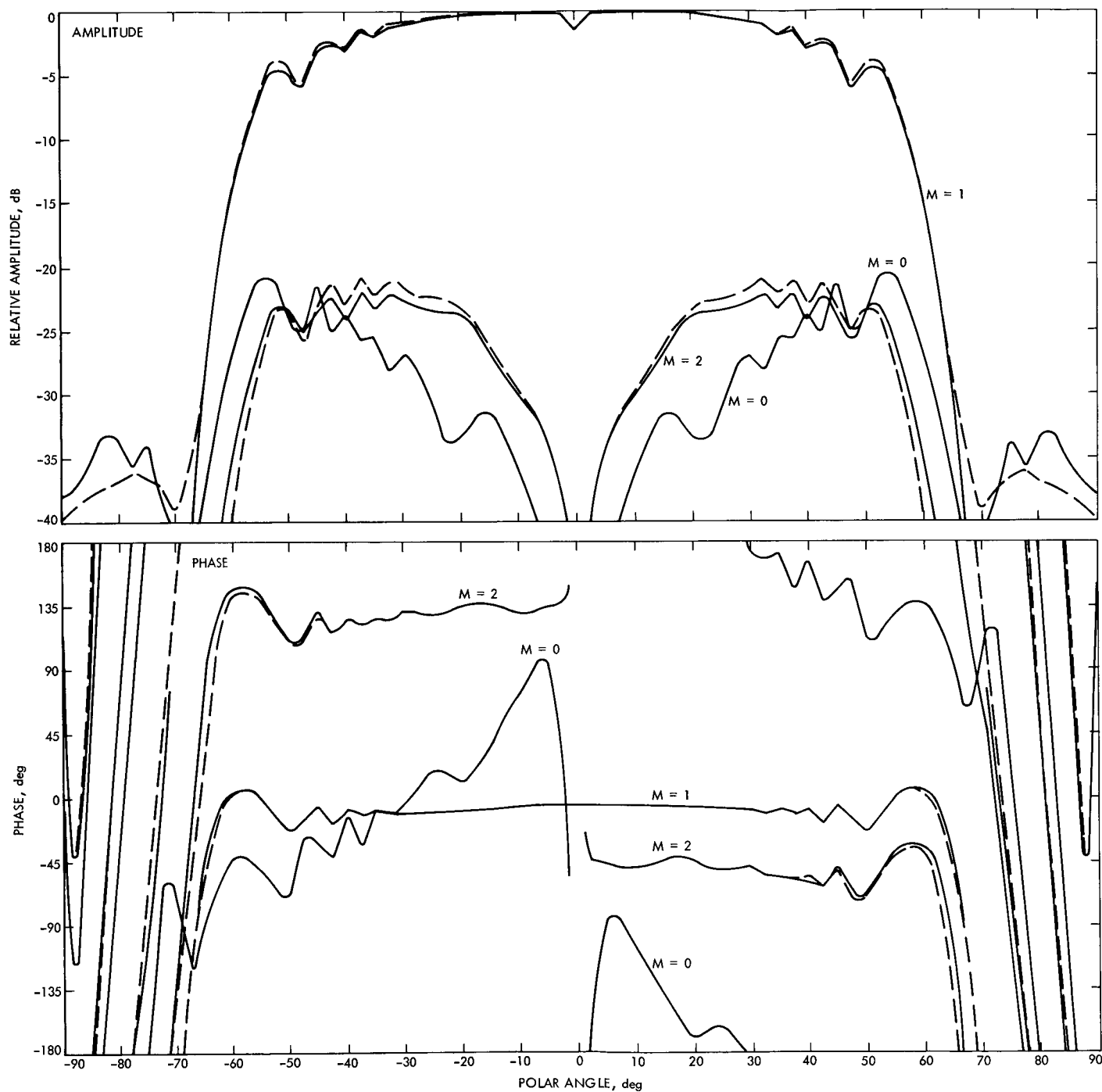


Fig. 3. Reflex feed subreflector scattered azimuthal Fourier component patterns

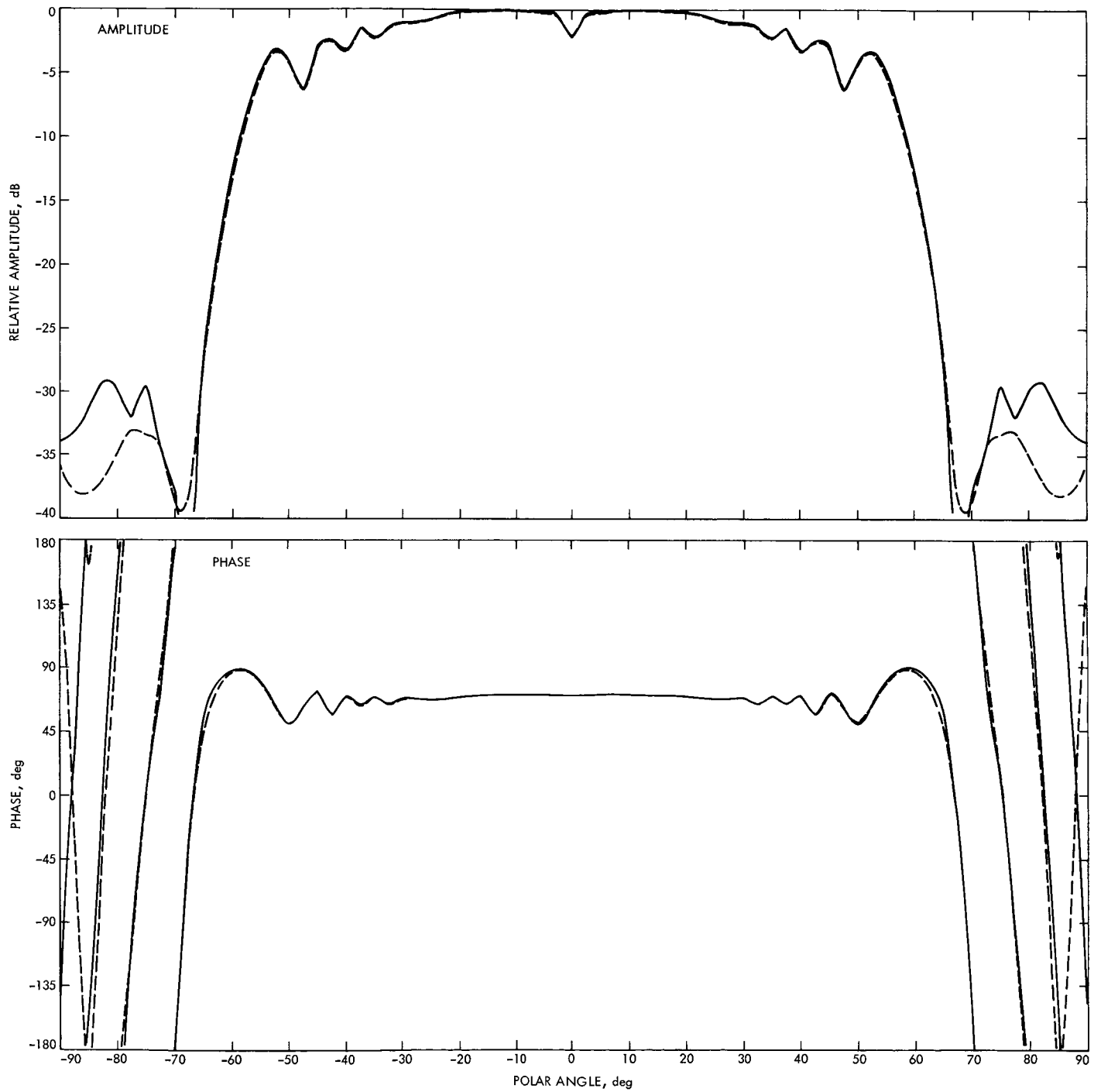


Fig. 4. Standard corrugated feedhorn scattered patterns

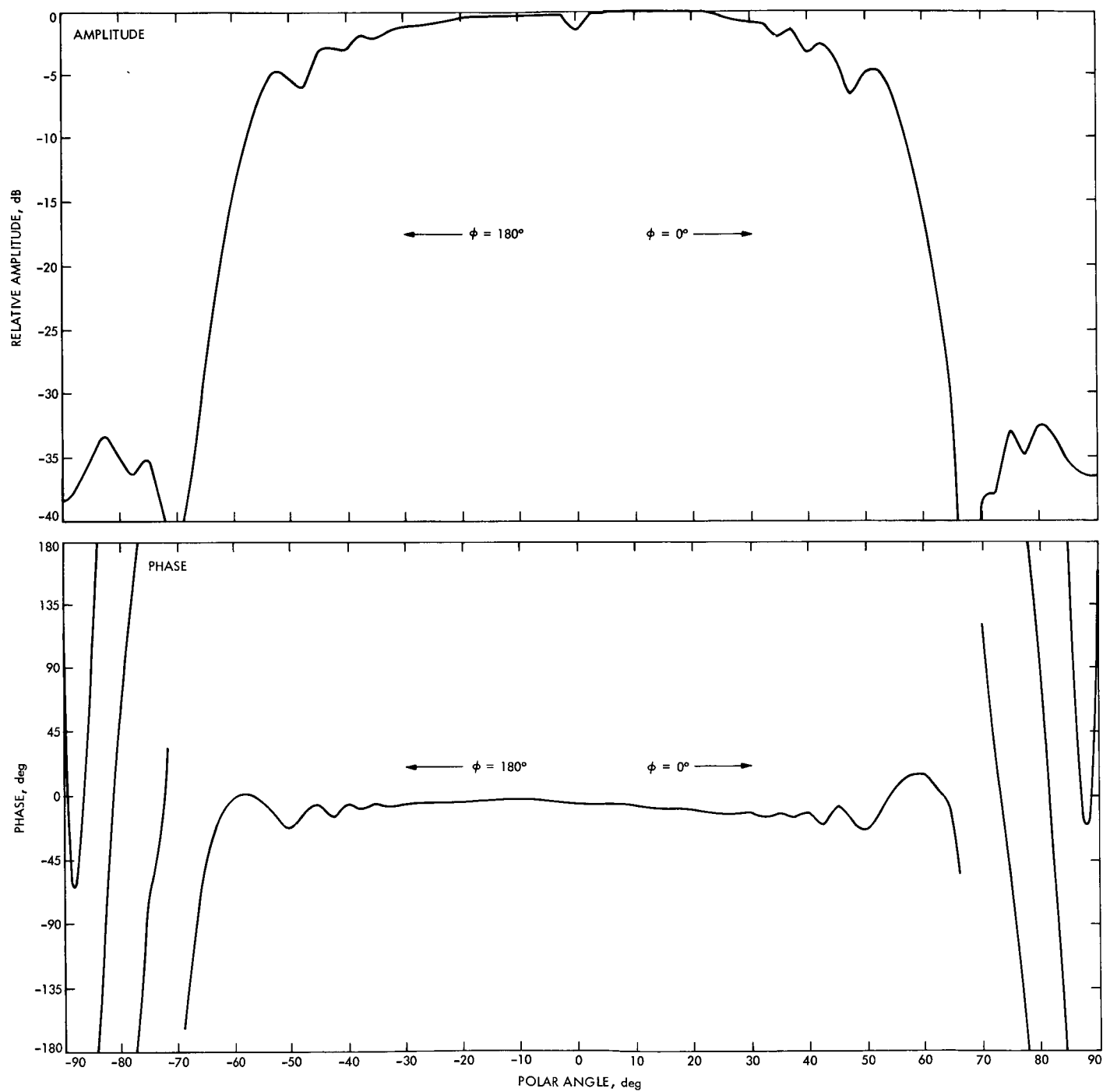


Fig. 5. Total reflex feed subreflector scattered patterns, $\phi = 0/180$ -deg cut

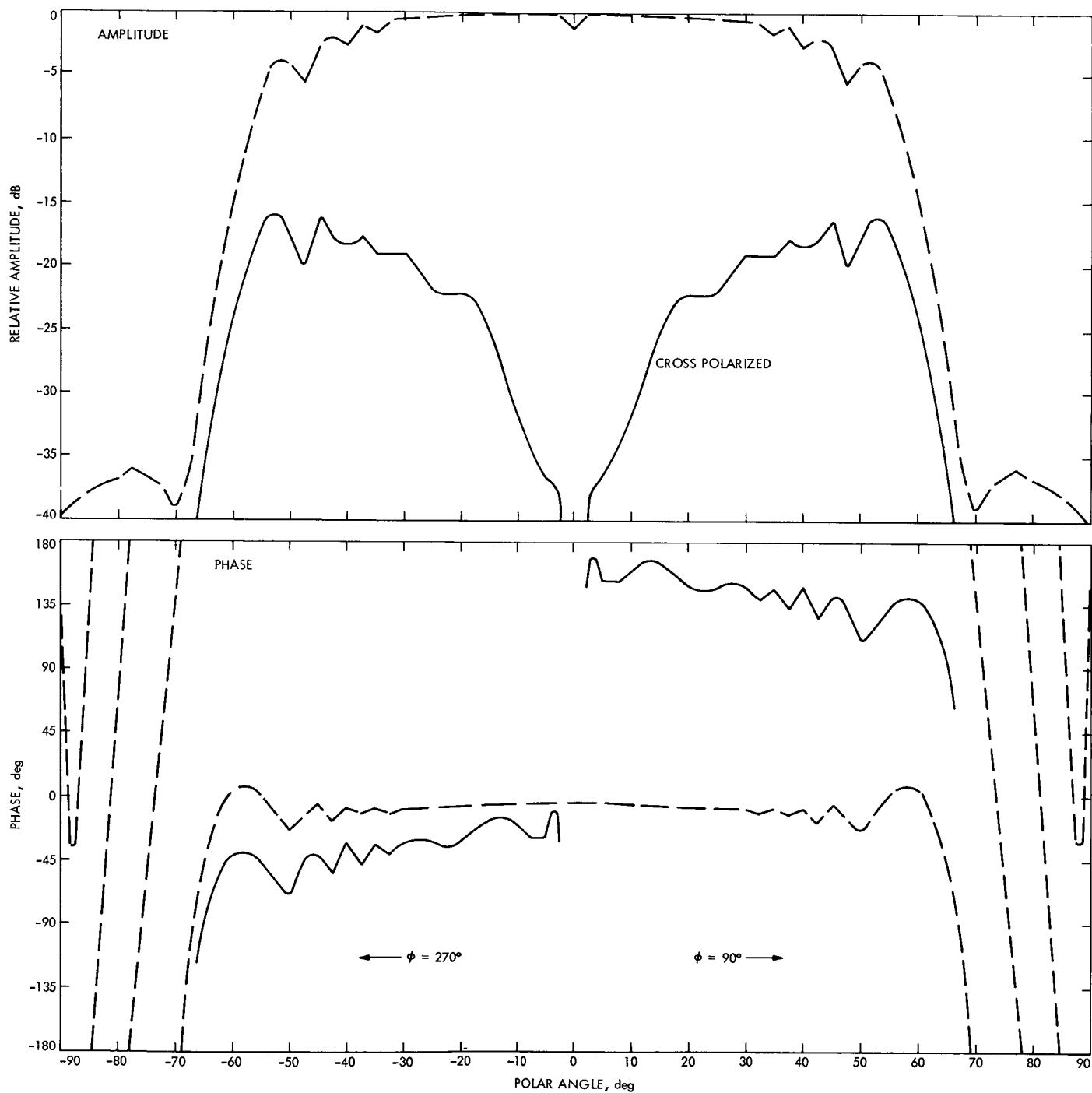


Fig. 6. Total reflex feed subreflector scattered patterns, $\phi = 90/270$ -deg cut

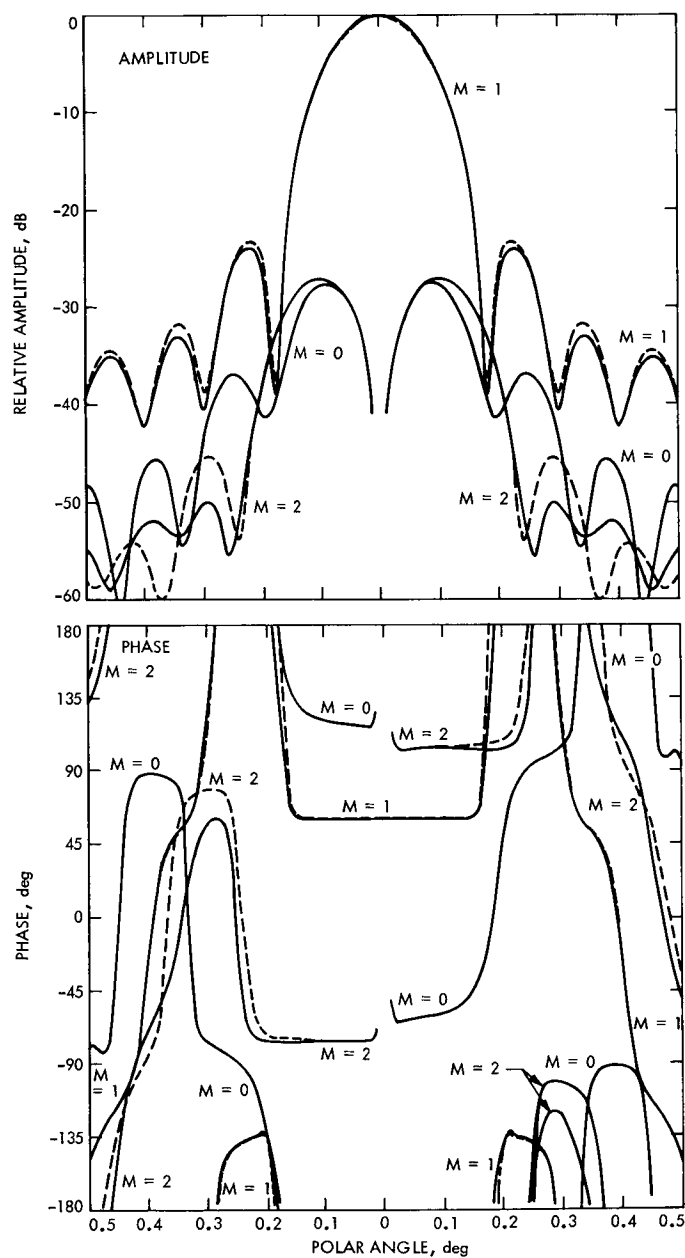


Fig. 7. S-band 64-m paraboloid azimuthal Fourier component patterns, reflex feed, no quadripod

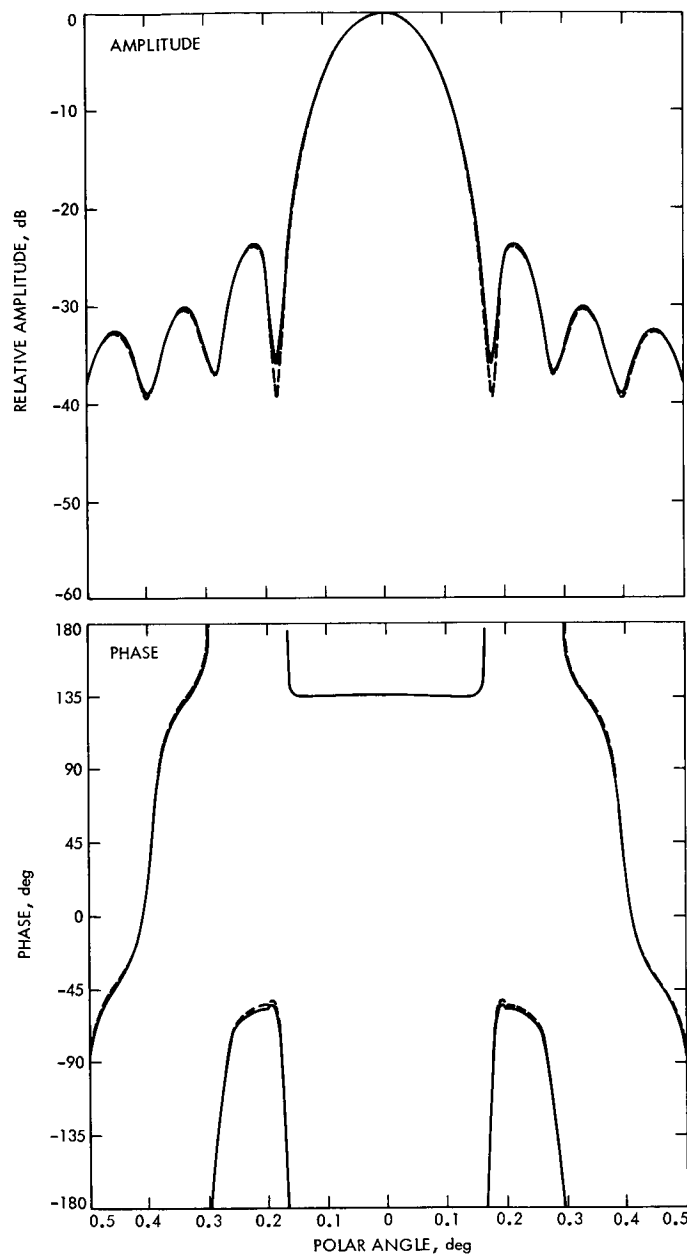


Fig. 8. S-band 64-m paraboloid patterns, standard corrugated feedhorn, no quadripod

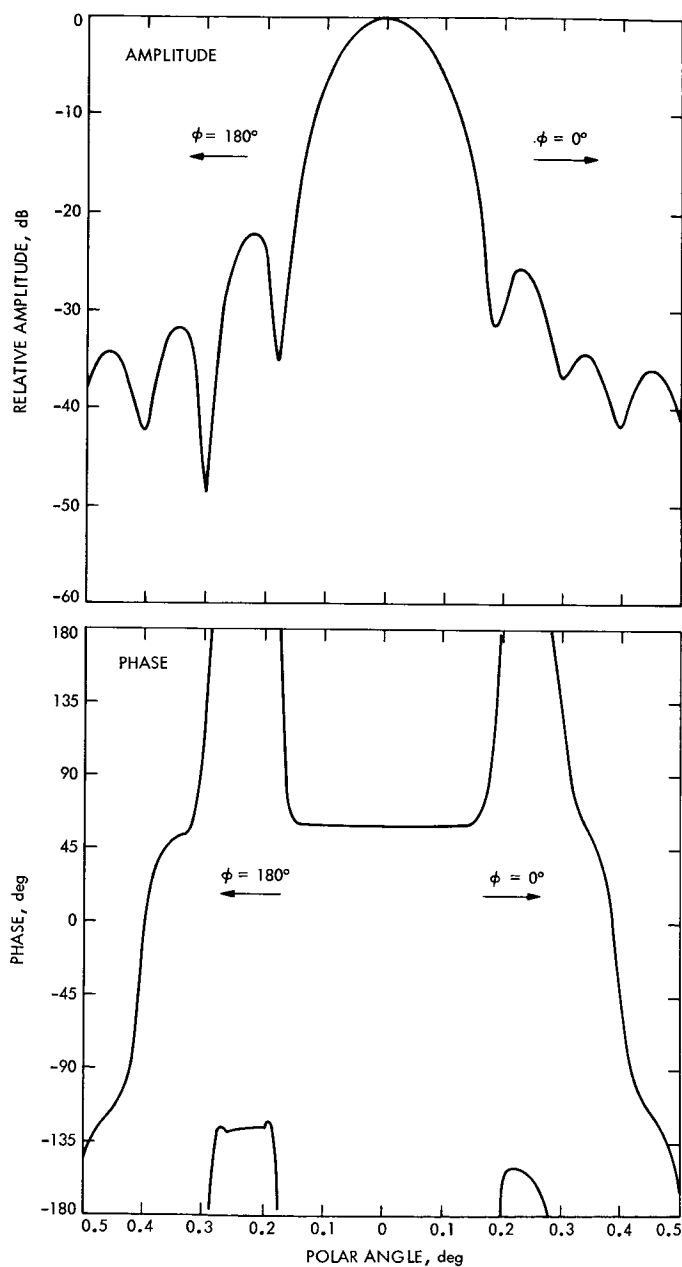


Fig. 9. S-band 64-m paraboloid total patterns, $\phi = 0/180$ -deg cut, reflex feed, no quadripod

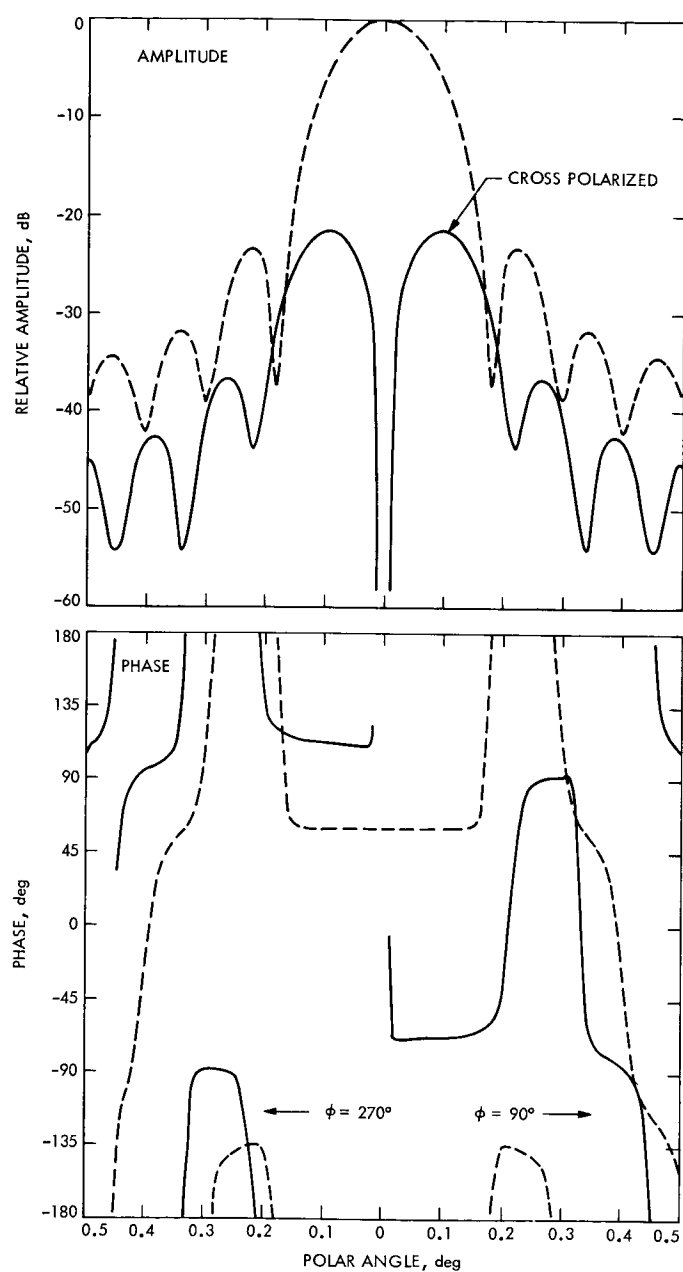


Fig. 10. S-band 64-m paraboloid total patterns, $\phi = 90/270$ -deg cut, reflex feed, no quadripod

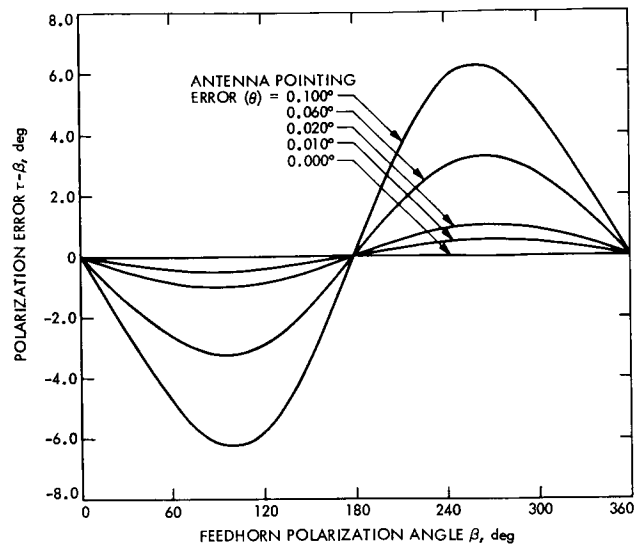


Fig. 11. Polarization error vs feedhorn polarization angle

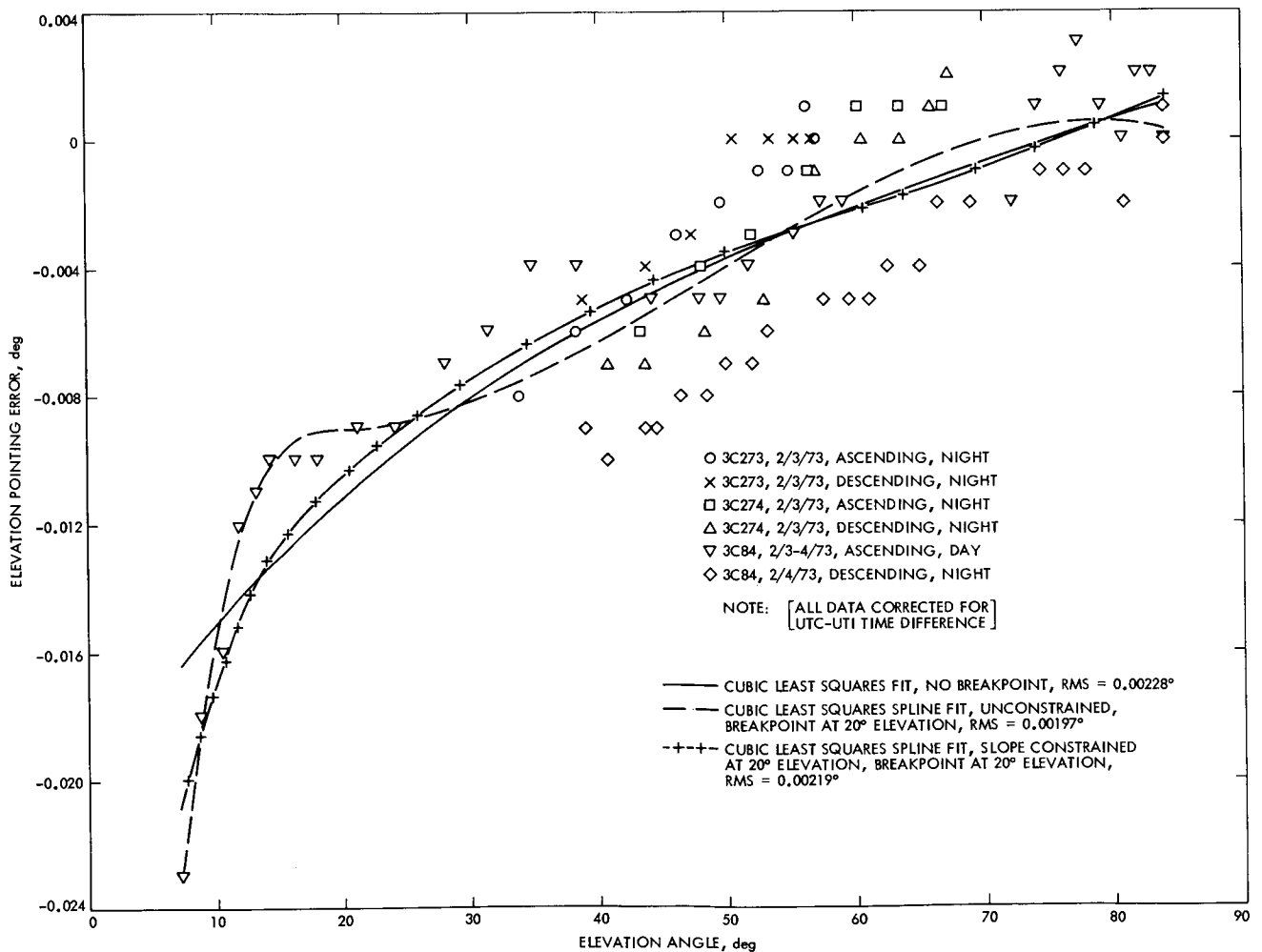


Fig. 12. DSS 14 Ku-band elevation pointing error, February, 1973

Demonstration of Intercontinental DSN Clock Synchronization by VLBI

W. J. Hurd

Communications Systems Research Section

The prototype system for DSN clock synchronization by VLBI has been demonstrated to operate successfully over intercontinental baselines in a series of experiments between Deep Space Stations at Madrid, Spain, and Goldstone, California. As predicted by analysis and short baseline demonstration, the system achieves reliable synchronization between 26-m and 64-m antenna stations with 17 and 37 K nominal system temperatures using under one million bits of data from each station. Semi-real-time operation is feasible since this small amount of data can be transmitted to JPL and processed within minutes. The system resolution is 50 to 400 ns, depending on the amount of data processed and the source intensity. The accuracy is believed to be comparable to the resolution, although it could be independently confirmed to only about 5 μ s using LORAN C.

I. Introduction

The prototype for a semi-real-time system for DSN clock synchronization by radio interferometry was first demonstrated on a short baseline in August 1972 (Refs. 1 and 2). A series of three experiments has now been conducted between Madrid, Spain, and Goldstone, California, to demonstrate that the system performs as expected on intercontinental baselines. The series of experiments had three primary classes of objectives, all of which were achieved:

- (1) To confirm that the system achieves the predicted resolution with the predicted amount of data; this implies that there are radio sources available which act as strong enough point sources over the long baseline.

- (2) To check the system accuracy by demonstrating consistent results at different times of day and with different radio sources and, by direct comparison with other clock sync systems, to within the accuracy of these systems.
- (3) To gain experience in operating VLBI systems so as to uncover potential problem areas and facilitate the design of a higher-accuracy, operational clock sync system.

Using one 64-m and one 26-m antenna, several sources were available which were strong enough to achieve resolutions of from 200 to 400 ns with about 1 million bits of data and 50 to 100 ns with several million bits. We believe

that the system accuracy is consistent with these resolutions. However, the absolute accuracy could be confirmed only to the approximate 5-10 μ s accuracy of LORAN C.

II. Description of Experiments

The three experiments were conducted on April 12, April 30, and June 11, 1973. On the first of these days, two 26-m antenna stations were used, DSS 12 at Goldstone and DSS 62 at Madrid. The last two experiments used the 64-m antenna at DSS 14, together with DSS 62. To maximize the use of station time and to obtain a rough check on the accuracy, the last two experiments were run simultaneously with another VLBI experiment (conducted by J. Faneslow of Section 391). The purpose of this other experiment was to measure the platform parameters, the source positions, and UT1. The two independent experiments agreed in their estimates of clock offset to within about 10 μ s, the approximate accuracy of the platform parameter experiment.

The data were acquired and processed in the same manner as for the first clock sync demonstration (Refs. 1-3). Coherent bursts of about 0.31 Mbits of usable data, as limited by the computer memory size, were taken at 10-s intervals and recorded onto magnetic tape. Since the sampling rate was 0.5 Mbps, the burst length was only about 0.62 s, but the burst frequency was limited by the 200-bpi magnetic tape density. Each full tape of data consisted of 72 bursts. However, some tapes contained less data due to tape failures. In the joint experiments, the source schedule of the platform parameter experiment was followed, which sometimes allowed only 2 or 3 min between sources. When only one tape unit was operational, the number of bursts of data on each tape was reduced due to the time required to change tapes. Other short tapes were caused by tape errors.

The tapes were mailed to JPL for processing. The maximum likelihood estimator function (Ref. 3) was calculated for each burst of data, and then the function values were accumulated in a nonoptimal manner over enough successive bursts of data to achieve an adequate estimator signal-to-noise ratio. The accumulation was nonoptimal only because fringe phase coherence was not maintained between bursts. This resulted in little degradation for strong input signal-to-noise cases, when only 2 or 4 bursts were required, but in significant degradation for weak sources and when both stations had 26-m antennas. The system was not designed to operate in these situations because too much data is required for satisfactory operation.

III. Results

Estimates of clock offset were obtained for two tapes of data on April 12, using two 26-m antennas, and for ten and five tapes of data on April 30 and June 11, respectively, using one 26-m and one 64-m antenna. The nominal system temperatures were 17 K at the 64-m station and 37 K at the 26-m stations. Successful estimates were not obtained for all pairs of tapes on any day. On the first day, this was because the signal-to-noise ratios were too low on all but the strongest source. On the two days using the 64-m antenna, the failures are believed to be due mainly to tape failures. This is discussed further in Section IV.

The clock offset estimates are presented in Table 1, together with estimates of the resolution obtained and of the amount of data required for reliable measurement. The first three columns identify the case by date, time (GMT), and radio source name. The fourth column indicates the number of subcases into which the data were divided, and the fifth column indicates the number of coherent bursts of 0.31 Mbits of data that were combined noncoherently in each subcase. The sixth column is the average estimate of clock offset for the case, in microseconds, with positive values indicating that the clock at DSS 62 is early. The seventh and eighth columns are the estimated resolutions for one subcase and for the entire case in nanoseconds. For cases with more than one subcase, the resolution for one subcase is taken as the sample standard deviation, and the overall resolution is this standard deviation divided by the square root of the number of subcases. For the four cases having such a low signal-to-noise ratio that there was only one subcase, the estimated resolutions were obtained from the value of the estimator function. These estimates are quite unreliable. The final column in Table 1 is the estimated amount of data required to obtain reliable estimates for that source, on that day, and with the system parameters used. It is the amount of data required for an estimator signal-to-noise ratio of 10 and a resulting resolution of 366 ns.

A. Data Requirements for Reliable Results

Of primary importance is that reliable results were obtained with four radio sources with one million or fewer bits of data when using the 64-m antenna. These sources are 4C39.25, OJ287, DA193, and NRAQ190. The flux densities were not estimated directly from the data, because this requires considerable additional computer time. However, from the estimator signal-to-noise ratios and the nominal system temperatures, we estimate the correlated flux densities for these sources to range from 1 to 2 fu. There are enough radio sources of this strength that clock synchronization is attainable at any time of day between

DSS 14 and Spain or Australia. Similar performance will be achievable between Spain and South Africa when DSS 63, a 64-m station, is operational in Spain.

B. Resolution and Consistency

The results for the ten cases of April 30 are shown as a function of time in Fig. 1. The straight line has a slope equal to the rate of change in the clocks, $-0.6 \mu\text{s}/\text{day}$, as predicted by the fringe rate data taken in the platform parameter VLBI experiment on that day. The error bars shown are the estimated resolutions. At best, the accuracy would be the resolution plus a degradation of up to about 100 ns due to propagation and geometrical effects. This should be added in a mean square sense. (There is also a constant error due to time delays in the stations, which would not show up in the results.)

Overall, all of the clock offset estimates fall as close to the straight line as expected except for the case for DW0224+67 and the two cases for 3C371. Although these sources are quite weak, especially 3C371, there appears to be some significant error for these cases. The cause for this error has not yet been satisfactorily explained. However, one likely cause is that the time delay predictions were in error due to the high declinations of the sources, +67 deg for DW0224+67 and +69 deg for 3C371. The highest declinations for the other sources are +56 deg for OL553 and +41 deg for 3C84. Furthermore, the geometry was so unusual for 3C371 that the received frequency was higher for DSS 62 than for DSS 14, just the opposite from the usual case, because the antennas were pointed on the opposite from usual sides of due north. This can happen only with high declination sources.

C. Comparison to LORAN C and Platform Experiment

The clock offset estimates obtained in these experiments agree with estimates made on each day using LORAN C, to within the approximate 5–10 μs accuracy that could be expected. For the last two days, the results also agree with the VLBI platform parameter experiment, to the accuracy of that experiment. There was, however, a constant 200- μs offset with respect to LORAN C. This was determined to arise because some of the 1-s period reference signals at DSS 62 occurred 200 μs early because of reference to the wrong edge of a 200- μs duration pulse.

The comparisons to LORAN C and the platform experiment are shown in Table 2. The first column identifies the experiment date. The second column is the difference between the DSS 62 and the LORAN C Mediterranean chain clock. The nominal accuracy is about 2 μs , but ambiguities often cause errors in 10- μs increments. The third column

is the sum of all known corrections from the LORAN C Mediterranean clock to the DSS 12 or 14 clock, that is, LORAN C to the U.S. Naval Observatory (USNO), USNO to the National Bureau of Standards (NBS), NBS to the Goldstone master clock, and the Goldstone clock to DSS 12 or 14. Each of these legs introduces some error, typically on the order of 1 μs . The fourth column is the estimate of clock offset between the stations obtained from LORAN C. The last two columns are the offsets obtained by the VLBI platform parameter experiment and by this experiment, corrected for the known 200- μs error at DSS 62.

The clock offsets measured in this experiment agree with LORAN C to within an average of 5 μs and to the VLBI platform experiment to an average of 11 μs . These results are consistent with the accuracies of LORAN C and the platform experiment.

IV. Problems, Causes, and Solutions

The two major problems in the series of experiments were that results were not obtained for any day until the data from the last experiment were processed and that good results were not obtained at all for a number of cases for which the signal-to-noise ratio should have been adequate. A number of possible causes for lack of results were studied while an unsuccessful attempt was being made to process the data. These investigations will influence the design of the final operational system.

The delay in achieving results was caused primarily by the 200- μs error in the predicted clock offset. This area of clock offset was not searched until after the large offset error was discovered by the VLBI platform parameter experimenters. Even then, there was a delay in obtaining good results due to a discrepancy between the software and the hardware which was caused by a system modification made after the short baseline experiments. One of the ramifications of this change was overlooked. Aside from leading to a more complete analysis of the system, this processing problem will have no effect on the future system.

A. Search Range and Variable Bandwidths

The 200- μs offset error will have an effect on the future system. It pointedly illustrates that large errors can occur, even when the system is supposedly calibrated with LORAN C. It also illustrates the problems which could occur if synchronization is lost and the best available timing information available is by radio broadcast, with errors on the order of milliseconds. An operational system

should be capable of efficiently searching as wide a region of clock offsets as possible. This is best accomplished by enabling data acquisition with a number of selectable bandwidths and sampling rates. Lower bandwidths and sampling rates enable wider searches because the wide region encompasses fewer samples. Programable digital filtering would be the most flexible and economical method for achieving this.

B. Local Oscillator Frequency Adjustment

One possible cause for bad data was that the third (10-MHz) local oscillator (LO) was offset at the Goldstone station in order to compensate for the fringe rate or doppler frequency difference. This LO was manually adjusted for each case, and it is possible that the frequency synthesizer was improperly set for some cases. This problem can be avoided by accounting for the fringe rate entirely in the data processing. There would be some cost in computer time.

C. Synchronization of Samples to Station Clock

Another possible trouble area is in synchronization of the samples to the station clocks. In these experiments,

the hardware was resynchronized to the frequency and timing system (FTS) 1-pps and 1-MHz signals at the beginning of each burst of data, i.e., every 10 s. It would probably be more reliable to synchronize the system to the station clock only once for any experiment. Since the resolution of the present FTS is only on the order of 0.1 to 1.0 μ s, a higher-resolution clock will be required in any case for the more accurate clock sync system. This high-resolution clock could either be a part of the clock sync hardware or be in the form of a new timing system.

V. Conclusion

The prototype VLBI clock synchronization system has been demonstrated to operate as predicted over transcontinental baselines. Resolutions of 50–400 ns were achieved, and the accuracy is believed to be approximately the same. A wideband system is being designed which will achieve a resolution of 1–10 ns, depending on the available receiver bandwidth. The accuracy of this system will be limited by atmospheric and geometric effects and by errors in calibrating time delays in the stations rather than by the system bandwidth and resolution.

References

1. Hurd, W. J., "A Demonstration of DSN Clock Synchronization by VLBI," in *The Deep Space Network Progress Report*, Technical Report 32-1526, Vol. XII, pp. 149–160, Jet Propulsion Laboratory, Pasadena, Calif., Dec. 15, 1972.
2. Hurd, W. J., "An Analysis and Demonstration of Clock Synchronization by VLBI," in *Proceedings of the Fourth Annual NASA and Department of Defense Precise Time and Time Interval Planning Meeting*, Goddard Space Flight Center, Greenbelt, Md., Nov. 14–16, 1972, pp. 100–122 (NASA Report X-814-73-72), to appear in the *IEEE Trans. Instr. Meas.*
3. Hurd, W. J., "DSN Station Clock Synchronization by Maximum Likelihood VLBI," in *The Deep Space Network Progress Report*, Technical Report 32-1526, Vol. X, pp. 82–95, Jet Propulsion Laboratory, Pasadena, Calif., Aug. 15, 1972.

Table 1. Clock offset estimates, estimated resolution, and data required for reliable performance

Date, 1973	Time, GMT	Source	Number of subcases	Number of bursts per subcase	Estimated clock offset, μ s	Resolutions for one subcase, ns	Resolution for entire case, ns	Minimum data required, Mbits
4/12	2152	4C39.25	4	36	134.63	345	172 (2 tapes)	10
4/30	1756	NRAQ190	15	4	125.77	340	90	1.1
	1812	3C84	8	8	125.17	510	180	5
	1845	DW0224 + 67	8	8	124.41	470	170	4
	1906	NRAQ190	6	8	125.59	220	90	0.9
	2118	3C371	1	38	122.7	400 ^a	400 ^a	14
	2208	4C39.25	8	4	125.49	190	70	0.4
	2242	QL553	1	72	126.6	370 ^a	370 ^a	22
	2300	QJ287	23	2	125.56	240	50	0.3
5/1	0007	3C371	1	54	123.3	220 ^a	220 ^a	6
	0022	4C39.25	9	4	125.24	150	50	0.2
6/11	1726	DA193	16	4	203.16	220	60	0.5
	1848	OI363	8	8	203.39	470	170	4
	1905	DA193	16	4	202.71	190	50	0.4
	1923	4C39.25	16	4	203.25	210	50	0.4
	1941	3C371	1	71	200.8	1000 ^a	1000 ^a	50

^aFor these cases the signal-to-noise ratio is so low that the estimates of resolution and data required may have large errors.

Table 2. Comparison of clock offset estimates

Date, 1973	LORAN C, uncorrected (DSS 62 to LORAN C), μ s	LORAN C, corrections (DSS 12/14 to LORAN C), μ s	LORAN C offset estimate (DSS 62 to DSS 12/14), μ s	VLBI platform parameter estimate, μ s	Offset estimate of this experiment, μ s
4/12	-62	+1	-61	-	-65
4/30	-74	+7	-67	-84	-74
6/11	+3	-4	-1	-9	+3

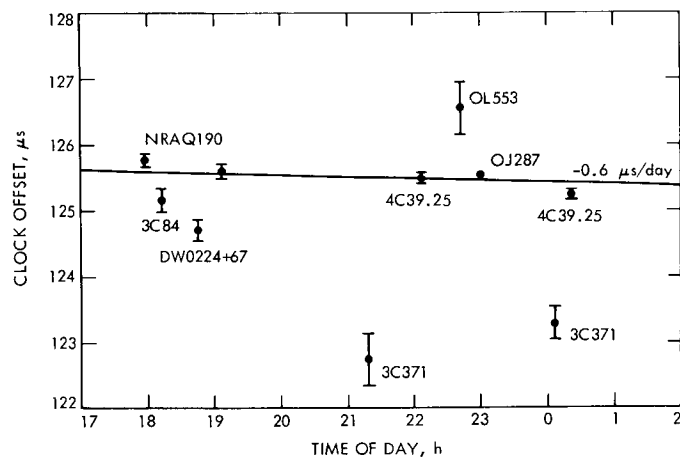


**Fig. 1. Clock offset estimates for April 30, 1973,
with $1\text{-}\sigma$ resolutions**

Digital DC Offset Compensation of Analog-to-Digital Converters

S. S. Brokl and W. J. Hurd
Communications Systems Research Section

A digital dc offset restoration system is described for use with wide bandwidth analog-to-digital converters (ADC). The main feature is that the system compensates for offsets in the conversion device itself, as well as for analog input offsets. A 1-bit ADC realization is described which operates at 40 Mbps using transistor-transistor logic in the dc restore circuitry. Conversion rates of over 100 Mbps can be achieved using emitter-coupled logic exclusively. This high-speed ADC is used in spectral analysis of planetary radar returns.

I. Introduction

A digital dc offset compensation system is presented for use with analog-to-digital (A/D) conversion systems. The system is described with application to a 1-bit A/D converter used in a planetary radar spectral analysis system. The application easily extends to higher-resolution converters in other data acquisition systems. The system has two major advantages over conventional analog techniques such as capacitor or transformer coupling: first, the frequency response of the system does not depend on the characteristics of a capacitor or transformer high-pass filter; and second, offsets in the converter itself are compensated for, as the final digitized signal, rather than just the analog input, is ensured to have zero offset.

The digital feedback used to compensate for input offsets utilizes an up/down counter (UDC) to integrate the converter output. The integrator output is fed back to the

converter input through a digital-to-analog (D/A) converter and an amplifier. The system stabilizes when, on the average, the ADC output has an equal number of plus ones and minus ones. The UDC used in the feedback not only compensates for but measures the input offsets digitally, since the offset is linearly related to the digital value stored in the counter.

Application of the restoration technique to higher-resolution converters is accomplished by replacing the first stage of the UDC with an adder and accumulator, with overflow to the UDC.

II. Mathematical Model

Figure 1 shows a linearized model of the A/D converter with dc restoration. The effect of the limiter is assumed to be only a gain. To determine this gain, assume that the

input is zero mean gaussian noise with rms voltage σ , plus a small signal $s(t)$, with $s(t) \ll \sigma$. Then at any time the expected value of the limiter output is

$$\sqrt{\frac{2}{\pi}} \frac{1}{\sigma} s(t)$$

so the limiter gain is

$$K_L = \sqrt{\frac{2}{\pi}} \frac{1}{\sigma} \quad (1)$$

The up-down counter and D/A converter act as an integrator. The gain of an integrator is the voltage change in one second when the input is 1. If the counter has N total stages, and the D/A converter output voltage range is from $-V$ to $+V$ volts, then the output voltage changes $2^{-N} (2V)$ volts at each count. Since there are $1/T$ counts per second, the gain is

$$K = 2^{1-N} \left(\frac{V}{T} \right) \quad (2)$$

The closed-loop transfer function of the linearized system is

$$\frac{e_o(s)}{e_i(s)} = \frac{K_L}{1 + \frac{K_L K}{s}} \quad (3)$$

This is equivalent to an RC high-pass filter with gain K_L and cutoff frequency $K_L K$ rad/s. In terms of the system parameters, the cutoff frequency is

$$f_c = \frac{1}{\pi} \sqrt{\frac{2}{\pi}} \frac{2^{-N} V}{\sigma T} \text{ Hz} \quad (4)$$

It is important to note that the cutoff frequency is inversely proportional to the rms input voltage.

III. Implementation

Figure 2 is a block diagram of the converter which was constructed using the dc offset compensation. The high-speed comparator and clock shaper are Advanced Micro Devices AM68534E. Used as 1-bit A/D converters, these emitter-coupled logic (ECL) circuits have an aperture time of only 0.4 ns. The converter outputs were translated from

ECL to transistor-transistor logic (TTL) levels, and the high speed U/D controller and UDC were constructed with TTL. This enabled the required clock rate of 40 MHz. Clock rates in excess of 100 MHz could be achieved using ECL exclusively.

The high-speed U/D controller operates on the serial input bits in pairs. It generates one up clock pulse to the UDC if both bits of a pair are plus one, a down clock pulse if both are minus one, and no clock pulse if the two bits are different. The effect is to act as an additional counter stage and to reduce the clock rate to the UDC integrated circuit (IC) chips by a factor of 2. The controller also keeps the 16-bit UDC from overflowing if the offset number is too great by inhibiting counting for minimum and maximum values of the counter.

The 12 most significant bits (MSB) of the UDC go to an Analog Devices "L" series Minidac. A Teledyne Philbrick 131901 is used as the level adjusting feedback amplifier. It was set for a gain of 2. Since the dc restore signal is applied to the negative input of the differential comparator, its voltage, when stabilized, is equal to the input offset voltage plus any offset introduced in the converter.

IV. Experimental Results

The 1-bit converter was operated at a 40-MHz clock rate over a wide range of input offsets and spectral components. Figure 3 is a photograph of the low-frequency portion of the output spectral density when the input signal was wideband gaussian noise, low-pass-filtered to 20 kHz to be within the bandwidth of the spectrum analyzer. The input signal level was 0.6 V rms, which, from Eq. (4), results in a calculated 3-dB cutoff frequency of $f_c = 250$ Hz. The measured spectral density agrees with this to within the resolution of the display.

V. Conclusion

The main feature of the dc restoration technique is its ability to correct for dc offsets introduced by the conversion device itself as well as for large dc offsets in the input signal. Using emitter-coupled logic for the filtering as well as for the converter, the dc restoration technique could operate at the highest conversion rates possible with the A/D converter chip, which is in excess of 100 MHz.

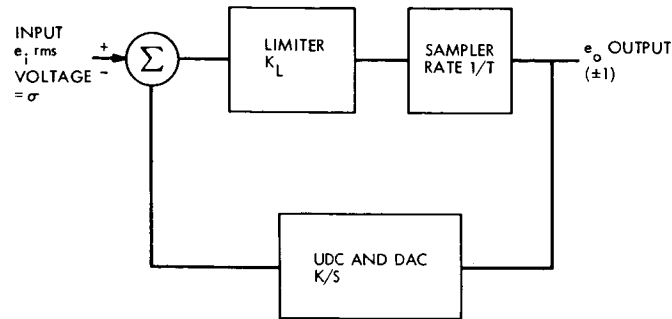


Fig. 1. Linearized model of ADC with digital dc restorer

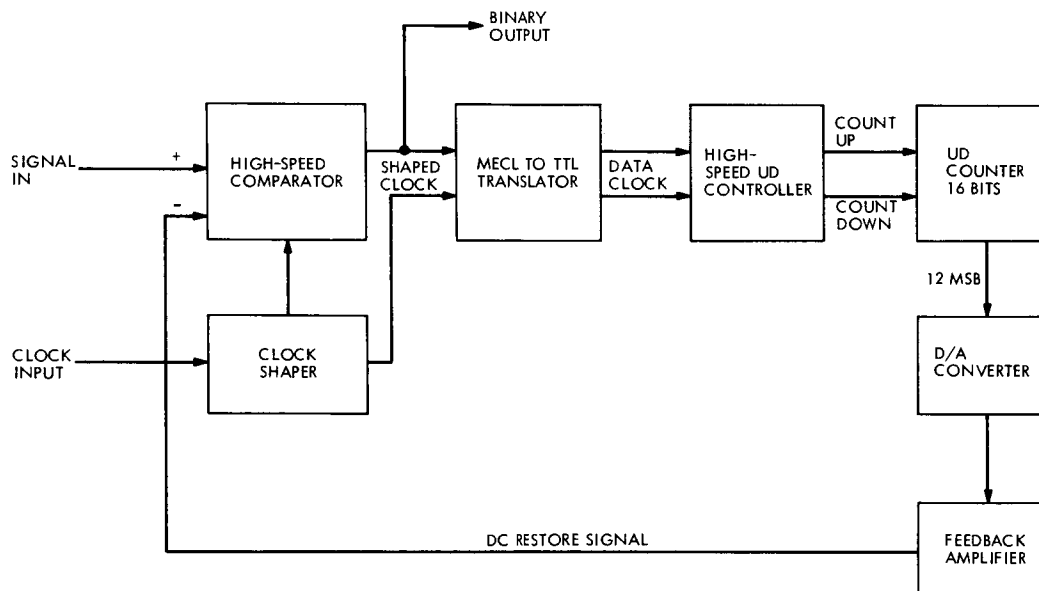


Fig. 2. Block diagram of the 1-bit ADC with digital dc restorer



**Fig. 3. A/DC low-frequency output spectral density
(horizontal, 50 Hz/cm; vertical, 10 dB/cm)**

A System Analysis of Error Sources in the Technique Used for Ionospheric Calibration of Deep Space Probe Radio Metric Data

K. W. Yip and B. D. Mulhall
Tracking and Orbit Determination Section

A system analysis has been performed on the error sources in the technique used for ionospheric calibration of deep space probe radio metric data. This analysis is based on the Chapman ionospheric model. Although it has been proven that this model is inadequate in ranging for low elevation angles ($\lesssim 15$ deg) of the spacecraft and large solar zenith angles ($\gtrsim |60|$ deg), this analysis should still be valid for most of the daytime because of the very conservative values adopted for the variations of these Chapman ionospheric parameters. It is found that if a close-by source of total electron content (TEC) data is used, the uncertainty is $\sim 10\%$ at low elevation angles and less than $\sim 3\%$ for elevation angles higher than ~ 20 deg. The corresponding values for the distant mapping of TEC data are $\sim 10\%$ and $\sim 8\%$, respectively.

I. Introduction

The charged particles in the ionosphere and the interplanetary space plasma along the ray path of the radio signal transmitted to and received from a spacecraft have various effects upon the signal. The two effects which concern orbit determination are the phase path decrease and group path delay. This increase in phase velocity and decrease in group velocity is a function of the wave frequency; thus the plasma has a dispersive effect on the spectrum of the radio signal.

As the number of charged particles along the ray path changes, the phase path changes and shifts the transmitted carrier frequency. This frequency shift cannot be distinguished from the doppler effect unless the change

in the number of charged particles is determined. Similarly, the charged particles delay the energy of the transmitted radio signal, a result that increases the round-trip light time of this signal and therefore corrupts range data, since these measurements are based on the time required for the energy to propagate from the tracking station to the spacecraft and return.

The ionosphere causes two types of navigational errors: random and systematic. Random errors in the doppler observable can be reduced by taking data over many passes. Systematic errors cannot be reduced by averaging. If the systematic error is essentially constant over each pass, it will corrupt the estimate of geocentric range rate, the parameter a of the Hamilton-Melbourne model

(Ref. 1), rather than station location. However, if the error is a time-varying function with a diurnal period, then estimates of station spin radius r_s will be corrupted by antisymmetric (odd) errors, and station longitude λ by symmetric (even) errors.

Earth's ionosphere is caused by ultraviolet radiation from the Sun ionizing the upper atmosphere. Consequently, the density of charged particles in the ionosphere increases and decreases with a diurnal period. For post-flight analysis (Ref. 2), the diurnal variation of the ionosphere will corrupt the station location estimates. For in-flight orbit determination, the ionospheric effect will corrupt the estimate of the probe's orbit.

The quantity most important in the determination of ionospheric effect is the total electron content (TEC) along the line of sight to the spacecraft:

$$I(t) = \int_0^s N(s, t) ds \quad (1)$$

where $N(s, t)$ is the electronic distribution along the ray path S at time t . This is related to the corresponding range change by the equation

$$\Delta\rho(t) = \frac{A}{f^2} I(t) \quad (2)$$

where $A = 40.3$ in mks units, and f is the transmitted frequency in hertz.

Figure 1 is a block diagram of the steps involved in the ionospheric calibration technique described in this article. The details of this approach have been well documented in Ref. 3. The discussions in the following sections are divided according to these steps, with more emphasis placed on the error analyses. The results of these analyses in terms of the line-of-sight one-way range changes in the spacecraft view period are tabulated in Table 1.

II. Recapitulation of the Ionospheric Calibration Technique

For the convenience of the reader, a brief summary of the entire calibration technique is made here.

Since the idea of the "ionospheric reference point" is going to come up again and again in the following discussion, it is appropriate to familiarize the reader with this concept. This point is defined as the point where the

radio signal ray path passes a reference altitude, namely, 350 km (Ref. 3). This reference altitude is also the height which best satisfies the "thin shell approximation" (Ref. 4) in the Faraday data reduction. Ionospheric conditions at this point are used to typify conditions along the entire ray path.

As shown in Fig. 1, the ionospheric data come either from ionosonde measurements or Faraday rotation observations to geostationary satellites. Ionosonde data are measured vertically from the station and, as a result, information at the zenith of the station is obtained. Faraday rotation measurements, on the other hand, yield data along the line of sight to the geostationary satellite. To be compatible with ionosonde TEC, these Faraday values are multiplied by the cosine of the angle between the zenith at the reference point (Ref. 3) and the ray path. Consequently, ionosonde and Faraday rotation data can be mapped in exactly the same manner, the only difference being that the Faraday rotation data are related to a point under the slanted column, rather than the zenith of the monitoring station.

To calibrate range changes due to ionospheric effects, the program takes in the diurnal variations of the zenith TEC for the days when calibrations are required. Of course, if there are periods in the TEC data spans where no data are available, no calibration can be performed for the corresponding periods. (This assumes that no model for the TEC data is to be used. There is, however, a capability in the program in cases when the model data are desired. A description of the evaluation of these diurnal models is given in Ref. 5.) Usually, the locations of the ionospheric observatories and the tracking stations are different and space-time translations (Ref. 3) of the zenith TEC are required. After these zenith TEC values are mapped to the tracking station, they are re-converted to the line-of-sight (to the spacecraft) values by the ray-trace technique (Ref. 6). The corresponding range changes due to the ionosphere are then computed from Eq. (2), together with the geomagnetic latitude adjustment factor (Ref. 3). These range functions $\Delta\rho(t)$ are fitted by polynomials in time, and the coefficients are then used for the computations of range changes and range rates at any time during the respective passes when the TEC data are available.

This one-way range change can be used as a calibration by the Orbit Determination Program (ODP) or this calibration program can convert it to a doppler calibration. The doppler calibration can be obtained either by taking the time derivative of the one-way range polynomial or by the "four-path differencing" technique. This latter

method takes into account the fact that we are calibrating two-way doppler which has been differenced over the count time. The details of this approach have been outlined in Ref. 3 and are not repeated here.

III. Error Sources

The different stages in the ionospheric calibration technique (see Fig. 1) where possible errors may occur are:

- (1) Instrumentation errors such as equipment noise which are however negligible.
- (2) Computing zenith TEC from ionosonde or Faraday rotation measurements.
- (3) Performing the space-time translation of these data.
- (4) Converting from zenith TEC to TEC along the desired lines of sight.
- (5) Curve fitting of the range change values.
- (6) Computing doppler calibration.
- (7) Curve fitting of doppler values.

Before going any further, it should be mentioned that all of the following analyses are based on a Chapman ionosphere (Ref. 7). In other words, the electronic distribution of the ionosphere is given by

$$N(z) = N_{\max} \exp \left\{ \frac{1}{2} \left(1 - z - \frac{1}{\cos \chi} e^{-z} \right) \right\} \quad (3)$$

where

$$z = (h - H_{\max})/B$$

h = altitude above Earth

H_{\max} = altitude above Earth where the peak electron density occurs

N_{\max} = maximum electron density (occurring at H_{\max})

B = scale height of ionosphere

χ = solar zenith angle

This is a good representation of the ionospheric distribution in relation to range calibration in the daytime for not too small elevation angles (≥ 15 deg) and not too large solar zenith angles (≤ 60 deg) (see Ref. 8).

Since this equation is the basis for some of the major operations in this ionospheric calibration scheme, strictly speaking, this error analysis is relevant only to range

calibrations in the daytime and within the range of angles just mentioned. However, in spite of the fact that in some of the following analyses the ranges of angles are exceeded, it is felt that these estimates are still valid for most of the daytime, all the more so since very conservative values have been adopted for the variations of these Chapman ionospheric parameters.

A. Instrumental Errors

Since the ionosonde data are supplied by external sources and their instrumental errors are difficult to ascertain exactly, the analysis is primarily concerned with the Faraday rotation measurements. Fortunately, except for some early missions, this data source is used almost exclusively. From an experiment performed some time ago (Ref. 9), the equipment noise is found to be about three orders of magnitude below the signal level. Thus, it is valid to conclude that there is no error associated with the value of the Faraday rotated angle Ω .

B. Computation of Zenith TEC

1. **Computation from ionosonde data.** Basically, the ionosonde measurement involves the analysis of radar-like echoes from the ionosphere over a wide range of operating frequencies (Ref. 10). As long as there is a reflection from the ionosphere, this particular frequency is related to the density at this height h (derived from the "virtual" height (Ref. 10) computed from the time of flight of this echo) by

$$N = Af^2 \quad (4)$$

where $A = 1.24 \times 10^{-2}$ electrons/m³/Hz²; N = density of electrons, electrons/m³; and f = reflected frequency, Hz. At some frequency ($f_o F2$), however, the signal pierces through the ionosphere. Thus, only $N(h)$ for the lower ionosphere can be obtained. For the upper ionosphere, therefore, assumptions for the electronic profile and scale height (Ref. 3) have to be made. This is where most of the uncertainties come in, since this upper portion of the ionosphere past the $F2$ peak contains the majority ($>75\%$) of the electrons. This is the basis for the authors' opinion that errors in ionosonde data are probably the cause for apparent disagreement between Faraday rotation and ionosonde measurements when the two data types are compared.

2. Computation from Faraday rotation data

a. **Conversion from raw measurements to TEC.** The reduction of the Faraday rotation measurements involves

the "thin shell approximation" (Ref. 4). Instead of the actual Faraday rotation equation

$$\Omega = \frac{R}{f^2} \int_0^s \|H\| \cos \theta(s) N(s) ds \quad (5)$$

where

Ω = Faraday rotation of polarization vector
(with π ambiguities removed), rad

$R = 2.97 \times 10^{-2}$, mks units

f = transmitted frequency, Hz

S = ray path to satellite, m

$\|H\| \cos \theta$ = tangential component of Earth's magnetic field at a reference point along ray path, A-t/m

$N(s)$ = electron density at point s along ray path, electrons/m³

the "thin shell" approximation involves picking an appropriate value for the quantity $\|H\| \cos \theta$ and then pulling it outside of the integral. In other words,

$$\Omega = \frac{R}{f^2} \langle \|H\| \cos \theta \rangle_{\text{ref alt}} \int_0^s N(s) ds = \frac{R}{f^2} \langle \|H\| \cos \theta \rangle_{\text{ref alt}} I \quad (6)$$

and I , of course, is the TEC along this particular line of sight. The subscript "reference altitude" refers to the altitude along the ray path where the tangential component of Earth's magnetic field will best satisfy the above equality. A constant reference altitude of 350 km has been used.

The first question concerns itself with the validity of picking a constant reference altitude for the whole day, and, if this is valid, what is the best value to use. An analysis in this respect has already been performed using a Chapman ionosphere (Ref. 11). It is found that with the Chapman parameters of B (scale height) = 39 km, $H_{\text{max}} = 300$ km, and $N_{\text{max}} = 5 \times 10^6$ electrons/cm³, the reference altitude remains constant at 350 ± 25 km irrespective of the elevation angle and direction of the ray path and the solar zenith angle (as long as this is less than ~ 60 deg). Therefore, at Goldstone (colatitude = 57.4 deg),

$$\cos \chi = 0.5388 \sin \delta + 0.8425 \cos \delta \cos \phi \quad (7)$$

and even near dusk or dawn ($|\phi| \cong \pi/2$), the value of χ is ≤ 60 deg. It should be noticed that when χ approaches $\pi/2$, the parameters for the Chapman ionosphere inevitably

vary from those given above. As a matter of fact, it becomes questionable whether a Chapman ionosphere is a good representation at all. An analysis is now under way for the derivation of a model for the nighttime ionosphere so that a model for the ionosphere both night and day (Refs. 8 and 12) will be obtained. Before this is completed, however, the analysis carried out here will give an accurate picture for most of the daytime. A similar analysis for the nighttime including the dawn and dusk transition zones will be performed as soon as the completed model becomes available.

Though a constant reference altitude (for a fixed set of Chapman parameters) is a valid concept to use, the values of the parameters may vary during the day, thus causing the reference altitude to change as well. Figures 2 and 3 show the $\|H\| \cos \theta$ factor as a function of the height in kilometers above Earth for two different orthogonal directions (N-S and E-W). It can be seen that within the reasonable range of reference altitude from 300 to 400 km, the maximum error introduced when one is 50 km off from the "true" altitude is $\sim 2\%$. This estimate is based on a ray path going in the E-W direction, which is reasonable since most of the Faraday rotation data at Goldstone come from observing ATS-1, which is in a westerly direction.

b. Conversion from slant to zenith TEC. Figure 4 shows the geometry of this situation. In the ionospheric calibration program, the conversion is accomplished by taking the cosine of the reference angle α . To be consistent with the eventual translation from zenith to spacecraft line-of-sight TEC values, a "ray-trace" technique should be used in reverse for the elevation angle γ . Tables 2 and 3 illustrate the comparisons between these two approaches for several sets of the Chapman ionospheric parameters, the variations of the solar zenith angle being taken from the July 12, 1965 pass of the Mariner 4 mission and the October 18, 1967 pass of the Mariner 5 mission (see Subsection D and Table 4). The values of H_{max} between 250 and 350 km and B between 29 and 49 km cover the usual range of variations in these parameters as deduced from inspections of ionosonde data. It is seen that for the two different configurations of solar zenith angle variation, the use of the simple cosine introduces errors which are less than 2% for an elevation angle of 35.5 deg. This angle, incidentally, is the value subtended by the line of sight from Goldstone to ATS-1. This error, though small, will be removed in the future version of the program.

C. Space-Time Translation of Zenith TEC

To relate ionospheric measurements to radio tracking data, mapping (or translation in space-time coordinates)

is performed by calculating reference points for both the measurement and the probe-station line of sight. The mapping consists of making use, at one place, the zenith TEC measured at the reference points of another place. This operation is based on the assumption that, at the same local time, two stations have identical zenith TEC values even though they are located quite far apart. This is not exactly true, and the following scheme has been devised to check the uncertainties involved.

A month of zenith TEC in July and in September and October of 1971 from Stanford was time-translated to Goldstone and compared with the zenith TEC measured there in the same periods. Table 5 shows the averages of the daily differences in zenith TEC over a 1/2-h duration and an 8-h span for a whole month. The shorter time span analysis may be more appropriate to VLBI measurements since short-term mapping discrepancies are critical to these observations while the longer time span is appropriate to range corrections for spacecraft tracking. Table 5a gives average discrepancy with the time span centered at 12 noon local time, while Table 5b gives the average discrepancy with the time span centering at 6 p.m. local time. These comparisons give an estimate of the uncertainties involved in "local" (or close-by) mapping of zenith TEC data. Of course, similar analyses for different parts of the year have to be done so that any seasonal variations may be detected. However, without going through lengthy analysis, these comparisons will at least indicate the magnitudes of errors involved when "local mappings" are applied.

For "distant" mapping, the TEC data from Hamilton, Massachusetts, in July and September of 1971 were time-translated to Goldstone and compared. Again, Tables 6a and 6b show averages of the discrepancies for the same daily time spans mentioned above. There are, however, no Massachusetts data available in October for a similar comparison and only the September data have been used.

It should also be noted that if there are any uncertainties involved in the "magnetic latitude" factor (Ref. 3) used in the TEC reduction they would also have been absorbed in the above averages.

An inspection of the daily residuals revealed no definite pattern. In other words, these differences would look like part of a sine function on one day, part of a cosine function on the next, or simply display no trend at all. Since, as mentioned, the station spin radius will be corrupted by odd errors and station longitude by even ones, it is therefore difficult to translate this mapping discrepancy in terms of station location errors.

D. Mapped Zenith TEC to Line of Sight

This analysis is similar to that given in Subsection B-2-b. The elevation angle pertaining to the line of sight, however, is varying during the view period. The calibration proceeds by making use of the following equation to scale the range change at zenith to any arbitrary elevation angles (Ref. 3):

$$R(\gamma) = \frac{\{[(R_e + h_2)^2 - R_e^2 \cos^2 \gamma]^{1/2} - [(R_e + h_1)^2 - R_e^2 \cos^2 \gamma]^{1/2}\}}{(h_2 - h_1)} \quad (8)$$

where

R_e = radius of the Earth, km

γ = elevation angle

h_1 = 215 km

h_2 = 454 km

$R(\gamma)$ is a very good approximation to the ray-trace solution for a Chapman ionosphere with parameters $N_{\max} = 5 \times 10^6$ electrons/cm³, $H_{\max} = 300$ km, and $B = 39$ km, and this expression is normalized to unity at $\gamma = 90$ deg. This factor $R(\gamma)$ is multiplied to the respective "mapped" zenith TEC values to obtain the corresponding TEC and range changes (by Eq. 2) at the different elevation angles in the view period. This approach, however, does not take

into account the effect of the variation of the solar zenith angle in the pass. In other words, in the expression giving the Chapman ionosphere (Eq. 3), χ has been taken to be zero.

As shown in Ref. 13, the range changes for the same elevation angle but different solar zenith angles are quite different. For example, with similar Chapman parameters, the difference in range changes at an elevation angle of 30 deg for $\chi = 0$ deg and $\chi = 34$ deg is almost a meter.

To check this point, ray-trace solutions of the range changes due to a Chapman ionosphere with and without (i.e., $\chi = 0$ deg) solar zenith angle are compared. The numbers in Table 4a are taken from portions of the July 12, 1965 pass of the Mariner 4 mission (Sun-Earth-probe (SEP) angle = 78.1 deg) tracked by DSS 11, while those

in Table 4b are taken from portions of the October 18, 1967 pass of the Mariner 5 mission ($\text{SEP} = 48.2^\circ$) tracked by the same station. Note that since these are worst-case estimates, the fact that the zenith TEC mapping analysis (step 3, Fig. 1) pertains to the 1971 data while the zenith to line-of-sight analysis pertains to the 1965 and 1967 missions is irrelevant. In Table 4, the elevation angles at the different times of the pass and the corresponding solar zenith angles are tabulated. Tables 7a and b show the corresponding range changes and the ratios $R(\gamma)$ obtained with and without the solar angles. It can be seen that for low elevation angles ($\leq 15^\circ$) and large solar angles ($\geq 50^\circ$), as in the Mariner 5 configuration, the effect of including the solar zenith angle variation in the Chapman expression can cause a deviation of $\geq 2\%$ in the values of the normalized ratio $R(\gamma)$, and thus a similar deviation in the values of the one-way range changes.

These comparisons, however, are based on a fixed set of ionospheric parameters H_{max} and B . There is no reason why these values should be constant throughout the view period. Figures 5 and 6 show the percentage discrepancy involved for these two passes if H_{max} and B take on different values. The zero percentage line (x-axis) is, of course, pertinent to the calibration technique as outlined in this article, i.e., with $H_{\text{max}} = 300 \text{ km}$, $B = 39 \text{ km}$, and $\chi = 0^\circ$. As seen from the figures, the discrepancy at low elevation angles due to the variation of H_{max} can be more than 6% for both configurations, while that for the B variation is less than 1% for the Mariner 4 mission but can be more than 4% for the Mariner 5 mission. From Fig. 5, it is interesting to note that the sensitivity of the normalized ratios $R(\gamma)$, and therefore the range changes on the scale height B , is quite small even at low elevation angles, provided that the solar zenith angles are also small at the same time.

It should be noted that the curves in these figures are computed from a fixed maximum offset from the nominal values of the ionospheric parameters. Since these values vary during the view period and from day to day, the uncertainty in each pass resulting from this mapping technique is anywhere between the extrema of these curves. In other words, the uncertainties entailed are usually less than those indicated by the two outer-most curves.

E. Curve Fitting of One-Way Range Changes

The product delivered to the orbit determination program (ODP) from this calibration scheme is the one-way range change coefficients due to ionospheric effects. Thus, the one-way range values along the different lines of sight

to the spacecraft in a view period have to be fitted with a polynomial in time, and the ionospheric "Adjust Resid" coefficients are then handed over to the ODP. In these curve fittings, however, there may be some difficulty in deciding what the best order of the time polynomial would be. Of course, the optimal approach would be to supply the ODP with different sets of range coefficients resulting from fittings of different orders, obtain the state and/or station solutions from the ODP for each set, and then compare the sizes of the remaining O - C residuals. This approach will be applied and the sensitivity of the results on the different orders will be published in a different paper in the near future.

In the meantime, however, this comparison has been carried out in two different ways: (1) the capability of the different fitted curves to reproduce the actual one-way range changes, which is indicated by the standard deviation associated with each fitted curve; and (2) the consistency of the station location changes Δr_s and $\Delta \lambda$ as given by the different fitted curves. This second approach makes use of the Hamilton-Melbourne formulation for a single pass of the spacecraft (Ref. 1). Note, however, that since the solar zenith angle effect is not taken into account in the Chapman profiles in the present calibration scheme, the resultant station location changes may not be exact. Nevertheless, if the changes obtained from the different orders are consistent, the indication is that the one-way range coefficients are insensitive to any reasonable order of curve fitting. Now several other operations (steps 6, 7, and 8 in Fig. 1) have to be performed on the one-way range changes before the station location changes can be obtained and extra uncertainties may be introduced. However, as shown in the following section, the uncertainties resulting from these extra operations are negligibly small and are predominated by the order of the one-way range fit. Moreover, any extra uncertainties would only accentuate the discrepancies between the different fitting orders. This comparison is, therefore, a valid approach.

The Mariner 9 mission, tracked by DSS 14 in December 1971, has been calibrated for the ionosphere using this program with the one-way range values fitted to time polynomials of maximum orders of 5, 7, and 10. Note that fitting orders higher than ~ 10 are undesirable since the extra curvatures in the fitted curves are detrimental to the doppler curves. Besides, the ODP will smooth the range curves to some extent, thus effecting a lower order fit anyway. Figure 7 shows the standard deviations associated with the passes. Not only are the standard deviations small in magnitude ($\leq 0.1 \text{ m}$), but also, for most of the time, the differences in these values between the three

different orders are quite small (< 0.05 m) as well. This is, of course, due to the usually rather smooth variations of the range points. Thus, the different orders are all good fits to the actual values. Moreover, as shown in Fig. 8, the station location changes are not very sensitive to the maximum order of the fit. A change of this order by a power of five results in a change in the monthly averaged standard deviations of 0.027 m, a change of Δr_s by about $\frac{1}{2}$ m, and a change of $\Delta\lambda$ by about 1 m *only* in a few days out of the whole month.

Thus, for reasonable orders of curve fitting, the one-way range coefficients are almost unaffected. The contribution from this operation to the total uncertainty is taken to be the largest of the three monthly averaged standard deviations, which in this case is the one with the lowest order of fit. This is root-sum-squared with the uncertainties introduced in the other steps and the RSS values (Table 1) are then the errors associated with the ionospheric one-way range coefficients delivered to the ODP.

F. Doppler Evaluation and Curve Fitting

As shown in Fig. 1, instead of supplying the ODP with the one-way range coefficients, this ionospheric calibration program also has the capability of doing the "four-path differencing" (Ref. 3) internally and then supplying coefficients of the resultant doppler, i.e., range rate, to the ODP. Although this mode of interface is seldom used at present, a brief analysis will be made for the sake of completeness.

Again, the analysis of this mode of operation can be made only in terms of station location changes without the detailed approach outlined in the preceding section involving the ODP. Moreover, since the solar zenith angle effect has not been taken into account in this scheme and the calibrations from the global model (Refs. 8 and 12) are not yet available for comparison, this is only a discussion on the general properties of the evaluation and fitting of the doppler effects. Data from Mariner 9 in December 1971 have been further analyzed in this connection.

Note that in order to get the station location changes due to the ionosphere from the one-way range corrections, the doppler points computed from the range curve have to be fitted with a time polynomial as well. This may introduce some error to the values of Δr_s and $\Delta\lambda$. However, since a high order (up to 19) polynomial has been used, the doppler points have been represented very well. The error caused by this second curve fitting to the station location changes should therefore be quite small.

A careful inspection of Fig. 8 and the associated range and doppler plots for the individual days reveals much more information about the evaluation of the range rate. Although the $\Delta\lambda$ solutions almost always agree quite well for the different maximum orders of the range fit polynomials, there are a few days when the low-order fit to the range curves gives $\Delta\lambda$ values that are different by more than a meter from the results of the higher order fit. Inevitably, this can be traced to the lower density of TEC data points in the pass, especially in the beginning and in the end. Thus, any variation in any one of these TEC points can greatly affect the shapes and phases of the different fitted curves. Consequently, the station location solutions are affected as well. Notice that data gaps close to the middle of the pass have little or no effect on these solutions. Note also that for an incomplete pass of only 4 or 5 h a very large error in $\Delta\lambda$ can result. The $\Delta\lambda$ solution of -7 m on December 7 has been omitted for this reason. Figures 9 and 10, which show the range and doppler curves on December 13 for two different fitting orders, serve to illustrate this point quite well.

IV. Conclusions

Table 1 shows a summary of all the one-way range change error sources and their magnitudes as a function of elevation angle in the ionospheric calibration technique as schematically outlined in Fig. 1. The RSS values are then the uncertainties associated with the ionospheric one-way range changes delivered to the ODP. Note that these are worst-case estimates, and the uncertainties encountered in this calibration technique are usually smaller. Whenever relevant, classifications according to seasons are also indicated. As mentioned, these uncertainties are primarily concerned with the daytime ionosphere. The worst-case total uncertainty is root-sum-squared and is also tabulated in Table 1. Although the two Mariner 4 and 5 passes worked out in detail here do not cover all possible solar zenith angle and elevation angle configurations, they are representative of all past planetary missions. Moreover, the analysis of this Mariner 5 configuration illustrates very well the amplification of the diurnal effect of the TEC by the elevation angle effect, as pointed out by Trask and Mulhall in Ref. 14.

Although at the expense of more tedious and time consuming programs, most of the sources of error in this ionospheric calibration scheme can be removed. However, before this can be pursued, the global ionospheric model developed by O. H. von Roos and the author, and which is valid both day and night, has to be checked out for its

sensitivities on the different model parameters and its feasibility of implementation. If improvements are to be obtained and implementation is found to be feasible, this

new model will replace the mapping scheme outlined here. Otherwise, improvement for this present technique will be implemented.

References

1. Hamilton, T. W., and Melbourne, W. G., "Information Content of a Single Pass of Doppler Data from a Distant Spacecraft," in *The Deep Space Network*, Space Programs Summary 37-39, Vol. III, pp. 18-23. Jet Propulsion Laboratory, Pasadena, Calif., May 31, 1966.
2. Mottinger, N. A., and Sjogren, W. L., "Station Locations," in *Tracking System Analytic Calibration Activities for the Mariner Mars 1969 Mission*, Technical Report 32-1499, pp. 19-34. Jet Propulsion Laboratory, Pasadena, Calif., Nov. 15, 1970.
3. Mulhall, B. D., Ondrasik, V. J., and Thuleen, K. L., "The Ionosphere," in *Tracking System Analytic Calibration Activities for the Mariner Mars 1969 Mission*, Technical Report 32-1499, pp. 45-68. Jet Propulsion Laboratory, Pasadena, Calif., Nov. 15, 1970.
4. Mulhall, B. D., *Mathematical Formulations for Ionospheric Calibration and Comparison, Part I: Ionospheric Data Pre-Processing*, IOM 391.3-529, Feb. 1972 (JPL internal document).
5. Yip, K. W., and Mulhall, B. D., *A Model for the Diurnal Variation of Ionospheric Total Electron Content*, TM 391-318, Apr. 1972 (JPL internal document).
6. Liu, A., and Cain, D., *Ionospheric Range and Angular Corrections*, TM 312-694, Mar. 1966 (JPL internal document).
7. Chapman, S., "The Absorption and Dissociative or Ionizing Effect of Monochromatic Radiation in an Atmosphere on a Rotating Earth," *Proc. Phys. Soc. (London)*, Vol. 43, p. 25, 1931.
8. von Roos, O. H., and Yip, K. W., "Derivation of a General Expression for Ionospheric Range Corrections Valid for Arbitrary Solar Zenith Angles, Azimuths, Elevation Angles and Station Locations," in *The Deep Space Network Progress Report*, Technical Report 32-1526, Vol. XI, pp. 53-61. Jet Propulsion Laboratory, Pasadena, Calif., Oct. 15, 1972.
9. Mulhall, B. D., and Yip, K. W., *High Frequency Fluctuations in the Earth's Ionosphere as Determined from Faraday Rotation Measurements*, IOM 391.3-568, May 1972 (JPL internal document).
10. Rishbeth, H., and Garriott, O. K., *Introduction to Ionospheric Physics*, p. 51, Academic Press, Inc., New York, 1969.
11. von Roos, O. H., and Yip, K. W., *Determination of the Total Electron Content from Faraday Rotation Measurements*, TM 391-330, May 1972 (JPL internal document).

References (contd)

12. von Roos, O. H., and Escobal, P. R., "A Global Model of the Earth's Ionosphere: The Nighttime Ionosphere," in *The Deep Space Network Progress Report*, Technical Report 32-1526, Vol. XV, pp. 32-47. Jet Propulsion Laboratory, Pasadena, Calif., June 15, 1973.
13. Yip, K. W., *A New Technique for Ionospheric Range Calculations*, TM 391-278, Feb. 1972 (JPL internal document).
14. Trask, D. W., and Mulhall, B. D., "Tracking System Analytic Calibration Description," in *Tracking System Analytic Calibration Activities for the Mariner Mars 1969 Mission*, Technical Report 32-1499, pp. 1-17. Jet Propulsion Laboratory, Pasadena, Calif., Nov. 15, 1970.

Table 1. Worst-case one-way range uncertainties

Elevation angle, deg	Faraday rotation, %	Slant to zenith TEC, %	Mapping, % ^a				Zenith to line-of-sight TEC, %		Time polynomial fit to one-way range, % ^a	RSS error in July, %			
			Local		Distant					Mariner 4 configuration		Mariner 5 configuration	
			July	Sept–Oct	July	Sept	Mariner 4 configuration	Mariner 5 configuration		Local	Distant	Local	Distant
0.83	2.0	2.0	0.5	0.3	7.7	4.1	7.9	—	2.0	8.4	11.4	—	—
3.36	2.0	2.0	0.5	0.3	7.7	4.1	7.3	10.3	2.0	7.9	11.0	10.7	13.2
5.00	2.0	2.0	0.5	0.3	7.7	4.1	7.0	9.6	2.0	7.6	10.8	10.0	12.7
10.00	2.0	2.0	0.5	0.3	7.7	4.1	5.8	7.6	2.0	6.5	10.0	8.1	11.2
15.00	2.0	2.0	0.5	0.3	7.7	4.1	4.4	5.6	2.0	5.3	9.3	6.3	9.9
20.00	2.0	2.0	0.5	0.3	7.7	4.1	3.1	4.1	2.0	4.2	8.7	5.0	9.1
25.00	2.0	2.0	0.5	0.3	7.7	4.1	2.2	3.0	2.0	3.6	8.5	4.1	8.7
30.00	2.0	2.0	0.5	0.3	7.7	4.1	1.6	2.1	2.0	3.3	8.3	3.5	8.4
40.00	2.0	2.0	0.5	0.3	7.7	4.1	1.0	1.1	2.0	3.0	8.2	3.0	8.2
50.00	2.0	2.0	0.5	0.3	7.7	4.1	0.7	0.7	2.0	3.0	8.2	3.0	8.2
60.00	2.0	2.0	0.5	0.3	7.7	4.1	—	0.4	2.0	—	—	2.9	8.2

^aAn average percentage based on an 8-h view period centered around noon local time and a zenith TEC value of 3×10^{17} electrons/m² (~ 4 m in S-band).

Table 2. Possible discrepancies in line-of-sight to zenith conversion of TEC

χ , deg ^a	γ , deg	Ray trace (1) ^b	Ray trace (2) ^b	Ray trace (3) ^b	Ray trace (4) ^b	Ray trace (5) ^b	$\cos \alpha$
18.2	35.5	0.6356	0.6285	0.6425	0.6340	0.6371	0.6357
13.6	35.5	0.6355	0.6284	0.6423	0.6339	0.6370	0.6357
15.7	35.5	0.6355	0.6284	0.6424	0.6339	0.6370	0.6357
21.1	35.5	0.6358	0.6286	0.6426	0.6341	0.6373	0.6357
30.7	35.5	0.6361	0.6290	0.6430	0.6344	0.6378	0.6357
40.3	35.5	0.6368	0.6297	0.6436	0.6349	0.6386	0.6357
65.8	35.5	0.6401	0.6332	0.6468	0.6374	0.6428	0.6357

^aFrom July 12, 1965 pass of Mariner 4 mission.

^bChapman ionospheric parameters:

$$N_{\max} = 5 \times 10^6 \text{ electrons/cm}^3$$

- | | | |
|--|--|--|
| (1) $H_{\max} = 300$ km
$B = 39$ km | (3) $H_{\max} = 350$ km
$B = 39$ km | (5) $H_{\max} = 300$ km
$B = 49$ km |
| (2) $H_{\max} = 250$ km
$B = 39$ km | (4) $H_{\max} = 300$ km
$B = 29$ km | |

Table 3. Possible discrepancies in line-of-sight to zenith conversion of TEC

χ , deg ^a	γ , deg	Ray trace (1) ^b	Ray trace (2) ^b	Ray trace (3) ^b	Ray trace (4) ^b	Ray trace (5) ^b	$\cos \alpha$
65.6	35.5	0.6401	0.6331	0.6468	0.6373	0.6427	0.6357
51.9	35.5	0.6379	0.6309	0.6447	0.6357	0.6400	0.6357
47.4	35.5	0.6374	0.6304	0.6442	0.6354	0.6394	0.6357
52.1	35.5	0.6380	0.6309	0.6447	0.6357	0.6401	0.6357
55.6	35.5	0.6384	0.6314	0.6452	0.6361	0.6406	0.6357
60.1	35.5	0.6391	0.6321	0.6458	0.6366	0.6415	0.6357

^aFrom October 18, 1967 pass of Mariner 5 mission.

^bChapman ionospheric parameters; see footnote b in Table 2.

Table 4. Ionospheric calibration configurations

(a) Mission: Mariner 4; DSS: 11; Date: 7/12/65; SEP = 78.1 deg

UT, hr	ϕ , deg ^a	χ , deg	γ , deg
19.06	345.9	18.2	0.83
19.81	357.15	13.6	9.95
20.23	3.45	13.6	14.88
20.62	9.30	15.7	19.46
21.25	18.75	21.15	26.69
22.11	31.65	30.7	35.78
22.91	43.65	40.25	43.06
25.00	75.0	65.75	51.90

(b) Mission: Mariner 5; DSS: 11; Date: 10/18/67; SEP = 48.2 deg

16.66	309.9	65.6	61.03
18.23	333.45	51.9	54.65
19.04	345.6	47.4	47.25
19.63	354.45	45.75	39.03
20.33	4.95	45.65	32.97
20.80	12.0	46.8	27.43
21.80	27.0	52.1	15.29
22.26	33.9	55.6	9.65
22.78	41.7	60.1	3.36

^a ϕ = local time reckoned from noon.

Table 5. Average discrepancy in local zenith TEC mapping between Stanford and Goldstone, Calif.

(a) Average discrepancy with time span centered at 12 noon		
Data span	$12.00^h \text{ (noon)} \pm 0.25$	$12.00^h \text{ (noon)} \pm 4.00$
July 1–31	$-0.09 \pm 0.20 \text{ meter (16)}^a$	$-0.02 \pm 0.21 \text{ meter (16)}^a$
Sept 12–Oct 12	$-0.02 \pm 0.39 \text{ meter (20)}^a$	$-0.01 \pm 0.34 \text{ meter (18)}^a$
(b) Average discrepancy with time span centered at 6 p.m.		
Data span	$6.00^h \text{ (p.m.)} \pm 0.25$	$6.00^h \text{ (p.m.)} \pm 4.00$
July 1–31	$0.00 \pm 0.25 \text{ meter (15)}^a$	$0.19 \pm 0.10 \text{ meter (11)}^a$
Sept 12–Oct 12	$0.16 \pm 0.36 \text{ meter (19)}^a$	$0.01 \pm 0.21 \text{ meter (14)}^a$
^a Number of days in average.		

Table 6. Average discrepancy in distant zenith TEC mapping between Hamilton, Mass., and Goldstone, Calif.

(a) Average discrepancy with time span centered at 12 noon		
Data span	$12.00^h \text{ (noon)} \pm 0.25$	$12.00^h \text{ (noon)} \pm 4.00$
July 1–31	$0.40 \pm 0.67 \text{ meter (19)}^a$	$0.30 \pm 0.61 \text{ meter (19)}^a$
Sept 12–30	$0.54 \pm 1.01 \text{ meter (11)}^a$	$0.16 \pm 0.46 \text{ meter (10)}^a$
(b) Average discrepancy with time span centered at 6 p.m.		
Data span	$6.00^h \text{ (p.m.)} \pm 0.25$	$6.00^h \text{ (p.m.)} \pm 4.00$
July 1–31	$-0.49 \pm 0.49 \text{ meter (18)}^a$	$-0.28 \pm 0.30 \text{ meter (15)}^a$
Sept 12–30	$0.90 \pm 1.20 \text{ meter (12)}^a$	$-0.83 \pm 0.55 \text{ meter (8)}^a$
^a Number of days in average.		

Table 7. Solar zenith angle effect on $\Delta\rho$ (γ) and R (γ)

(a) Mission: Mariner 4; DSS: 11; Date: 7/12/65; SEP = 78.1 deg							
γ , deg	Ray-trace solution with different χ values			Ray-trace solution with $\chi = 0$ deg			
	χ , deg	$\Delta\rho$, m	$R(\gamma)$	χ , deg	$\Delta\rho$, m	$R(\gamma)$	
0.83	18.2	19.1747	3.1899	0	19.7289	3.1990	
90.0	18.2	6.0111		0	6.1672		
9.95	13.6	17.1654	2.8232	0	17.4318	2.8265	
90.0	13.6	6.0801		0	6.1672		
14.88	13.6	15.2724	2.5119	0	15.5049	2.5141	
90.0	13.6	6.0801		0	6.1672		
19.46	15.7	13.5462	2.2386	0	13.8187	2.2407	
90.0	15.7	6.0511		0	6.1672		
26.69	21.15	11.2166	1.8833	0	11.6266	1.8852	
90.00	21.15	5.9559		0	6.1672		
35.78	30.7	8.9439	1.5640	0	9.6576	1.5660	
90.0	30.7	5.7187		0	6.1672		
43.06	40.25	7.4628	1.3851	0	8.5546	1.3871	
90.0	40.25	5.3878		0	6.1672		
51.90	65.75	4.8610	1.2299	0	7.6055	1.2332	
90.0	65.75	3.9522		0	6.1672		
(b) Mission: Mariner 5; DSS: 11; Date: 10/18/67; SEP = 48.2 deg							
61.03	65.6	4.4565	1.1242	0	6.9428	1.1258	
90.0	65.6	3.9640		0	6.1672		
54.65	51.9	5.7878	1.1947	0	7.3769	1.1962	
90.0	51.9	4.8445		0	6.1672		
47.25	47.4	6.6201	1.3047	0	8.0596	1.3069	
90.0	47.4	5.0739		0	6.1672		
39.03	45.75	7.6012	1.4755	0	9.1221	1.4791	
90.0	45.75	5.1517		0	6.1672		
32.97	45.65	8.4865	1.6458	0	10.1862	1.6517	
90.0	45.65	5.1564		0	6.1672		
27.43	46.8	9.4126	1.8447	0	11.4363	1.8544	
90.0	46.8	5.1026		0	6.1672		
15.29	52.1	11.8539	2.4524	0	15.3456	2.4883	
90.0	52.1	4.8337		0	6.1672		
9.65	55.6	12.8846	2.7795	0	17.5469	2.8452	
90.0	55.6	4.6355		0	6.1672		
3.36	60.1	13.2401	3.0406	0	19.4331	3.1511	
90.0	60.1	4.3544		0	6.1672		
Chapman ionospheric parameters: $N_{\max} = 5 \times 10^6$ electrons/cm ² ; $H_{\max} = 300$ km; $B = 39$ km.							

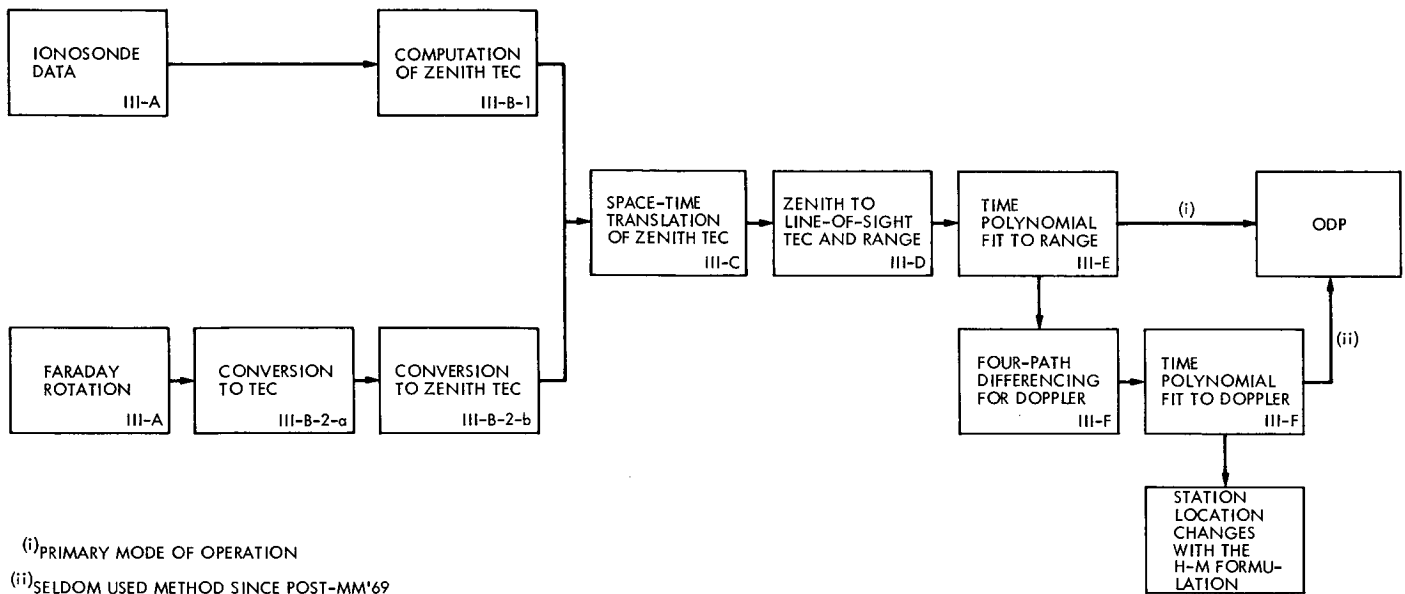


Fig. 1. Block diagram for an ionospheric calibration scheme

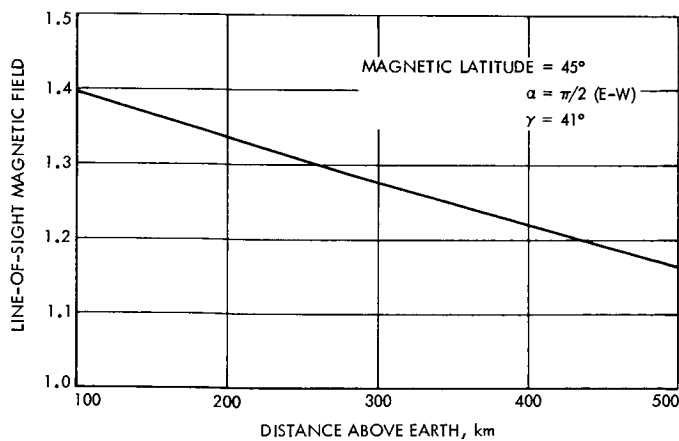


Fig. 2. Variation of line-of-sight magnetic field with geocentric distance in E-W direction

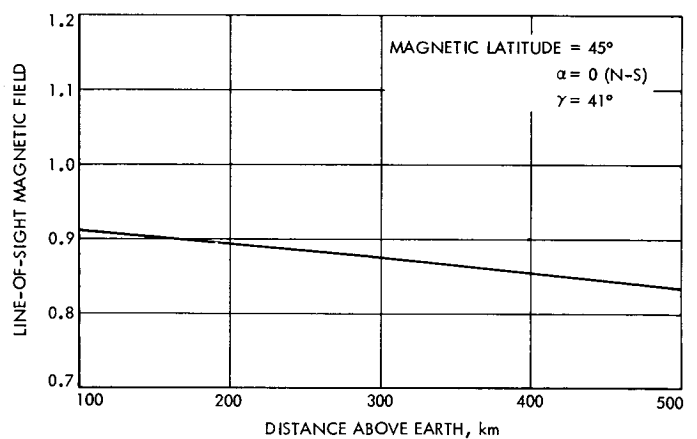
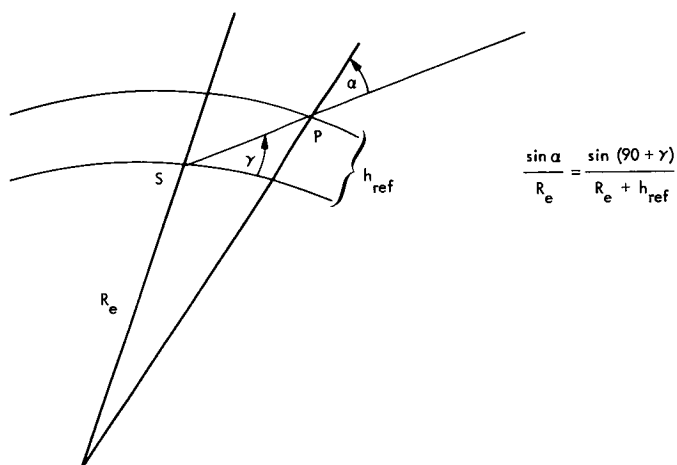


Fig. 3. Variation of line-of-sight magnetic field with geocentric distance in N-S direction



γ = ELEVATION ANGLE OF RAY PATH TOWARD GEOSTATIONARY SATELLITE FROM OBSERVATORY S
 α = "REFERENCE ANGLE" BETWEEN RAY PATH AND ZENITH OF IONOSPHERIC REFERENCE POINT P
 h_{ref} = REFERENCE ALTITUDE, 350 km
 R_e = RADIUS OF EARTH

Fig. 4. Geometry of the ionospheric reference point P

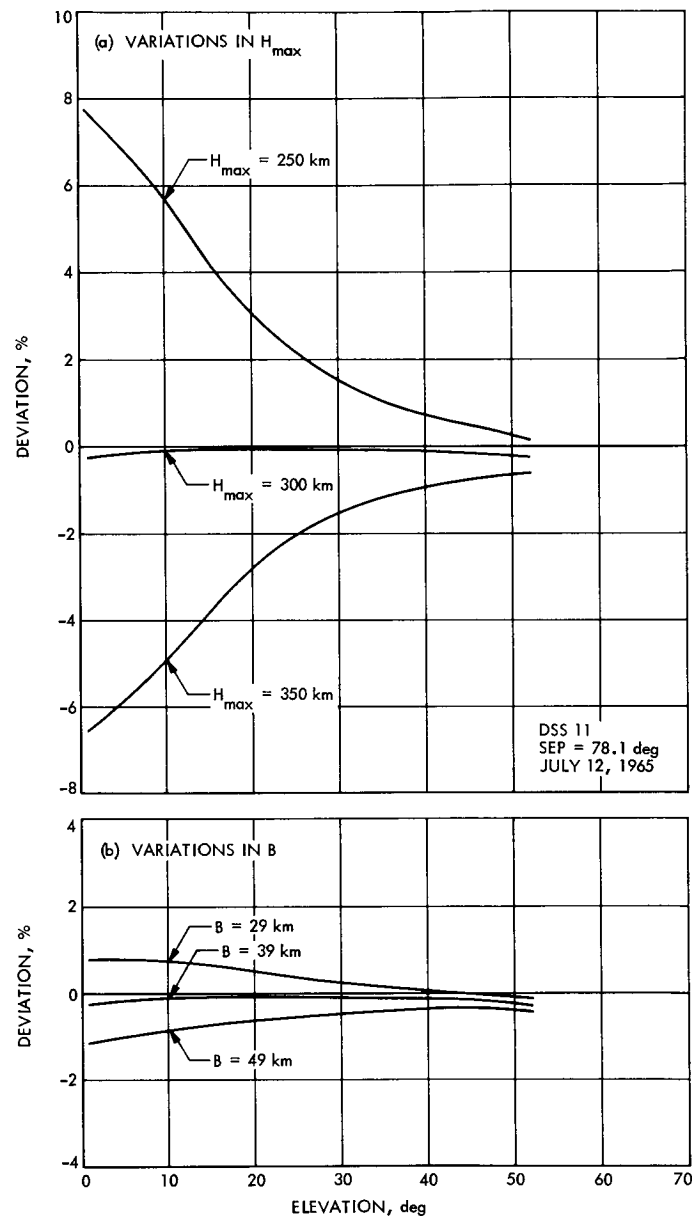


Fig. 5. Percentage discrepancy due to variations in H_{max} and B for the Mariner 4 pre-encounter configuration

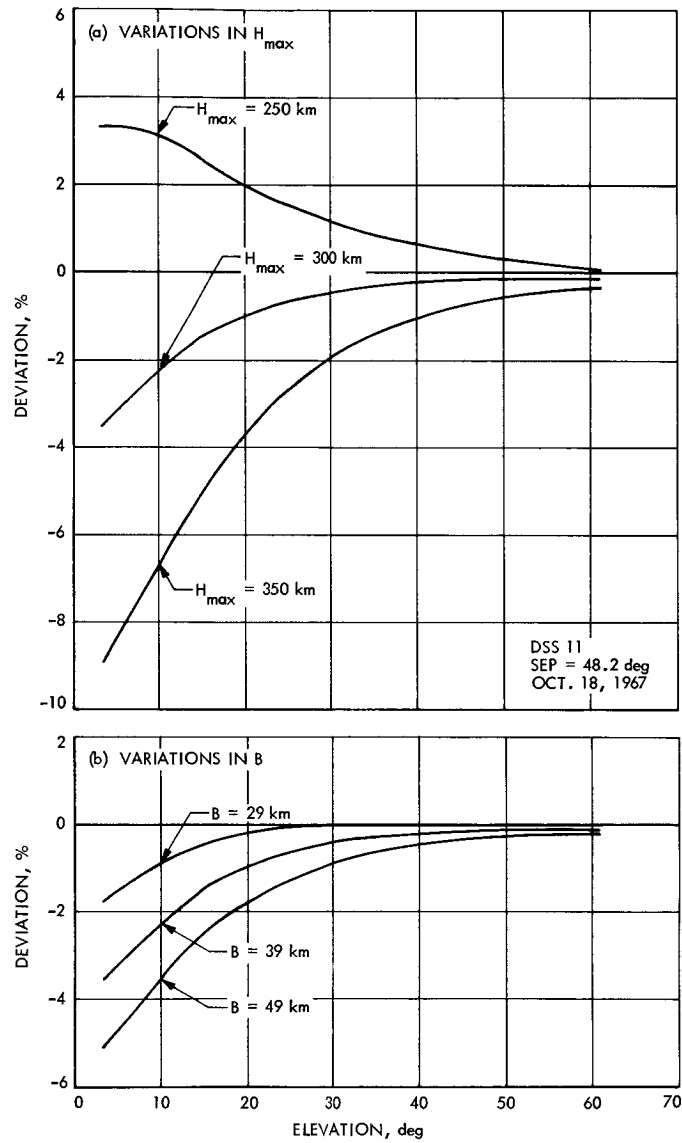


Fig. 6. Percentage discrepancy due to variations in H_{\max} and B for the Mariner 5 pre-encounter configuration

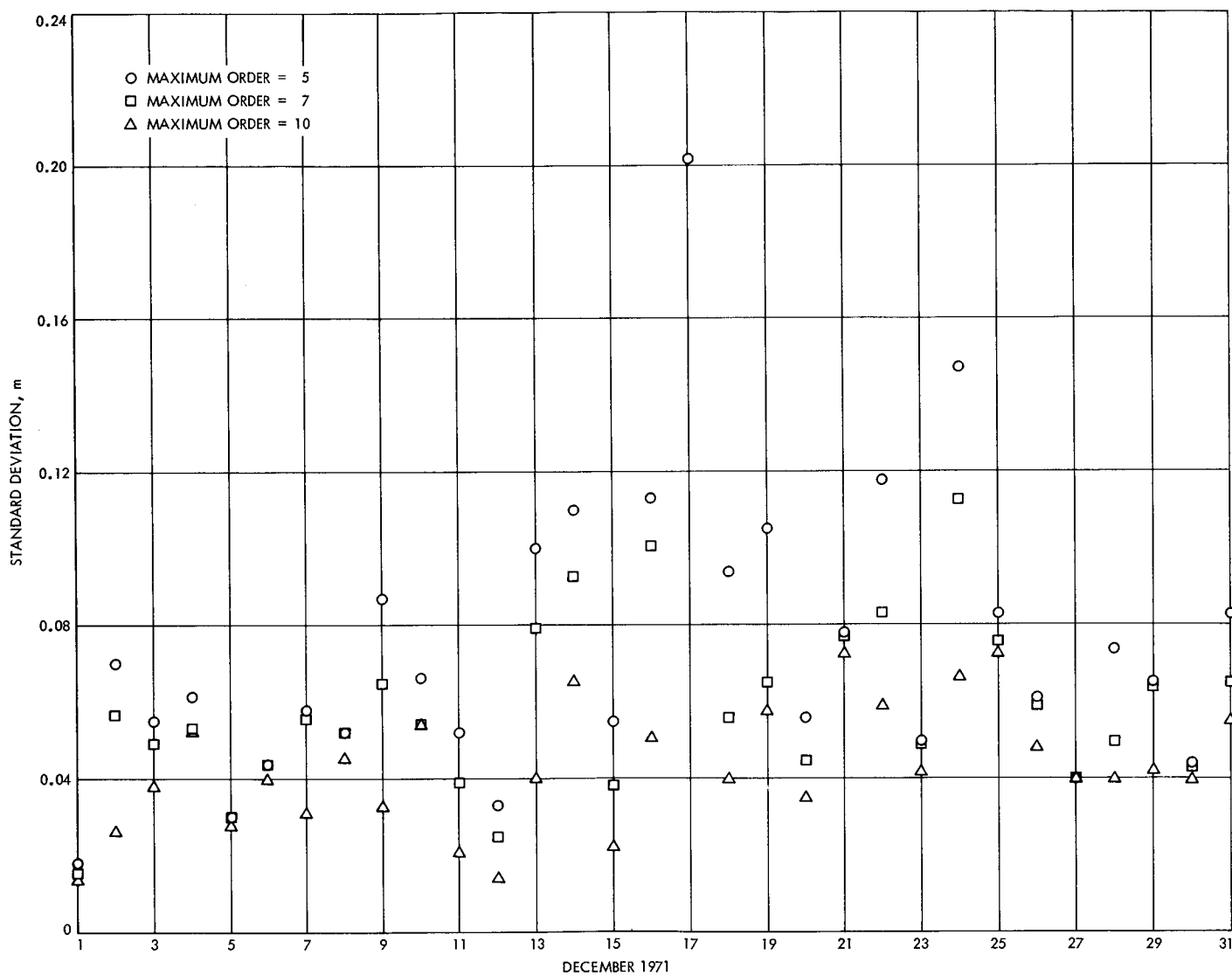


Fig. 7. Standard deviations from fitting of one-way range change

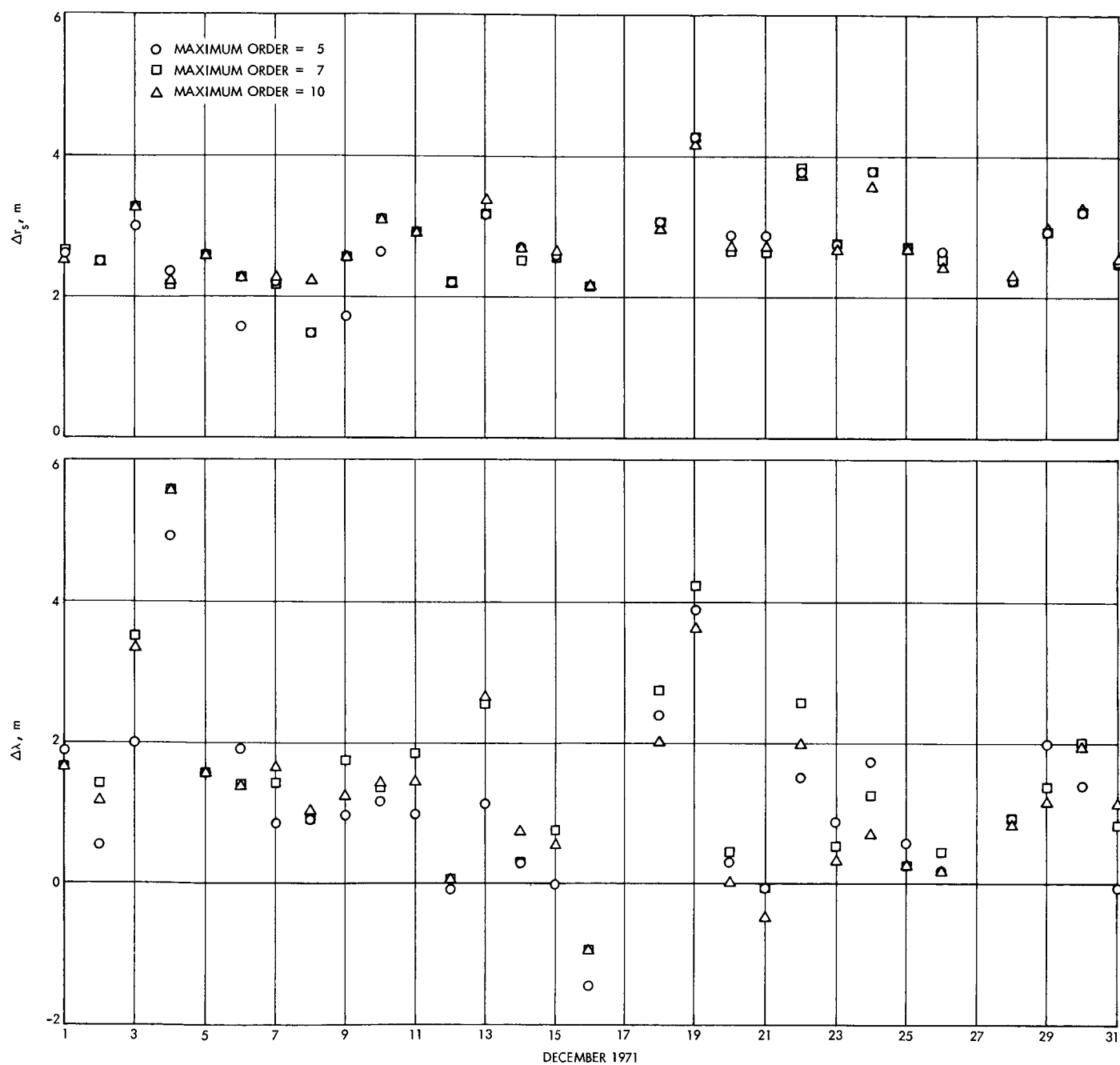


Fig. 8. Ionospheric station location changes for Mariner 9

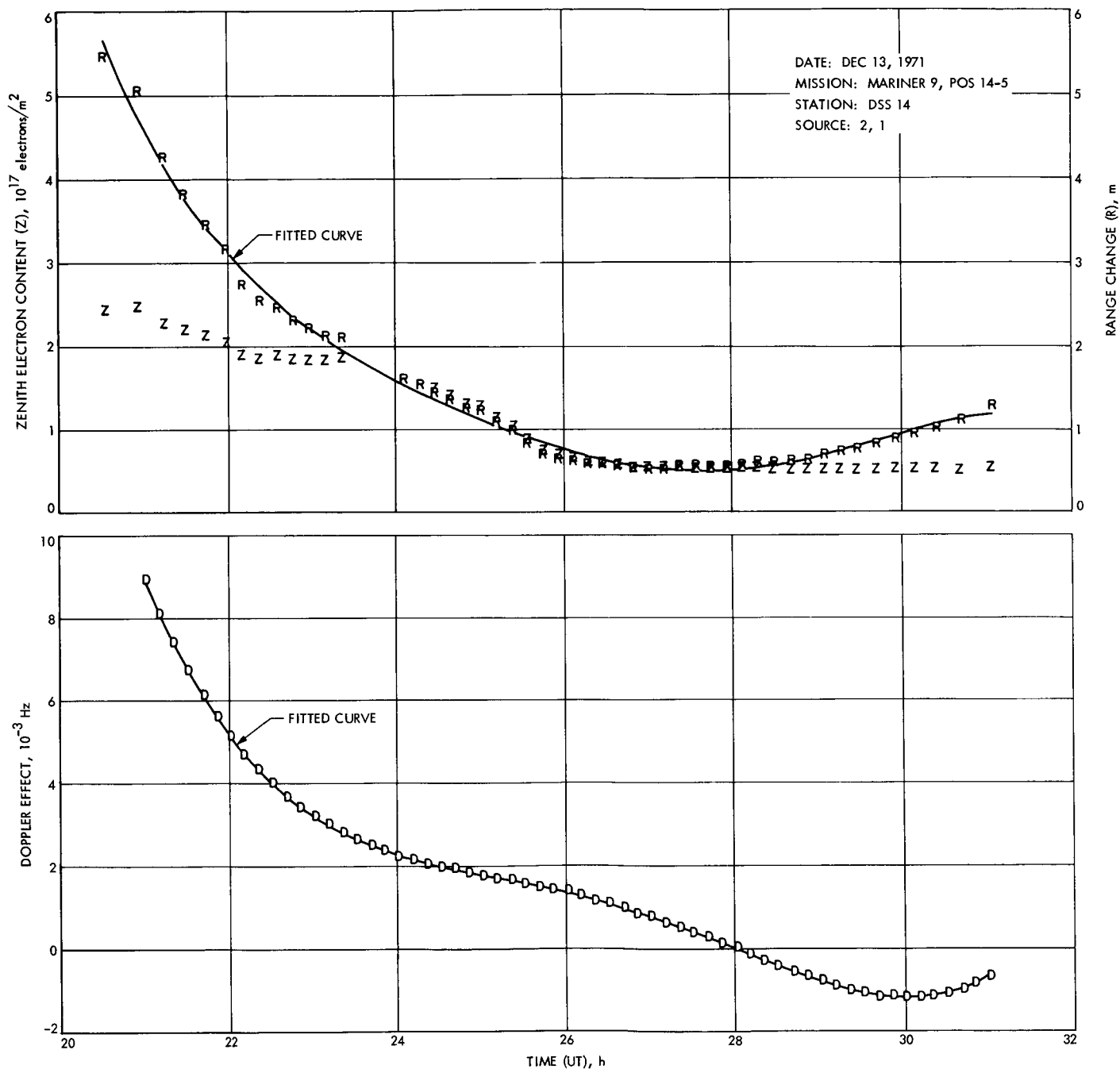


Fig. 9. Ionospheric range change and doppler effect for maximum order of range fit of 5

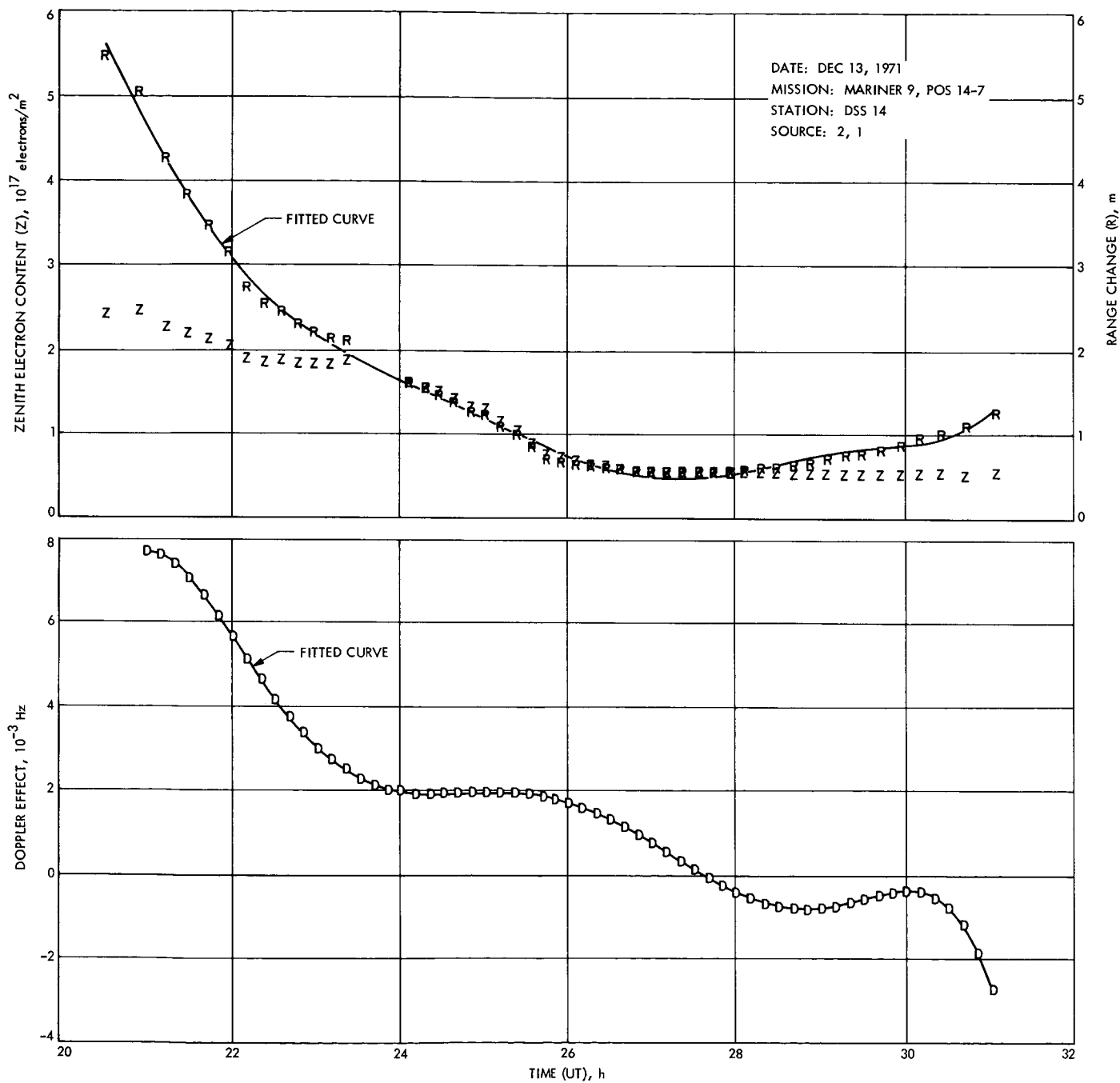


Fig. 10. Ionospheric range change and doppler effect for maximum order of range fit of 7

S/X Experiment: Preliminary Tests of the Zero Delay Device

T. Y. Otoshi and P. D. Batelaan
Communications Elements Research Section

Preliminary testing of the zero delay device for the S/X experiment was performed at the Telecommunications Development Laboratory. The test setup consisted of a Block IV exciter, the zero delay device under test, a Block III receiver for S-band reception, a Block IV receiver for X-band reception, and a Mini-Mu ranging machine. Group delay through the system was measured as a function of received signal level and zero delay device temperature. The test results are presented and discussed.

I. Introduction

Fabrication of a zero delay device (ZDD), developed for the S/X experiment (Ref. 1), has recently been completed. This device will be installed on the side of the Mod-III section of the 64-m-diam antenna at DSS 14. The ZDD will simulate a spacecraft radio system mounted on the ground antenna itself. It is used for routine tracking precalibrations and will enable group delay and phase stability of the ground radio system to be calibrated as functions of antenna pointing coordinates and ambient temperatures. As was described in a previous article (Ref. 2), the ZDD in the operational configuration at DSS 14 will be used with a Block IV exciter, Block IV S-band receiver, Block IV X-band receiver, and a Mu-2 ranging system. Additional discussions on the principle of operation and detailed block diagrams of the ZDD may be found in Ref. 2.

II. Test Setup

The Block IV exciter/receiver systems and the Mu-2 ranging system are scheduled for installation at DSS 14 in October 1973. Owing to the unavailability of these systems, preliminary checkout of the ZDD assembly was attempted in the laboratory. The use of a Hewlett-Packard 5360A computing counter and other group delay measurement schemes was found to be only partially satisfactory.

It was suggested by L. Brunn of the Spacecraft Telecommunications Systems Section that preliminary ZDD tests be done at the Telecommunications Development Laboratory (TDL). The test equipment and setup at TDL were found to be ideally suited for testing the ZDD assembly. In addition to a Block III receiver for S-band testing, TDL was also equipped with a temperature-controlled test chamber, RF screen room, Mini-Mu ranging

machine, and an SDS 920 computer for both phase and group delay data processing. An engineering model Block IV exciter/receiver for X-band testing was made available by the R.F. Systems Development Section.

Figure 1 shows the ZDD placed in the TDL temperature-controlled test chamber. For these temperature tests, phase-stable cables (Flexco F182) were used for all critical RF transmission lines leading into and out of the temperature-controlled environment. A block diagram of the test setup is shown in Fig. 2. Some modifications made to the original ZDD block diagram (Ref. 2) to facilitate testing at TDL were (1) substitution of phase-stable cables for the S- and X-band horns, (2) removal of an S-band 45-dB pad, (3) substitution of a 2113-MHz bandpass filter by a 6-dB pad, and (4) substitution of a 40-dB X-band pad by a 3-dB pad. The substituted pads were chosen to make the received S/X signal levels be approximately the same as anticipated when the ZDD is used on the 64-m-diam antenna with the 400-kW transmitter turned on.

Tests were made by sequentially switching between the S-band Block III receiver and the X-band Block IV receiver. The following operating conditions existed for the calibrations at TDL:

S-band Block III receiver
Noise figure = 6.1 dB
RF bandwidth = 12 Hz
Threshold = -158 dBm

X-band Block IV receiver
Noise figure = 14 dB
RF bandwidth = 3 Hz
Threshold = -155 dBm

Uplink ranging modulation index = 69.2 deg

ZDD power levels: refer to Fig. 2

ZDD mixer oven temperature = 51.9°C

Group delay and phase data were obtained as functions of signal level and the physical temperature of the ZDD assembly. Signal levels were varied by means of the S- and X-band step attenuators on the ZDD assembly. The test chamber temperatures selected for the ZDD tests were 4, 21, and 34°C. The actual temperature extremes in the Mod III section, where the ZDD assembly will be installed, are expected to be well within the temperature range of 0 to 34°C.

III. Test Results and Discussion

Group delay ranging data and phase data were processed by means of special TDL computer programs written for the SDS 920 computer. Output data from the computer was provided every 20 or 30 seconds. However, these integration periods could be changed at the option of the operator. These output data were then averaged manually to obtain an overall mean and standard error applicable to the total integration time at a particular signal level setting or temperature. These mean values of group delay with standard error limits are shown plotted as functions of received signal levels and temperature for S- and X-band frequencies in Figs. 3 to 10.

It is of interest to note in Fig. 3 that at 21°C ambient temperature, the mean value for the S-band group delay changed about 1.6 ns when signal levels were varied over a 40-dB dynamic range. Figure 7 shows that the X-band group delay at 21°C changed about 4 ns when signal levels were varied over a 30-dB range. Similar observations of group delay changes at other temperatures are summarized in Table 1 for convenience of further study. The overall or worst case group delay change as functions of both temperature and signal level was found to be about 5 ns for S-band and 7 ns for X-band.

Table 2 is a summary of group delay repeatability tests at a particular strong signal level setting. The elapsed time between settings was 1 hour or more. The worst change or drift observed at 21°C was 0.77 ns for S-band and 1.56 ns for X-band.

The causes of the group delay changes at the stronger signal levels are not clearly understood at the present time. The changes should not be attributable to the ZDD attenuators because group delay changes of the individual attenuators are less than 0.05 ns over a 69-dB range and 4.4 to 37.8°C temperature range (Ref. 3). Repeatability of the ZDD attenuators was typically better than ± 0.02 ns. Some of the group delay changes might be attributed to the ranging system itself. Changes of about ± 2 ns have been previously observed on TDL ranging tests of spacecraft radio equipment (Ref. 4).

The data presented in this article should be considered to be preliminary and not necessarily applicable to the final installed configuration at DSS 14. Phase data which were also obtained on the ZDD assembly at TDL are currently being analyzed. The phase test results will be reported in a subsequent article.

Acknowledgments

The ZDD assembly was fabricated and assembled by R. B. Lyon of the Communications Elements Research Section. Jim Weese of the Spacecraft Telecommunications Systems Section and Boyd Madsen of The Boeing Company assisted with the TDL tests. The engineering model Block IV receiver was provided by H. Donnelly, C. Johns, and R. Weller of the R.F. Systems Development Section.

References

1. Levy, G. S., Dickinson, R., and Stelzried, C. T., "RF Techniques Research: S/X Band Experiment," in *Supporting Research and Advanced Development*, Space Programs Summary 37-61, Vol. III, pp. 93-95, Jet Propulsion Laboratory, Pasadena, Calif., Feb. 20, 1970.
2. Otoshi, T. Y., and Batelaan, P. D., "S/X Band Experiment: Zero Delay Device," in *The Deep Space Network Progress Report*, Technical Report 32-1526, Vol. XIV, pp. 73-80, Jet Propulsion Laboratory, Pasadena, Calif., Apr. 15, 1973.
3. Otoshi, T. Y., "S/X Band Experiment: Zero Delay Device Step Attenuator Evaluation," in *The Deep Space Network Progress Report*, Technical Report 32-1526, Vol. XV, pp. 84-87, Jet Propulsion Laboratory, Pasadena, Calif., June 15, 1973.
4. Brunn, L., private communication, June 1973.

Table 1. Summary of peak group delay changes observed as functions of signal level and temperature

Temperature, °C	Maximum, ns	Minimum, ns	Difference, ns
S-band mean values for signal levels 18 to 58 dB above threshold			
21.0	232.26	230.69	1.57
4.4	231.35	229.23	2.12
34.0	232.29	230.69	1.60
Postcalibration, 21.0	231.07	227.37	3.70
34°C for max; 21°C postcali- bration for min	232.29	227.37	4.92
X-band mean values for signal levels 5 to 35 dB above threshold			
21.0	279.08	275.06	4.02
4.4	274.40	272.01	2.39
34.0	276.24	272.89	3.35
Postcalibration, 21.0	273.39	272.07	1.32
21°C for max; 4.4°C for min	279.08	272.01	7.07

Table 2. Summary of group delay system drift tests at strong signal level

Temperature, °C	Initial, ns	Final, ns	Change, ns	Elapsed time, h
S-band mean values for signal level 58 dB above threshold				
21.0	230.75	229.98	0.77	1.1
4.4	229.23	229.41	-0.18	1.3
34.0	230.76	230.60	0.16	1.5
Postcalibration, 21.0	229.32	229.17	0.15	1.3
X-band mean values for signal level 35 dB above threshold				
21.0	277.83	279.39	-1.56	2.1
4.4	273.65	274.40	-0.75	1.3
34.0	274.32	273.06	1.26	2.0
Postcalibration, 21.0	272.90	272.41	0.49	1.1

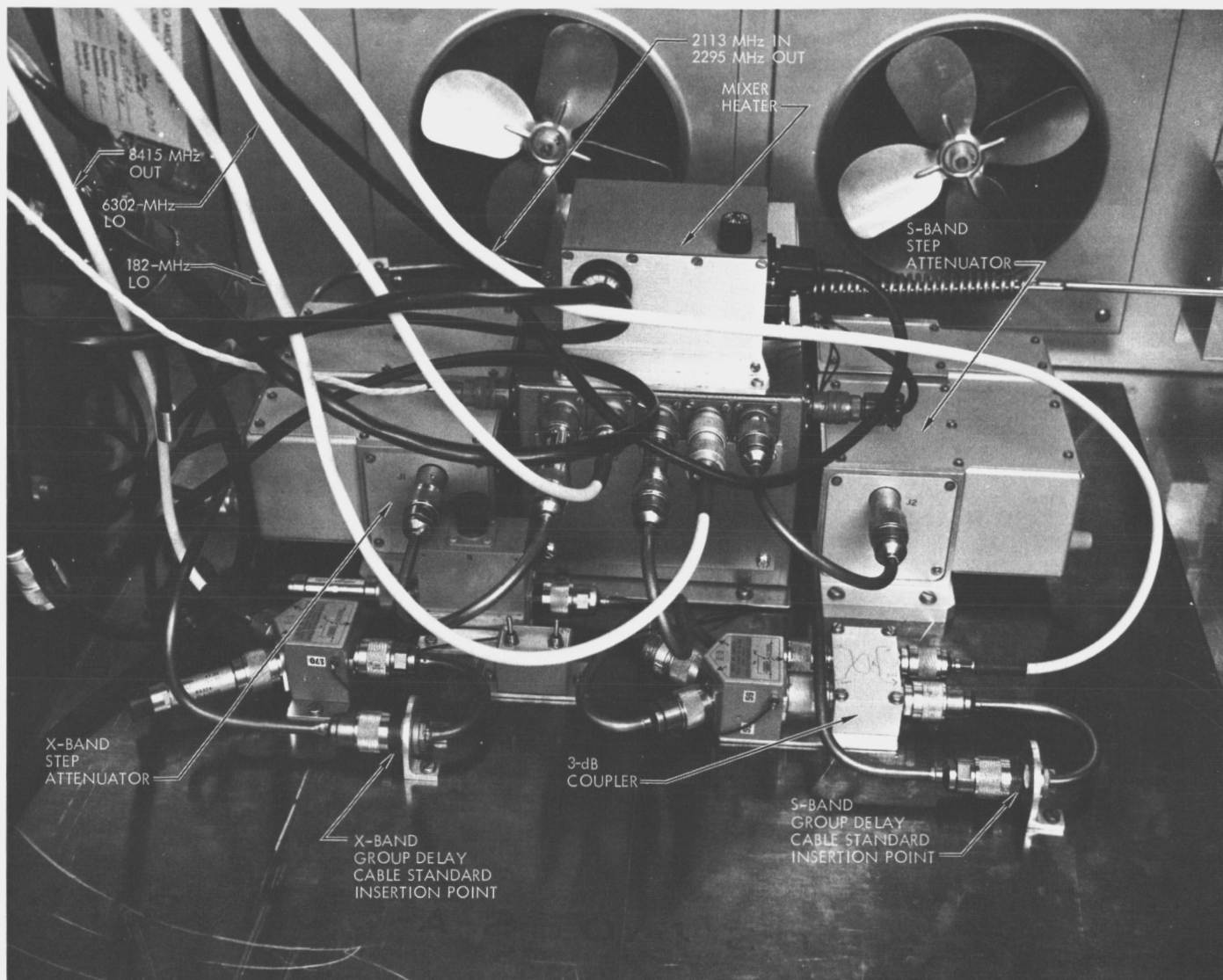


Fig. 1. Modified ZDD assembly in TDL temperature control chamber

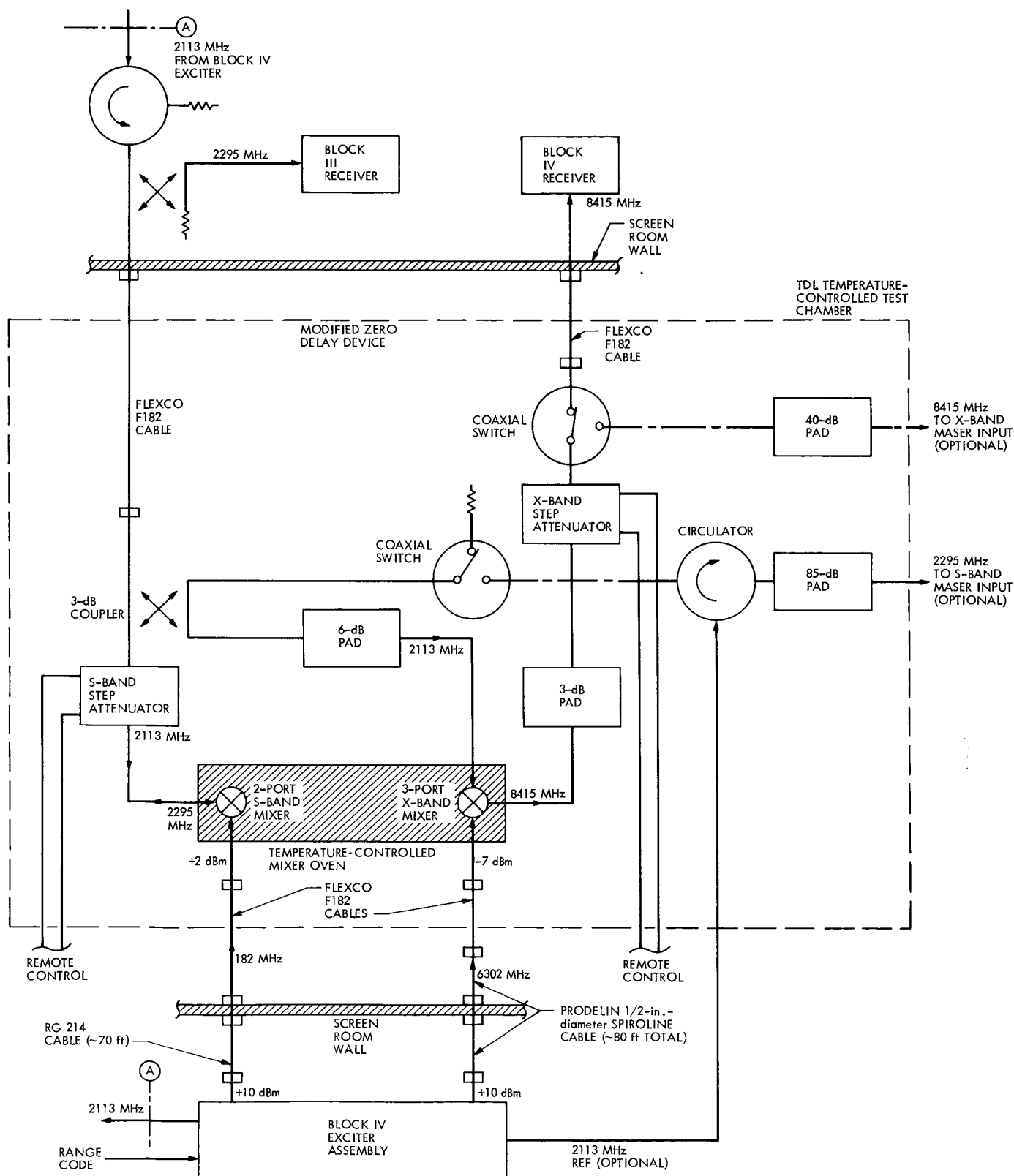


Fig. 2. Block diagram of test setup for ZDD tests at TDL

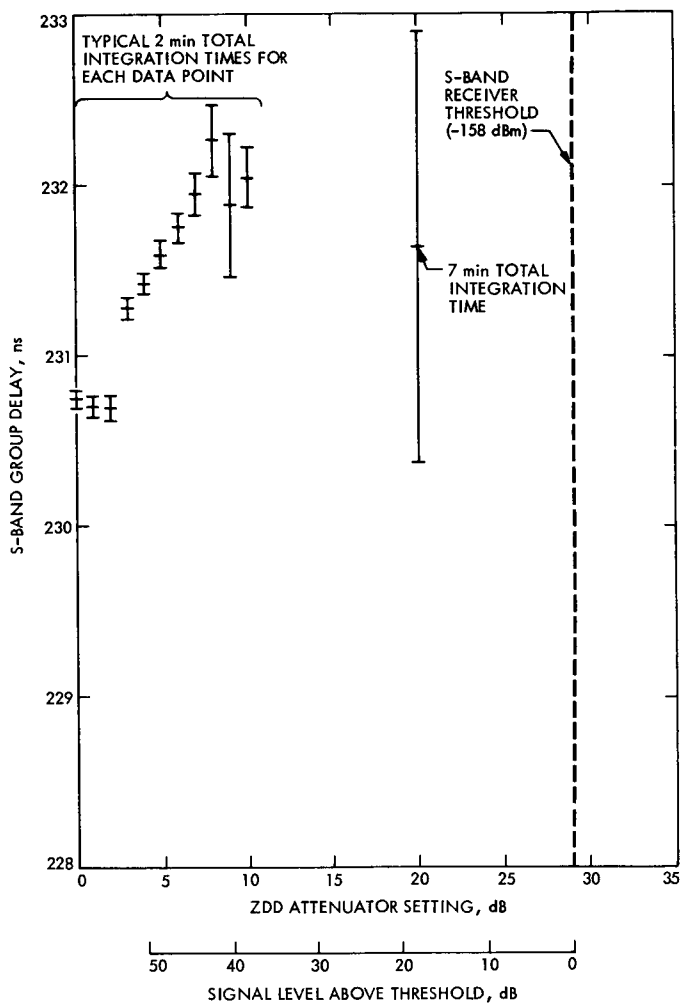


Fig. 3. Total system group delay via the 2113-MHz/2295-MHz path of the ZDD at 21°C

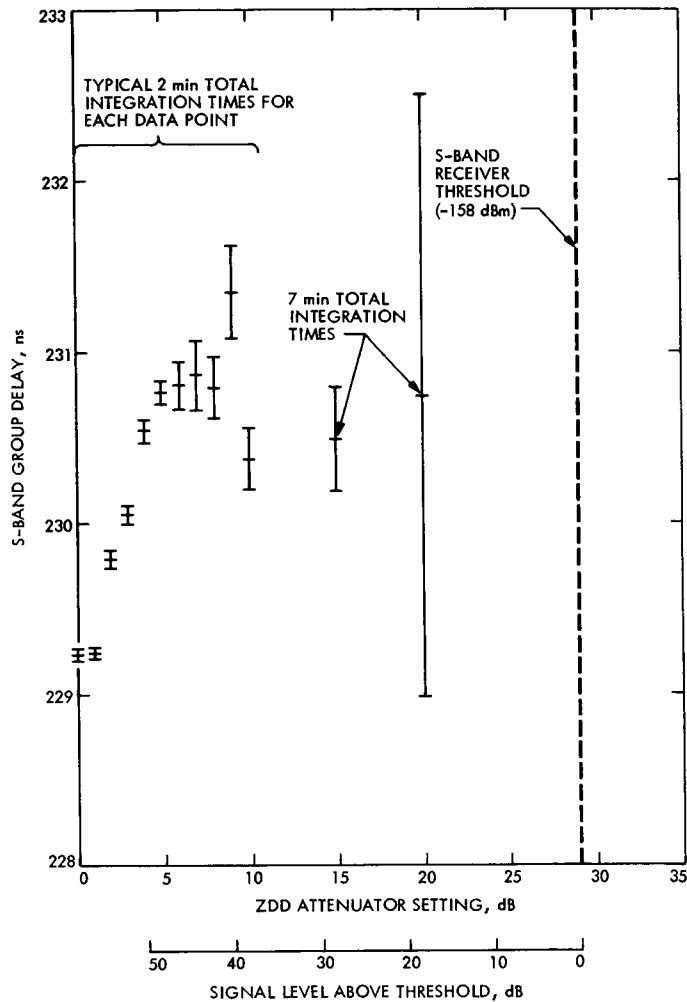


Fig. 4. Total system group delay via the 2113-MHz/2295-MHz path of the ZDD at 4.4°C

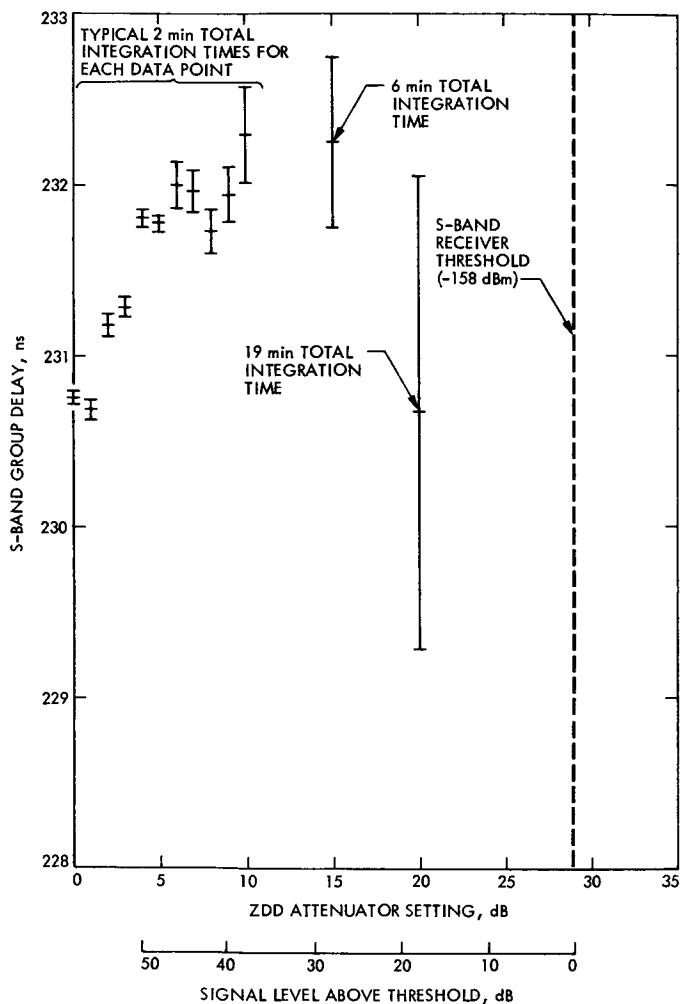


Fig. 5. Total system group delay via the 2113-MHz/2295-MHz path of the ZDD at 34°C

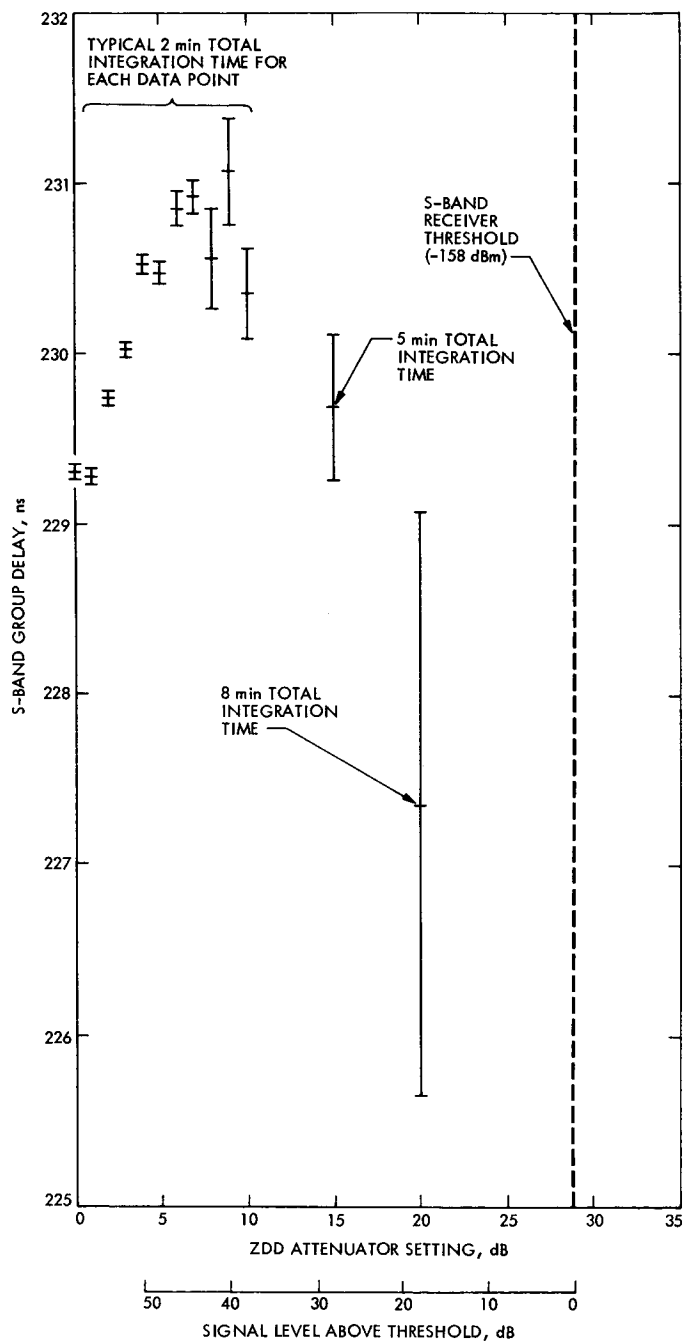


Fig. 6. Postcalibration of the total system group delay via the 2113-MHz/2295-MHz path of the ZDD at 21°C

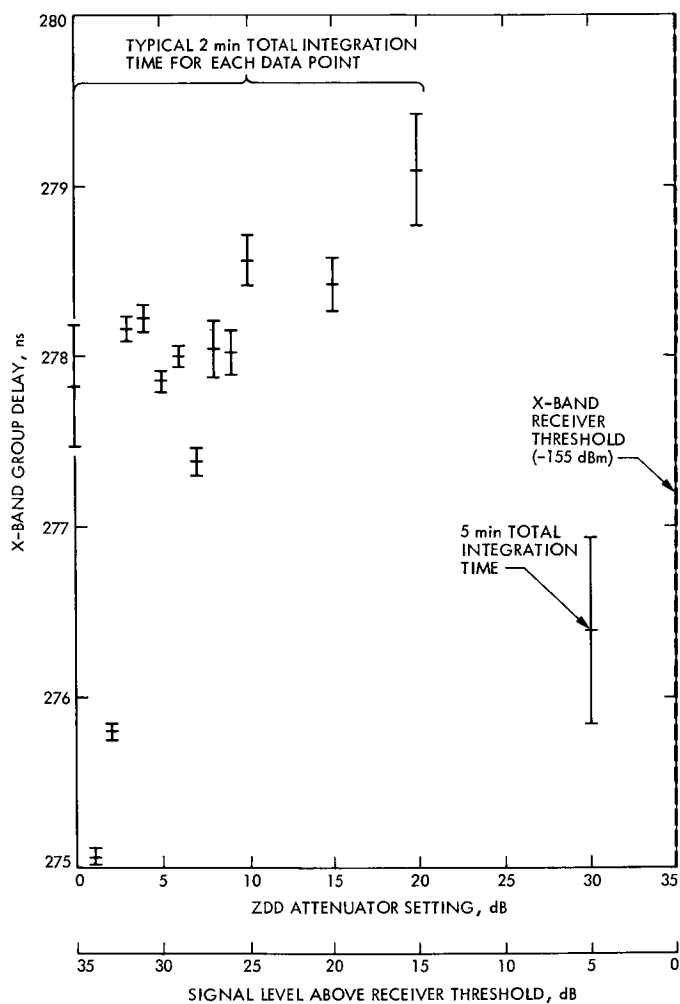


Fig. 7. Total system group delay via the 2113-MHz/8415-MHz path of the ZDD at 21°C

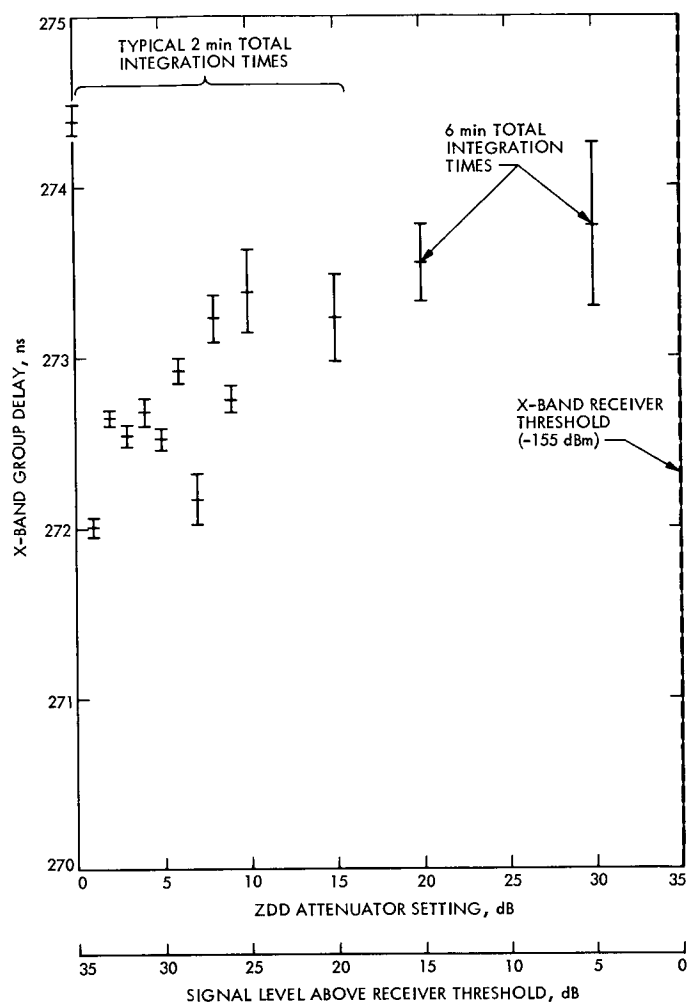


Fig. 8. Total system group delay via the 2113-MHz/8415-MHz path of the ZDD at 4.4°C

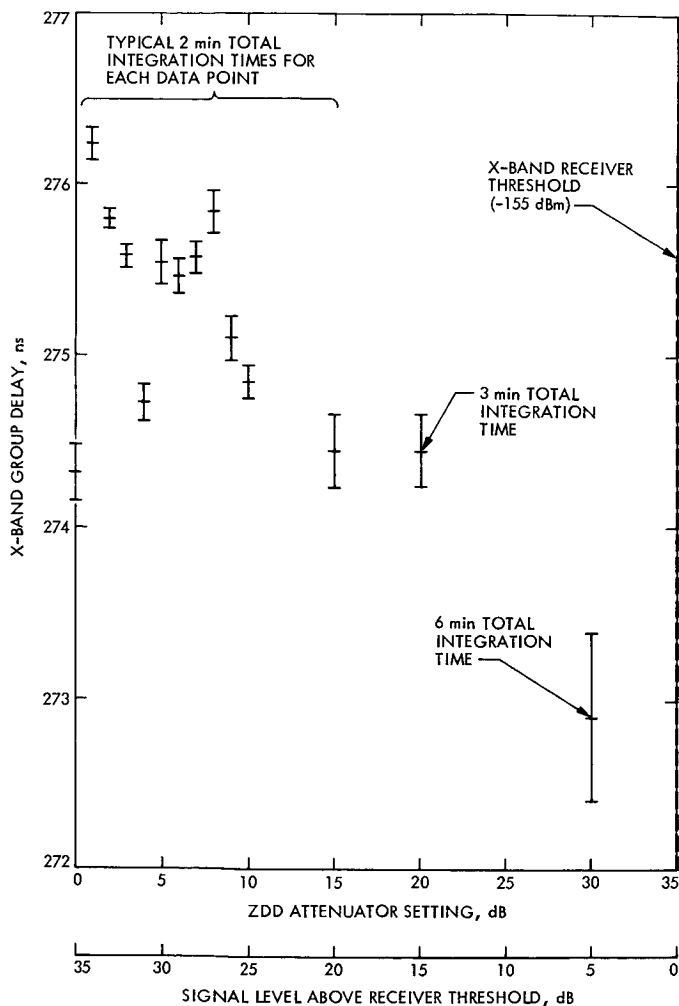


Fig. 9. Total system group delay via the 2113-MHz/8415-MHz path of the ZDD at 34°C

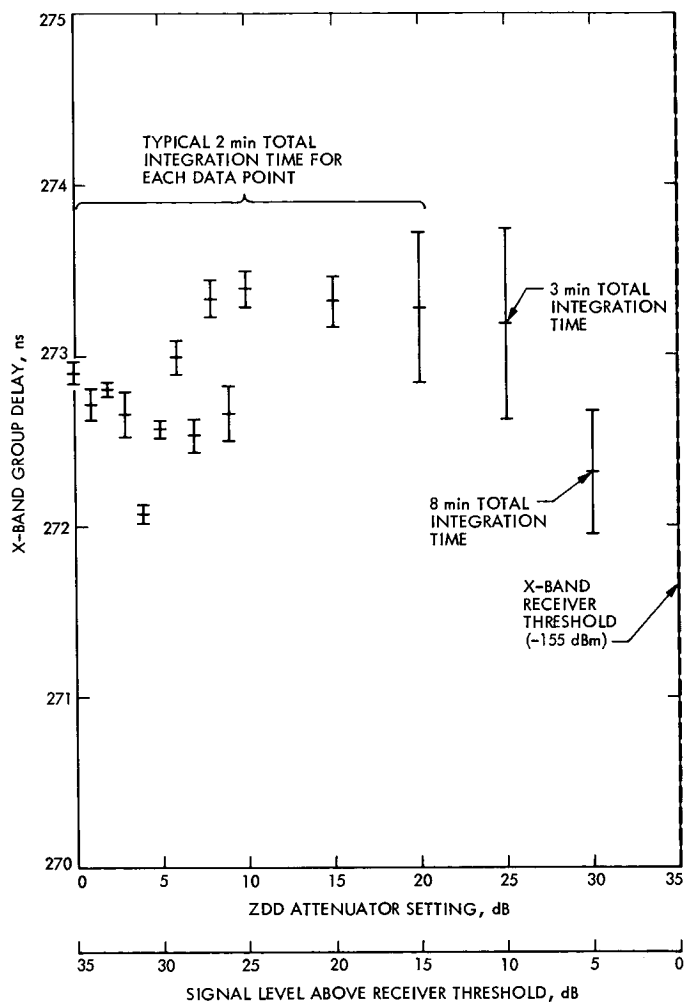


Fig. 10. Postcalibration of the total system group delay via the 2113-MHz/8415-MHz path of the ZDD at 21°C

Computation of RF Boresight Direction From Reflector Distortions

M. S. Katow and M. Mori
DSIF Engineering Section

The direction of the radio-frequency (RF) boresight as computed by use of the RMS and Radiation programs is calculated by (1) using the same NASTRAN-computed distortion data and (2) searching for the maximum gain location of the focus. For small gravity distortions of the 64-m antenna, the values compare within 0.000004 rad (0.0003 deg).

I. Introduction

The direction of the RF boresight of the 64-m antenna may be calculated using the distortion data of the reflector structure. As shown in Refs. 1 and 2, best-fitting of the distortion data with the RMS program combined with the deflection data of the RF phase center provides one answer by ray-tracing. A direction answer may also be output from the Radiation program (Ref. 3), where the same distortion data may be input. The Radiation program integrates the illumination function over the antenna aperture, taking into account the pathlength and surface phasing error caused by the distortion at each point on the surface, and outputs a far-field radiation pattern. A rigorous comparison of the two outputs should provide an insight into the accuracy of the RF boresight calculation using the more versatile RMS program.

In the RMS best-fitting process, it is obvious that in fitting the almost circular shape of the paraboloid to a set of distortions, the accuracy of the rotated position of the best fit paraboloid used in ray-tracing is vulnerable to the quality of the distortion data. In this report, the distortion data were computed by the NASTRAN computing pro-

gram using the 1/2 models as described in Ref. 1. The two sets used were for the standard and the modified reflector structure.

The reflection factor was first upgraded with the use of X-band propagation constant in the Radiation program. The description of the method of including the pathlength errors by offsets is included. Then the RF boresight direction is computed using X-band with the Radiation program and compared to the answer using the RMS program. An additional comparison is made using the Radiation program to search for the position of the RF phase center which produces the maximum gain. This position should be the same as the position of the focus of the best fit paraboloid.

II. Reflection Factor

Since specific illumination taper of the RF feed can be input to the JPL Radiation program, this method of determining the reflection factor was used, although general solutions are available in the literature. The phase center was laterally displaced by effectively moving the paraboloid laterally.

In addition to the distortion data, which in this series of computations were set to zero error, a Y-offset dimension was input to the Radiation program. This Y-offset was then added to the coordinates of each node defining a perfect paraboloid. The algorithm in the Radiation program then computes the pathlength error at each node. The number of nodes includes one at the center, followed by 24 nodes in the first row and 48 nodes for 8 more rows for a total of 409 nodes.

Figure 1 defines the algorithm where the basic assumption is made that the deflected surface remains parallel to the original tangent at the undeformed node. Then from the normal vector NT of the offset or the distortion vector NR, vector NS, which is equal to vector NU, may be computed. Vector NV equals $NS \times \cos \psi$. Thus the pathlength error equals NS plus NV or $NU(1 + \cos \psi)$.

The illumination taper curve shown in Fig. 2 was assumed to be symmetric about the axis of revolution, although in the tricone setup the pattern is known to be slightly asymmetric. As compared to the reflector factor using a uniform illumination, the factor increase with a taper is from 0.83+ to 0.84+.

Figure 3 illustrates the ray-tracing picture when the reflector is moved laterally, with the computed answers delineated in Table 1.

III. Boresight Direction Using the RMS Program

The results described in Ref. 1 will be used with corrections for the change in the reflection factor of 0.83 used in Ref. 1 to 0.8419 computed for X-band and for an error discovered for the X-rotation value for the modified case: -0.0002818 corrected to -0.0002815 . The results are shown in Table 2 and illustrated in Fig. 4, the symbols being defined as follows:

C = undeformed paraboloid vertex

C_3 = best fit paraboloid vertex

F = undeformed paraboloid focus point

F_3 = RF phase center

F_4 = best fit paraboloid focus point

The same illumination taper values shown in Fig. 1 were input into the RMS program, in which the surface areas of a normal dish assignable to each node are computed and multiplied by the illumination factor, resulting in a weighting factor for each node during the best fitting calculation.

IV. Maximum Gain Direction From Radiation Program

As shown in Fig. 4, by effectively moving the focus F_4 of the best fit paraboloid on F , the undeformed focus in the Radiation program, the Radiation program should output the minimum gain loss or the maximum gain of the RF pattern with a boresight direction corresponding to angle θ of the axis of the best fit paraboloid. A search for the maximum gain angle θ was made by varying the Y-offset WW. Effectively, the focus F_4 was moved to position F using the Z-offset value from the RMS output. The results of this effort are shown in Table 3.

V. Conclusions

The calculated boresight direction matches with 0.000004 rad (0.0003 deg) when the comparisons are made between the RMS and Radiation program methods. When the comparison is made by the search for the maximum gain method, the difference using the distortion data from the standard configuration appears for unknown reasons to be too large, while there is a close match with the modified configuration.

References

1. Katow, M. S., "64-m-Diameter Antenna: Computation of RF Boresight Direction," in *The Deep Space Network Progress Report*, Technical Report 32-1526, Vol. XIV, pp 68-72, Jet Propulsion Laboratory, Pasadena, Calif., Apr. 15, 1973.
2. Katow, M. S., and Schmele, L. W., "Antenna Structures: Evaluation Techniques of Reflector Distortions," in *Supporting Research and Advanced Development*, Space Programs Summary 37-40, Vol. IV, pp. 176-184, Jet Propulsion Laboratory, Pasadena, Calif., Sept. 30, 1968.
3. Bathker, D., "Radiation Pattern Programs," in *Computer Programs for Antenna Feed System Design and Analysis*, Technical Report 32-479, Vols. I and II, edited by A. Ludwig, Jet Propulsion Laboratory, Pasadena, Calif., Apr. 15, 1967.

Table 1. Reflection factors

Radio frequency	Propagation constant	Offset, cm	(in.)	Incidence angle, rad	Reflection angle, rad	Reflection factor
S-band, 2300 MHz	1.22089	2.54	(1.0)	0.0537	0.0420	0.8417
		5.08	(2.0)	0.1074	0.09045	0.8424
		7.62	(3.0)	0.1610	0.1359	0.8441
		10.16	(4.0)	0.2147	0.1817	0.8463
X-band, 8448 MHz	4.49749	2.54	(1.0)	0.0537	0.0452	0.8417
		5.08	(2.0)	0.1074	0.09035	0.8412
		7.62	(3.0)	0.1610	0.13555	0.8419
		10.16	(4.0)	0.2147	0.18075	0.8419

Table 2. Computed RF boresight directions

Program	Deflection		Description	64-m antenna: gravity distortion at zenith look, aligned at 45° elevation angle, offsets					
	Symbol			Standard structure			Modified/new braces		
	Angular	Linear		Angle, rad	Linear cm	Linear (in.)	Angle, rad	Linear cm	Linear (in.)
RMS	—	OP	RF phase center	—	3.058	−1.204	—	−2.644	−1.041
	α	NN	Incidence angle	0.002559	6.939	2.732	0.002921	7.920	3.118
	β	—	Reflection angle	0.002154	5.842	2.300	0.002459	6.668	2.625
	θ	MM	Best fit paraboloid (X-rotation)	−0.002612	7.081	2.788	−0.002815	7.633	3.005
	δ		RF boresight direction	0.000458	1.239	0.488	0.000356	0.965	0.380
	—	VV	Best fit paraboloid (vertex Y-offset)	—	−10.962	−4.316	—	−12.909	−5.082
	—	CC	Best fit paraboloid (vertex Z-offset)	—	−0.616	−0.243	—	−0.600	−0.237
	—	WW	Best fit paraboloid (focus point)	—	3.881	1.528	—	5.276	2.077
	—	C ₃ F ₃	Best fit paraboloid (focal length)	—	2711.618	1067.566	—	2711.625	1067.569
Radiation	δ	—	RF boresight direction	0.000460	—	—	0.000352	—	—
		CF	Undeformed focal length	—	2710.926	1067.294	—	2710.926	1067.294
	—	—	Y-offset	—	3.058	−1.204	—	−2.644	−1.041
	—	—	Z-offset	—	−.616	−0.243	—	−0.600	−0.237
Difference	δ		RF boresight direction	0.000002			0.000004		

Table 3. Maximum gain direction

Data description	Maximum gain angle θ							
	Radiation, X-band					RMS		
	cm	Y-offset, (in.)	cm	Z-offset (in.)	θ , rad	cm	Y-offset (in.)	θ (X-rotation), rad
Standard	3.772 (± 0.025)	1.485 (± 0.010)	0.617	-0.243	0.002580 (± 0.000009)	3.879	1.527	0.002612
Modified	5.276 (± 0.008)	2.077 (± 0.003)	0.602	-0.237	0.002814 (± 0.000002)	5.276	2.077	0.002815

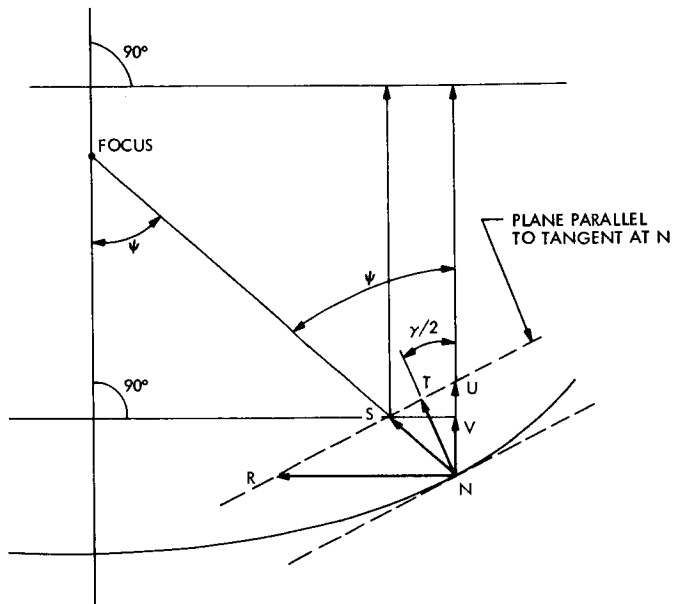


Fig. 1. Pathlength error definition

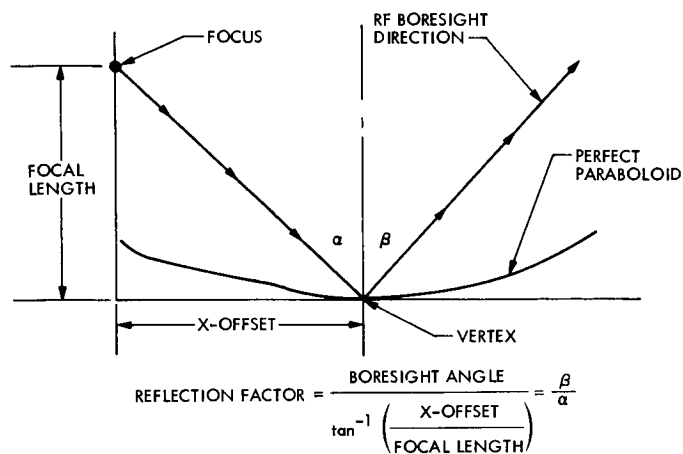


Fig. 3. RF boresight direction due to lateral offset

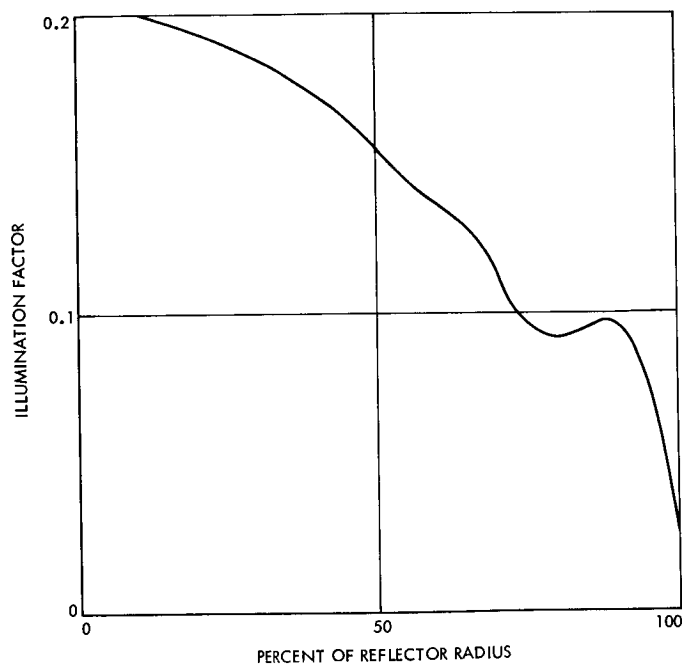


Fig. 2. 64-m-antenna RF feed illumination taper

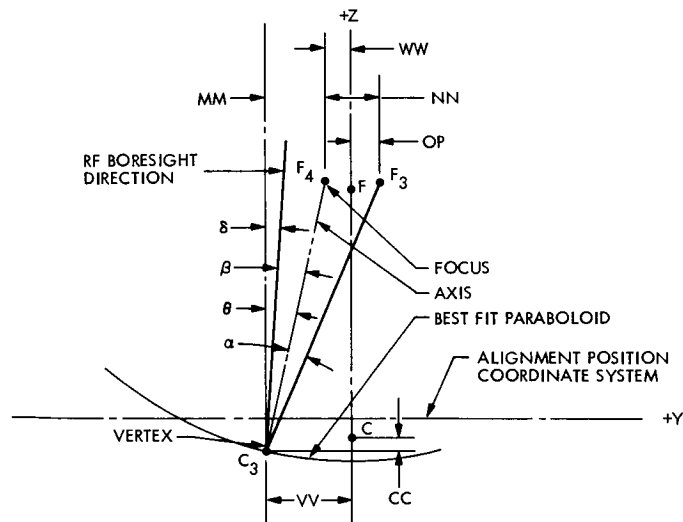


Fig. 4. RF ray tracing on the best fit paraboloid

A Note on Noisy Reference Detection

J. W. Layland

Communications Systems Research Section

Telemetry systems supported by the DSN employ coherent detection of a bi-phase phase-shift keyed (PSK) waveform. The coherent reference for the detector is supplied by a bandpass limiter/phase-locked loop. Phase noise in this coherent reference is often a critical factor in establishing link performance. Lindsey has analyzed the performance of the DSN receivers under the extreme assumptions that (a, high-rate) the phase error of the coherent reference is constant over the symbol interval, and that (b, low-rate) the phase error of the coherent reference varies rapidly over the symbol interval. Blake/Lindsey and Tausworthe, subsequently developed techniques to approximate the DSN receiver performance between these extremes. Under close examination, however, it becomes apparent that with typical DSN parameters, the approximations used by Blake and Lindsey become suspect above 15–30 bits/s, and hence do not validly cover many of the interesting data rates. The interpolation proposed by Tausworthe depends upon approximating the log of the error probability by the first few terms of a Taylor series in the variational part of the decision variable. Again, there must be some ranges of defining parameters (not necessarily of practical interest) where his approximation becomes invalid. It is the intent of this article to develop a refined approximation to the performance of the DSN receivers with a (hopefully) wider validity range than previous techniques.

I. Introduction

Telemetry systems supported by the DSN employ coherent detection of a bi-phase PSK waveform. The coherent reference for the detector is supplied by a bandpass limiter/phase-locked loop. Phase noise in this coherent reference is often a critical factor in establishing link performance. Lindsey (Ref. 1) has analyzed the performance of the DSN receivers under the extreme assumptions that (a, high-rate) the phase error of the coherent reference is constant over the symbol interval, and that (b, low rate) the phase error of the coherent reference

varies rapidly over the symbol interval. Blake and Lindsey (Ref. 2) and Tausworthe (Ref. 3) subsequently developed techniques to approximate the DSN receiver performance between these extremes. Under close examination, however, it becomes apparent that with typical DSN parameters, the approximations used by Blake and Lindsey (Ref. 2) become suspect above 15–30 bits/s, and hence do not validly cover many of the interesting data rates. The interpolation proposed by Tausworthe depends upon approximating the log of the error probability by the first few terms of a Taylor series in the variational part of the

decision variable. Again, there must be some ranges of defining parameters (not necessarily of practical interest) where his approximation becomes invalid. It is the intent of this article to develop a refined approximation to the performance of the DSN receivers with a (hopefully) wider validity range than previous techniques.

The system parameter which characterizes the high-, medium- and low-rate situations is the normalized data rate defined as the ratio of the data rate \mathcal{R} to the two-sided phase-locked loop bandwidth W_L at its operating point. Most of the significant performance variation occurs in the range of δ from 0.5 to 10. For the DSN receiver with its nominal design point loop bandwidth of 12 Hz, W_L varies between 20 and 60 Hz at typical operating points, so the medium-rate approximate analysis is applicable to all data rates below about 500 bits/s.

II. System Model

The system in which we are interested consists of a limiter-controlled phase-locked loop which tracks the carrier of the signal received from a spacecraft, followed by an integrate-and-dump correlation detector using the output of the phase-locked-loop for the coherent reference. For uncoded telemetry, the decision statistics emitted by the correlation detector can be represented by

$$D_t = \frac{1}{T} \int_t^{T+t} \cos(\omega_c t + \hat{\phi}(t)) \cdot [A m_t \cos(\omega_c t + \phi_c(t)) + n(t)] dt \quad (1a)$$

$$= A m_t \cdot \frac{1}{T} \int_t^{T+t} \cos(\hat{\phi}(t) - \phi_c(t)) dt + N_t \quad (1b)$$

This expression involves the implicit assumption that $n(t)$ is independent of the phase $\hat{\phi}(t)$, and neglects losses due to bit timing errors, subcarrier synchronization errors, waveform distortions, etc. The modulation term m_t is ± 1 . For coded telemetry, m_t would be replaced in Eq. (1b) by the appropriate cross-correlation between received and tentative reference code words.

The critical feature of Eq. (1b) is its dependence upon the reference phase error $\phi_e(t) = \hat{\phi}(t) - \phi_c(t)$, which is a band-limited low-pass random process whose bandwidth is the phase-locked-loop bandwidth. For a first-order tracking loop, ϕ_e has autocorrelation function

$$R_{\phi_e}(\tau) = \sigma_{\phi_e}^2 \exp(-2W_L |\tau|) \quad (2)$$

Furthermore, if the signal-to-noise ratio in the operating loop bandwidth ρ_L is large, $\phi_e(t)$ is essentially Gaussian

with $\sigma_{\phi_e}^2 = 1/\rho_L$. For moderate $\rho_L (> 3)$, quasi-linear loop theory shows that $\phi_e(t)$ is well approximated by a Gaussian process with $\sigma_{\phi_e}^2 = \exp(\sigma_{\phi_e}^2/2)/\rho_L$. In the following, we will use ρ'_L to denote an equivalent quasi-linear loop signal-to-noise ratio (SNR), so that $\sigma_{\phi_e}^2 = 1/\rho'_L$. For the high-rate performance model, $W_L \cdot T < 1$, $\phi_e(t)$ is constant during the integration period, and the probability distribution of D_t is well known (Ref. 1).

For the low-to-medium rate performance model, Blake and Lindsey propose the approximation

$$D_t \sim A m_t \left\{ 1 - \frac{1}{2} \cdot \frac{1}{T} \int_0^T \phi_e^2(t) dt \right\} + N_t \quad (3)$$

The parameter

$$x = \frac{1}{T} \int_0^T \phi_e^2(t) dt$$

has a density function $g(x)$ which is well approximated by (Refs. 2 and 4)

$$g(x) = \rho'_L \left(\frac{\beta}{2\pi} \right)^{1/2} (\rho'_L x)^{-3/2} \exp \left\{ -\frac{\beta}{2} [\rho'_L x - 2 + 1/\rho'_L x] \right\} \quad (4)$$

The parameter $\beta \triangleq W_L T = 1/\delta$. As noted by Ref. 2, the approximation is very close for $\beta > 5$, but becomes invalid for $\beta < 1$. The density $g(x)$ has its maximum at

$$\rho'_L \cdot x = \left[1 + \left(\frac{3}{2\beta} \right)^2 \right]^{1/2} - \left(\frac{3}{2\beta} \right)$$

and a zero at the origin.

Let $y = \rho'_L x$. The first few moments of y can be readily calculated to be

$$\bar{y}^0 = 1, \bar{y}^1 = 1, \bar{y}^2 = (1 + \beta)/\beta, \bar{y}^3 = (3 + 3\beta + \beta^2)/\beta^2$$

From this, the variance of y can be seen to be $V\{y\} = 1/\beta$. However, for very large δ , small β , the distribution of x is properly Chi-square with one degree of freedom, and thus the variance of y should be 2. Clearly for small β , the true and approximate distributions are rapidly divergent. Suppose we can find some function $B(\cdot)$ such that letting $\beta' = B(\delta)$ forces equality of the second moments of $g(x)$ and the true density for x . Then clearly

$$\beta'_\infty = B(\infty) = \frac{1}{2}$$

At this value, $\bar{y}^3 = 19$, as contrasted to the true value for a Chi-square (1) of 15. While $g(x, \beta')$ is a closer approximation to the true density than $g(x, \beta)$, its third (and higher) moments remain in error. Tausworthe (Ref. 3) has calculated the second central moment for

$$\xi = \frac{1}{T} \int_0^T \cos \phi_e(\tau) d\tau$$

for use as an interpolation formula. We may use his calculation directly as $B(\cdot)$:

$$\beta' = B(\delta) = 1/\{\delta - (\delta^2/4)(1 - e^{-4/\delta})\} \quad (5)$$

This calculation is identical to the second central moment calculated for

$$x = \frac{1}{T} \int_0^T \phi_e^2(t) dt$$

There are a number of other plausible choices for an approximation to the density function for x , most of which fit reasonably at some values of δ , and do not fit for others. The preferred choice among those considered is

$$h(y) = \sqrt{\frac{a}{\pi}} \exp(\sqrt{2ab}) y^{-1/2} \exp(-ay - b/y) \quad (6)$$

where $y = \rho_L' x$. This density is fully defined by the parameters a and b , which are determined by the requirement that the first two moments of y match those of the true distribution:

$$\bar{y} = 1, \bar{y}^2 = 1 + 1/B(\delta) \quad (7)$$

The parameters a and b are thus determined:

$$\left. \begin{aligned} a &= \frac{B(\delta)}{4} (1 + \sqrt{1 + 4/B(\delta)}) \\ b &= a - 1 + 1/4a, \sqrt{ab} = a - 1/2 \end{aligned} \right\} \quad (8)$$

The third moment of $h(y)$ is readily calculated to be

$$\bar{y}_h^3 = 1 + \frac{3}{2a} + \frac{3}{2a^2} + \frac{5}{8a^3} \quad (9)$$

where a is given by Eq. (8).

This should be compared against the third moment of $g(x, \beta')$, which is

$$\bar{y}_g^3 = 1 + 3/B(\delta) + 3/B(\delta)^2 \quad (10)$$

and against the third moment of the actual distribution.

The n th order moments of the actual distribution can be calculated for small n by reference to the definition in terms of an exponential-memory Gaussian process:

$$y = \frac{1}{T} \int_0^T (\phi_e(t)/\sigma_{\phi_e})^2 dt \quad (11)$$

By definition,

$$\begin{aligned} \bar{y}^3 &= \frac{1}{T^3} \sigma_{\phi_e}^{-6} \int_0^T \int_0^T \int_0^T E\{\phi_e(t) \cdot \phi_e(s) \cdot \phi_e(z)\} ds dt dz \\ &= \frac{1}{T^3} \int_0^T \int_0^T \int_0^T \{1 + 6 \exp(-4W_L|t-s|) \\ &\quad + 8 \exp[-2W_L(|t-s| + |s-z| \\ &\quad + |z-t|)]\} ds dt dz \\ &= 1 + \frac{12}{\eta} \left[1 - \frac{1}{\eta} (1 - e^{-\eta}) \right] \\ &\quad + \frac{48}{\eta^2} \left[1 + e^{-\eta} - \frac{2}{\eta} (1 - e^{-\eta}) \right] \end{aligned} \quad (12)$$

where

$$\eta = 4W_L T = 4/\delta$$

Figure 1 shows a comparison of the actual third moment of y (line 1), the third moment of $g(x, \beta')$ (line 2), and the third moment of $h(y)$ (line 4). On this basis, $h(y)$ appears to provide the best approximation over the entire range of δ .

III. Detector Performance

For uncoded communications, the error probability is simply the probability that $m_t \cdot D_t$ is negative. Assuming that N_t and $\cos(\phi_e(t))$ are independent, this is equal to the expected value (over the distribution of x) of the probability that $m_t \cdot D_t$ is negative conditioned on x :

$$P_e = \int_0^\infty f(x) \Pr \left\{ 1 - \frac{x}{2} < -N_t/A \right\} dx \quad (13)$$

And if R denotes the bit signal-to-noise ratio ($R = E_b/N_0 = S \cdot T/N_0$),

$$P_e = \int_0^\infty f(x) \operatorname{erfc} \left\{ \sqrt{2R} \left(1 - \frac{x}{2} \right) \right\} dx \quad (14)$$

This probability is shown in Fig. 2 for several different models, for δ in the range 0.1 to 10. The "+" on this figure

corresponds to the high-rate model calculation (Ref. 1). Line 1 was calculated using Tausworthe's interpolation formula, line 2 using $g(x, \beta')$, line 3 using $g(x, \beta)$, and line 4 using $h(x)$. Both the $h(x)$ calculations and Tausworthe's interpolation agree with the high-rate model for large δ .

We are now faced with interpreting and evaluating these models. For δ above about 0.3, the performance for $g(x, \beta)$ is rapidly diverging from $g(x, \beta')$ as a result of the second-moment misfit. Below this point, there is little difference between these and the low-rate model results. Ergo, there is little reason to use the unmodified $g(x, \beta)$ model to interpolate for medium-rate performance.

In Fig. 1, the third moments of $g(x, \beta')$ and $h(x)$ are respectively above and below the actual third moment. If we believe that, in the presence of identical second moments, the value of the third moment is an indication of the weight of the distribution at large values, or values which tend to cause errors, then we should expect that the actual error probability would fall between these two models. In Fig. 2, the Tausworthe interpolation falls outside this interval for almost all values of δ , implying that we should reject the hypothesis that Tausworthe's interpolator is accurate at the intermediate data rates. Further evidence to that effect can be obtained by interpreting the Tausworthe interpolation in terms of a density function on ξ , the most straightforward choice being the interpolation between the known densities at the high-rate and low-rate extremes. The second and third moments of this

fabricated density differ significantly from the moments of the actual distribution. The most reasonable candidate for an accurate approximation would appear to be calculations utilizing $h(x)$.

Figures 3, 4, and 5 compare these models for several other values of carrier loop SNR (ρ_L), and bit SNR (R). In the vicinity of 10^{-3} and higher error probability, typical of video missions, the calculated results differ little, and it is most reasonable to utilize the Tausworthe interpolation formula since it is simplest to compute. At lower error probability values, the models diverge significantly, and while these low error probabilities may not be interesting per se, for uncoded systems this divergence is interesting in that we may expect a similar divergence for *coded* systems at error probabilities which are of interest to deep space missions.

IV. Summary

This article has compared several methods of calculating noisy reference telemetry performance at intermediate data rates, i.e., where the data rate to loop bandwidth ratio is on the order of 0.1 to 10. In general, at bit error probabilities of about 10^{-3} , which have been typical of uncoded video missions, the interpolation formula proposed by Tausworthe (Ref. 3) provides acceptable answers. At low bit error probabilities, or for coded systems, evidence presented herein implies that the noisy reference calculation based upon the density function $h(y)$ in Eqs. (6) and (8) provides more accurate answers than previous techniques.

References

1. Lindsey, W. C., *Performance of Phase-Coherent Receivers Preceded by Bandpass Limiters*, Technical Report 32-1162, Jet Propulsion Laboratory, Pasadena, Calif., Sept. 1967.
2. Lindsey, W. C., and Blake, I. F., "Effects of Phase-Locked Loop Dynamics on Phase-Coherent Communications," in *Supporting Research and Advanced Development*, Space Programs Summary 37-54, Vol. III, Jet Propulsion Laboratory, Pasadena, Calif., Dec. 31, 1968, pp. 192-195.
3. Tausworthe, R. C., "Efficiency of Noisy Reference Detection," in *Supporting Research and Advanced Development*, Space Programs Summary 37-54, Vol. III, Jet Propulsion Laboratory, Pasadena, Calif., Dec. 31, 1968, pp. 195-201.
4. Grenander, U., Pollack, H. O., and Slepian, D., "The Distribution of Quadratic Forms in Normal Variates . . .", *J. Soc. Ind. Appl. Math.*, Vol. 7, No. 4, pp. 374-401, Dec. 1959.

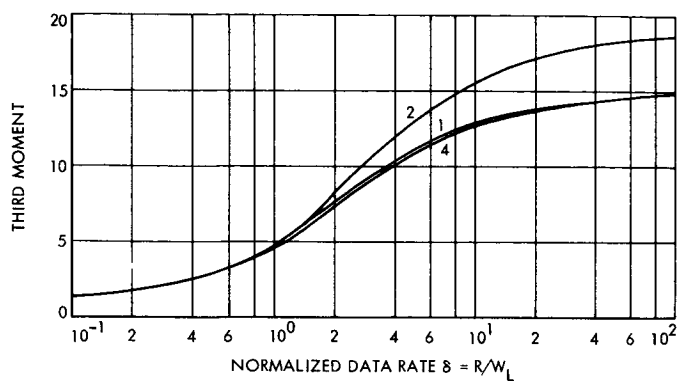


Fig. 1. Third moments of distribution

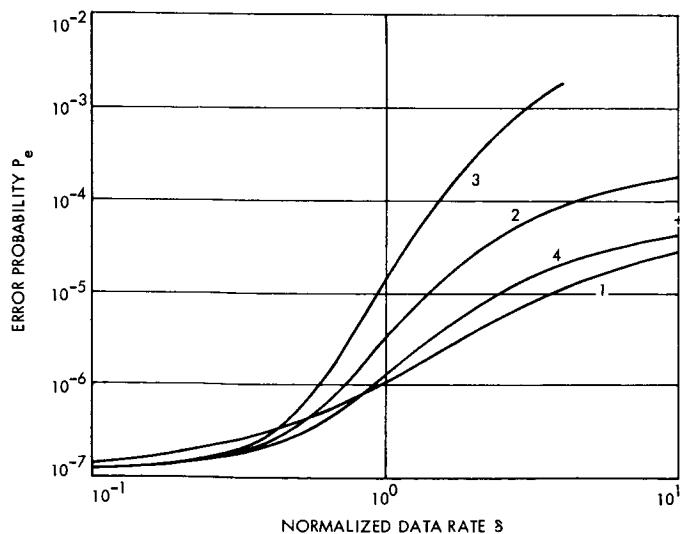


Fig. 2. Calculated error probability vs normalized data rate for loop SNR = 10, bit SNR = 15

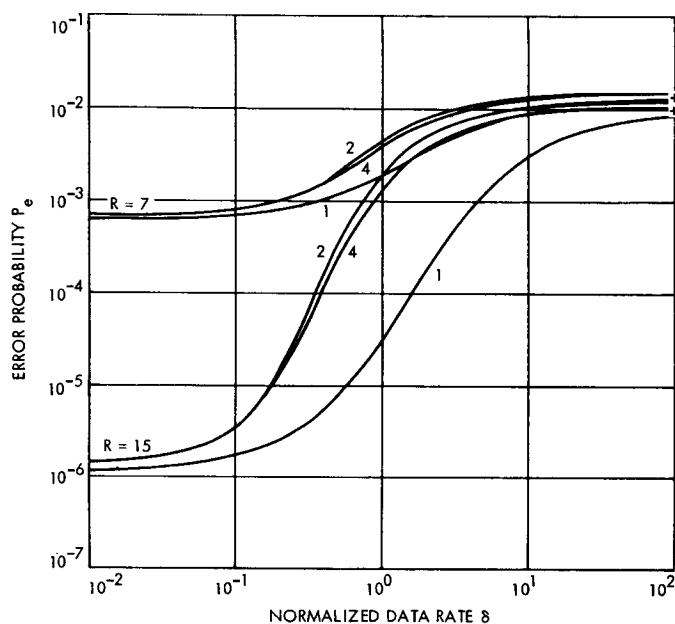


Fig. 3. Calculated error probability vs normalized data rate for loop SNR = 4, bit SNR = 7 and 15

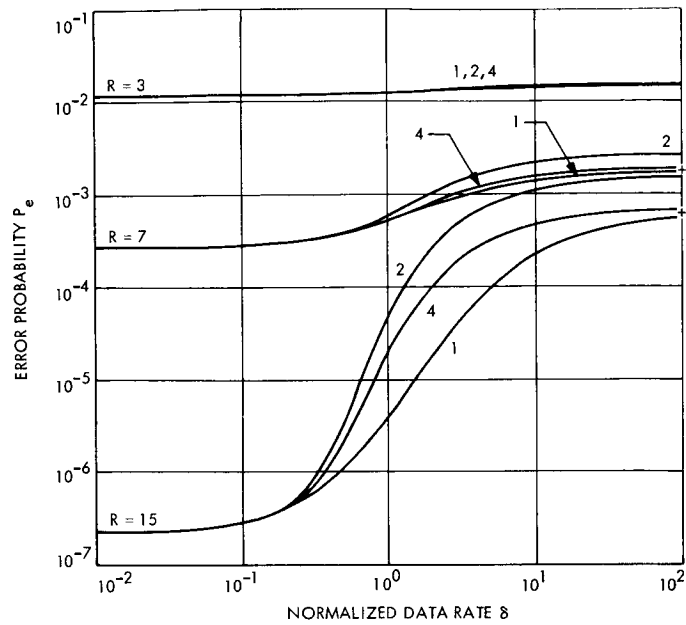


Fig. 4. Calculated error probability vs normalized data rate for loop SNR = 7, bit SNR = 3, 7, and 15

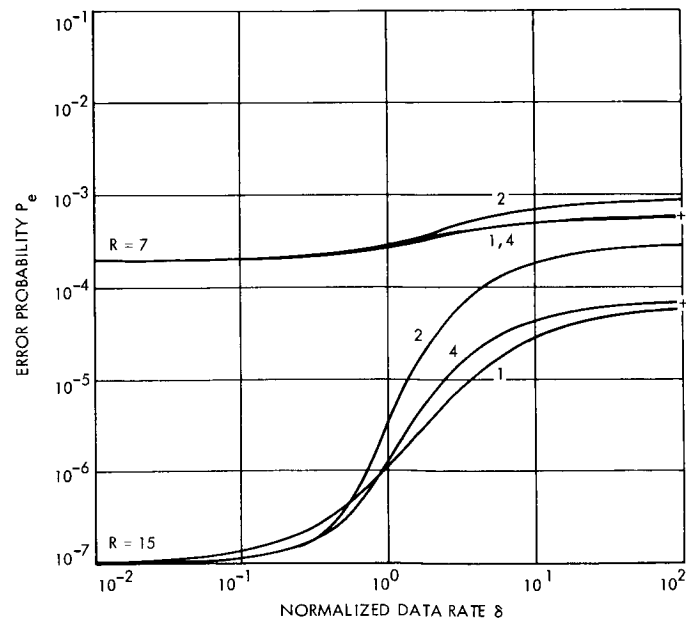


Fig. 5. Calculated error probability vs normalized data rate for loop SNR = 10, bit SNR = 7 and 15

64-Meter-Diameter Antenna Hydrostatic Bearing Runner Joint Leak Tests

G. P. Gale and H. P. Phillips
DSIF Engineering Section

Oil leaks from the hydrostatic bearing runner joint areas of the 64-m antenna installations at DSS 43 and DSS 63 have been the cause of concern since the erection of these antennas. This article describes the type of leak tests made on a model of the joint seal, the possible causes for leaks, and results after replacing the joint seals at DSS 63.

I. Introduction

The oil leaks from the hydrostatic bearing at the 64-m antenna installations at DSS 43 and DSS 63 are not serious enough to adversely affect the operation of the bearings at present, although considerable time and effort must be spent to prevent unsightly streaks down the outside of the pedestal. However, if the leaks are allowed to continue, the oil will soak into the grout under the runner and may cause it to fail. The leaks were observed primarily in the areas surrounding the runner joints, especially when a hydrostatic bearing pad was over a joint, indicating either a break in the seal or a plugging of the vent holes back into the reservoir.

The hydrostatic bearing runner forms the bottom of an oil reservoir for the bearing with the oil depth approximately 21.5–23 cm deep. The runner is made up of 11 equal segments of steel plates 17.75 cm thick and 1.12 m

wide to form a bearing 25.25 m in diameter. The joints between the segments are subject to the full bearing recess pressure, approximately 85 Kg per cm². The joint is designed so that leakage through the interface between the ends of adjacent segments goes into a seal cavity which is vented back into the reservoir outside of the high-pressure area. Hence, the seal between the segments must only withstand the pressure due to the depth of the oil plus the small pressure drop across the vent holes (see Fig. 1).

A model of the runner joint seal elements, arranged to duplicate the sealing problems, was constructed as a basis for determining the causes of the leaks and for devising a method of correction.

II. Test Method

The leak tests were made on a full-scale steel model of the joint seal part of the hydrostatic bearing runner section

joint. A hand-pump hydraulic actuator was used as a pressure source. A small sealed cavity was bolted in place over the joint to simulate the effect of the hydrostatic bearing pad pressure cavities. Collector pipes were positioned to cover the vent holes so the function of these holes could be observed. The head pressure of these collector pipes was about 9.5 cm of oil, as compared to 25.5–23 cm oil depth in the actual runner. The viscosity of the oil used in the hydraulic actuator at room temperature is slightly lower than the viscosity of the hydrostatic bearing oil at operating temperature. Therefore, the leak rates were slightly higher than for an actual joint.

The first series of tests was made with the joint between the runner sections bolted tightly together, metal to metal, as in an ideal runner joint assembly. The joint seal extrusion (Fig. 1) was fed through the wedge cavity before the seal support strip and wedges were installed. The joint seal extrusion was lifted into place by the seal support strip during assembly without stretching it. The ends of the joint seal extrusion were trimmed, with about 6 mm extending beyond the runner. The end caps and gaskets were placed as shown in Fig. 1. The 6-mm extensions of the joint seal extrusion were forced into the seal slot as the end caps were tightened.

When an oil pressure of approximately 140 Kg per cm² was applied to the joint, the combined weep rate (out of both weep collector pipes) was between 10 and 15 cc per min. In the actual hydrostatic bearing, this weepage is returned to the oil reservoir. There was no leakage past the joint seal extrusion to the bottom of the joint, and there was no leakage past the ends of the joint seal extrusion. The vertical cracks at the ends of the joint, which are normally covered by the reservoir walls, were left uncovered. There was slight weepage (too small to measure), but only when the oil at the joint was under pressure.

When the collector pipes over the weep holes were plugged, full hydrostatic bearing oil pressure existed across the joint seal extrusion. Under this condition there was no leakage past the joint seal extrusion to the area under the runner joint. However, there was a combined leakage rate of approximately 25 cc per min from the end cracks, which are normally covered by the reservoir wall.

The second series of tests was performed with the joint between the runner sections spaced apart by 0.025-mm shims. This condition approximates the condition of an actual runner joint, considering imperfections in manufacture and assembly. Under these conditions the combined weepage rate out of both weep collector pipes was

approximately 97 cc per min when an oil pressure of 100 ± 5 Kg/cm² was applied. With this high rate of flow, several pump strokes were required; it was difficult to maintain a steady pressure. There was no leakage or weepage past the joint seal extrusion under the runner joint, and there were no leaks past the ends of the joint seal extrusion. There was weepage out of the cracks at the ends of the joint (which are normally covered by the reservoir wall). However, this weepage was present only when pressure was applied and was too small to measure.

When the collector pipes over the weep holes were plugged, the leakage rate remained about 100 cc per min, but the oil squirted out of the end cracks, which now had a gap because of the 0.025-mm shim. There was no leakage past the joint seal extrusion to under the runner joint. Unplugging the weep hole collector pipes reduced the leakage out of the end cracks to a slight weep, as before.

The third series of tests was performed with the joint spaced apart 0.025 mm and with the seal support strip and wedges emplaced before the joint seal extrusion was pulled into place. The joint seal extrusion was cut to a length of 110 cm and was pulled through the seal cavity until the trailing end was flush with the edge of the runner. The joint seal extrusion stretched until approximately 25 cm extended out of the leading end before the trailing end was flush. The excess 25 cm was cut off flush with the edge of the runner. The joint seal extrusion did not appear to retreat into the slot. The end caps were emplaced, and the oil at the joint was pressurized to approximately 100 kg/cm² (1500 psi). There were no leaks past the joint seal to under the runner, and the amount of weeping at the end cracks was too small to be measured.

When the end caps were removed, it was found that the end of the joint seal extrusion, which had been pulled out and cut off flush, had retreated into the slot approximately 6 mm. There was indication of some leakage around the end of the joint seal extrusion. The trailing end had also retreated about 1.5 mm, but it had remained in contact with the end cap seal gasket, which had been extruded into the seal slot. When a slight force was applied to the ends of the joint seal extrusion (as could occur if room-temperature vulcanizing compound (RTV) was packed into the ends of the seal cavity), it caused the pulled end to retreat into the hole approximately 3.8 cm and the trailing end somewhat less. Therefore, if the ends of the seal slot were packed, the packing could extend beyond the weep holes and plug them. This would cause excessive leakage out of the end cracks and around the end of the joint seal extrusion as noted above.

III. Recommendations

The recommended assembly technique is as follows:

- (1) Feed the joint seal extrusion through the wedge and seal support strip hole.
- (2) Straighten the joint seal extrusion but do not stretch it. Position the joint seal extrusion so that it extends at least 5 cm beyond each side of the runner.
- (3) Lift the joint seal extrusion straight up into the seal cavity with the seal support strip.
- (4) Place the upper, center, and lower wedges under the support strip, forcing the joint seal extrusion vertically upward, into the seal slot, until the support strip just makes contact with the top of the wedge cavity. Do not force the support strip beyond this.
- (5) Cut off the ends of the joint seal extrusion so that it extends between 5 and 10 mm outside the runner joint.
- (6) Clean all traces of oil and dirt from the end cap seal area with a solvent.
- (7) Apply a limited amount of plastic sealing compound over the end of the wedges and the seal support strip.

Seal the slot area and the edge of the runner up to (and covering) the bottom edge of the reservoir wall.

- (8) While the plastic sealing compound is still soft, emplace the end caps and their gaskets and bolt them tight, forcing the 5-mm extension of the joint seal extrusion back into the runner joint seal slot.
- (9) After the end caps have been installed, apply a liberal amount of plastic sealing compound to the area between the reservoir wall and the end cap gasket to seal that area from any possible leakage from the crack between the runner sections left exposed in this area.

IV. Conclusion

Following these tests the hydrostatic bearing runner joint seals were replaced at DSS 63. When the seals were removed, it was discovered that the seal extrusion had retreated back into the seal slot and that the ends of the seal slot, including the weep passages, had been filled with a silastic material (Fig. 2). When the seals were replaced, rods were pushed into the weep holes to prevent any blockage. These rods were then removed and a flow check made to assure that the weep holes were open. No runner joint leaks have been observed at DSS 63 since the seals were replaced.

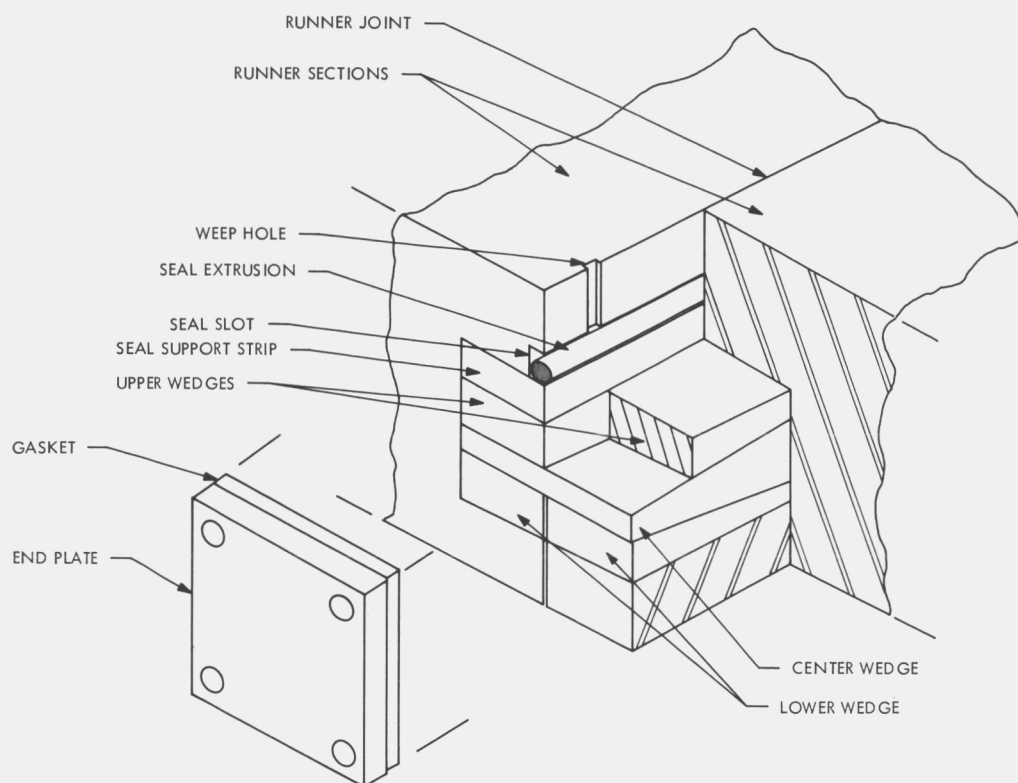


Fig. 1. Cutaway of runner joint showing joint seal

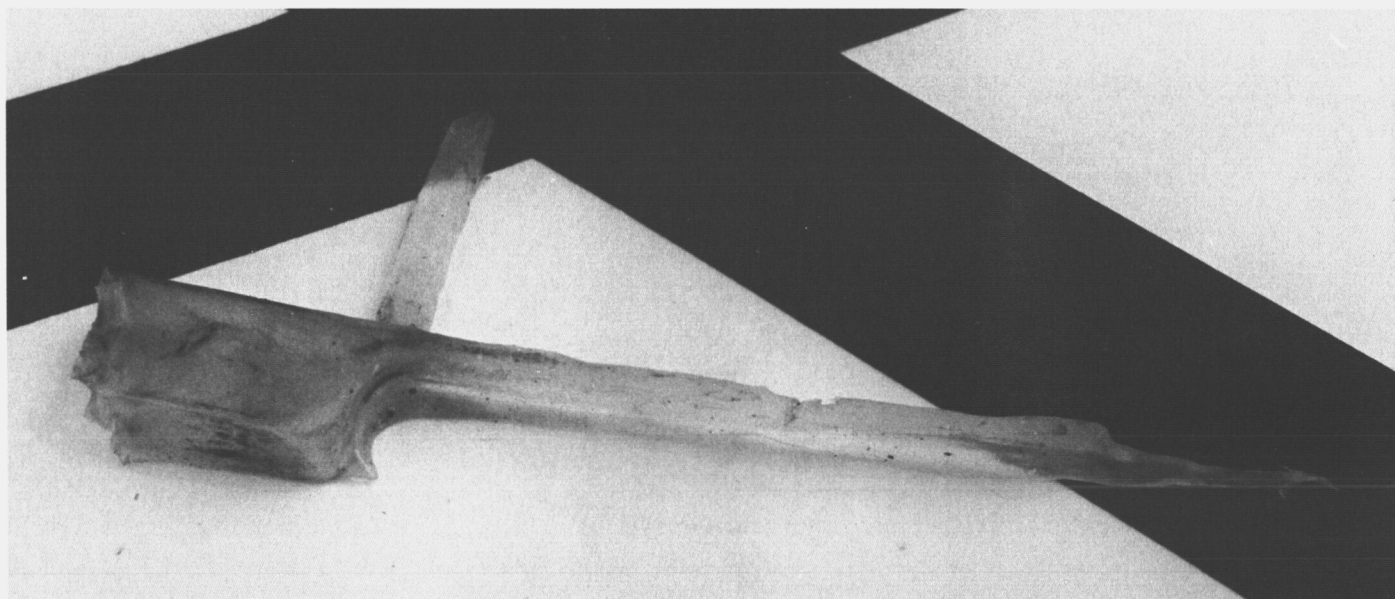


Fig. 2. Silastic seal plug removed from DSS 63

64-Meter-Diameter Antenna With New Braces: Installation Description and Computed Performance for Gravity Loads

V. B. Lobb and M. S. Katow
DSIF Engineering Section

The performance of the 64-m antenna was improved for gravity loading by addition of two reaction bars or braces in the elevation wheel assembly. The installation is described. The performance is delineated in RF gain loss curves vs elevation angle changes from the 45-deg setting position of the Cassegrainian RF system. The gain loss curves were analytically calculated using distortion data computed by the NASTRAN program, which was then best-fitted by the RMS program.

I. Introduction

Based on predictions (Ref. 1) of improved performance of the 64-m antenna for gravity loadings, new reaction bars or braces were added in the elevation wheel assembly. The joints were designed to allow the major portion of the installation to be made during the nontracking time each day, with the final assembly being made at a shut-down period. The uncommonly large sizes and weights of the parts created special problems which required unique solutions.

In Ref. 1, only the direct solutions from the NASTRAN structural computing program consisting of the symmetric and the antisymmetric gravity loadings were given. In other words, the *OH* and *OZ* gravity components of Fig. 1 of 1.0 values were used and their respective distortion rms values were computed. (For definitions of symbols used in Fig. 1, see Tables 1 and 2). For comparisons of the performance to the field RF calibrations, the distortion rms must be computed as changes from the 45-deg elevation

angle, which is the setting position of the surface panels of the paraboloid and the Cassegrainian RF system. Then, using the Ruze equation and the Radiation program, the performance degradation in dB may be computed.

II. Installation

The structural changes to the antenna were made by removing four existing knee bars and replacing them with two new braces (Fig. 49 of Ref. 1). For practical considerations, the design was modified, with the addition of another work point and cross bar to contain the resulting force component. The new braces (Fig. 2) and end joints (Fig. 3) are heavy structural members which weigh 1000 kg/m. These heavy weights and the need to field-drill 140 3.3-cm holes through material up to 7.6 cm thick required that work platforms be built and attached to the antenna. Because a large portion of the work was to be done without tracking interference, these work platforms were made of steel and left in place for 5 months. The site

crane was used to erect the brace joints, which weighed from 2 to 4 metric tons each. During the shutdown of DSS 14 for hydrostatic bearing regrout, a 90-ton, 200-ft truck crane was used to erect the main braces which weigh 16 metric tons each. The brace connects to the elevation bearing casting. This presented a problem in getting an acceptable bearing area on a rough casting. Welding was considered and deemed feasible but was rejected because potential weld and casting cracking was deemed too risky. A special fixture (Fig. 4) was designed which adapted a milling head to special ways, which were attached to the casting and allowed a bearing surface to be machined into the casting.

Difficulty in finding a large impact wrench was encountered in installing the 300 3.2-cm high strength bolts, which require 7500 newtons of torque. A cross check of final installed bolted force was made by measuring the nut rotation. Many of the bolts were tightened using a slugging wrench and the turn-of-the-nut method.

III. Analysis

The distortion rms error was computed (Ref. 2) for the 75-deg elevation angle, for example, as shown in Fig. 1, by using for the equivalent gravity loading, the sum of the symmetric gravity vector $0Z-0Z'$ plus the antisymmetric vector $0H-0H'$. The best fit paraboloid moves off center to a position, also illustrated in Fig. 1, where a phase center offset occurs. This results in additional gain loss over that of the distortion rms of the surface panel support points about the best fit paraboloid.

Although an axial displacement of the phase center also occurs, little or no gain loss results because of a focusing operation by a Z-axial movement of the subreflector. This is done presently at the 64-m site only for operation at X

and higher frequencies where there is a marked loss in gain by the axial defocused condition.

The Ruze gain loss equation used is

$$\text{Gain loss} = e^{-16 \pi^2 (\sigma/\lambda)^2}$$

where

σ = rms $\frac{1}{2}$ -pathlength error

λ = RF wavelength

For the phase center lateral offset, the Radiation program was used to compute the curve shown in Fig. 5.

Table 2 delineates the computations from the best fit paraboloid position, using for the basic phase center offset the calculated number for the 90-deg elevation case as described in Ref. 3.

IV. Analysis Results

To clearly define the effect of the structural modifications, the gain losses in equivalent rms distortion and dB of only the surface panel supporting points of the reflector structure were computed and delineated in Table 2 and by curves in Fig. 6. Figure 6 also shows the calculated curve for the premodification case.

For an additional step in improving the performance, the gain loss curve for zero lateral offsets is also shown. These theoretical values have not, as yet, been completely confirmed by field calibration. However, these corrections are practically feasible for the 64-m antenna since the tricone subreflector's lateral drives can be servoed with minor alterations. It should be noted that the resulting RF boresight direction changes must be compensated in the basic pointing system at the same time.

References

1. Katow, M. S., "210-ft-diam Antenna Reflector Upgrade Study—Phase 1," in *The Deep Space Network*, Space Programs Summary 37-62, Vol. II, pp. 109-113, Jet Propulsion Laboratory, Pasadena, Calif., Mar. 31, 1970.
2. Katow, M. S., and Schmele, L. W., "Antenna Structures: Evaluation Techniques of Reflector Distortions," in *Supporting Research and Advanced Development*, Space Programs Summary 37-40, Vol. IV, pp. 176-184, Jet Propulsion Laboratory, Pasadena, Calif., Aug. 31, 1966.
3. Katow, M. S., "64-m-Diameter Antenna: Computation of RF Boresight Direction," in *The Deep Space Network Progress Report*, Technical Report 32-1526, Vol. XIV, pp. 68-72, Jet Propulsion Laboratory, Pasadena, Calif., Apr. 15, 1973.

Table 1. Definition of symbols

<i>D</i>	rms distortion of surface panel support points
<i>F</i>	focus point of the best fit paraboloid
<i>L</i>	equivalent rms due to lateral offset of the phase center
<i>MM</i>	focal point offset from vertex
<i>NN</i>	RF phase center offset to focus of the best fit paraboloid
<i>OG</i>	full gravity vector
<i>O'G'</i>	full gravity vector
<i>OH</i>	antisymmetric gravity component at 45-deg elevation angle
<i>O'H'</i>	antisymmetric gravity component at 75-deg elevation angle
<i>OZ</i>	symmetric gravity component at 45-deg elevation angle
<i>O'Z'</i>	symmetric gravity component at 75-deg elevation angle
<i>PP</i>	RF phase center offset due to the Cassegrain system gravity deflections
<i>V</i>	vertex of the best fit paraboloid
<i>VV'</i>	vertex offset
<i>WW</i>	focal point offset from Z-axis of the basic coordinate system

Table 2. Best fit paraboloid data

Elevation angle, deg	X-rotation θ , rad	Y-offset VV' , cm	<i>MM</i> , cm	<i>WW</i> , cm	<i>PP</i> , cm	<i>NN</i> , cm	Focal length, M	RMS		Gain <i>D</i> , dB	Loss <i>L</i> , dB	Total gain loss, dB
								<i>D</i> , mm	<i>L</i> , mm			
90	-0.002815	-12.909	7.63	-5.28	2.65	7.92	27.11625	0.50	1.21	-0.14	-0.79	-0.93
75	-0.001782	-8.166	4.83	-3.34	1.68	5.02	27.11562	0.35	0.77	-0.07	-0.33	-0.40
60	-0.000821	-3.762	2.22	-1.54	0.78	2.32	27.11324	0.18	0.35	-0.018	-0.067	-0.09
30	0.000627	2.864	-1.70	1.16	-0.60	-1.76	27.10398	0.20	0.27	-0.022	-0.040	-0.06
15	0.001016	4.636	-2.75	1.88	-0.97	-2.85	27.09773	0.40	0.44	-0.087	-0.105	-0.19
0	0.001142	5.195	-3.09	2.10	-1.10	-3.20	27.09095	0.60	0.49	-0.20	-0.13	-0.33

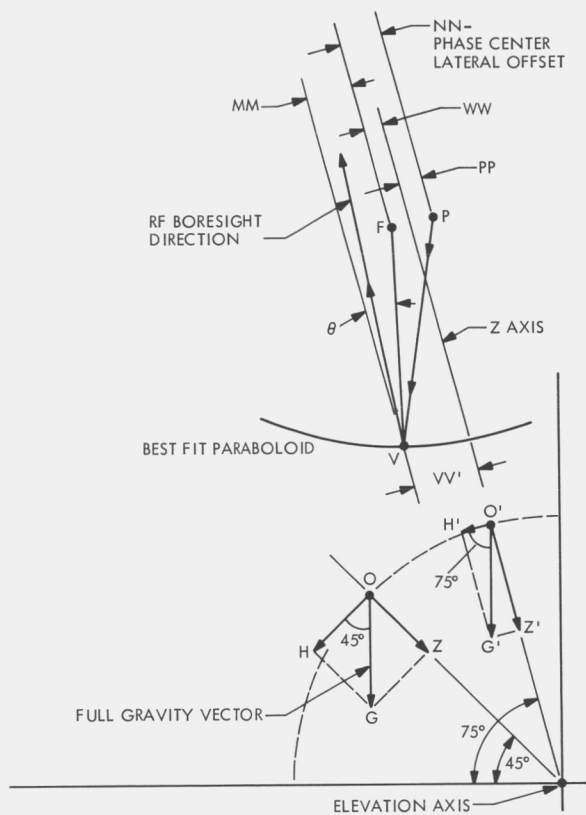


Fig. 1. The best fit paraboloid position and the gravity components

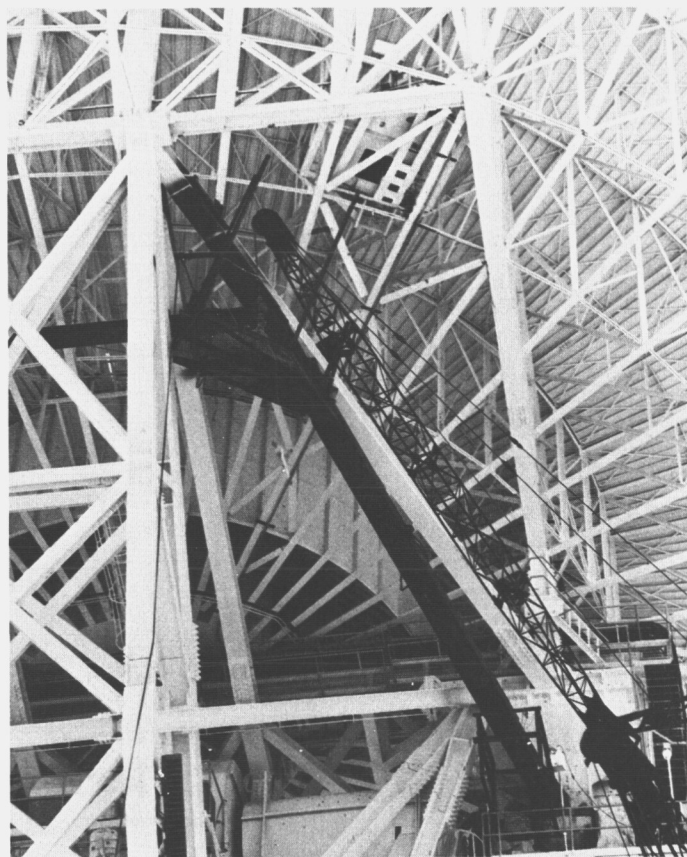


Fig. 2. New braces: 64-m-diam antenna



Fig. 3. New end joints: 64-m-diam antenna

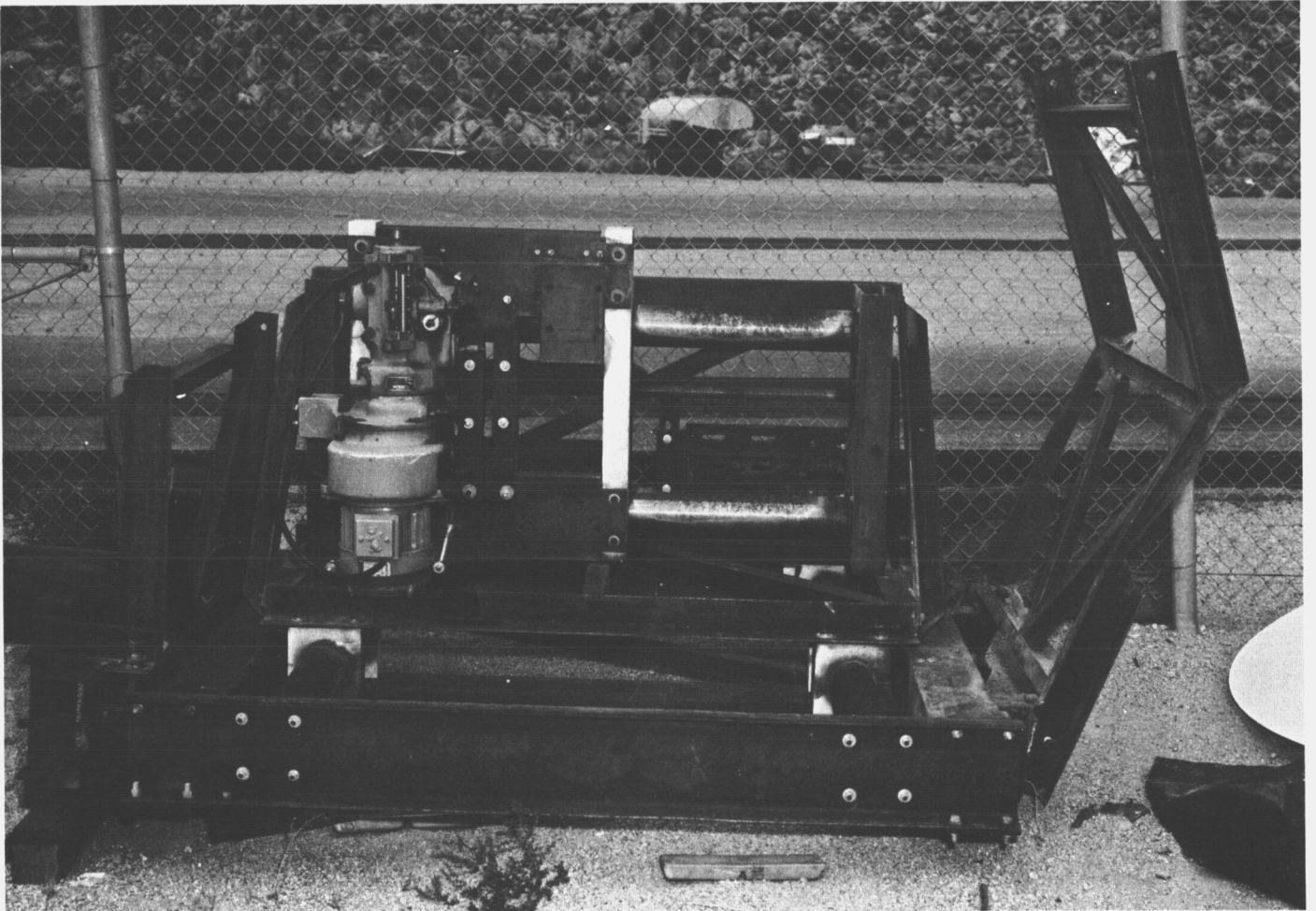


Fig. 4. Special fixture for milling elevation casting

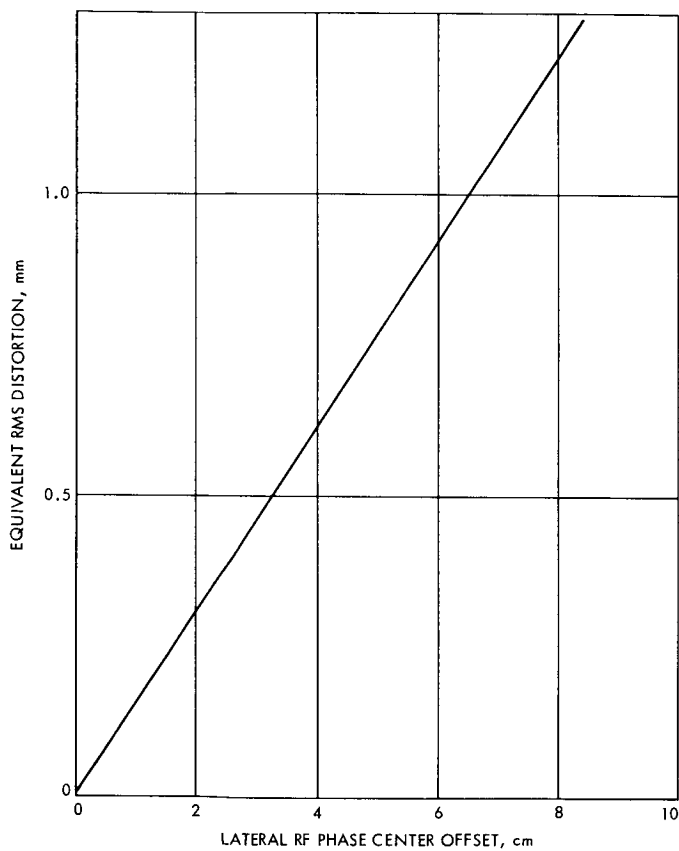


Fig. 5. RMS (equivalent) vs RF phase center offset

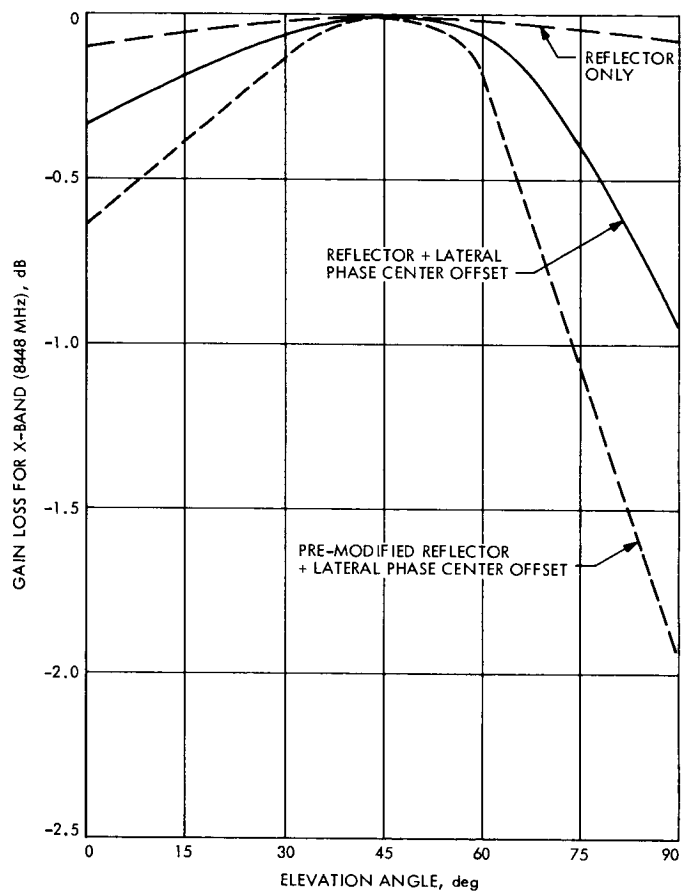


Fig. 6. Gain loss vs elevation angle

DSN Research and Technology Support

E. B. Jackson
R.F. Systems Development Section

The activities of the Development Support Group at Goldstone are discussed and progress noted on continuing efforts. Activities reported include planetary radar support for the MVM'73 missions, sky survey radio source activity, dual uplink carrier testing, testing 100-kW klystrons for use at DSSs 43 and 63, 400-kW transmitter testing of ignitrons and power supplies, support of DSS 14 400-kW transmitter, and very long baseline interferometry (VLBI) activity with National Radio Astronomy Observatory (NRAO), Effelsburg, Germany, and DSS 43.

I. Introduction

During the two months ending August 6, 1973, the Development Support Group utilized almost its entire resources in operation of the Venus Station (DSS 13) both as a supporting research and technology (SRT) test bed station and in its new role as the DSN High Power Transmitter Maintenance Facility. Only machine shop support for these operations and occasional special testing were conducted at the Microwave Test Facility.

II. Section 331 Support

Continuing support of the Mariner Venus/Mercury 1973 spacecraft mission, two Venus and eight Mercury

ranging missions were supplied with pseudonoise (PN) code and code timing signals transmitted to DSS 14 via the intersite microwave link. A total of 73 hours of data gathering was thus supported.

The development receiver which had been removed from DSS 14 for maintenance (Ref. 1) was reinstalled. The $\times 32$ multiplier in the receiver's local oscillator chain, whose output power had decreased by 6 dB, was replaced. A filter was designed, fabricated, and installed to reduce spurious signals being generated in the $\times 2$ multiplier which precedes the $\times 32$, and interstage attenuators were added to optimize overall performance. The receiver was reinstalled during the week ending July 15, 1973, and performance has been good since that time.

III. Section 333 Support

The station receiver (tuned to 2295 MHz), the 26-m antenna, a computing counter (HP-5360A) with a systems programmer (HP-5376A), an SDS-910 computer (for antenna pointing), a punched paper tape reader for timing and programming, a chart recorder, and a digital printer were interconnected to form an automated total power radiometer called a noise adding radiometer (NAR). Operating theory and a description of an earlier version of this radiometer are given in Ref. 2.

This automated system is used on weekends or on mid-night shifts when the station is normally closed. The 26-m antenna is placed into a fixed position (usually 180 deg Az and 80-87 deg El), and the NAR is started when the on-duty crew leaves the station. When the station is reopened the outputs of the chart recorder and digital printer are collected and forwarded to Section 333 for analysis. During this reporting period, a total of 434 hours of data was thus collected on radio sources passing through the fixed 26-m antenna beam.

IV. Section 335 Support

A. Dual Uplink Carrier Testing

With baseline performance established at an intermodulation product (IMP) level weaker than -180 dBm, long-term testing for stability evaluation continued. A total of 181 hours of testing was conducted during this period.

The diplexer which was removed in May 1973 because of increased noise and IMP was carefully examined under magnification. Hairline cracks were discovered on the interior broad wall surfaces of both hybrid sections. This particular diplexer was the prototype for all subsequent diplexers of this type, and the manufacturer tells us that it had fabrication seams where we observed the hairline cracks. Subsequent production models do not have these particular fabrication seams.

B. 100-kW Klystron Testing

It is planned to equip the two overseas 64-m antennas (DSSs 43 and 63) with 100-kW DSN transmitters. The klystrons to be used are Varian Associates Model X3060, originally manufactured in 1965 and 1966. They have been kept in controlled environment storage with periodic activation of the built-in vacuum pump and filament to ensure maintenance of internal vacuum.

During this last two-month period these tubes have undergone acceptance class testing in a special test fixture

designed and constructed for versatile testing of components of the 100/400-kW transmitters. Additionally, these klystrons were retuned to 2115 MHz (previously tuned to 2388 MHz) with an approximate instantaneous bandwidth of 10 MHz. Six klystrons were in storage and five of them have proved to be serviceable.

C. 400-kW Transmitter Testing

Whenever certain protective circuits on the 100/400-kW transmitters are actuated, the high-voltage dc (60–66 kV) is rapidly (less than 100 μ s) removed by short-circuiting the high-voltage dc power supply through a load resistor to prevent excessive current being drawn. The switch which effects this short circuit is an ignitron whose igniter is pulsed from the protective circuit.

The single ignitron used in this circuit at DSS 14 has proved to be marginal with regard to its ability to "hold off" normal operating high voltage without premature breakdown. To correct this difficulty, a new system employing two smaller ignitrons in series has been designed, fabricated, tested, and installed at DSS 13 for long-term operational evaluation prior to installation at DSS 14. This test installation was made during the week ending June 24, 1973.

The klystron focusing magnet, motor field and generator field excitation in the 100/400-kW transmitter system have been furnished by specially designed and built SCR power supplies. Recently, Hewlett Packard has introduced a line of similar power supplies which may prove suitable for this application (10 kW dc at voltages from 110 to 400 V). During the past two months several of these Hewlett Packard supplies have been undergoing evaluation at DSS 13 along with measurements of the transfer function of the entire high-voltage dc control system.

V. Section 422 Support

In support of the DSN High Power Transmitter Maintenance Facility, DSS 13 personnel removed the outer shell from an X-3075 klystron and repaired the input coaxial connector, which had become waterlogged. The klystron was then installed into the test fixture for acceptance testing. However, the tuning of the klystron cavities had shifted to the extent that neither DSS 13 personnel nor a representative from the manufacturer were able to retune the klystron, and it was returned to Varian Associates for repair.

To compensate, insofar as possible, for the loss of the 400-kW transmitter left inoperative by the loss of this

klystron, DSS 13 personnel modified a DSN 400-kW transmitter cabinet and installed a 100-kW klystron and associated magnet therein. This provides a 100-kW capability for spacecraft support, pending repair and return from Varian Associates of one of the 400-kW klystrons.

The 10-W transistorized S-band driver amplifier was removed from the DSS 13 400-kW 2388-MHz transmitter and used to replace a defective unit at DSS 14. This exchange, which was effected by DSS 13 personnel, enabled the planetary ranging in support of MVM⁷³ to continue at DSS 14.

VI. Section 825 Support

A. Very Long Baseline Interferometry (VLBI)

By special arrangement we provided 58 hours of cooperative VLBI observations of the radio sources in Table 1. The first series of observations was cooperative with the

100-m antenna at Effelsburg, Germany, and the 43-m antenna at NRAO in Greenbank, West Virginia. The second series of observations, reduced to only six hours by failure of both maser/refrigerators at DSS 43, was cooperative with DSS 43 only. Preliminary analysis of the data from the first series verifies the presence of fringes between DSS 13 and NRAO and between DSS 13 and Effelsburg. The data from the second series have not yet undergone examination.

B. Pioneer 10 and 11 Spacecraft Support

The NAR described earlier is also used to obtain measurements of the radiation from the planet Jupiter and certain radio source calibrators to provide a comparison set of radiation measurements against which the measurements telemetered back by Pioneer 10 and 11 can be compared. During this two-month period, 152 hours were expended observing the targets tabulated in Table 2, measurements being made at 2295 MHz.

References

1. Jackson, E. B., "DSN Research and Technology Support," in *The Deep Space Network Progress Report*, Technical Report 32-1526, Vol. XVI, pp. 102-104, Jet Propulsion Laboratory, Pasadena, Calif., Aug. 15, 1973.
2. Batelaan, P. D., Goldstein, R. M., and Stelzried, C. T., "A Noise-Adding Radiometer for Use in the DSN," in *The Deep Space Network, Space Programs Summary 37-65, Vol. II*, pp. 66-69, Jet Propulsion Laboratory, Pasadena, Calif., Sept. 30, 1970.

Table 1. VLBI observations

Radio source	Cooperating stations (in addition to DSS 13)
3C84	Effelsburg, NRAO
3C274	↓
3C279	
3C345	
3C373	
CTA-21	
DW-0742+10	
P1347-03	Effelsburg, NRAO
3C345	DSS 43
3C454	↓
CTA102	
NAR 0512	
BL LAC	
2145+06	
0048-09	
0332-403	
0202-17	
0122-00	
0438-43	
1633+38	
0022-42	DSS 43

Table 2. Sources observed with NAR at 2295 MHz

3C48	3C286
3C123	3C309.1
3C138	3C318
3C147	3C348
3C218	3C353
3C274 (Virgo A)	Jupiter
3C283	NGC 7027

Precise Measurement of Spacecraft Signal Power

J. W. Newton
Communications Systems Research Section

The precision signal power measurement (PSPM) technique is a computer-based method for the automatic measurement of signal powers at the standard DSN receiver. Using sampled-data techniques, a table of spectral estimates is created from which accurate signal/noise ratios are derived and the signal strength computed. The process is continuous, fast, and automatic. Recent improvements give an extended dynamic range running from below -185 dBm to above -125 dBm and accuracies within 0.2 dB over this range.

I. Introduction

Precise and continuous knowledge of the power of received spacecraft signals becomes increasingly important as communication ranges lengthen. Tradeoff of sensitivity margins for range, data rate, or both are possible if the received power can be precisely known and continuously monitored.

The PSPM technique has been shown (Ref. 1) to be capable of an accurate, continuous measure of received power over a range of 30 – 35 dB, extending from below receiver threshold up to the vicinity of -150 dBm. Its accuracy over this range approaches 0.25 dB. The stability of measurements is closely predictable (Ref. 2) and has been verified in practice.

Simplifications and improvements have been made in the original system both in hardware and software. Field trials at the Mars Deep Space Station (DSS 14) have

shown the desirability of operating the system from the 50 -MHz intermediate frequency (IF) point rather than from the 10 MHz IF. The mechanism limiting the strong-signal end of the dynamic range has been identified and this limitation overcome, now permitting the range to extend above -130 dBm.

II. System Improvements

Field testing of the initial PSPM system at DSS 14 indicated the advisability of moving the measurement point further upstream in the standard Deep Space Network receiver, out of the area of AGC-controlled amplification. While the PSPM technique is inherently insensitive to gain variations (since it is specifically a measure of signal-to-noise ratio and free of gain-stability constraints), some of the minor nonlinearity discovered at this time was attributable to system parameters changing with the controlled gain. Also, a fully automatic system

requires either the measurement or the tracking of system noise temperature, and this increases the requirements for gain stability. The increased sensitivity of the PSPM to additive noise when operating in the strong-signal region was recognized at this time, as was the necessity for local control of a semifixed gain.

As a result, the decision was made to adapt the PSPM hardware to operate at 50-MHz IF conditions and to connect the equipment to the standard receiver through a directional coupler in the input lead from the antenna.

In Fig. 1 the received spacecraft signal is amplified, down-converted to a 50-MHz intermediate frequency and reamplified before leaving the antenna for the long cable run to the control room. Here, before entering the remainder of the DSN receiver, a small sample is extracted by means of a hybrid coupler for the mutual use of the noise-temperature measurement and the PSPM equipments. It is once more down-converted within the PSPM, band-limited in the anti-aliasing filter, and then sent to the computer for processing. The PSPM now shares with the DSN noise-temperature measurement equipment a connection accurately monitoring antenna signal-to-noise ratio and suitably isolated from downstream perturbations.

The anti-aliasing filter of the PSPM set has been changed from a 2-pole Butterworth to a 6-pole Chebyshev. The sharp cutoff of the new filter makes the bandwidth useable out to 22 Hz and makes it unnecessary to consider any foldover above the 25-Hz sampling bandwidth. The passband ripple of 0.1 dB has been undetectable in the spectra produced.

The initial PSPM computer program first measured the receiver bandwidth shape using a long noise run, and this shaping function was then used to divide all measurement runs, thus normalizing the system frequency response. This precaution has been found unnecessary in practice and has been omitted from recent programs. The upstream frequency-shaping factors in the DSN reception system—maser, preselector, mixer, preamplifier—have such broadband responses that their effect on the 25-Hz passband of the PSPM has been imperceptible. The only noticeable shaping is contributed by the aliasing filter, which is essentially flat over the majority of its range. The sharp cutoff of the new filter also improves performance by extending the flat portion further into the upper range.

The incoming signal may be assumed to appear in the receiver passband precisely at 50 MHz since the receiver operates so as to phase-lock the signal to this frequency using a local reference. If the sampling process is con-

trolled by a pulse synchronously derived from this same reference, then the signal's position in time and frequency is rigidly fixed with respect to this reference and may be shifted across the sampled spectrum by adjustment of a second local oscillator (LO). With the second LO set for 49,999,987.50 Hz, the received signal falls within the center of the derived power spectrum, namely at 12.5 Hz. The signal area is now defined quite closely. Presently 10% of the spectrum is assigned to signal area and 5% at each end of the spectrum discarded to avoid end effects, leaving 80% of the record to be used to define the mean noise spectral density. This amounts to almost a doubling of the stability of the process compared to the previous practice of dividing the spectrum fifty-fifty between signal and noise regions.

The laboratory testbed generator has been modified and upgraded to reflect this change in design. The stable noise source has been reduced in power, band-shaped, and suitably shielded from extraneous noise pickup to approximate the frequency, power level, and bandwidth seen at the measurement point in the Block III DSN receivers. The 50-MHz signal source is simulated by a frequency synthesizer operating at a low output power level. These noise and signal generators have been tested for stability and the entire system tested for linearity and isolation. Signal-to-noise ratios of high accuracy may be generated by mixing in a hybrid transformer appropriate increments of signal and noise obtained from step attenuators connected to these generators.

The interim PSPM set is a new design employing considerable local gain at 50 MHz and at baseband, and care has been taken to minimize the addition of noise at either frequency band. The set has been carefully tested to assure good gain linearity over the expected operating range.

Preliminary measurements at Goldstone indicate that the new PSPM set meets all practical requirements and that the new testbed generator correctly models the behavior of the DSN receiver front end.

III. Range Extension

Concurrently with these changes and improvements, effort was expended to identify and overcome the mechanism blocking the upward extension of the dynamic range of the PSPM technique. As the initial PSPM system was operated in the range above -150 dBm, the process seemed to approach a limit asymptotically, and no manipulation of program or hardware materially improved upon this limit.

The PSPM employs techniques specifically developed to work best in the weak signal region. At the weak signal limit the process can be seen to disintegrate as the signal records become statistically indistinguishable from the adjacent noise records. In the strong-signal region, no such obvious mechanism operates to limit the measurement process. In the investigation of the strong-signal limiting effect, extensive use was made of output line-printer histograms of the spectra under study. In the strong-signal case two effects were observed: (1) the presence of a perceptible ripple superimposed upon the noise records, and (2) insufficient resolution in a 24-bit word to characterize adequately noise records of small amplitude.

The observed ripple arises from a basic property of the Fourier transform when it is applied to data containing a strong periodic signal observed for a limited period of time. This describes the PSPM strong-signal case precisely. The technique begins to depart from linearity as the signal record begins to predominate over the adjacent noise records. The Fourier transform of such a signal will possess $\sin x/x$ ripples adjacent to the signal record which swing above and below zero. The presence of this ripple will be obscured if the signal is mixed with sufficient noise, and the power in the spectral noise records will bias the ripple above the baseline. As these 'aids' disappear with increasing signal, the ripple will constitute the majority of the noise record; since its amplitude does not change, the PSPM process appears to limit.

This ripple effect is removed from the PSPM system by controlling the location of the signal record within the derived power spectrum and by evaluation of the transform at those points in the spectrum where the ripple has nulls. If the number of frequency evaluation points of the discrete Fourier transform is chosen to equal the number of lags over which the original sampled correlation table was taken, then the nulls will occur at a frequency spacing equal to the Nyquist frequency divided by the number of frequency points. Arranging the second LO offset from 50 MHz to be equal to some integral multiple of this fre-

quency spacing will put the totality of the signal power into one signal record; the nulls will fall at the adjacent points and the ripple will disappear.

The remaining small nonlinearities were removed by optimizing the mathematical resolution, particularly in the transform subroutine. A 24-bit fixed-point single-precision computational capability will encompass the 60-dB range of the improved PSPM program, but no loss of significance can be permitted. Such a loss occurred in the use of the cosine subroutine. To obtain the desired strong-signal performance it was necessary to round off the cosine arguments, to modify the subroutine itself to round off, and to do similar fine-tuning throughout the transform computation. For any future program a floating-point capability would be more desirable.

With the changes noted—optimized mathematical computation, synchronous sampling, and the null-cancellation technique—the PSPM system now makes stable, accurate measurements into the region above -130 dBm.

IV. Summary

The PSPM interim set has been improved by moving the operating frequency to 50 MHz and by removing internal noise and gain compression. The new operating frequency eliminates effects attributable to the AGC-controlled stages within the DSN receiver. A measurement testbed has been provided which models the performance of the DSN receiver and permits testing and development to proceed in the laboratory under field conditions. The sampling of data is now accurately timed by pulses synchronous with the station frequency base. By arranging that these pulses are also coherent with the sampling computations and with the frequency offset, the dynamic range of the system has been extended from below receiver threshold to above -130 dBm under one set of operating conditions. The dynamic range now extends over a 60-dB interval.

References

1. Newton, J. W., "Digital Device Development: Precise Measurement of Spacecraft Signal Power," in *The Deep Space Network*, Space Programs Summary 37-58, Vol. II, pp. 42-50, Jet Propulsion Laboratory, Pasadena, Calif., July 31, 1969.
2. Winkelstein, R., "Precision Signal Power Measurement," in *JPL Quarterly Technical Review*, Vol. 2, No. 2, pp. 18-24, Jet Propulsion Laboratory, Pasadena, Calif., July 1972.

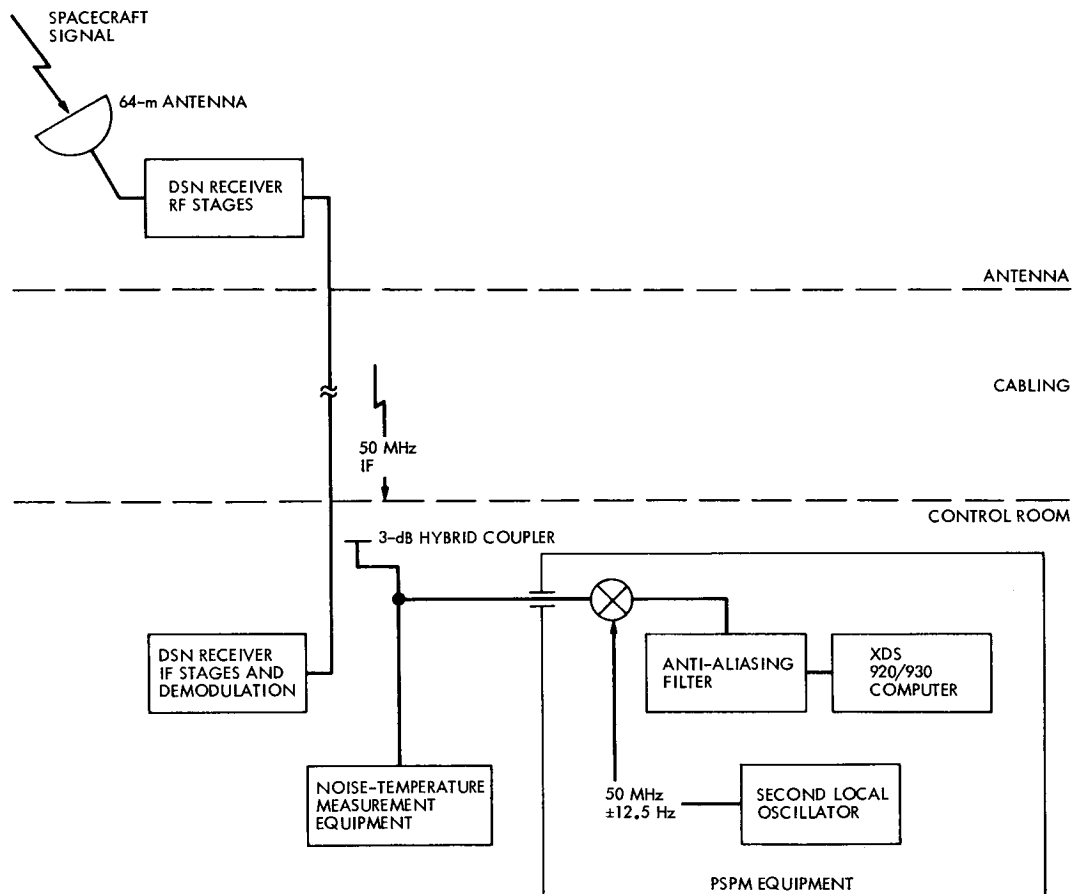


Fig. 1. PSPM equipment and measurement point

Dual-Carrier Intermodulation Caused by a Zero-Memory Nonlinearity

C. A. Greenhall

Communications Systems Research Section

Intermodulation products of a dual carrier distorted by a zero-memory nonlinearity F are calculated. Conversely, given certain of the intermodulation (IM) coefficients, the odd part F_o of the nonlinearity can be recovered. If the coefficients decrease fast enough, then F_o is analytic. The value of F_o is explicitly calculated for two cases of exponentially decreasing intermodulation products.

I. Introduction

This report is part of a study of intermodulation products (IMPs) which have been observed in dual-carrier tests at DSS 14 (Ref. 1). The main feature of the data on IMP amplitudes is that the amplitude of the n th IMP (counting away from the dual-carrier midfrequency) falls off exponentially with n . The data on the dependence of IMP amplitude on carrier power are much more tenuous.

It has been proposed that the IM distortion can be accounted for by nonlinear current-voltage characteristics of metal oxide contacts at bolted joints in the antenna structure. The present article describes analytically what sort of zero-memory characteristics could give rise to the observed IMP data. No physical assumptions are made.

The main mathematical tool is Chebyshev transform inversion, as described by N. Blachman (Ref. 2). This tool was created for the study of harmonic distortion, but we will see that it is also very useful for the study of IM distortion.

II. Formulas for Intermodulation Products

Given a zero-memory nonlinearity $y = F(x)$, $-L < x < L$, let the input be the symmetric dual carrier

$$\begin{aligned}x(t) &= \frac{1}{2} v (\cos \omega_1 t + \cos \omega_2 t) \\&= v \cos \omega_+ t \cos \omega_- t\end{aligned}$$

where

$$0 \leq v < L$$

$$0 < \omega_1 < \omega_2$$

$$\omega_+ = \frac{1}{2}(\omega_1 + \omega_2)$$

$$\omega_- = \frac{1}{2}(\omega_2 - \omega_1)$$

The output is then

$$y(t) = F(v \cos \omega_+ t \cos \omega_- t)$$

If $-L < v < L$ and F , let us say, is bounded and Borel measurable on $[-v, v]$, then the function $F(v \cos \theta \cos \phi)$ of the variables θ and ϕ has a double Fourier series:

$$F(v \cos \theta \cos \phi) \sim \sum_{\mu=-\infty}^{\infty} \sum_{\nu=-\infty}^{\infty} c_{\mu\nu}(v) \cos(\mu\theta + \nu\phi)$$

where

$$c_{\mu\nu}(v) = (4\pi^2)^{-1} \int_{-\pi}^{\pi} \int_{-\pi}^{\pi} F(v \cos \theta \cos \phi) \cos(\mu\theta + \nu\phi) d\theta d\phi$$

The IMP of index $(\mu, \nu) \neq (0, 0)$ is

$$2c_{\mu\nu}(v) \cos(\mu\omega_+ + \nu\omega_-)t$$

The IMPs with which we are concerned are

$$2c_{1, 2n+1}(v) \cos(\omega_2 + n(\omega_2 - \omega_1))t, \quad n = 1, 2, \dots$$

(Note that $c_{1, 2n} = 0$.)

Write f_o to mean the odd part of a function f ; that is,

$$f_o(x) = \frac{1}{2}(f(x) - f(-x))$$

After exploiting symmetries, we get

$$c_{1\nu}(v) = (1/\pi^2) \int_{-\pi}^{\pi} d\phi \cos \nu\phi \int_0^{\frac{1}{2}\pi} d\theta \cos \theta F_o(v \cos \theta \cos \phi) \quad (1)$$

III. Inversion of the Mapping $F_o \rightarrow \{c_{1\nu}(v)\}$

We would like to deduce properties of F from properties of the $c_{1\nu}(v)$. Equation (1) shows that we can get information about only the odd part of F .

Let us adopt some notation for the inner integral of Eq. (1). For $n = 0, 1, 2, \dots$, define an operator T_n by

$$(T_n f)(x) = (2/\pi) \int_0^{\frac{1}{2}\pi} f(x \cos \theta) \cos n\theta d\theta \quad (2)$$

Blachman (Ref. 2) calls this the n th-order Chebyshev transform. (However, he integrates from 0 to π ; the definition above makes T_0 and T_1 one-one.) Then

$$c_{1\nu}(v) = (2\pi)^{-1} \int_{-\pi}^{\pi} (T_1 F_o)(v \cos \phi) \cos \nu\phi d\phi \quad (3)$$

is just half the ν th cosine coefficient of $(T_1 F_o)(v \cos \phi)$; i.e.,

$$(T_1 F_o)(v \cos \phi) \sim 2 \sum_{\nu=1}^{\infty} c_{1\nu}(v) \cos \nu\phi \quad (4)$$

Thus, if we can sum the series in Eq. (4), we can get $T_1 F_o$. Then, as Ref. 2 shows, F_o can easily be obtained from $T_1 F_o$. Let us make precise the information we need here. Denote by B_v the space of bounded Borel measurable functions on $[-v, v]$, and by A_v the space of functions analytic in a neighborhood of $[-v, v]$. Then T_n takes B_v and A_v into themselves.

Proposition 1. (a) If $f, g \in B_v$ and $T_1 f = T_1 g$ almost everywhere, then $f = g$ almost everywhere.

(b) $T_1 : A_v \rightarrow A_v$ has a two-sided inverse $U_1 : A_v \rightarrow A_v$, given by

$$(U_1 f)(x) = \int_0^{\frac{1}{2}\pi} (tf(t))'(x \cos \theta) d\theta \quad (5)$$

(c) If $f \in B_v$ and $T_1 f \in A_v$, then f is almost everywhere equal to the analytic function $U_1 T_1 f$.

The notation in Eq. (5) means that the function $(tf(t))'$ is to be evaluated at $t = x \cos \theta$. Proposition 1 is proved in the Appendix.

We know now that if $T_1 F_o$, as determined by Eq. (4), is analytic on $[-v, v]$, then F_o is also analytic on $[-v, v]$, and can be got by applying U_1 to $T_1 F_o$.

Fortunately, the IMP data indicate that the $c_{1\nu}$ decay exponentially with ν . This is just the condition we need to show that $T_1 F_o$ is analytic on $[-v, v]$.

Proposition 2. Let f be a bounded Borel measurable function on $[-1, 1]$. Then f is (essentially) analytic on $[-1, 1]$ if and only if the coefficients

$$c_\nu = (2\pi)^{-1} \int_{-\pi}^{\pi} f(\cos \phi) e^{-i\nu\phi} d\phi \quad (6)$$

satisfy

(\star) $|c_\nu| \leq A\rho^{|\nu|}$, $-\infty < \nu < \infty$, for some A and ρ with $A > 0$, $0 < \rho < 1$.

Proof. Let $p(w) = (w + w^{-1})/2$.

Let f be analytic in a neighborhood Ω of $[-1, 1]$. Define $g(w) = f(p(w))$, $w \in \Omega$. Then g is analytic in an annulus $G_r = \{w: r^{-1} < |w| < r\}$, and so has a Laurent series that converges there. Since $g(e^{i\phi}) = f(\cos \phi)$, the c_ν are the Laurent coefficients of g . Hence

$$\sum_{-\infty}^{\infty} |c_\nu w^\nu| < \infty \text{ for } r^{-1} < |w| < r$$

This implies (\star).

Conversely, assume (\star). Define

$$g(w) = \sum_{-\infty}^{\infty} c_\nu w^\nu$$

Then again g is analytic in some annulus G_r , and $g(e^{i\phi}) = f(\cos \phi)$. If $|w| = 1$ then $g(w) = g(w^{-1})$. By analytic continuation, this must hold everywhere in G_r . Since

$$(z + i\sqrt{1-z^2})(z - i\sqrt{1-z^2}) = 1$$

it follows that

$$g(z + i\sqrt{1-z^2}) = g(z - i\sqrt{1-z^2}) \quad (7)$$

for all $z \in p(G_r)$, a region that contains $[-1, 1]$. Thus Eq. (7) defines a function $f^*(z)$ on $p(G_r)$ such that $f^* = f$ on $[-1, 1]$. The function f^* is analytic except possibly at 1 and -1 , but since f^* is continuous, it is analytic at 1 and -1 also.

Letting $f(x) = (T_1 F_o)(vx)$ in Proposition 2 and then applying Proposition 1, we have shown

Proposition 3. For a fixed dual-carrier amplitude v , assume that the IM coefficients $c_{1\nu}(v)$ of the zero-memory characteristic F decay at least as fast as an exponential ρ^ν , $0 < \rho < 1$. Then the odd part F_o is completely determined on $[-v, v]$ and is analytic on $[-v, v]$.

The function F_o is obtained by summing the series in Eq. (4) and then applying the inverse Chebyshev transform U_1 .

Proposition 3 is a worthwhile result if only because it gives us a condition for F_o to be smooth.

IV. Calculation of the Zero-Memory Characteristic Assuming Exponentially Decreasing IM Coefficients

The data point to the hypothesis

$$|c_{1\nu}(v)| = A\rho^\nu, \quad \nu = 1, 3, 5, \dots$$

where $A > 0$ and $0 < \rho < 1$. We have no information about the signs of the $c_{1\nu}$, that is, about the phases of the IMPs relative to the carrier components. Let us take two cases, namely

$$\text{Case 1. } c_{1,2n+1}(v) = A\rho^{2n+1}$$

$$n = 0, 1, 2, \dots$$

$$\text{Case 2. } c_{1,2n+1}(v) = (-1)^n A\rho^{2n+1}$$

and calculate F_o in each case. Fortunately, each F_o is an elementary function. Put $f_o(x) = F_o(vx)$, $-1 \leq x \leq 1$. Then $(T_1 f_o)(x) = (T_1 F_o)(vx)$.

Take Case 1. By Eq. (4),

$$(T_1 f_o)(\cos \theta) = 2A \sum_{n=0}^{\infty} \rho^{2n+1} \cos(2n+1)\theta$$

$$= 2A\rho(1-\rho^2) \cos \theta / [(1+\rho^2)^2 - 4\rho^2 \cos^2 \theta]$$

$$(T_1 f_o)(x) = Abx/(a^2 - x^2)$$

where

$$a = (1 + \rho^2)/(2\rho), \quad b = (1 - \rho^2)/(2\rho) \quad (8)$$

By Proposition 1,

$$f_o(x) = (U_1 T_1 f_o)(x)$$

$$= 2Aa^2b \int_0^{\frac{1}{2}\pi} (a^2 - x^2 + x^2 \sin^2 \theta)^{-2} x \cos \theta d\theta$$

After doing the integration and returning to F_o , we get

$$F_o(x) = (Ab/a) \Phi(x/(av)), \quad -v \leq x \leq v \quad (9)$$

where

$$\Phi(x) = (1-x^2)^{-3/2} \text{Sin}^{-1}x + (1-x^2)^{-1}x \quad (10)$$

It makes sense to put $M = Ab/a$, $x_o = av$. Since $F_o(x) = M\Phi(x/x_o)$ for $-v \leq x \leq v$, we can compute $c_{1v}(v)$ in the form $A\rho^v$ for any lesser v by solving for A and ρ in terms of M and v/x_o .

Case 2 is similar, except that now

$$(T_1 f_o)(x) = Aax/(b^2 + x^2)$$

$$F_o(x) = (Aa/b) \Psi(x/(bv)), -v \leq x \leq v \quad (11)$$

$$\Psi(x) = (1 + x^2)^{-3/2} \sinh^{-1} x + (1 + x^2)^{-1} x \quad (12)$$

We collect our calculations:

Proposition 4. Assume Case 1 for a particular v . Then $F_o(x) = M\Phi(x/x_o)$, $-v \leq x \leq v$, where

$$M = A(1 - \rho^2)/(1 + \rho^2)$$

$$x_o = v(1 + \rho^2)/(2\rho)$$

For all lesser v , Case 1 also holds, with

$$A = M(1 - (v/x_o)^2)^{-1/2}$$

$$\rho = (v/x_o)/[1 + (1 - (v/x_o)^2)^{1/2}]$$

The same is true for Case 2, but Φ is replaced by Ψ and the formulas are

$$M = A(1 + \rho^2)/(1 - \rho^2)$$

$$x_o = v(1 - \rho^2)/(2\rho)$$

$$A = M(1 + (v/x_o)^2)^{-1/2}$$

$$\rho = (v/x_o)/[1 + (1 + (v/x_o)^2)^{1/2}]$$

The two cases are qualitatively different, since Φ blows up at ± 1 , but Ψ is analytic on the whole real line.

V. Conclusions

If we know the whole sequence of IM coefficients $c_{1v}(v)$ of a zero-memory nonlinearity F acting on a symmetric dual carrier of amplitude v , then we have complete knowledge of the odd part $F_o(x)$ for $-v \leq x \leq v$. If the c_{1v} decay at least as fast as an exponential, then F_o is analytic on $[-v, v]$. We have calculated F_o explicitly for the cases $c_{1v} = A\rho^v$ and $c_{1v} = A(-1)^{1/2(v-1)}\rho^v$, which were suggested by data. We do not know whether the resulting F_o 's have any physical meaning.

References

1. "Viking Dual Carrier Test Review," DJM-72-141, Jet Propulsion Laboratory, Pasadena, California, December 28, 1972 (JPL internal document).
2. Blachman, N. M., "Detectors, Bandpass Nonlinearities, and Their Optimization: Inversion of the Chebyshev Transform," *IEEE Transactions on Information Theory*, Vol. IT-17, 1971, pp. 397-405.

Appendix

Proof of Proposition 1

Lemma. Let $f \in B_v$. Then for $-v \leq x \leq v$,

$$(2/\pi) x \int_0^{1/2\pi} \int_0^{1/2\pi} f(x \cos \theta \cos \phi) \cos \theta d\theta d\phi = \int_0^x f \quad (13)$$

Proof (Blachman). Think of θ and ϕ as being latitude and longitude on the first octant Ω of the unit sphere. Then $\cos \theta \cos \phi$ is a Cartesian coordinate ξ , $\cos \theta d\theta d\phi = d\sigma$, the element of area, and the left side of Eq. (13) is

$$(2/\pi) x \int \int_{\Omega} f(x\xi) d\sigma \quad (14)$$

Now $d\sigma = d\xi d\alpha$, where α is longitude about a pole placed where the ξ -axis meets the sphere. Thus (14) equals

$$\begin{aligned} (2/\pi) x \int_0^1 d\xi \int_0^{1/2\pi} d\alpha f(x\xi) &= x \int_0^1 f(x\xi) d\xi \\ &= \int_0^x f \end{aligned}$$

Define the operators M , J , and D :

$$(Mf)(x) = xf(x), (Jf)(x) = \int_0^x f, (Df)(x) = f'(x)$$

Then the following formulas hold:

$$MT_1T_0 = MT_0T_1 = (2/\pi)J \quad \text{on} \quad B_v \quad (15)$$

$$T_0M = MT_1 \quad \text{on} \quad B_v \quad (16)$$

$$DT_0 = T_1D \quad \text{on} \quad A_v \quad (17)$$

By Fubini's Theorem, Eq. (15) is just a restatement of the lemma. Equations (16) and (17) are quickly verified.

Proof of Proposition 1. If $f \in B_v$ and $T_1f = 0$ almost everywhere, then by Eq. (15), $(2/\pi)Jf = MT_0T_1f = 0$. Hence $f = 0$ almost everywhere. This proves (a).

By definition, $U_1 = (\pi/2)T_0DM$. On A_v

$$MU_1T_1 = (\pi/2)MT_0DMT_1$$

$$= (\pi/2)MT_0DT_0M$$

$$= (\pi/2)MT_0T_1DM$$

$$= JDM = M$$

and

$$MT_1U_1 = (\pi/2)MT_1T_0DM$$

$$= JDM = M$$

Since we are dealing with analytic functions, (b) is proved.

Part (c) follows quickly from (a) and (b).

A different proof of Proposition 1(b) uses power series. See Ref. 2.

Network Control System Development

J. N. Edwards

DSIF Digital Systems Development Section

The development of the DSN Network Control System has been authorized to provide centralized computer control and monitoring of Deep Space Station equipment status and data flow. The NCS is being implemented with an interim (Block I) capability for current spacecraft-support requirements. A transition (Block II) and a final (Block III) NCS, providing future spacecraft support requirements, will be implemented by a complex of minicomputers with dedicated subsystem functional capability.

I. Introduction

This is the fifth report describing the JPL DSN Network Control System (NCS). The NCS provides centralized computer control and monitoring of all the JPL Deep Space Station (DSS) equipment and data flow status. The previous reports presented (1) project plan and resources, (2) system functions and interface requirements, (3) data flow and hardware allocations, and (4) detailed descriptions of hardware and software configurations and development progress for the Block I and Block III NCS. This report discusses recent progress in hardware and software activities and describes a redefinition of implementation guidelines for the NCS.

II. Revised NCS Implementation Guidelines

A change in implementation plans for the NCS has been defined in accordance with resources and mission support requirements. Definitions are as follows:

Old name	New date	New name
Interim NCS	3rd quarter CY73	Block I
Transition	2nd quarter CY74	Block II
Final NCS	2nd quarter CY75	Block III

The change in plans is associated with scheduled facility refurbishment for Block III NCS. Schedule requirements

for mission support have necessitated the transitional (Block II) configuration which will provide functional features complementary to those provided by Block I. The Block II functions will be implemented with minicomputers and software scheduled for Block III. Facilities for Block II will be located in areas designated for Block III that do not require refurbishment and will provide required mission support with minimal configuration revision to attain Block III capability.

A detailed description of NCS Block II will be given in a subsequent report. The Block II configuration has essentially no impact on the Block I and III configuration status as reported herein.

III. Block III NCS Facilities

The location of the Network Data Processing Area (NDPA) for the Block III NCS is planned for JPL, Building 202. Revised cost estimates for facility modifications based on revised design requirements were submitted for approval on June 18, 1973.

The floor space allocations in the Ground Communication Facility (GCF) Central Communications Terminal (CCT) for the Communications Log Processor (CLP) and display processors have been negotiated. The GCF log magnetic tape storage area requirements are pending evaluation of the revised NCS/Mission Control Computing Center (MCCC) logging/recall interface definition.

IV. Block III NCS Hardware

The system design for the Block III NCS has continued after firm identification of the Sigma-5 computers for the Network Support Controller (NSC). The lease arrangements for processor and peripherals have been prepared, and standard interface peripherals for the NSC and real time monitor (RTM) processors have been defined.

A series of interface block diagrams for hardware interfaces has been defined for various multimode data flow paths. The hardware data flow path for received high-speed data (HSD) from Deep Space Stations is shown in Fig. 1. The GCF data signal is checked for error indication by the GCF decoder and distributed to the MCCC and the NCS receive buffer. The receive buffer then distributes to redundant Communication Log Processors (CLP) data channels. The initialized data channel-A logs data on disk and magnetic tape for the NCS GCF log. Data are distributed via the 230.4-kbs data link to the remote NDPA Communications Processor (NCP). The NCP distributes

data to the appropriate RTM or other processors via the star switch controller (SSC). The redundant CLP-B logs data on disk to back up failure of prime CLP disk/tape logging.

The SSC-1/2 shown in Fig. 1 is a sequenced multipoint data router. It provides bilateral communication between any of the 12 processors connected to its terminals. The SSC-1/2/3 are redundant half-duplex units providing backup data paths available to each processor. Similarly, SSC-4/5 provide multipath access between the two CLP and two display processors. The SSC design is complete, and prototype models are in fabrication.

Interface definitions have been established for the processor transmit and receive communication buffers of Fig. 1. Figure 2 shows buffers and equipments utilized for wideband data (WBD) interfaces. The initialized CLP-A data is switch-selected to the transmit buffer. The WBD is sent via a voltage-to-current (V/I) converter to the coded multiplexer demultiplexer (CMDM). The CMDM accepts data blocks with numbered access priority. Data are then appended with serial error correction bits and transmitted to the DSS. Selected transmitted data are also entered into the GCF log via the initialized CLP-A. Received WBD from the DSS are decoded to detect GCF transmission errors, and distributed to the MCCC and the NCS. Received data are sent via a current-to-voltage converter to the receive communications buffer. The received data are routed to the initialized CLP-A for logging and retransmission to the NCP-A. Received data are also distributed to backup CLP-B for logging on disk. The transmit and receive buffers of Fig. 2 for WBD are the same design as for HSD and for 230.4-kbs data as shown in Fig. 1. Transmit and receive buffer specifications and prototype designs are near completion.

The NCS has a requirement to operate with a Remote Mission Operation Center (RMOC) other than via the MCCC. This configuration provides complete command-operation of a DSS by a RMOC via the GCF lines, with concurrent DSS configuration and monitoring by JPL NCS. The design of the NCS GCF filler multiplexer (GCF-FM) for the final NCS is essentially complete. Fabrication will be scheduled after testing of the prototype which has been fabricated for the Block I NCS. The GCF-FM is described in Ref. 1.

The hardware specifications for the NCS minicomputer and peripherals have been completed and reviewed for procurement. Extensive bid evaluation is in-process for hardware procurement.

V. Block III NCS Software

The software design for the Block III NCS has included iterative evaluation of the functional requirements and operations features to be provided by the system. The basic design has progressed, and has resulted in completion of a baseline design document which provides definition of all NCS subsystem design concepts and interfaces. Current effort is directed toward completion of a detailed software requirement document for each of the functional subsystems. The software design group has also generated extensive software benchmark tests and evaluation criteria for the minicomputer procurement.

The network support controller will be implemented in Block I and Block III NCS by Sigma-5 processors and peripherals. Programs for formatting and generation of predicts are being identified and configured for optimum transition between the two system configurations.

VI. Block I NCS Facility

The Block I NCS data processing area facility and equipment installations in JPL Building 202 are complete and in full operation. This includes power, air conditioning, offices, intercom, administrative TTY, magnetic tape safe, and maintenance support activities. Facilities in JPL Building 230 for GCF link communications equipments and input/output (I/O) processor equipment have been provided and checked for support of remote equipments.

VII. Block I NCS Hardware

The Block I NCS data processing hardware is installed and has been tested with applicable diagnostic software. The communications link hardware and PDP-8 processor in the Central Communications Terminal (CCT) is also installed and has been diagnostically tested. Remote display peripherals in the Space Flight Operations Facility (SFOF) are installed and are undergoing final check with software in the data processing area.

The timing system and interfaces are installed and have been diagnostically tested. The GCF-FM for multiplexed synchronous communications with an RMOC has been designed and fabricated and is ready for functional/system testing.

VIII. Block I NCS Software

A. System Configuration

The definition of tasks for the Block I software is related to the applicable DSN 822-series functional requirements

and to the available hardware/software implementation subsystems as shown in Fig. 3. Functions include real-time receiving from and transmitting to Deep Space Stations. This NCS interface is via the HSD lines and the GCF HSD modem equipments. The NCS interface is provided by the software multiplex/distribution in the PDP-8 I/O communications processor located in the GCF CCT. The I/O data are transferred via a wideband data line to the real-time Sigma-5 processor. The real-time Sigma-5 provides GCF accountability for all received data, and for data processing/analysis. It also generates local/remote data displays for monitoring operational status of the DSN in real-time.

The data to be transmitted to the DSS are input by keyboard or by preprocessed magnetic tape. Tape data are stored on disk file for transmission, in accordance with remote network operations control. Selected command-configuration transmission data from the NCS are echo-checked from the DSS to NCS in real-time to confirm correct transmission to the DSS.

The Sigma-5 non-real-time processor accepts tape, card, and keyboard inputs. It does off-line preprocessing, formatting, and generation of designated schedules, sequence of events, and predicts for tracking and telemetry subsystems. These preformatted data are then transferred by tape to the real-time Sigma-5 for transmission to the various DSSs.

B. System Status

The configuration baseline design has been completed in accordance with the system functional requirements for all software. A project design review was completed for all software. Design and coding are complete for all modules in the three processors.

Software module verification testing is near completion. The acceptance test procedures have been completed and selected system testing is underway. Significant system testing progress has been achieved, with key features summarized below:

- (1) System initialization has been confirmed for all processors.
- (2) GCF accountability for HSD lines is functional.
- (3) Real-time data are transferred from the PDP-8 to the Sigma-5.
- (4) The printer dump of real-time HSD is functional.
- (5) Generation of real-time data displays with multiple format paging is functional.

- (6) Displays have been checked for local and remote peripheral interfaces at the processor.
- (7) Formatting and processing of data on the off-line processor has been provided, with various tape transfers to the real-time machine for disk file storage.

Other features relating to NCS data transmission and verification are in final phases of verification and acceptance testing. An extended effort was required in some areas to facilitate problems relating to hardware cross-

talk, operating system anomalies, and revised functional requirements. A definitive anomaly reporting system has been incorporated to identify software anomalies and assure certified corrective action. An extensive effort is being directed to provide complete design, coding, operation procedures, operations tapes, commercial diagnostics, and special system configuration diagnostics data; this will be included with system software data transfer from development to operations.

A subsequent report will describe the detailed features of the Block I NCS software design and operation.

Reference

1. Edwards, J. N., "Network Control System," in *The Deep Space Network Progress Report*, Technical Report 32-1526, Vol. XIV, pp. 141-145, Jet Propulsion Laboratory, Pasadena, Calif., Apr. 15, 1973.

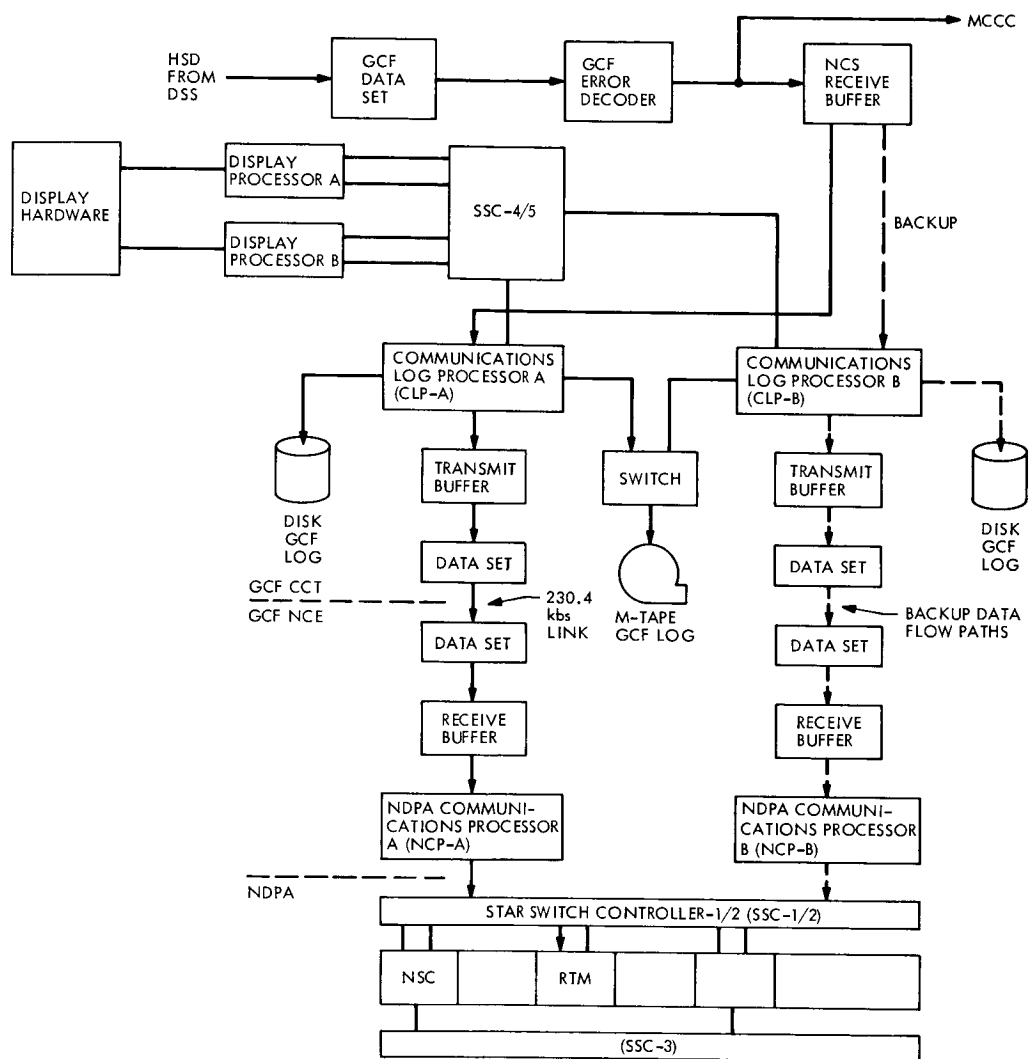


Fig. 1. DSS to NCS high-speed data receive data flow path

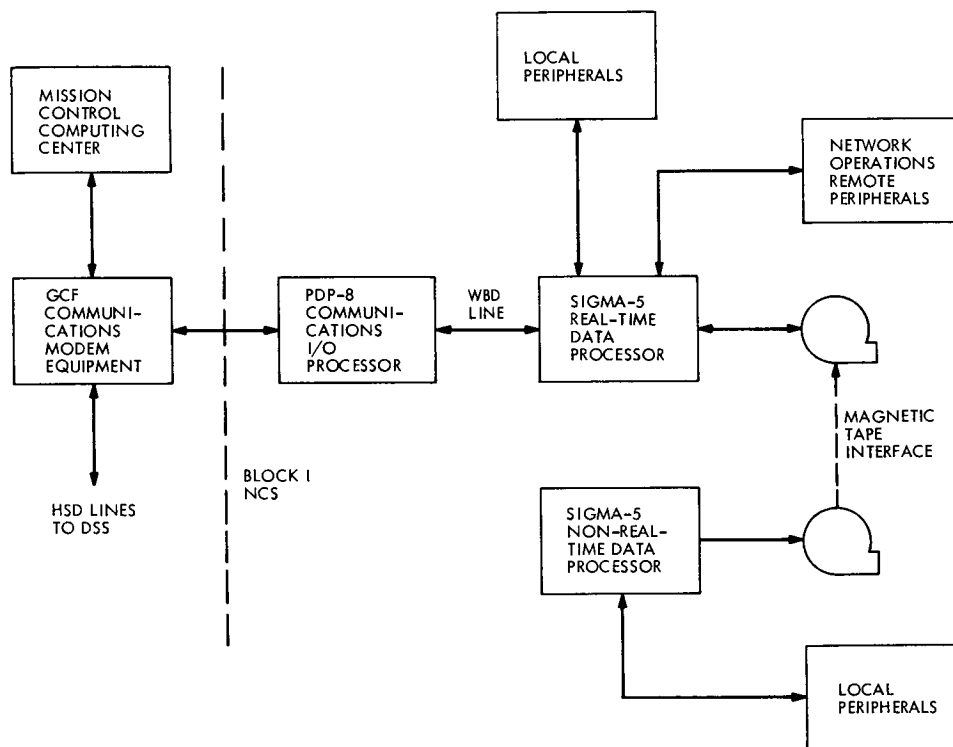


Fig. 3. Block I network control system hardware/software subsystem

A New Dual Ignitron High-Voltage Crowbar

E. J. Finnegan

R.F. Systems Development Section

A crowbar is described which is capable of holding off 100,000 V dc using two mercury pool ignitrons connected in series. This crowbar assembly will replace the single high-voltage ignitron in the 400-kW transmitter at DSS 14 and will be part of the DSN 100-kW transmitters being constructed overseas. It was necessary to develop a higher voltage device in order to improve the reliability of the crowbar used to protect the high-powered RF klystron from self-destruction. The single ignitron has trouble operating over 60,000 V. An engineering model was built and has been operating satisfactorily at DSS 13.

I. Introduction

DSS 14 utilizes a 400-kW transmitter to generate radio signals that are used to command and monitor spacecraft. The klystron tubes which amplify the RF signals operate at high voltage and are therefore subject to damage due to high-voltage arcing. Since the cost of these tubes is very high, a great deal of effort is applied to their protection. One of the protective devices used is a crowbar that senses high-voltage arcs and short-circuits the destructive high currents from the klystron until the high voltage is completely removed. Ignitron tubes are used to perform the short-circuit functions. Open circuited, they are capable

of holding off high voltages without significant leakage; when fired the dc drop is only several volts even at kilo-ampere currents.

II. Crowbar Background

A prototype dual ignitron crowbar was designed and tested to check feasibility, and from this prototype a more rugged engineering model was fabricated using NL 1040 ignitrons (Ref. 1). These ignitrons are capable of withstanding 50,000 V; two in series will operate reliably at 100,000 V (Fig. 1). The engineering model has been operating at DSS 13 for two months. An infrared gallium

arsenide laser and light pipe is being used in conjunction with it to trigger the crowbar.

III. Description

The circuit functions in the following manner. When the klystron arcs, the high current is sensed and triggers a light-emitting diode (LED) which generates photons. The photons propagate through fiber optics to the high-voltage deck; the fiber optics isolate the high-voltage deck. The photon pulse is then detected by a photo diode and amplified in order to turn on the ignitron assembly. The system time delay is less than 4 μ s. The energy available from the capacitor is $1/2 CV^2$ (Fig. 1) or 1800 J. The energy reaching the tube without a crowbar would be $1/2 CV^2 (R_t/R_3)$ or 45 J (R_t is typically 0.1 ohm when the klystron arcs) and this would be destructive to the tube. The energy reaching the tube with a crowbar and R_4 would be

$$1/2 CV^2 \left(\frac{R_t}{R_3 + R_4} \right) \left(\frac{2T}{CR_3 + R_5} + \frac{L}{CR_3 R_5} \right) = 8 \text{ J}$$

where

$T = 4 \mu$ s, response time of the new ignitron assembly

$L = 100$ nH, ignitron inductance

R_t = typically 0.1 ohm when the klystron arcs as determined by tube laboratories experimentally

$C = 1 \mu$ f

$V = 60,000$ V

This should be safe for most tubes. The exact amount of energy that will destroy a klystron is unknown and therefore intuitive.

IV. Conclusion

The engineering model will continue to be tested at DSS 13; another ignitron assembly will be fabricated and installed at DSS 14, thus giving faster crowbar protection and more reliability for the 400-kW klystron.

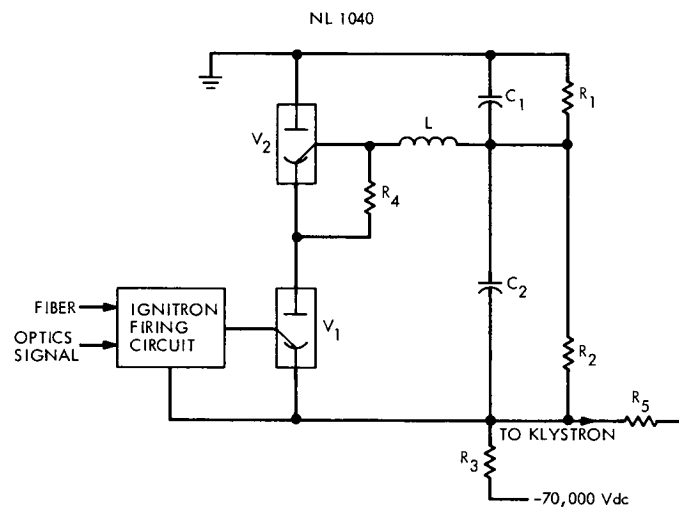


Fig. 1. Dual ignitron schematic diagram

X-Band Traveling Wave Maser Amplifier

D. L. Trowbridge
R.F. Systems Development Section

An X-band traveling wave maser amplifier (maser) has undergone preliminary tests in the laboratory. The masers are being developed for use in the 64-meter-diameter antenna Deep Space Stations to meet ground support requirements of the Viking 1975 flight project.

The maser has 53 dB net gain, with 43 MHz instantaneous 1-dB bandwidth at 8420 MHz. Mechanical tuning of the pump klystrons enables the maser to be tuned to 8600 MHz, with 43 MHz instantaneous 1-dB bandwidth at 45 dB net gain.

I. Introduction

An X-band traveling wave maser amplifier (maser) is being developed for operational use in the 64-meter-diameter antenna Deep Space Stations. The primary purpose of the maser is to meet ground support requirements of the Viking 1975 Project, which requires an instantaneous 1-dB bandwidth of 35 MHz covering the frequency band of 8400 to 8435 MHz.

A design goal of 35 MHz, 1-dB instantaneous bandwidth, and 8400 to 8435 MHz, with 45 ± 1 dB net gain, was established in November 1972 as the result of flight project and ground system requirements.

A maser has been designed and a preliminary test has been completed. Design criteria and preliminary test results are described in this article.

The test maser provides 53 dB gain, with an instantaneous 1-dB bandwidth of 43 MHz over the Viking 1975 frequency band. Mechanical tuning of the pump klystrons enables the maser to be tuned to 8600 MHz, with 43 MHz instantaneous 1-dB bandwidth at 45 dB net gain. The test results show that the gain/bandwidth design goal has been achieved, and indicate the possibility of future applications over a much wider frequency tuning range.

II. Maser Description

The assembled maser is shown in Fig. 1 (A) with the cover (B) removed. The slow wave structure (C) is machined from a solid piece of copper. The structure consists of two parallel comb sections, connected in series by sections. The signal is coupled from the input and output coaxial lines to the comb sections with loops that termi-

nate near the base of each comb at the left-hand end. Pump frequency radiation enters the maser through an opening in the center of the flange at the left and is coupled to the ruby through shaped alumina dielectric strips, as shown in Fig. 2. The alumina strips improve the pump match into the ruby.

III. Maser Comb Design and Loading

A previous X-band maser (Ref. 1) was designed for a broad tuning range. The maser for Viking 1975 requires a larger gain/bandwidth product over the frequency range of 8400 to 8435 MHz. This requirement resulted in a new maser design for Viking 1975. The new design features a comb structure which provides (1) an increased fill factor, (2) improved isolator performance, and (3) improved slowing factor adjustment capability. It also features an improved technique for maintaining constant contact pressure between the ruby, alumina, and comb section finger surface.

The nonsymmetrical comb channel design, as shown in Fig. 3, together with optimized finger geometry, provides an improved fill factor over previous X-band masers (Ref. 1). The narrow channel width filled with ruby, combined with the finger geometry, maximizes orientation of the RF magnetic field in the direction of maximum transition probability. The larger channel filled with alumina provides larger regions of circular polarization for optimum isolator performance. Optimized fill factor and isolator performance result in higher net gain per unit length.

A beryllium copper strip with mounting screws on each side of the maser supplies pressure to pins which protrude through the maser sidewall (Fig. 3). The pins transfer pressure through the alumina strip, comb section, and ruby bar to insure consistent surface contact and sufficient pump heat conduction.

The 7.54-cm-length comb sections are loaded with ruby on the inner side of the comb and alumina (which supports the isolator material) on the outer side. This type of construction is similar to that of previous X-band masers.

The ruby bars, as in previous masers, are fabricated from "0-degree" Czochralski ruby with 0.05 to 0.07% Cr_2O_3 . C-axis orientation is along the length of the comb. The alumina strip, as shown in Figs. 3 and 4, is constructed from two alumina bars glued together, with a 0.64-mm-width dimensional offset. The offset produces a step area

on the top and bottom edges of the strip. The bottom step is used for isolator mounting, and the step at the top of the strip provides a coarse slowing adjustment. The ruby bar is bevel-shaped on one edge and provides a vernier slowing adjustment.

A range of slowing was achieved with the structure by using variable amounts of comb loading. Equivalent electrical lengths were measured over the range of 6.23 to 13.60 m. The slowing factor of the test maser was adjusted to yield the desired gain-bandwidth product over the 8400 to 8500 MHz band. The ratio of the slowing factor vs frequency of the test maser was measured with the results shown in Fig. 5. The equivalent electrical length is approximately 8 m.

IV. Isolator Performance

The isolator consists of 96 polycrystalline yttrium iron garnet (YIG) squares, each with dimensions of $0.635 \times 0.635 \times 0.0762$ mm. The squares are glued to the alumina strips, as shown in Figs. 3 and 4, on the bottom step. The isolators are positioned at a 45-deg angle to the finger surface, with one corner keyed in a locating slot cut in the alumina strip. The isolators are located in the optimized region of circular polarization, determined for this structure as defined by Chen and Tabor (Ref. 2). A reverse-to-forward loss ratio of 70 to 1, with the reverse loss greater than 200 dB and a forward loss of 3 dB, has been achieved. The minimum isolator forward loss occurred at the desired frequency location in the structure bandpass, as shown in Fig. 5. Previous X-band masers (Ref. 3), using strip-shaped isolators, achieved a reverse-to-forward loss ratio of 20 to 1. Isolator geometry and dimensional tolerances have been determined to place isolator resonance at the correct magnetic field strength in reference to ruby absorption. This results in maximized reverse loss at the correct frequency and bandwidth with tolerance to magnet field rotation. The isolator is capable of ± 4 deg rotation in the magnetic field without degradation to maser performance.

V. Maser Test Conditions

The test maser was cooled by submersion in liquid helium under controlled helium gas supply pressure. A Varian Electromagnet Model 3603 and Varian Field Regulated Power Supply Model V-FR2503 were used to supply a uniform-strength adjustable field. Field spreading was accomplished with two coils mounted to the bottom of the

maser structure and connected in a figure eight manner, with one aiding and one bucking the main magnet field. Push-push pumping was performed by dual klystrons at different frequencies (as reported in Ref. 4).

VI. Pump Modulation

Preliminary tests were conducted to determine the effect of pump frequency modulation on the gain/bandwidth performance of the maser, using field spreading to obtain the desired bandwidth. In an early test, a 1-dB instantaneous bandwidth of 40 MHz centered at 8277 MHz, with 35 dB net gain (as shown in Fig. 6), was achieved without pump frequency modulation. A 1 dB instantaneous bandwidth of 38 MHz centered at 8277 MHz, with 46 dB net gain (Fig. 7), was obtained with pump frequency modulation at a 20-kHz rate and modulation amplitude adjusted for maximum maser gain. The pump level was adjusted for proper pump saturation for both tests. Tests indicate that an increase of approximately 10 dB in net gain at the same bandwidth can be realized by using pump modulation. Pump modulation was used on previous S-band and X-band masers operating in a uniform field (Ref. 5).

VII. Maser Performance

Gain vs frequency curves, with the maser tuned to 8420 MHz, 8500 MHz, and 8575 MHz, are shown in Figs. 8, 9, and 10, respectively. An instantaneous 1-dB bandwidth of 43 MHz is achieved at the center frequencies of 8420 MHz, with 53 dB net gain; 8500 MHz, with 46 dB net gain; and 8575 MHz, with 45 dB net gain. A net gain of 45 dB can be obtained at any frequency between 8400 and 8600 MHz, with an instantaneous 1-dB bandwidth of 40 MHz or greater, by mechanically tuning the two pump klystrons.

VIII. Conclusion

A new X-band maser has been designed to meet Viking 1975 requirements. The test results indicate that the requirements for gain/bandwidth have been met with a considerable margin. The structure shows a capability for operation up to 8600 MHz with appropriate accessory equipment. Minor adjustments will be made when the maser is installed in an operational closed-cycle refrigerator. Future tests will include gain stability, noise temperature, group delay, and match measurements.

Acknowledgment

The X-band maser described in this article is the product of a combined effort. The assistance of R. Clauss in providing his experience in maser design and R. Quinn in fabrication techniques is gratefully acknowledged. Thanks are also due to E. Wiebe for special test equipment and facilities support.

References

1. Clauss, R., Wiebe, E., and Quinn, R., "Low Noise Receivers: Microwave Maser Development," *The Deep Space Network Progress Report*, Technical Report 32-1526, Vol. XV, pp. 71-80, Jet Propulsion Laboratory, Pasadena, Calif., June 15, 1973.
2. Chen, F. S., and Tabor, W. J., "Filling Factor and Isolator Performance of a Traveling Wave Maser," *The Bell System Technical Journal*, pp. 1005-1033, May 1964.
3. Clauss, R., "Low Noise Receivers: Microwave Maser Development," in *The Deep Space Network*, Space Programs Summary 37-57, Vol. II, pp. 87-90, Jet Propulsion Laboratory, Pasadena, Calif.
4. Clauss, R., "RF Techniques Research: System Studies for Frequencies Above S-Band for Space Communications," in *The Deep Space Network*, Space Programs Summary 37-61, Vol. III, pp. 90-93, Jet Propulsion Laboratory, Pasadena, Calif., Feb. 1970.
5. Clauss, R., Reilly, H. F. Jr., and Reid, M. S., "Low Noise Receivers: Microwave Maser Development," in *The Deep Space Network*, Space Programs Summary 37-62, Vol. II, pp. 74-78, Jet Propulsion Laboratory, Pasadena, Calif., March 1970.

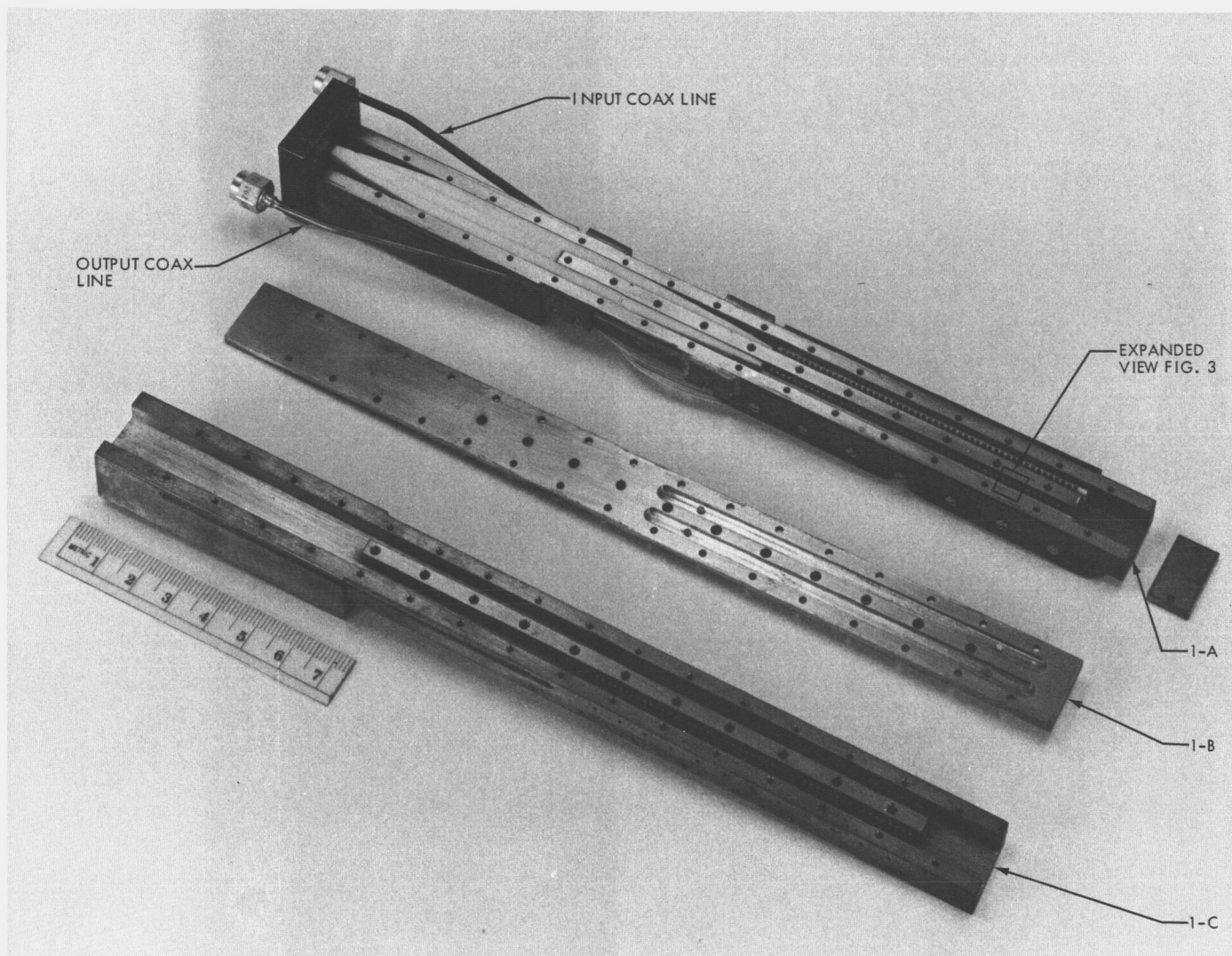


Fig. 1. Assembled X-band maser and slow wave structure

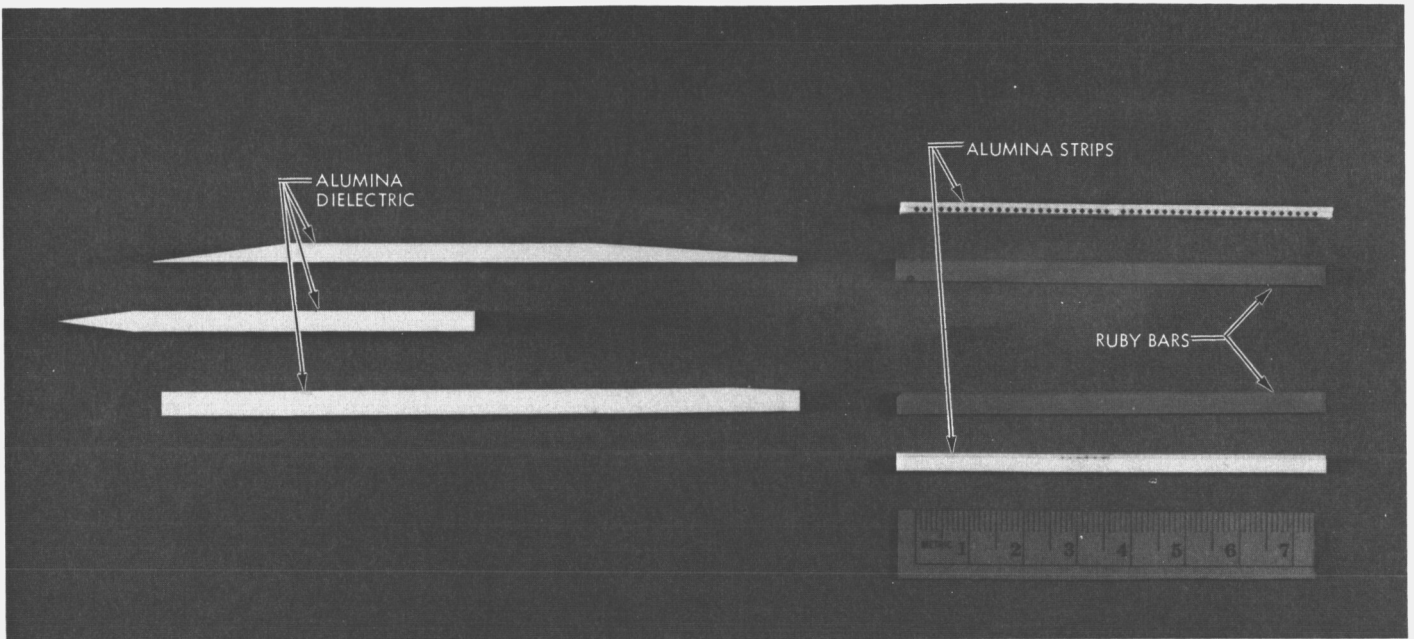


Fig. 2. Shaped alumina dielectric bars with ruby bars and alumina strips

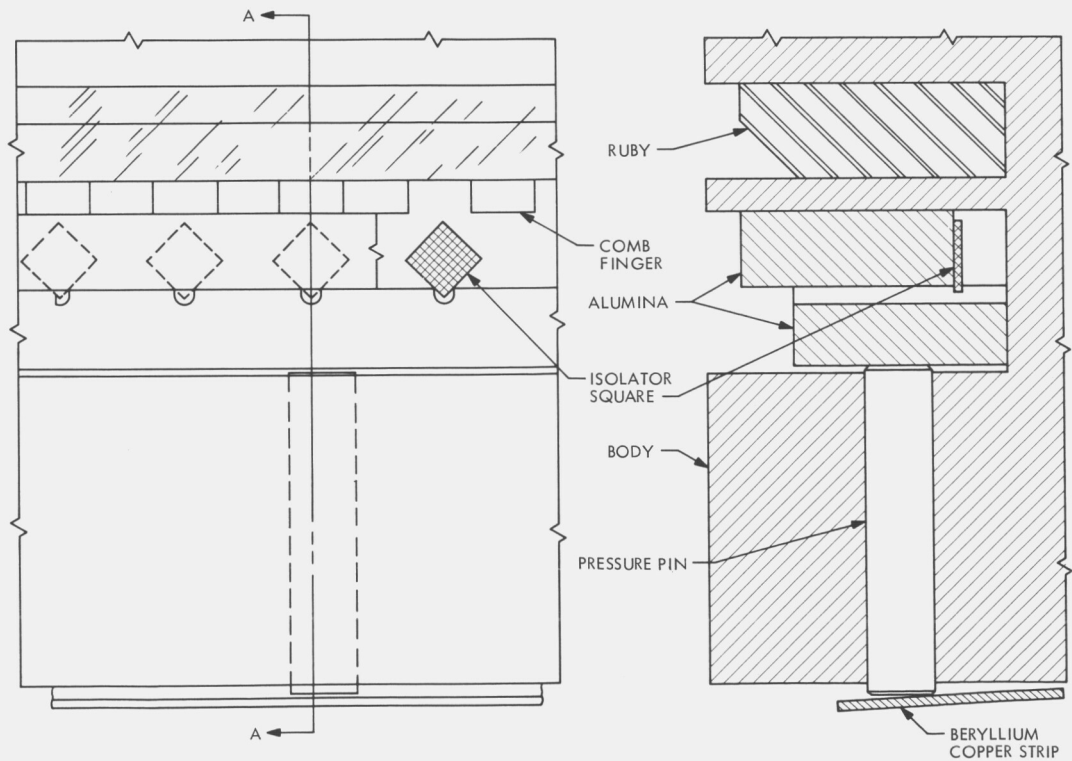


Fig. 3. Comb structure loading and isolator location

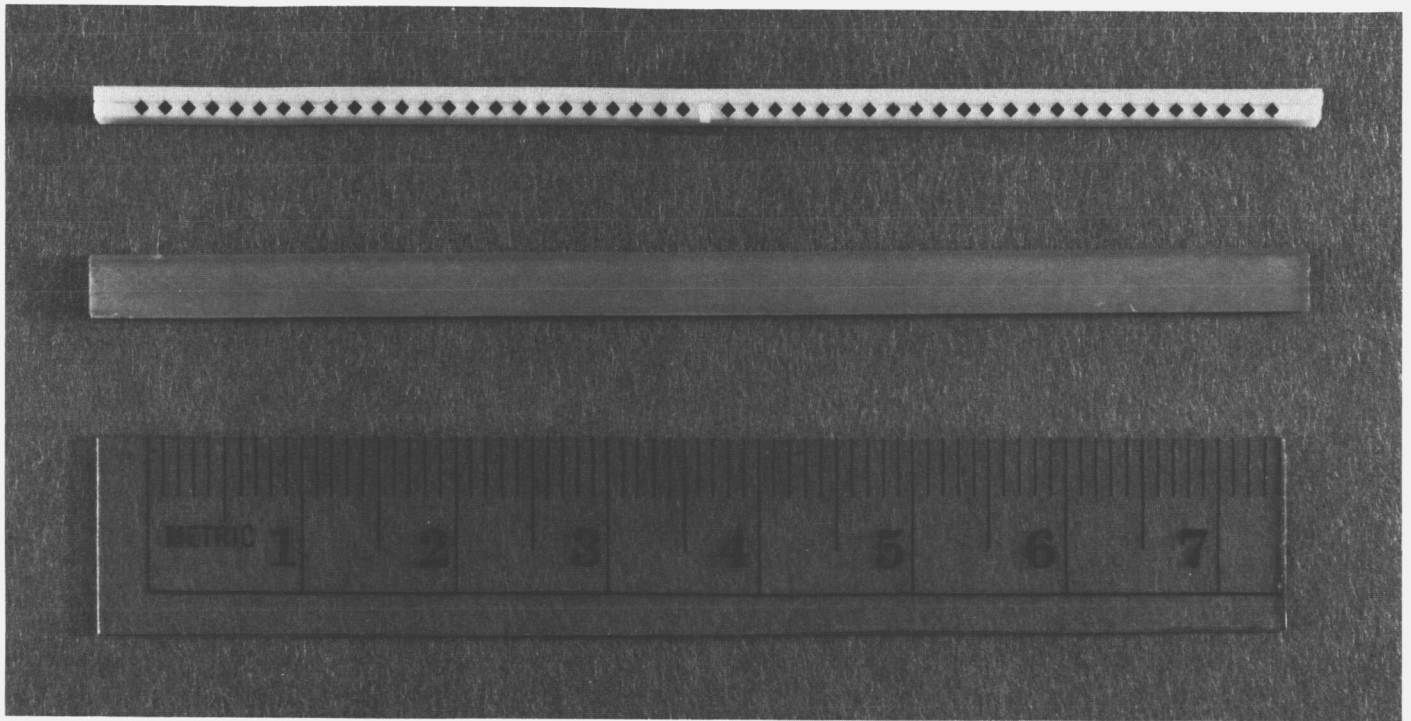


Fig. 4. Alumina strip with mounted isolator squares and ruby bar

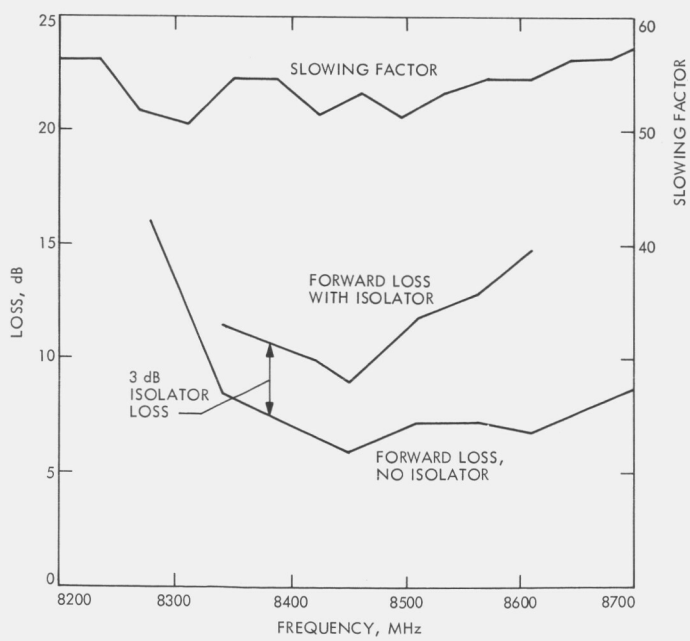


Fig. 5. Maser forward loss and slowing factor vs frequency

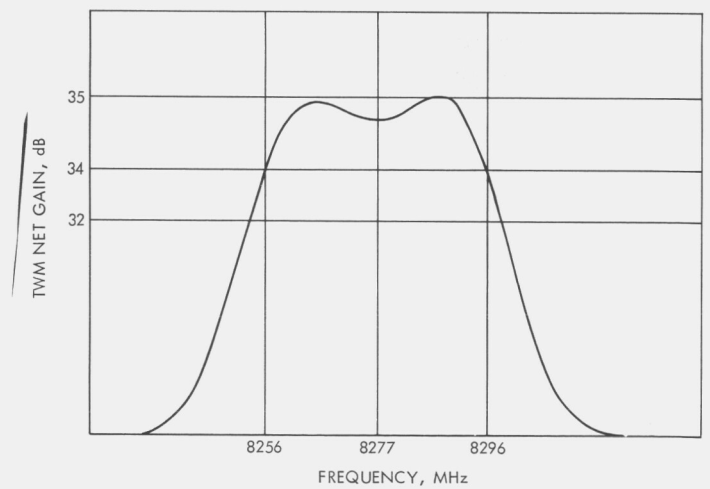


Fig. 6. Maser gain vs frequency without pump frequency modulation

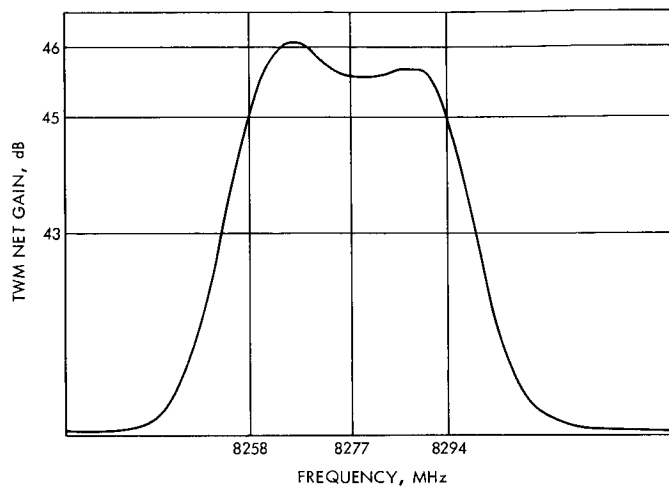


Fig. 7. Maser gain vs frequency with pump frequency modulation

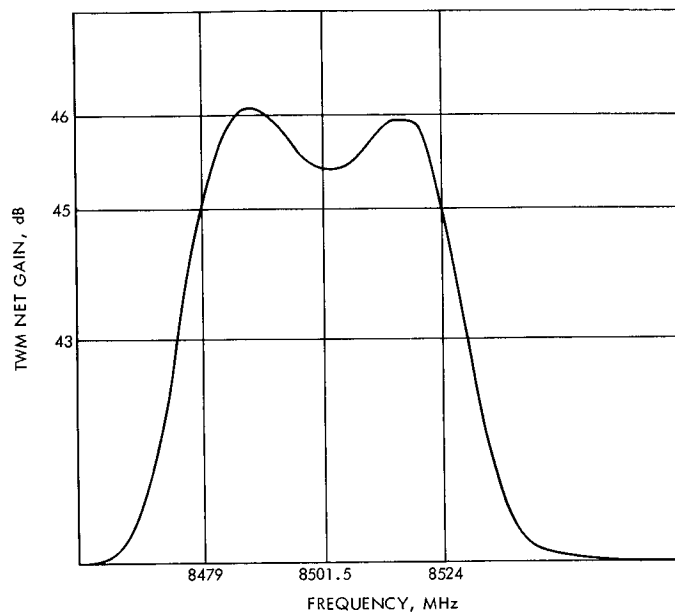


Fig. 9. Maser gain vs frequency at mid-structure tuning range

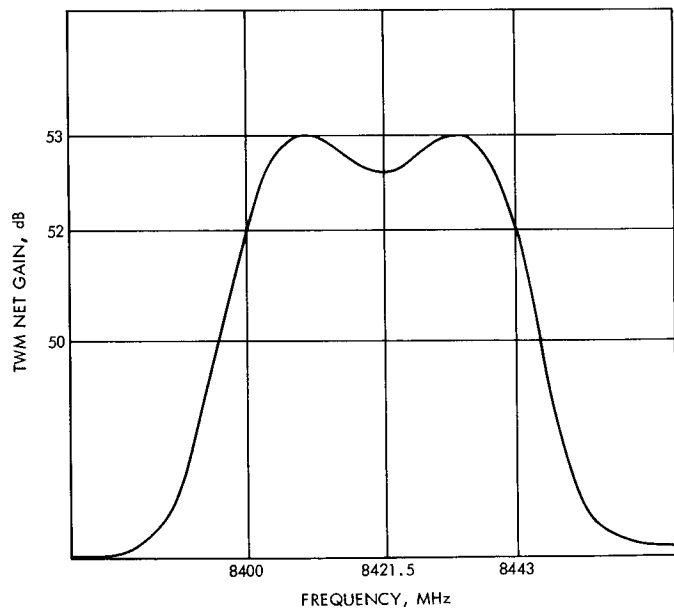


Fig. 8. Maser gain vs frequency at frequency band required for Viking 1975

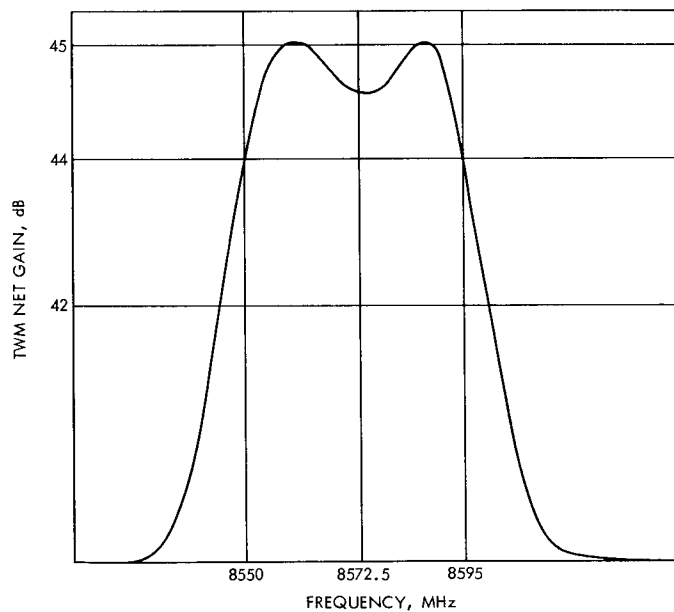


Fig. 10. Maser gain vs frequency at upper end of structure tuning range

X-Band Antenna Feed Cone Assembly

R. W. Hartop

R.F. Systems Development Section

A new X-band feed cone assembly has been designed for the DSN 64-meter-diameter antenna stations. Unique features of the cone assembly are described and progress to date is reported.

In support of Viking and future projects, the DSN must provide for X-band signal reception at the three existing 64-meter antenna stations. Currently a research and development X-band cone assembly is in operation at DSS 14, but the overseas stations have no X-band capability.

To meet this requirement, a new X-band cone assembly, shown in Fig. 1, has been designed. It utilizes the standard cone shell with the addition of an extension at the top to support the X-band horn and provide a weather seal.

Because of the much smaller size of X-band components as compared to S-band, several new features have been incorporated in this design. The cone shell has been converted to a two-story design with the addition of a new floor at the intermediate level. The traveling wave maser rests upon a stand which attaches to this new floor.

The feed assembly includes the horn, a polarizer for right circular polarization (RCP) reception, a transition to rectangular waveguide, spacing waveguides for mode

control, and a waveguide switch to select either the feed or a calibrated ambient load for system performance measurements. The entire feed assembly is structurally one piece and can be removed and replaced without affecting its precision alignment. Only the output waveguide, the switch control cable, and the mounting bolts on the top plate need be removed to effect a complete replacement. This innovation will permit the retrofit of more advanced X-band feed systems as the requirements

develop. Examples of future changes that may be desired are higher illumination efficiency feed horns, polarization diversity, and uplink (higher power) capability.

At this time the cone shells for three assemblies are on hand and fabrication of the microwave components is nearly complete. Waveguide switches have been procured (Ref. 1). Work remaining includes the fabrication of bracketry and the assembly of the complete cones.

Reference

1. Hartop, R. W., "X-Band Waveguide Switches," in *The Deep Space Network Progress Report*, Technical Report 32-1526, Vol. XV, pp. 48-50, Jet Propulsion Laboratory, Pasadena, Calif., June 15, 1973.

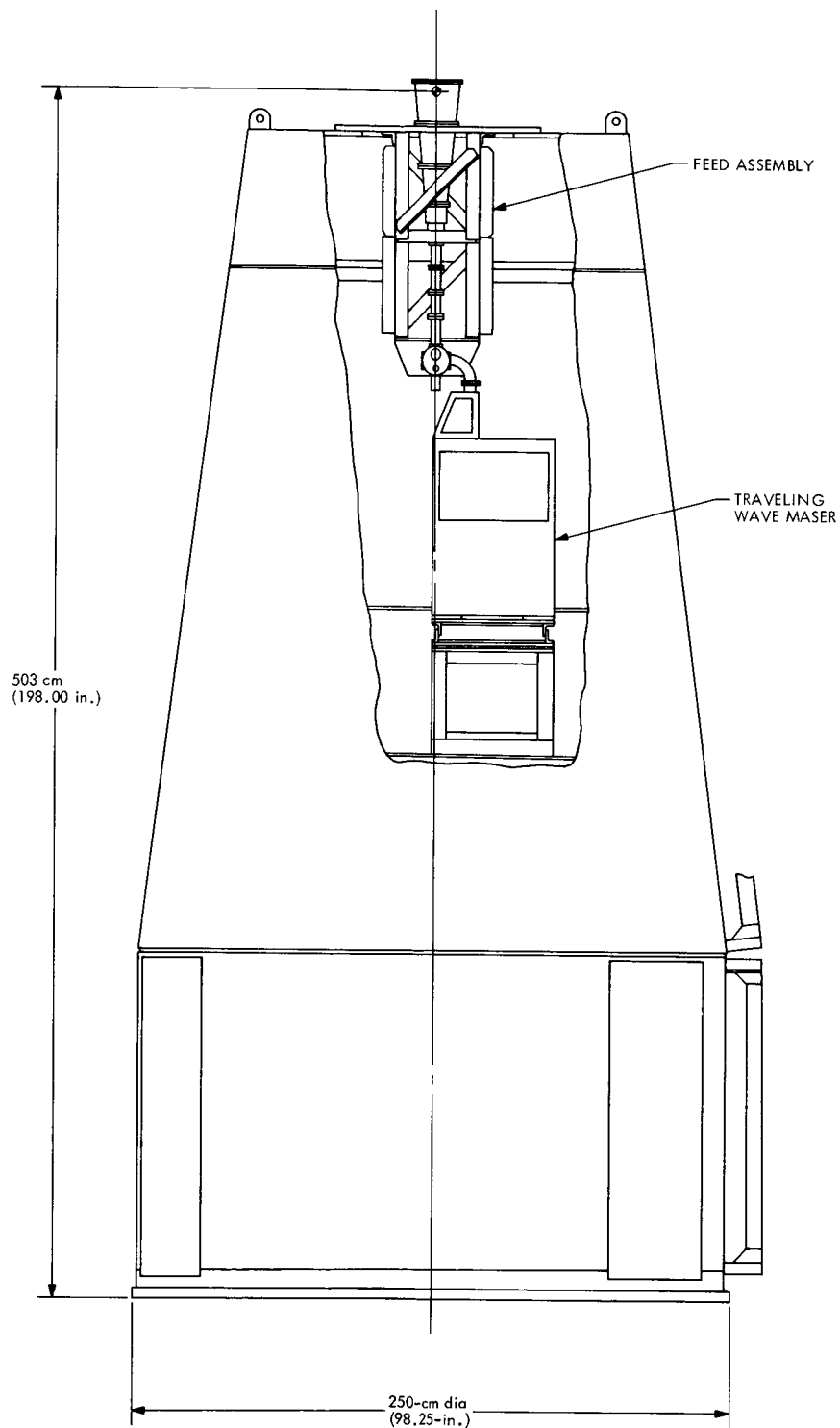


Fig. 1. X-band receive only (XRO) cone assembly

X-Band Traveling Wave Resonator (TWR)

R. B. Kolbly
R.F. Systems Development Section

This article covers the design philosophy and operation for an X-band traveling wave resonator (TWR). This equipment will be used to test high-power components for X-band planetary radar.

I. Introduction

It is required that the personnel of the Development Support Group, Section 335, design and build a traveling wave resonator (TWR) to test low-loss components at power levels up to +90 dBm (1×10^6 W) at 8495 MHz ± 50 MHz.

II. Background

There have been several TWRs for high-power CW testing (Refs. 1 and 2). The Development Support Group has built and operated a TWR (Ref. 3) to power levels up to +87 dBm (5×10^5 W). One of the main problems with high-power TWR testing is removing the heat dissipated in the waveguide. When a TWR is operating properly, all input power is dissipated in the resonant structure.

III. Theory of Operation

For a lossy TWR structure with no discontinuities, the power multiplication is given by the following formula:

$$M = \left[\frac{C}{1 - T(1 - C^2)^{1/2}} \right]^2 \quad (1)$$

where

M = power multiplication factor

C = voltage coupling coefficient of directional coupler

T = voltage transmission coefficient of TWR = $10^{-A/20}$
where A = one-way resonator loss in decibels

Setting $dM/dc = 0$ for a constant T to give coupling efficiency for optimum gain when T is fixed, we have:

$$C_{\text{opt}} = (1 - T^2)^{1/2} \quad (2)$$

Equation (1) is plotted for various values in Fig. 1.

IV. Practical Considerations

It is expected that a TWR for 8495 ± 50 MHz will have a total length of approximately 2.5 m with a loss of approximately 0.06 dB/m or a total loss of 0.15 dB. The losses of components to be tested are expected to vary between 0.01 and 0.06 dB. Therefore, the TWR system will have a minimum loss of 0.16 dB and a maximum loss of 0.21 dB.

Solving Eq. (2) for its value, we determine:

$$0.19018 < C_{\text{opt}} < 0.21726$$

The power gain at these coupling coefficients corresponds to:

$$M_{\text{opt}} = \frac{1}{C_{\text{opt}}^2}$$

This corresponds to a power gain of approximately 21 to 27. Since we desire a power gain of greater than 20, the optimum coupling for this requires a C of 0.2236 (13.0 dB). By using a coupler of this value, a maximum of 0.13 dB attenuation in the ring could be tolerated. By referring to Fig. 1, an optimum value for this application (maximum loss for a specified power gain) would be 15 dB. This would allow the resonator gain to be greater than 20 for all values of attenuation greater than approximately 0.16 dB. Figure 2 presents a practical traveling wave resonator.

V. RF Drive

For initial testing of the X-band TWR, it is planned to use the old 20-kW X-band klystron from the R&D clock sync project. With the anticipated TWR parameters, this klystron will allow circulating powers of up to 500 kW. Use of this klystron in connection with the klystron power supplies and support equipment located at the old Microwave Test Facility will avoid committing a high-power X-band klystron (250 kW) and its associated power supply to TWR development. Also, use of this low-power klystron will eliminate the use of warranty time on a new klystron during the relatively long time required to develop and test the TWR.

When it becomes necessary to develop higher power in the TWR than can be generated using the 20-kW klystron, the TWR can be used with the 250-kW klystron. Also, the microwave components used in the TWR are being designed to operate from 7.0 to 8.5 GHz in order to support future development of an X-band DSN uplink, so it would be possible to use the 150-kW clock sync transmitter as a source of RF drive for the TWR.

VI. Mechanical Construction

The main directional coupler should be of similar construction to the one used in the 500-kW TWR (described in Ref. 3), a multihole sidewall coupler 0.9 m (3 ft) long or less. However, hard solder should be used in all joints, and coolant lines would have to be installed on all arms. The main resonator should be constructed of 3.175 mm (0.125 in.) wall WR-125 oxygen-free high conductivity (OFHC) copper guide with standard thick JPL CPR-type flanges. The input and output tuners will be similar to the ones used in the 500-kW S-band TWR with water cooling added.

VII. Cooling

At 500 kW CW, WR-125 OFHC waveguide will have dissipative losses of approximately 7 kW per meter. Also, a properly adjusted TWR will dissipate all of its input power in the resonant structure. Therefore, the cooling should be adequate to remove all of the incident RF energy as heat. Cooling lines will be hard-soldered to the waveguide, and a special coolant manifold will be used to assure adequate coolant flow.

References

1. Milosevic, C. J., and Vauley, R., "Traveling-Wave Resonators," *IRE Trans. PGMTT*, April 1958, pp. 136-141.
2. Miller, S. J., "The Traveling-Wave Resonator and High-Power Microwave Testing," *Microwave J.*, Sept. 1960, pp. 50-58.
3. Kolbly, R. B., "High-Power Continuous Wave (CW) S-band Traveling Wave Resonator," in *The Deep Space Network*, Space Programs Summary 37-40, Vol. III, pp. 24-26, Jet Propulsion Laboratory, Pasadena, Calif., July 31, 1966.

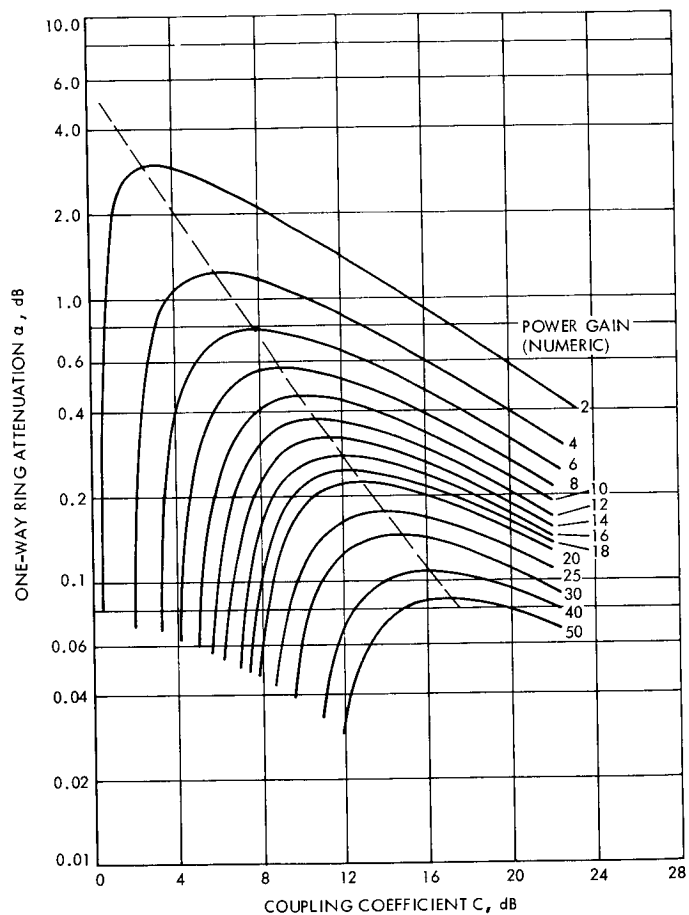


Fig. 1. Traveling-wave resonator characteristics

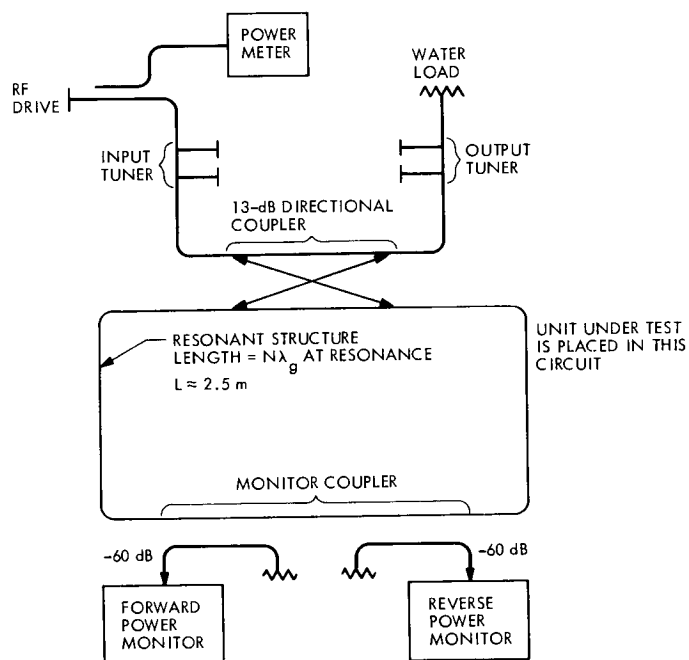


Fig. 2. Block diagram of traveling-wave resonator

A Re-Examination of Subcarrier Demodulator Performance

J. R. Lesh
Network Operations Section

The Subcarrier Demodulator Assembly (SDA) is re-examined, and a mathematical model is developed wherein an attempt is made to remove some of the restrictions placed on previous models. The resulting model is found to differ from the previous model at low symbol rates, when subcarrier doppler offsets exist, or when carrier tracking phase errors become significant.

I. Introduction

Since its inception, the Subcarrier Demodulator Assembly (SDA) has been studied quite extensively. The most notable of these studies was performed by Brockman (Refs. 1-5). In this article the SDA is re-examined with an attempt to include the effects of

- (1) SDA phase errors upon the SDA loop.
- (2) Carrier tracking loop phase errors.
- (3) A recent study involving the theory of soft limiters (Ref. 6).

The SDA model created in this study is then compared with the earlier Brockman model. The two models are found to deviate most when compared at low symbol rates, when subcarrier doppler offsets exist, or when carrier tracking errors are significant. For ease of comparison, the terminology used in this paper will match that used in the Brockman papers as closely as possible.

II. SDA Model

A block diagram of the data channel portion of the SDA is shown in Fig. 1. The input to the SDA is a signal of the form

$$u(t) = \sqrt{2} A \sin \{ \omega_c t + m_{ps} m(t) \cos [\omega_{sc} t + \theta_{sc}(t)] \} + n(t) \quad (1)$$

Here, A represents the rms signal amplitude, ω_c is the intermediate frequency (IF) carrier angular frequency, $m(t)$ is the binary data stream, assuming values of ± 1 , which biphas modulates the unit amplitude squarewave subcarrier

$$S(t) = \cos [\omega_{sc} t + \theta_{sc}(t)] \quad (2)$$

and m_{ps} is the phase modulation angle of the IF carrier. The resulting signal is then immersed in zero mean white Gaussian noise having a one-sided spectral density of

N_0 watts/Hz. This input signal is mixed with the locally generated estimate of the subcarrier signal

$$\hat{S}_D(t) = \cos[\omega_{sc}t + \hat{\theta}_{sc}(t)] \quad (3)$$

which is supplied by the error channel portion of the SDA. After bandpass filtering and mixing with the 10-MHz reference signal

$$\sqrt{2} \cos[\omega_c t + \phi_R(t)] \quad (4)$$

we have the demodulated data signal

$$A \sin m_{PS} \left(1 - \frac{2}{\pi} |\phi_{sc}(t)| \right) \cos[\phi_R(t)] m(t) \quad (5)$$

where

$$\phi_{sc}(t) = \theta_{sc}(t) - \theta_{sc}(t) \quad (6)$$

is the subcarrier loop phase error and $\phi_R(t)$ is the phase error of the receiver carrier tracking loop. The demodulated data signal is finally filtered and limited to produce the local estimate of the data stream $\hat{m}(t)$ for use in the error channel portion of the SDA.

Refer now to the block diagram of the error channel portion of the SDA shown in Fig. 2. The squarewave VCO produces, along with the subcarrier estimate $S_D(t)$, the quadrature estimate

$$\hat{S}_E(t) = \sin[\omega_{sc}t + \hat{\theta}_{sc}(t)] \quad (7)$$

This quadrature estimate is modulated by the local data estimate and is then mixed with the incoming signal to produce a signal $v(t)$, the amplitude of which is proportional to the subcarrier loop phase error

$$v(t) = \frac{2\sqrt{2}}{\pi} A \sin m_{PS} m(t) \hat{m}(t) \phi_{sc}(t) \cos \omega_c t + n(t) \quad (8)$$

This error signal is applied to the bandpass filter to provide the input $x(t)$ to the soft limiter. The expression for $x(t)$ is

$$x(t) = \frac{2\sqrt{2}}{\pi} A \sin m_{PS} \alpha' \phi_{sc}(t) \cos \omega_c t + n'(t) \quad (9)$$

where α' is the average of the product of $m(t)$ and $\hat{m}(t)$ and $n'(t)$ is the input noise term of one-sided spectral density N_0 but restricted to the bandwidth BW_{FA_2} (one produces, along with the subcarrier estimate $S_D(t)$, the sided) of the bandpass filter. In Brockman (Ref. 5), an expression is given for α' when the symbol transition probability is 0.5 and the ratio of data lowpass filter time constant to symbol period is 1/3. This expression, however, does not include the effects of degradation from either the subcarrier loop or the carrier tracking loop. To include these effects, we can compute an effective (average) signal strength into the data channel lowpass filter by first assuming that the subcarrier and carrier tracking loop phase errors are independent. Then, if we assume that the SDA phase error is Gaussian, we have that the signal voltage reduction due to the subcarrier loop phase error is, from Brockman (Ref. 2),

$$E \left[1 - \frac{2}{\pi} |\phi_{sc}(t)| \right] = 1 - \left(\frac{2}{\pi} \right)^{3/2} \exp \left[- \left(\frac{\phi_{sc}^2}{2\sigma_{sc}^2} \right) \right] \times \sigma_{sc} - \frac{2}{\pi} \phi_{scL} \operatorname{erf} \left(\frac{\phi_{scL}}{\sqrt{2}\sigma_{sc}} \right) \quad (10)$$

where ϕ_{scL} is the mean (static) SDA phase error and σ_{sc}^2 is the SDA phase variance. For the reduction effect of the carrier loop we recall from Lindsey (Ref. 7) that when the receiver static phase error is zero,

$$E \{ \cos[\phi_R(t)] \} = \frac{I_1(\rho)}{I_0(\rho)} \quad (11)$$

where $I_\nu(x)$ is the ν th-order modified Bessel function of argument x and ρ is the carrier tracking loop signal-to-noise ratio. For the case when a static receiver phase error is nonzero, the corresponding expression is much more complex but will be approximated by

$$E \{ \cos[\phi_R(t)] \} \approx \frac{I_1(\rho)}{I_0(\rho)} \cos \phi_{RL} \quad (12)$$

where ϕ_{RL} is the static phase error in the receiver loop. Using these results and defining R as the symbol energy to noise density ratio (ST_s/N_0) we have that the degraded signal-to-noise ratio R_d at the input to the data channel lowpass filter is

$$R_d = R \left\{ \left[1 - \left(\frac{2}{\pi} \right)^{3/2} \exp \left(- \frac{\phi_{sc}^2}{2\sigma_{sc}^2} \right) \sigma_{sc} - \frac{2}{\pi} \phi_{scL} \operatorname{erf} \left(\frac{\phi_{scL}}{\sqrt{2}\sigma_{sc}} \right) \right]^2 \times \left[\frac{I_1(\rho)}{I_0(\rho)} \cos \phi_{RL} \right]^2 \right\} \quad (13)$$

and the expression for α' becomes

$$\alpha' = (0.769) \left[\frac{0.887 + 0.2 R_d^{1.2}}{1 + 0.2 R_d^{1.2}} \right] \operatorname{erf} \left(\sqrt{\frac{2 R_d}{3}} \right) \quad (14)$$

Returning now to Eq. (9) and defining

$$K_1(t) = \frac{2\sqrt{2}}{\pi} A \sin m_{PS} \alpha' \cos \omega_c t \quad (15)$$

we see immediately that the diagram in Fig. 2 has the equivalent mathematical model shown in Fig. 3.

To proceed further with this model, we must determine the effects of the soft limiter. The limiter is assumed to have an error function transfer characteristic; that is, the output y is related to the input x by

$$y(x) = L \operatorname{erf} \left(\frac{C \sqrt{\pi}}{2L} x \right) \quad (16)$$

where L is the limiter output asymptotic saturation level and C is the slope of the limiter characteristic at the origin. Furthermore, if we combine the soft limiter with the 10-MHz mixer which follows it, we may treat the combination as a coherent soft limiter. Such a device was studied in Ref. 6, where it was found that for an input sinusoidal signal with an rms amplitude of A_{SL} immersed in narrow-band Gaussian noise of variance σ^2 , the resulting mean output voltage μ_y is given by

$$\mu_y = L \sqrt{\frac{2R_{SL}}{\pi(1+D)}} \exp \left[\frac{-R}{2(1+D)} \right] \times \left\{ I_0 \left[\frac{R}{2(1+D)} \right] + I_1 \left[\frac{R}{2(1+D)} \right] \right\} \cos \theta \quad (17)$$

where θ is the phase angle between the limiter input sinusoidal signal and the coherent detector reference, D is a soft limiter "softness" parameter which depends on the physical parameters of the limiter and the input noise power given by

$$D = \frac{2L^2}{\pi C^2 \sigma^2} \quad (18)$$

and R_{SL} is the soft limiter input signal-to-noise ratio given by

$$R_{SL} = \frac{A_{SL}^2}{\sigma^2} \quad (19)$$

The above expression for μ_y is valid if the detection angle θ is constant. In our case, θ is the random carrier loop phase angle $\phi_R(t)$, so that $\cos \theta$ must be replaced by its

average value given in Eq. (12). If we divide Eq. (17) by the input rms amplitude and use the definition of D , we find that the equivalent gain of the coherent soft limiter is given by

$$\text{Equivalent soft limiter gain} = \alpha_{SL} \frac{I_1(\rho)}{I_0(\rho)} \cos \phi_{RL} \quad (20)$$

where

$$\alpha_{SL} = C \sqrt{\frac{D}{1+D}} \exp \left[-\frac{R_{SL}}{2(1+D)} \right] \left\{ I_0 \left[\frac{R_{SL}}{2(1+D)} \right] + I_1 \left[\frac{R_{SL}}{2(1+D)} \right] \right\} \quad (21)$$

is the soft limiter average slope when the carrier tracking loop phase error is neglected.

To determine the noise at the coherent limiter output, let us define $1/\Gamma_{SL}$ as the ratio of output to input signal-to-noise density ratios. Then we have

$$\left(\frac{\text{Noise}}{\text{density}} \right)_{\text{out}} = \Gamma_{SL} \left(\frac{\text{Signal power out}}{\text{Signal power in}} \right) \left(\frac{\text{Noise}}{\text{density}} \right)_{\text{in}} \quad (22)$$

Since the input noise density is N_0 , we have, using Eq. (20),

$$\left(\frac{\text{Noise}}{\text{density}} \right)_{\text{out}} = \Gamma_{SL} \left[\alpha_{SL} \frac{I_1(\rho)}{I_0(\rho)} \cos \phi_{RL} \right]^2 N_0 \quad (23)$$

Now, if we define

$$K_2 = \frac{K_1(t)}{\sqrt{2} \cos \omega_c t} \quad (24)$$

we obtain the simplified mathematical model shown in Fig. 4. However, it is immediately clear that this model is the same as the one shown in Fig. 5, where we define

$$K_3 = K_2 \alpha_{SL} \frac{I_1(\rho)}{I_0(\rho)} \cos \phi_{RL} \quad (25)$$

In order to use the above model, we must first determine expressions for D , R_{SL} and Γ_{SL} . For the Block III SDA, the virtual signal level (noise-free loop error signal level when the loop phase error is $\pi/2$) at the input to the soft limiter has a strength of +10 dBmW and the limiter saturates at a level of +4 dBmW (sinusoidal). Thus we have

$$D = \frac{0.1599\pi^2 R}{8T_s BW_{FA_2}} \quad (26)$$

where BW_{FA_2} is the one-sided noise bandwidth of the error channel bandpass filter. To determine R_{SL} , we first note from Eq. (9) that the soft limiter input is a random amplitude sine wave immersed in bandlimited Gaussian noise. If we compute the average soft limiter input signal-to-noise ratio and use the fact that

$$R = \frac{ST_s}{N_0} = \frac{A^2 \sin^2 m_{PS} T_s}{N_0} \quad (27)$$

we obtain

$$R_{SL} = \frac{4(\alpha')^2 R}{\pi^2 T_s BW_{FA_2}} [\phi_{SCL}^2 + \sigma_{SC}^2] \quad (28)$$

For determining Γ_{SL} , we note that

$$\frac{1}{\Gamma_{SL}} = \frac{(SNR)_o B_o}{2(SNR)_i B_i}$$

where $(SNR)_i$ and $(SNR)_o$ are the coherent soft limiter input and zonal output signal-to-noise power ratios, B_i is the noise bandwidth of the input bandpass filter ($= BW_{FA_2}$), B_o is the coherent soft limiter output zonal bandwidth, and the factor of 1/2 is necessary for the bandpass-to-lowpass transformation. It was conjectured in Ref. 6 that the bandwidth ratio could be determined from the corresponding ratio for coherent hard limiters by

$$\left(\frac{B_o}{B_i}\right)_{\text{coherent soft limiter}} = \frac{1}{1+D} \left(\frac{B_o}{B_i}\right)_{\text{coherent hard limiter}} + \frac{D}{1+D} \quad (29)$$

where the hard limiter ratio has been experimentally determined by Springett and Simon (Ref. 8) as

$$\left(\frac{B_o}{B_i}\right)_{\text{coherent hard limiter}} = 1 + \left(\frac{4}{\pi\Gamma_0} - 1\right) \exp\left[-R_{SL} \left(1 - \frac{\theta}{2}\right)\right] \quad (30)$$

with Γ_0 determined by the shape of the input bandpass filter ($= 0.862$ for ideal rectangular filter) and θ , ($0 \leq \theta \leq \pi/2$), is the coherent limiter detection reference angle as before. Again we will replace θ by an equivalent angle

$$\theta_{EQ} = \cos^{-1} \left[\frac{I_1(\rho)}{I_0(\rho)} \cos \phi_{RL} \right] \quad (31)$$

Finally, a method for computing the ratio of the soft limiter signal-to-noise power ratios is given in Ref. 6.

The remainder of the subcarrier loop analysis follows in exactly the same manner as in the Brockman papers. For example, the loop noise bandwidth is given by

$$W_{SCL} = \frac{(KK_3 \tau_2^2 + \tau_1) KK_3}{2\tau_1 (KK_3 \tau_2 + 1)} \quad (32)$$

where τ_1 and τ_2 are the time constants of the loop filter which has a transfer function

$$F(S) = \frac{1 + \tau_2 S}{1 + \tau_1 S} \quad (33)$$

Likewise, the subcarrier loop phase error variance is given by

$$\sigma_{SC}^2 = \frac{\pi^2 T_s \Gamma_{SL} W_{SCL}}{8R (\alpha')^2} \quad (34)$$

and the static phase error is

$$\phi_{SCL} = \frac{\Omega_0}{KK_3} \quad (35)$$

where Ω_0 is the subcarrier offset frequency expressed in radians/second.

It is evident at this point that the subcarrier loop equations are given parametrically in terms of the loop static phase error and phase variance. To solve these equations, a two-dimensional Newton algorithm was used to determine simultaneously the values of ϕ_{SCL} and σ_{SC}^2 . The equations were found to be quite well behaved so that the solutions were obtained after just a few iterations.

III. Summary of the Results

A cursory comparison of the model presented here and the earlier Brockman model indicates a negligible difference in the effective signal strength degradation as given in Eq. (10). However, a more detailed examination shows that the two models differ when considering

- (1) Low symbol rates.
- (2) Subcarrier doppler offsets.
- (3) Carrier tracking loop phase errors.

We shall examine each of these in more detail.

A. Low Symbol Rates

At low symbol rates, the signal-to-noise spectral density ratio S/N_0 is generally quite small and usually results in

an increase in subcarrier loop phase noise. In the model presented here, this phase noise affects the loop equations to further degrade the loop performance. Comparisons of signal-to-noise ratio degradations for the two models at design point symbol rates are shown in Figs. 6–8.

B. Subcarrier Doppler Offsets

When the received subcarrier frequency differs from the value established by the SDA synthesizer, a static phase error (SPE) results within the subcarrier loop. Previous models have predicted that this error is a linear function of subcarrier offset frequency. In the above model, the subcarrier phase error is allowed to degrade (reduce) data limiter gain α' . At the same time, the SPE causes an increase in soft limiter input signal which, in turn, causes a reduction in the soft limiter gain. These gain reductions have the effect of diminishing the ability of the subcarrier loop to track doppler, which further increases the SPE. The result is that the SPE is related to the offset frequency in a parabolic manner as shown in Fig. 9.

Another quantity affected by subcarrier offsets is the loop phase jitter. The reduction of α' and α_{SL} causes the

loop bandwidth to decrease. At the same time, the increased loop error signal causes Γ_{SL} to decrease. However, at low signal-to-noise ratios, the reduction of α' occurs at a sufficiently fast rate to override the decreasing $\Gamma_{SL} W_{SCL}$ product so that the jitter increases. On the other hand, when the SNR is high the reduction of α' occurs much more slowly and results in a decreasing phase jitter. These variations in phase jitter, however, are quite small and for most purposes can be neglected.

C. Carrier Tracking Loop Phase Errors

When carrier tracking errors occur, the subcarrier loop gain is decreased directly at the error channel IF mixer as well as indirectly through α' and renders the loop more susceptible to doppler shift. The subcarrier phase jitter is also affected by tracking errors in a manner similar to that when doppler offsets exist. The main difference between the two is that when tracking errors exist the SDA jitter increases only when both the signal-to-noise ratio and the symbol rate are low. This occurs because the SDA phase jitter is small at high symbol rates (regardless of SNR) and hence produces little degradation of α' . As before, these variations in the value of jitter are extremely small and, for most practical purposes, can be neglected.

References

1. Brockman, M. H., "MMT Subcarrier Demodulator," SPS 37-46, Vol. III, Jet Propulsion Laboratory, Pasadena, Calif., July 1967, pp. 189–204.
2. Brockman, M. H., "Analysis of the Subcarrier Demodulator," SPS 37-48, Vol. II, Jet Propulsion Laboratory, Pasadena, Calif., November 1967, pp. 124–129.
3. Brockman, M. H., "Subcarrier Demodulator Analysis," SPS 37-49, Vol. II, Jet Propulsion Laboratory, Pasadena, Calif., January 1968, pp. 100–113.
4. Brockman, M. H., "MMTS: Performance of the Subcarrier Demodulator," SPS 37-52, Vol. II, Jet Propulsion Laboratory, Pasadena Calif., July 1968, pp. 127–141.
5. Brockman, M. H., "An Efficient and Versatile Telemetry Subcarrier Demodulation Technique for Deep Space Telecommunications," Proc. 4th Hawaiian International Conference on System Science, January 1971.
6. Lesh, J. R., "Signal to Noise Ratios in Coherent Soft Limiters," submitted to *I.E.E.E. Transactions on Communications*.
7. Lindsey, W. C., "Performance of Phase-Coherent Receivers Preceded by Bandpass Limiters," *I.E.E.E. Trans. Comm. Tech.*, Vol. Comm 16, No. 2, pp. 245–251, April 1968.
8. Springett, J. C., and Simon, M. K., "An Analysis of the Phase Coherent-Incoherent Output of the Bandpass Limiter," *I.E.E.E. Trans. Comm. Tech.*, Vol. Comm. 19, No. 1, pp. 42–49, February 1971.

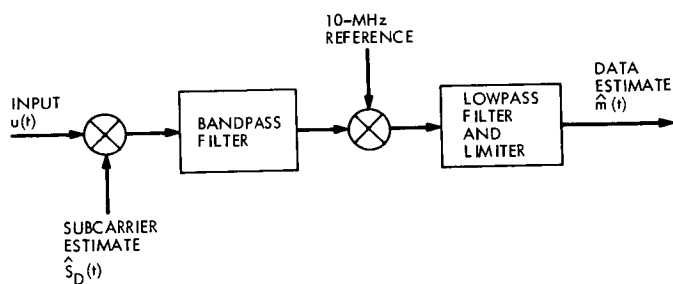


Fig. 1. Block diagram, SDA data channel

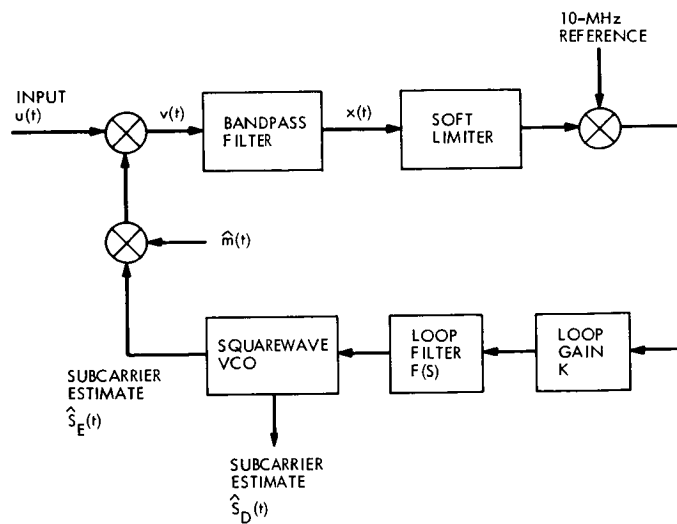


Fig. 2. Block diagram, SDA error channel

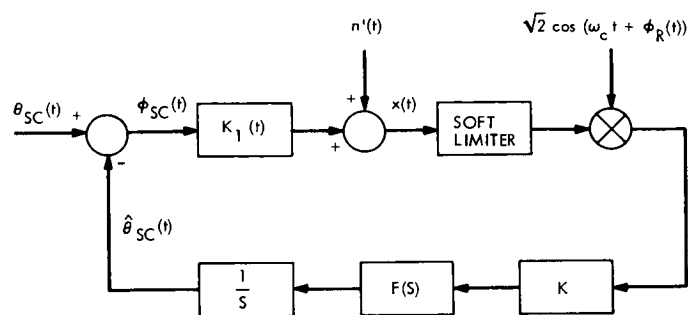


Fig. 3. Mathematical model, SDA error channel

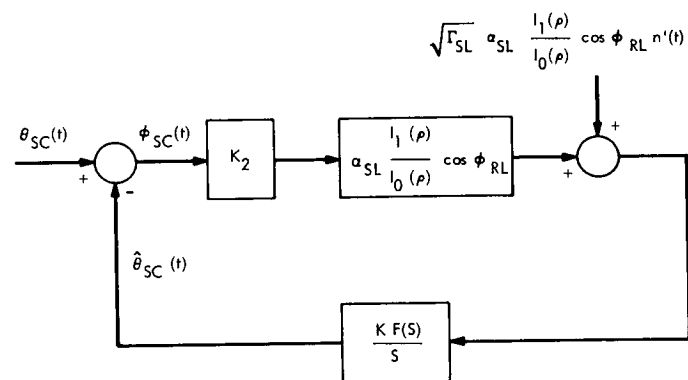


Fig. 4. Reduced mathematical model

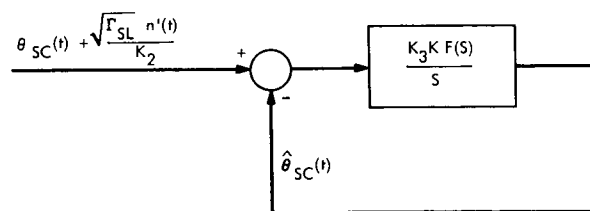


Fig. 5. Simplified mathematical model

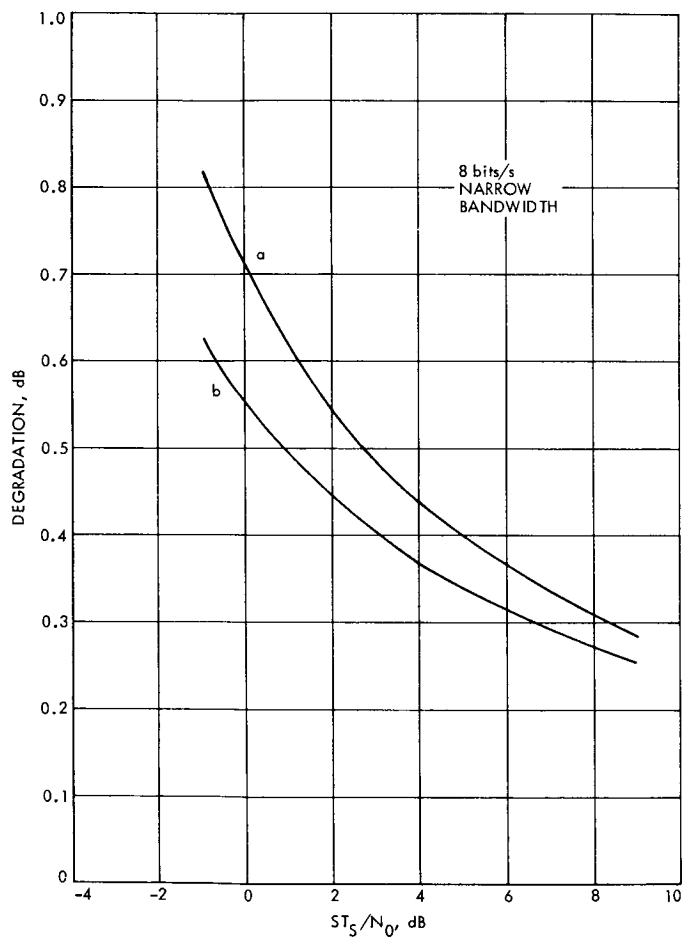


Fig. 6. SNR degradation, (a) new model, (b) previous model, at 8 bits/s

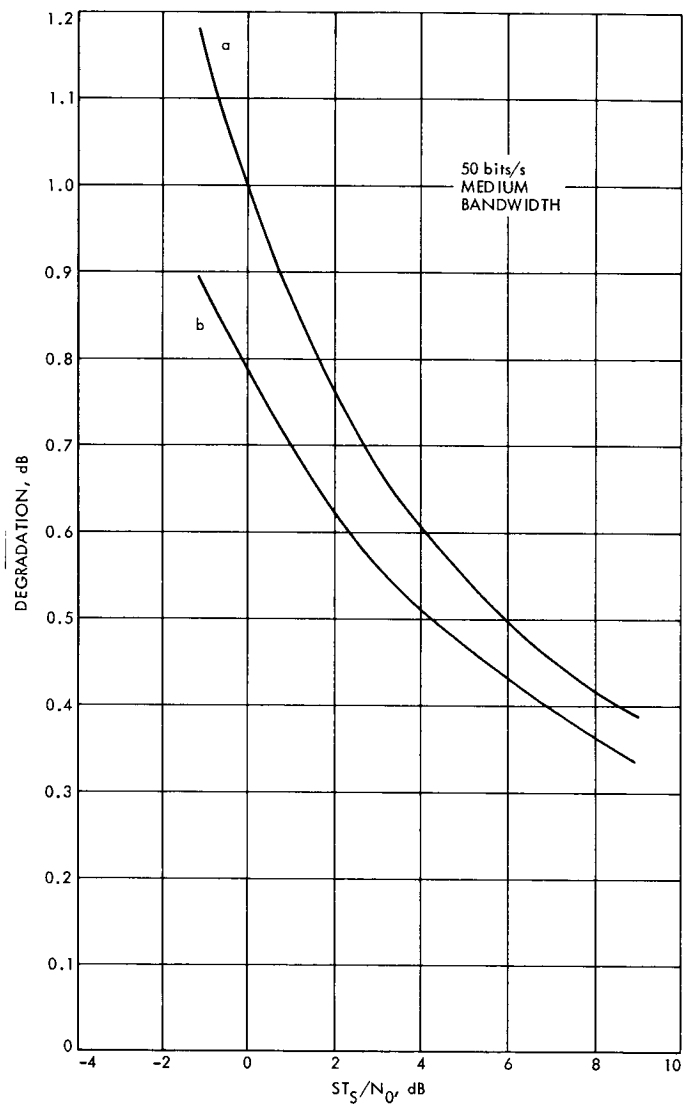


Fig. 7. SNR degradation, (a) new model, (b) previous model, at 50 bits/s

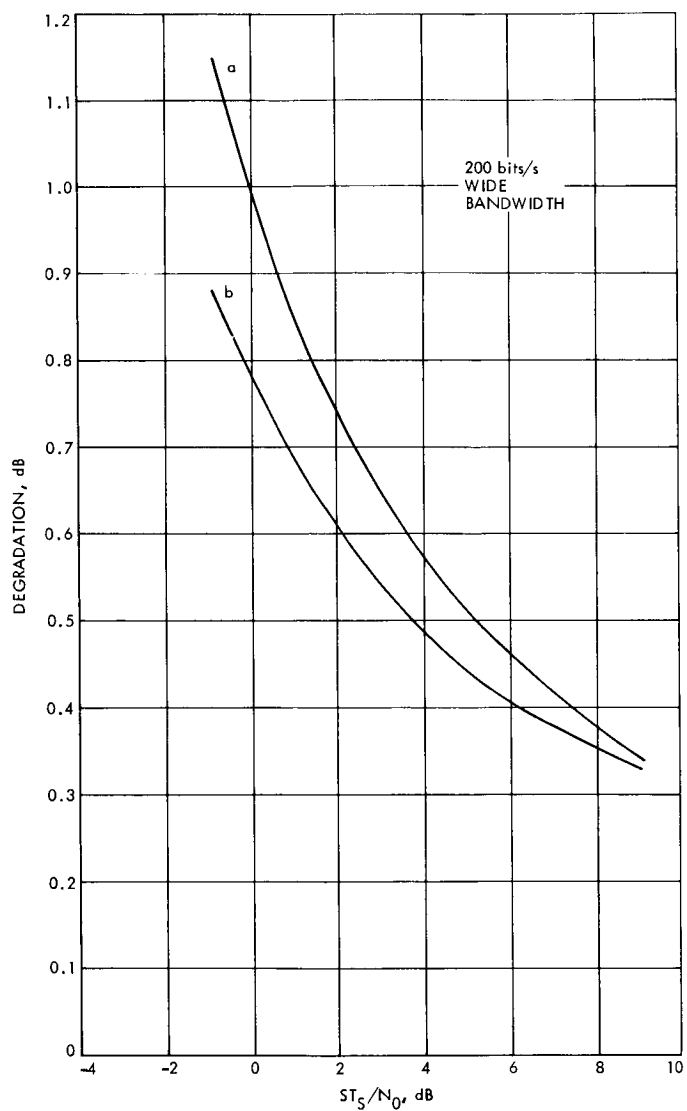


Fig. 8. SNR degradation, (a) new model, (b) previous model, at 200 bits/s

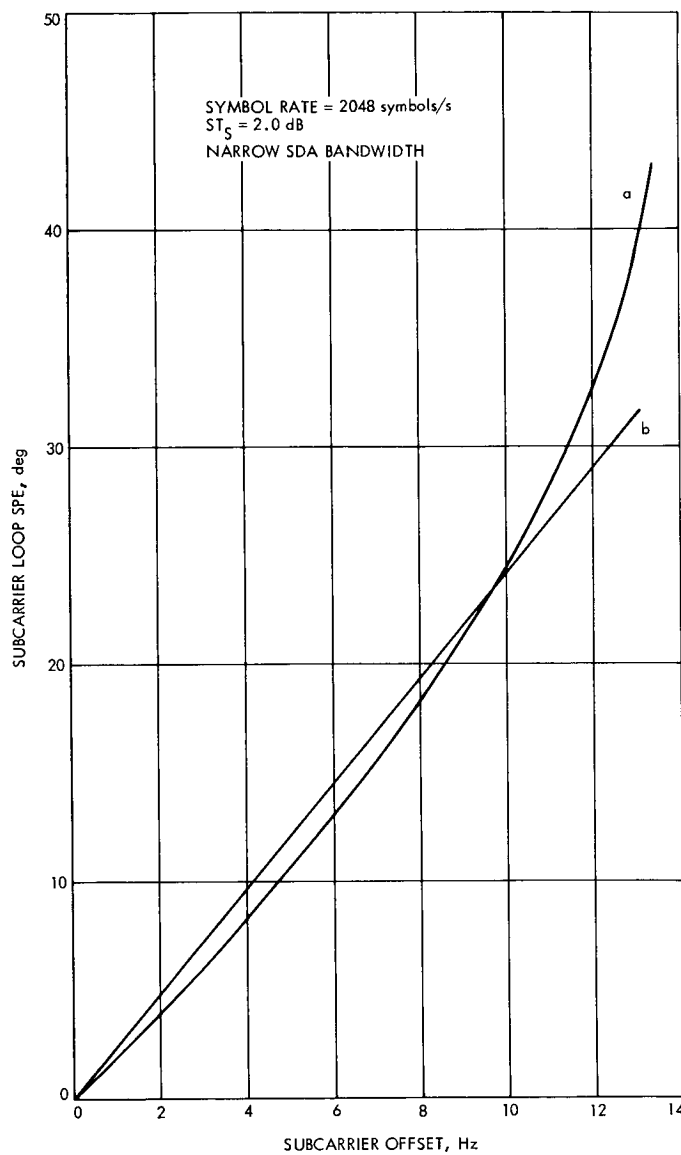


Fig. 9. Static phase error vs subcarrier offset for (a) new model, (b) previous model

Bibliography

- Anderson, J. D., *Determination of the Masses of the Moon and Venus and the Astronomical Unit from Radio Tracking Data of the Mariner II Spacecraft*, Technical Report 32-816. Jet Propulsion Laboratory, Pasadena, Calif., July 1, 1967.
- Anderson, J. D., et al., "The Radius of Venus as Determined by Planetary Radar and Mariner V Radio Tracking Data," *J. Atmos. Sci.*, pp. 1171-1174, Sept. 25, 1968.
- Anderson, J. D., "Determination of Astrodynamic Constants and a Test of the General Relativistic Time Delay With S-Band Range and Doppler Data From Mariners 6 and 7," *Space Research*, Vol. XI, pp. 105-112, Akademie-Verlag, Berlin, 1971.
- Barnum, P. W., et al., *Tracking and Data System Support for the Mariner Mars 1971 Mission: Orbit Insertion Through End of Primary Mission*, Technical Memorandum 33-523, Vol. III. Jet Propulsion Laboratory, Pasadena, Calif., May 15, 1973.
- Bathker, D. A., *Predicted and Measured Power Density Description of a Large Ground Microwave System*, Technical Memorandum 33-433. Jet Propulsion Laboratory, Pasadena, Calif., Apr. 15, 1971.
- Berman, A. L., *Tracking System Data Analysis Report, Ranger VII Final Report*, Technical Report 32-719. Jet Propulsion Laboratory, Pasadena, Calif., June 1, 1965.
- Butman, S., "Rate Distortion Over Band-Limited Feedback Channels," *IEEE Trans. Inform. Theory*, Vol. IT-17, No. 1, pp. 110-112, Jan. 1971.
- Butman, S., and Timor, U., "Interplex—An Efficient Multichannel PSK/PM Telemetry System," *IEEE Trans. Commun.*, Vol. COM-20, No. 3, pp. 415-419, June 1972.
- Cain, D. L., and Hamilton, T. W., *Determination of Tracking Station Locations by Doppler and Range Measurements to an Earth Satellite*, Technical Report 32-534. Jet Propulsion Laboratory, Pasadena, Calif., Feb. 1, 1964.
- Carey, C. N., and Sjogren, W. L., "Gravitational Inconsistency in the Lunar Theory: Confirmation by Radio Tracking," *Science*, Vol. 160, pp. 875-876, April-June 1968.
- Chadwick, H. D., and Springett, J. C., "The Design of a Low Data Rate MSFK Communication System," *IEEE Trans. Commun. Technol.*, Vol. COM-18, No. 6, pp. 740-750, Dec. 1970.
- Clark, B. G., et al., "High Resolution Observations of Compact Radio Sources at 13 cm," *Astrophys. J.*, Vol. 161, pp. 803-809, Sept. 1970.
- Curkendall, D. W., and Stephenson, R. R., "Earthbased Tracking and Orbit Determination—Backbone of the Planetary Navigation System," *Astronaut. Aeronaut.*, Vol. 7, May 1970.
- Curkendall, D. W., "Planetary Navigation: The New Challenges," *Astronaut. Aeronaut.*, Vol. 7, May 1970.

Bibliography (contd)

- Downs, G. S., and Reichley, P. E., "Observations of Interstellar Scintillations of Pulsar Signals at 2388 MHz," *Astrophys. J.*, Vol. 163, No. 1, Pt. 2, pp. L11-L16, Jan. 1971.
- Downs, G. S., et al., "Mars Radar Observation, A Preliminary Report," *Science*, Vol. 174, No. 4016, pp. 1324-1327, Dec. 24, 1971.
- Efron, L., and Solloway, C. B., *Proceedings of the Conference on Scientific Applications of Radio and Radar Tracking in the Space Program, Technical Report 32-1475*. Jet Propulsion Laboratory, Pasadena, Calif., July 1970.
- Flanagan, F. M., et al., *Deep Space Network Support of the Manned Space Flight Network for Apollo: 1962-1968*, Technical Memorandum 33-452, Vol. I. Jet Propulsion Laboratory, Pasadena, Calif., July 1970.
- Flanagan, F. M., et al., *Deep Space Network Support of the Manned Space Flight Network for Apollo: 1969-1970*, Technical Memorandum 33-452, Vol. II. Jet Propulsion Laboratory, Pasadena, Calif., May 1, 1971.
- Fjeldbo, G., and Eshleman, V. R., "Radio Occultation Measurements and Interpretations," in *The Atmospheres of Venus and Mars*, p. 225. Gordon and Breach, Science Publishers, Inc., New York, N.Y.
- Georgevic, R. M., *Mathematical Model of the Solar Radiation Force and Torques Acting on the Components of a Spacecraft*, Technical Memorandum 33-494. Jet Propulsion Laboratory, Pasadena, Calif., Oct. 1, 1971.
- Goldstein, R. M., "Radar Time-of-Flight Measurements to Venus," *Astron. J.*, Vol. 73, No. 9, Aug. 1968.
- Goldstein, R. M., and Rumsey, H., Jr., "A Radar Snapshot of Venus," *Science*, Vol. 169, Sept. 1970.
- Goldstein, R. M., "Radar Observations of Mercury," *Astron. J.*, Vol. 76, No. 10, pp. 1152-1154, Dec. 1971.
- Gordon, H. J., et al., *The Mariner 6 and 7 Flight Paths and Their Determination From Tracking Data*, Technical Memorandum 33-469. Jet Propulsion Laboratory, Pasadena, Calif., Dec. 1, 1970.
- Gray, R. M., and Tausworthe, R. C., "Frequency-Counted Measurements, and Phase Locking to Noise Oscillators," *IEEE Trans. Commun. Technol.*, Vol. COM-19, No. 1, pp. 21-30, Feb. 1971.
- Gulkis, S., and Gary, B., "Circular Polarization and Total-Flux Measurements of Jupiter at 13.1 cm Wavelength," *Astron. J.*, Vol. 76, No. 1, pp. 12-16, Feb. 1971.
- Hamilton, T. W., et al., *The Ranger IV Flight Path and Its Determination From Tracking Data*, Technical Report 32-345. Jet Propulsion Laboratory, Pasadena, Calif., Sept. 15, 1962.
- Holmes, J. K., "First Slip Times Versus Static Phase Error Offset for the First and Passive Second-Order Phase-Locked Loop," *IEEE Trans. Commun. Technol.*, Vol. COM-19, No. 2, pp. 234-235, Apr. 1971.
- Holmes, J. K., and Tegnalia, C. R., *Digital Command System Second-Order Sub-carrier Tracking Performance*, Technical Report 32-1540. Jet Propulsion Laboratory, Pasadena, Calif., Oct. 1, 1971.

Bibliography (contd)

- Holmes, J. K., "Performance of a First Order Transition Sampling Digital Phase-Locked Loop Using Random-Walk Models," *IEEE Trans. Commun.*, Vol. COM-20, No. 2, pp. 119-131, Apr. 1972.
- Kliore, A., "Radio Occultation Measurements of the Atmospheres of Mars and Venus," in *The Atmospheres of Venus and Mars*, by J. C. Brandt and M. E. McElrow, p. 205. Gordon and Breach Science Publishers, Inc., New York, N.Y., 1968.
- Kliore, A. J., et al., "Summary of Mariner 6 and 7 Radio Occultation Results on the Atmosphere of Mars," *Space Research*, Vol. XI, pp. 165-175, Akademie-Verlag, Berlin, 1971.
- Labrum, R. G., et al., *The Surveyor V, VI, and VII Flight Paths and Their Determination from Tracking Data*, Technical Report 32-1302. Jet Propulsion Laboratory, Pasadena, Calif., Dec. 1, 1968.
- Laeser, R. P., et al., *Tracking and Data System Support for the Mariner Mars 1971 Mission: Prelaunch Phase Through First Trajectory Correction Maneuver*, Technical Memorandum 33-523, Vol. I. Jet Propulsion Laboratory, Pasadena, Calif., Mar. 15, 1972.
- Layland, J. W., and Lushbaugh, W. A., "A Flexible High-Speed Sequential Decoder for Deep Space Channels," *IEEE Trans. Commun. Technol.*, Vol. COM-19 No. 5, pp. 813-820, Oct. 1971.
- Leavitt, R. K., *The Least-Squares Process of MEDIA for Computing DRVID Calibration Polynomials*, Technical Memorandum 33-542. Jet Propulsion Laboratory, Pasadena, Calif., May 15, 1972.
- Lieske, J. H., and Null, G. W., "Icarus and the Determination of Astronomical Constants," *Astron. J.*, Vol. 74, No. 2, Mar. 1969.
- Lindsey, W. C., and Simon, M. K., "The Effect of Loop Stress on the Performance of Phase-Coherent Communication Systems," *IEEE Trans. Commun. Technol.*, Vol. COM-18, No. 5, pp. 569-588, Oct. 1970.
- Lindsey, W. C., and Simon, M. K., "Carrier Synchronization and Detection of Polyphase Signals," *IEEE Trans. Commun.*, Vol. COM-20, No. 3, pp. 441-454, June 1972.
- Lorell, J., and Sjogren, W. L., *Lunar Orbiter Data Analysis*, Technical Report 32-1220. Jet Propulsion Laboratory, Pasadena, Calif., Nov. 15, 1967.
- Lorell, J., *Lunar Orbiter Gravity Analysis*, Technical Report 32-1387. Jet Propulsion Laboratory, Pasadena, Calif., June 15, 1969.
- Lorell, J., et al., "Celestial Mechanics Experiment for Mariner," *Icarus*, Vol. 12, Jan. 1970.
- Ludwig, A. C., et al., *Gain Calibration of a Horn Antenna Using Pattern Integration*, Technical Report 32-1572. Jet Propulsion Laboratory, Pasadena, Calif., Oct. 1, 1972.
- McNeal, C. E., *Ranger V Tracking Systems Data Analysis Final Report*, Technical Report 32-702. Jet Propulsion Laboratory, Pasadena, Calif., Apr. 15, 1965.

Bibliography (contd)

- Melbourne, W. G., et al., *Constants and Related Information for Astrodynamical Calculations*, Technical Report 32-1306. Jet Propulsion Laboratory, Pasadena, Calif., July 15, 1968.
- Melbourne, W. G., "Planetary Ephemerides," *Astronaut. Aeronaut.*, Vol. 7, May 1970.
- Miller, L., et al., *The Atlas-Centaur VI Flight Path and Its Determination from Tracking Data*, Technical Report 32-911. Jet Propulsion Laboratory, Pasadena, Calif., Apr. 15, 1966.
- Moyer, T. D., *Mathematical Formulation of the Double-Precision Orbit Determination Program (DPODP)*, Technical Report 32-1527. Jet Propulsion Laboratory, Pasadena, Calif., May 17, 1971.
- Mulhall, B. D., et al., *Tracking System Analytic Calibration Activities for the Mariner Mars 1969 Mission*, Technical Report 32-1499. Jet Propulsion Laboratory, Pasadena, Calif., Nov. 15, 1970.
- Mulholland, J. D., and Sjogren, W. L., *Lunar Orbiter Ranging Data*, Technical Report 32-1087. Jet Propulsion Laboratory, Pasadena, Calif., Jan. 6, 1967.
- Mulholland, J. D., *Proceedings of the Symposium on Observation, Analysis, and Space Research Applications of the Lunar Motion*, Technical Report 32-1386. Jet Propulsion Laboratory, Pasadena, Calif., Apr. 1969.
- Muller, P. M., and Sjogren, W. L., *Consistency of Lunar Orbiter Residuals With Trajectory and Local Gravity Effects*, Technical Report 32-1307. Jet Propulsion Laboratory, Pasadena, Calif., Sept. 1, 1968.
- Muller, P. M., and Sjogren, W. L., *Lunar Mass Concentrations*, Technical Report 32-1339. Jet Propulsion Laboratory, Pasadena, Calif., Aug. 16, 1968.
- Null, G. W., et al., *Mariner IV Flight Path and Its Determination From Tracking Data*, Technical Report 32-1108. Jet Propulsion Laboratory, Pasadena, Calif., Aug. 1, 1967.
- O'Neil, W. J., et al., *The Surveyor III and Surveyor IV Flight Paths and Their Determination From Tracking Data*, Technical Report 32-1292. Jet Propulsion Laboratory, Pasadena, Calif., Aug. 15, 1968.
- Otoshi, T. Y., and Stelzried, C. T., "A Precision Compact Rotary Vane Attenuator," *IEEE Trans. Micro. Theor. Technique*, Vol. MTT-19, No. 11, pp. 843-854, Nov. 1971.
- Pease, G. E., et al., *The Mariner V Flight Path and Its Determination From Tracking Data*, Technical Report 32-1363. Jet Propulsion Laboratory, Pasadena, Calif., July 1, 1969.
- Renzetti, N. A., *Tracking and Data Acquisition for Ranger Missions I-V*, Technical Memorandum 33-174. Jet Propulsion Laboratory, Pasadena, Calif., July 1, 1964.
- Renzetti, N. A., *Tracking and Data Acquisition for Ranger Missions VI-IX*, Technical Memorandum 33-275. Jet Propulsion Laboratory, Pasadena, Calif., Sept. 15, 1966.

Bibliography (contd)

- Renzetti, N. A., *Tracking and Data Acquisition Support for the Mariner Venus 1962 Mission*, Technical Memorandum 33-212. Jet Propulsion Laboratory, Pasadena, Calif., July 1, 1965.
- Renzetti, N. A., *Tracking and Data Acquisition Report, Mariner Mars 1964 Mission: Near-Earth Trajectory Phase*, Technical Memorandum 33-239, Vol. I. Jet Propulsion Laboratory, Pasadena, Calif., Jan. 1, 1965.
- Renzetti, N. A., *Tracking and Data Acquisition Report, Mariner Mars 1964 Mission: Cruise to Post-Encounter Phase*, Technical Memorandum 33-239, Vol. II. Jet Propulsion Laboratory, Pasadena, Calif., Oct. 1, 1967.
- Renzetti, N. A., *Tracking and Data Acquisition Report, Mariner Mars 1964 Mission: Extended Mission*, Technical Memorandum 33-239, Vol. III. Jet Propulsion Laboratory, Pasadena, Calif., Dec. 1, 1968.
- Renzetti, N. A., *Tracking and Data System Support for Surveyor: Missions I and II*, Technical Memorandum 33-301, Vol. I. Jet Propulsion Laboratory, Pasadena, Calif., July 15, 1969.
- Renzetti, N. A., *Tracking and Data System Support for Surveyor: Missions III and IV*, Technical Memorandum 33-301, Vol. II. Jet Propulsion Laboratory, Pasadena, Calif., Sept. 1, 1969.
- Renzetti, N. A., *Tracking and Data System Support for Surveyor: Mission V*, Technical Memorandum 33-301, Vol. III. Jet Propulsion Laboratory, Pasadena, Calif., Dec. 1, 1969.
- Renzetti, N. A., *Tracking and Data System Support for Surveyor: Mission VI*, Technical Memorandum 33-301, Vol. IV. Jet Propulsion Laboratory, Pasadena, Calif., Dec. 1, 1969.
- Renzetti, N. A., *Tracking and Data System Support for Surveyor: Mission VII*, Technical Memorandum 33-301, Vol. V. Jet Propulsion Laboratory, Pasadena, Calif., Dec. 1, 1969.
- Renzetti, N. A., *Tracking and Data System Support for the Mariner Venus 67 Mission: Planning Phase Through Midcourse Maneuver*, Technical Memorandum 33-385, Vol. I. Jet Propulsion Laboratory, Pasadena, Calif., Sept. 1, 1969.
- Renzetti, N. A., *Tracking and Data System Support for the Mariner Venus 67 Mission: Midcourse Maneuver Through End of Mission*, Technical Memorandum 33-385, Vol. II. Jet Propulsion Laboratory, Pasadena, Calif., Sept. 1, 1969.
- Renzetti, N. A., *Tracking and Data System Support for the Pioneer Project. Pioneer VI. Prelaunch to End of Nominal Mission*, Technical Memorandum 33-426, Vol. I. Jet Propulsion Laboratory, Pasadena, Calif., Feb. 1, 1970.
- Renzetti, N. A., *Tracking and Data System Support for the Pioneer Project. Pioneer VII. Prelaunch to End of Nominal Mission*, Technical Memorandum 33-426, Vol. II. Jet Propulsion Laboratory, Pasadena, Calif., Apr. 15, 1970.
- Renzetti, N. A., *Tracking and Data System Support for the Pioneer Project. Pioneer VIII. Prelaunch Through May 1968*, Technical Memorandum 33-426, Vol. III. Jet Propulsion Laboratory, Pasadena, Calif., July 15, 1970.

Bibliography (contd)

- Renzetti, N. A., *Tracking and Data System Support for the Pioneer Project. Pioneer IX. Prelaunch Through June 1969*, Technical Memorandum 33-426, Vol. IV. Jet Propulsion Laboratory, Pasadena, Calif., Nov. 15, 1970.
- Renzetti, N. A., *Tracking and Data System Support for the Pioneer Project. Pioneer VI. Extended Mission: July 1, 1966–July 1, 1969*, Technical Memorandum 33-426, Vol. V. Jet Propulsion Laboratory, Pasadena, Calif., Feb. 1, 1971.
- Renzetti, N. A., *Tracking and Data System Support for the Pioneer Project. Pioneer VII. Extended Mission: February 24, 1967–July 1, 1968*, Technical Memorandum 33-426, Vol. VI. Jet Propulsion Laboratory, Pasadena, Calif., Apr. 15, 1971.
- Renzetti, N. A., *Tracking and Data System Support for the Pioneer Project. Pioneer VII. Extended Mission: July 1, 1968–July 1, 1969*, Technical Memorandum 33-426, Vol. VII. Jet Propulsion Laboratory, Pasadena, Calif., Apr. 15, 1971.
- Renzetti, N. A., *Tracking and Data System Support for the Pioneer Project. Pioneer VIII. Extended Mission: June 1, 1968–July 1, 1969*, Technical Memorandum 33-426, Vol. VIII. Jet Propulsion Laboratory, Pasadena, Calif., May 1, 1971.
- Renzetti, N. A., *Tracking and Data System Support for the Pioneer Project. Pioneers VI–IX. Extended Missions: July 1, 1969–July 1, 1970*, Technical Memorandum 33-426, Vol. IX. Jet Propulsion Laboratory, Pasadena, Calif., Aug. 15, 1971.
- Renzetti, N. A., and Siegmeth, A. J., *Tracking and Data System Support for the Pioneer Project. Pioneers 6–9. Extended Missions: July 1, 1971–July 1 1972*, Technical Memorandum 33-426, Vol. XI. Jet Propulsion Laboratory, Pasadena, Calif., May 1, 1973.
- Siegmeth, A. J., Purdue, R. E., and Ryan, R. E., *Tracking and Data System Support for the Pioneer Project. Pioneers 6–9. Extended Missions: July 1, 1970–July 1, 1971*, Technical Memorandum 33-426, Vol. X. Jet Propulsion Laboratory, Pasadena, Calif., Aug. 15, 1972.
- Siegmeth, A. J., et al., *Tracking and Data System Support for the Pioneer Project. Pioneer 10—Prelaunch Planning Through Second Trajectory Correction December 4, 1969 to April 1, 1972*, Technical Memorandum 33-584, Vol. I. Jet Propulsion Laboratory, Pasadena, Calif., Apr. 1, 1973.
- Simon, M. K., "Nonlinear Analysis of an Absolute Value Type of an Early-Late Gate Bit Synchronizer," *IEEE Trans. Commun. Technol.*, Vol. COM-18, No. 5, pp. 589–596, Oct. 1970.
- Simon, M. K., and Lindsey, W. C., "Data-Aided Carrier Tracking Loops," *IEEE Trans. Commun. Technol.*, Vol. COM-19, No. 2, pp. 157–168, Apr. 1971.
- Simon, M. K., "On the Selection of an Optimum Design Point for Phase-Coherent Receivers Employing Bandpass Limiters," *IEEE Trans. Commun.*, Vol. COM-20, No. 2, pp. 210–214, Apr. 1972.
- Simon, M. K., "On the Selection of a Sampling Filter Bandwidth for a Digital Data Detector," *IEEE Trans. Commun.*, Vol. COM-20, No. 3, pp. 438–441, June 1972.

Bibliography (contd)

- Sjogren, W. L., et al., *The Ranger V Flight Path and Its Determination From Tracking Data*, Technical Report 32-562. Jet Propulsion Laboratory, Pasadena, Calif., Dec. 6, 1963.
- Sjogren, W. L., et al., *The Ranger VI Flight Path and Its Determination From Tracking Data*, Technical Report 32-605. Jet Propulsion Laboratory, Pasadena, Calif., Dec. 15, 1964.
- Sjogren, W. L., *The Ranger III Flight Path and Its Determination From Tracking Data*, Technical Report 32-563. Jet Propulsion Laboratory, Pasadena, Calif., Sept. 15, 1965.
- Sjogren, W. L., et al., *Physical Constants as Determined From Radio Tracking of the Ranger Lunar Probes*, Technical Report 32-1057. Jet Propulsion Laboratory, Pasadena, Calif., Dec. 30, 1966.
- Sjogren, W. L., *Proceedings of the JPL Seminar on Uncertainties in the Lunar Ephemeris*, Technical Report 32-1247. Jet Propulsion Laboratory, Pasadena, Calif., May 1, 1968.
- Sjogren, W. L., "Lunar Gravity Estimate: Independent Confirmation," *J. Geophys. Res.*, Vol. 76, No. 29, Oct. 10, 1971.
- Sjogren, W. L., et al., "Lunar Gravity via Apollo 14 Doppler Radio Tracking," *Science*, Vol. 175, No. 4018, pp. 165-168, Jan. 14, 1972.
- Spier, G. W., *Design and Implementation of Models for the Double Precision Trajectory Program (DPTRAJ)*, Technical Memorandum 33-451. Jet Propulsion Laboratory, Pasadena, Calif., Apr. 15, 1971.
- Springett, J. C., and Simon, M. K., "An Analysis of the Phase Coherent-Incoherent Output of the Bandpass Limiter," *IEEE Trans. Commun. Technol.*, Vol. COM-19, No. 1, pp. 42-49, Feb. 1971.
- Stelzried, C. T., *A Faraday Rotation Measurement of a 13-cm Signal in the Solar Corona*, Technical Report 32-1401. Jet Propulsion Laboratory, Pasadena, Calif., July 15, 1970.
- Stelzried, C. T., et al., "The Quasi-Stationary Coronal Magnetic Field and Electron Density as Determined From a Faraday Rotation Experiment," *Sol. Phys.*, Vol. 14, No. 2, pp. 440-456, Oct. 1970.
- Stelzried, C. T., "Operating Noise-Temperature Calibrations of Low-Noise Receiving Systems," *Microwave J.*, Vol. 14, No. 6, pp. 41-46, 48, June 1971.
- Stelzried, C. T., et al., "Transformation of Received Signal Polarization Angle to the Plane of the Ecliptic," *J. Space. Rock.*, Vol. 9, No. 2, pp. 69-70, Feb. 1972.
- Tausworthe, R. C., "Simplified Formula for Mean-Slip Time of Phase-Locked Loops With Steady-State Phase Error," *IEEE Trans. Commun.*, Vol. COM-20, No. 3, pp. 331-337, June 1972.
- Textor, G. P., Kelly, L. B., and Kelly, M., *Tracking and Data System Support for the Mariner Mars 1971 Mission: First Trajectory Correction Maneuver Through Orbit Insertion*, Technical Memorandum 33-523, Vol. II. Jet Propulsion Laboratory, Pasadena, Calif., June 15, 1972.

Bibliography (contd)

- Thornton, J. H., Jr., *The Surveyor I and Surveyor II Flight Paths and Their Determination From Tracking Data*, Technical Report 32-1285. Jet Propulsion Laboratory, Pasadena, Calif., Aug. 1, 1968.
- Timor, U., "Equivalence of Time-Multiplexed and Frequency-Multiplexed Signals in Digital Communications," *IEEE Trans. Commun.*, Vol. COM-20, No. 3, pp. 435-438, June 1972.
- Vegos, C. J., et al., *The Ranger IX Flight Path and Its Determination From Tracking Data*, Technical Report 32-767. Jet Propulsion Laboratory, Pasadena, Calif., Nov. 1, 1968.
- Winn, F. B., *Selenographic Location of Surveyor VI, Surveyor VI Mission Report: Part II. Science Results*, Technical Report 32-1262. Jet Propulsion Laboratory, Pasadena, Calif., Jan. 10, 1968.
- Winn, F. B., "Post Landing Tracking Data Analysis," in *Surveyor VII Mission Report: Part II. Science Results*, Technical Report 32-1264. Jet Propulsion Laboratory, Pasadena, Calif., Mar. 15, 1968.
- Winn, F. B., "Post Lunar Touchdown Tracking Data Analysis," in *Surveyor Project Final Report: Part II. Science Results*, Technical Report 32-1265. Jet Propulsion Laboratory, Pasadena, Calif., June 15, 1968.
- Winn, F. B., *Surveyor Posttouchdown Analyses of Tracking Data*, NASA SP-184. National Aeronautics and Space Administration, Washington, D.C., p. 369.
- Wollenhaupt, W. R., et al., *The Ranger VII Flight Path and Its Determination From Tracking Data*, Technical Report 32-694. Jet Propulsion Laboratory, Pasadena, Calif., Dec. 15, 1964.